University of Nottingham
UK | CHINA | MALAYSIA

Biotechnology and Biological Sciences Research Council

The molecular basis of atypicality in antipsychotic drug action

Hannah Jane Lockington, BSc (Hons)

Thesis submitted to the University of Nottingham

for the degree of Doctor of Philosophy

February 2025

I. ABSTRACT

Dopamine D2 receptor (D2R) antagonism is thought to be the pharmacological mechanism behind the clinical efficacy of antipsychotic drugs (APDs) in treating the positive symptoms of schizophrenia. Unfortunately, D2R antagonism is also associated with extrapyramidal symptoms (EPS) that encompass a range of motor side effects. More recently developed APDs are termed 'atypical' based on their low propensity to cause EPS. Despite several suggested hypotheses, no single mechanism has yet to account for all cases of atypicality in clinically prescribed APDs. This thesis explored two promising molecular mechanisms recently proposed to account for APD atypicality: (1) the reduced rebinding of atypical APDs to D2R resulting in surmountable D2R antagonism and (2) the low efficacy of atypical APDs as pharmacological chaperones of D2R, resulting in reduced D2R upregulation to the cell surface.

First, in-solution reads of fluorescent APDs with differing binding kinetics at D2R, spiperone-d2 and clozapine-Cy5, were optimised using the advanced spectroscopy technique, fluorescence correlation spectroscopy (FCS). In addition, the variable expression of SNAP-D2R in a CHO tetracycline-inducible SNAP-D2R cell line was characterised using confocal imaging and FCS. FCS was also used to investigate the membrane dynamics of SNAP-D2R within CHO tetracycline-inducible SNAP-D2R cells which revealed that a small percentage of receptors may form clusters on the plasma membrane.

Subsequently, the rebinding effects of these fluorescent APDs at D2R were investigated by measuring their concentration above cells with a range of SNAP-D2R expression levels. A high concentration of spiperone-d2 was found near the upper membrane of D2R-expressing cells which decreased further away from cells into the bulk aqueous solution. Interestingly, spiperone-d2 formed concentration gradients above cells that were dependent on the level of SNAP-D2R expression at the plasma membrane. These concentration gradients were indicative of spiperone-d2 rebinding to D2R and provided evidence of drug rebinding *in vitro*. In contrast, clozapine-Cy5, which has a slower association rate, showed negligible concentrating effects above

D2R-expressing cells. When an added concentration of 0.2 x K_d of each fluorescent APD was used, the concentrating effect at 3 μm above the membrane of high D2R-expressing cells was 95-fold greater for spiperone-d2 in comparison to clozapine-Cy5. This is consistent with the association rate of APDs at D2R being the driver for APD rebinding, resulting in sustained D2R antagonism leading to higher EPS risks.

The APD-induced trafficking of D2R to various cellular compartments was next investigated using a bystander BRET-based D2R trafficking assay and confocal imaging. Most notably, APDs showed differing efficacies as pharmacological chaperones of D2R by increasing D2R trafficking from the endoplasmic reticulum to the plasma membrane. Interestingly, APDs that showed high efficacy for D2R chaperoning were also associated with high EPS risks. However, the APD-induced upregulation of D2R at the plasma membrane was also shown to be acutely reversible *in vitro*.

Finally, the optimisation of the primary culture of striatal neurones from SNAP-D2R mice was carried out with the aim of extending studies into more therapeutically relevant cells. Determining the molecular basis behind the atypicality of APDs would enable better prediction of the EPS risks of future APDs, ultimately leading to the improved treatment of schizophrenia and other psychiatric disorders where psychosis is a primary symptom.

II. ACKNOWLEDGEMENTS

First, I would like to send huge thanks to my supervisors, Assoc. Prof. Rob Lane and Dr Steve Briddon, who have supported and guided me for the past four years. You have provided me with countless invaluable opportunities including enabling me to present my work to leaders in the dopamine field, trusting me to supervise students and, of course, organizing an incredible trip to New York to visit Jonathan Javitch's lab. Living and working in New York for four months was an amazing experience and a fantastic career opportunity. I am constantly reminiscing about the spring tulips, my weekend bagels and walks in Central Park. I would also like to thank the BBSRC for funding my research.

I want to thank Prof. Meritxell Canals for her advice and thought-provoking questions in our lab meetings which have helped develop core ideas in my project. In addition, thank you to all of our past and present Neuropharmacology lab members: Noemi Karsai, Julie Sanchez, Jackie Glenn, Laura Lemel, Raphael Haider, Lucy Adam, Lauren Brown and George Farmer. Whether through spirit-lifting TC chats or interesting scientific conversations, you have all helped me tremendously. I feel so lucky to have been able to complete my PhD in a supportive and encouraging lab filled with such fantastic people. Particular thanks to Julie who first showed me the ropes on how things are done in the Canals/Lane lab and for your massive help with anything I have ever needed scientific or otherwise. An additional special thank you to Noemi who joined the lab at the same COVID-impacted time as me and who has been my support system both in and out of the lab. Thank you for all your help, particularly during the times where I thought FCS might be the end of me. Of course, none of this would have been possible without Jackie whose constant hard work allows our lab to operate so smoothly – I know we are all so grateful to have you.

I also want to thank everyone from the wider Cell Signalling Research Group and COMPARE. I first joined this group for a summer studentship in Nick Holliday's lab in the second year of my undergraduate degree … and I haven't left since. Everyone always comments on the supportive and collaborative nature of Cell Signalling and COMPARE and it's true, it really is special, and that is thanks to you all

who make it such a welcoming and inclusive environment. I also want to mention Nicola Dijon, my first ever mentor in a lab environment, who taught me countless techniques and had a major role in shaping me into the scientist I am today. Thank you to Joelle Goulding, Tim Self and Seema Bagia for your help with FCS, confocal microscopy and analysis (including the pesky remote access!). Thank you to David Sykes for the kinetics advice and D2R discussions, and to members of Team Science who I had the pleasure of working with over the last two years. I was very lucky to have a fantastic student, Than Nguyen, who helped produce some interesting D2R trafficking data, many thanks Than. Special thanks also to members of 'Fat Tuesday' and the revitalising weekly treats and chats. Thank you also to the colleagues in the local vicinity of my desk who were often subjected to my rambling thoughts, scientific and otherwise: Marieke Van Daele, Noemi Karsai, Kelvin Cheung, Eddy Wragg, Clare Harwood, Lydia Ogrodzinski and Simon Platt. Special mention goes to Kelvin who has more recently dealt with me requesting access to the remote PC every week when a 2-minute job turned into a 20-minute one and he quite rightly reminded me he "only has 6 minutes left" on his timer. Your KFC is pending.

I would also like to thank Prof. Jonathan Javitch for the incredible opportunity to work in his lab at Columbia University for four months. Also, thank you to everyone in molecular therapeutics within NYSPI, in particular to Ying Zhu who I worked closely with every day for four months. Thank you for teaching me primary culture, for our incredible botanical garden trip and for always looking out for me. Special thanks also to Isabel Bravo who made me feel so welcome and showed me lots of cool NY spots. Thank you to the British Pharmacological Society (BPS) for granting me the Schachter award that assisted me with this visit and also for awarding me a vacation studentship back in 2019 which really initiated my journey in research.

Finally, a massive thank you to my family and loved ones. The biggest thanks, of course, goes to my Dad – thank you for your never-ending support. You have been my biggest cheerleader and always do everything you can to help me even when you stopped understanding my work years ago! I wouldn't be where I am today without you and I am eternally grateful. Thank you also to my incredible friends, you are all

always there for me and I am so thankful to have you. A special mention goes to Amanda Chaytor, Himawari Nishida, Milly Revill, Katherine Field and Penny Skipper who have had to endure my complaints throughout the seemingly endless write-up period. Thank you also to my adorable writing buddy, Fluffy. A final big thank you to Themiya Perera who has supported me through the difficult times and celebrated with me during the good ones – I couldn't have done it without you.

This thesis is the candidate's own work. All experiments were completed by the author, other than experiments completed by Than Nguyen which generated data showing the antipsychotic drug-induced concentration-dependent D2R trafficking to the plasma membrane or endoplasmic reticulum with and without antipsychotic drug washout in **Figure 5.5** and **Figure 5.8**. No part of this material has been submitted previously for a degree or any other qualification at any University.

III. ABBREVIATIONS

AC	Adenylyl cyclase
ACh	Acetylcholine
ANOVA	Analysis of variance
APD	Antipsychotic drug
BRET	Bioluminescence resonance energy transfer
BSA	Bovine serum albumin
cAMP	Cyclic adenosine monophosphate
CBS	Newborn calf serum
CHO	Chinese hamster ovary
cpm	Counts per molecule
Cy5	Cyanine-5
D2L	Dopamine D2 receptor (long isoform)
D2S	Dopamine D2 receptor (short isoform)
DAPI	4',6-diamidino-2-phenylindole
DARPP-32	Dopamine- and cAMP-regulated neuronal phosphoprotein
DAT	Dopamine transporter
DMEM	Dulbecco's modified Eagle's medium
DMSO	Dimethyl sulfoxide
DNase	Deoxyribonuclease
D-PBS	Dulbecco's phosphate buffered saline
EBSS	Earle's balanced salt solution
ECL	Extracellular loop
EPS	Extrapyramidal symptoms
ER	Endoplasmic reticulum
FBS	Foetal bovine serum
FCS	Fluorescence correlation spectroscopy
FDU	Fluorodeoxyuridine
FGA	First-generation antipsychotic drug

GDP	Guanosine diphosphate
GPCR	G protein-coupled receptor
GRK	G protein-coupled receptor kinase
GTP	Guanosine triphosphate
HBSS	HEPES-buffered saline solution
HEK	Human embryonic kidney
ICL	Intracellular loop
KA	Kynurenic acid
MEM	Minimum essential media
MSN	Medium spiny neurone
Nluc	Nanoluciferase
PBZ	Phenoxybenzamine
PCH	Photon counting histogram
PEI	Polyethylenimine
PET	Positron Emission Tomography
PKA	Protein kinase A
PKC	Protein kinase C
RGS	Regulators of G protein signalling
ROI	Region of interest
SEM	Standard error of the mean
SGA	Second-generation antipsychotic drug
TD	Tardive dyskinesia
TGA	Third-generation antipsychotic drug
TIRF	Total internal reflection fluorescence
TM	Transmembrane domain
TR-FRET	Time-resolved fluorescence resonance energy transfer
VMAT2	Vesicular monoamine transporter 2
VTA	Ventral tegmental area
WT	Wild type

TABLE OF CONTENTS

CHAPTER 1: GENERAL INTRODUCTION

1.1 DOPAMINE

1.1.1 BACKGROUND

Dopamine is a catecholaminergic neurotransmitter that was discovered over 60 years ago[1–3]. Since then, numerous physiological functions of dopamine have been found within the central nervous system and the periphery ranging from hormonal regulation to voluntary movement[4]. Dopamine is synthesized within the presynaptic terminal of dopaminergic neurones via a two-step process (**Fig. 1.1**)[5]. It is then sequestered into vesicles by the vesicular monoamine transporter 2 (VMAT2) and stored until release into the synaptic cleft in response to action potentials. Here, dopamine can activate G protein-coupled dopamine receptors that comprise five subtypes (D1R-D5R) and are located on both the presynaptic and postsynaptic nerve terminals[6]. Dopaminergic signalling is terminated through the reuptake of dopamine into presynaptic terminals via dopamine transporters (DATs) where it is either repacked into vesicles or metabolized[7]. Presynaptic autoreceptors, comprising mainly the D2R subtype, also regulate dopaminergic signalling by providing feedback inhibition of dopamine synthesis, release and reuptake (**Fig. 1.1**)[8].

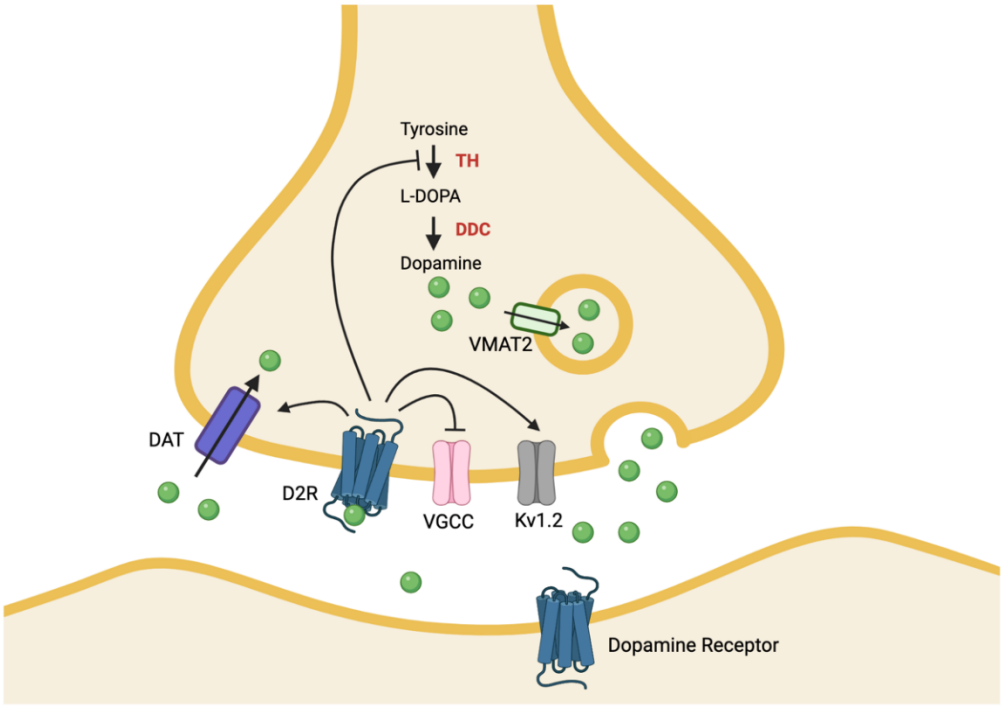

Figure 1.1: Dopamine synthesis, transport and metabolism at the synapse.

Tyrosine is hydroxylated to L-DOPA by tyrosine hydroxylase (TH) followed by L-DOPA decarboxylation by DOPA decarboxylase (DDC) to form dopamine. Dopamine is packaged into vesicles by the vesicular monoamine transporter 2 (VMAT2) and is released into the synaptic cleft where it can bind to pre- or postsynaptic dopamine receptors. The dopamine transporter (DAT) reuptakes dopamine into the presynaptic terminal where it is metabolized or repackaged into vesicles. The presynaptic autoreceptor, D2R, provides negative feedback by increasing the expression and activity of DAT and decreasing vesicle release by activating Kv1.2 channels and inhibiting voltage-gated calcium channels (VGCC). Long-term D2R activation also results in the inactivation of TH through protein kinase A-mediated phosphorylation.

Dopamine neurones are grouped into four major dopaminergic pathways (nigrostriatal, mesolimbic, mesocortical and tuberoinfundibular) which are involved in the vital functions of the CNS[4]. The nigrostriatal pathway extends from the substantia nigra pars compacta in the midbrain to the dorsal striatum and is involved in the regulation of voluntary movements[9]. Neurodegeneration of this pathway disrupts the basal ganglia motor circuit resulting in Parkinson's disease[10]. Dopaminergic neurones of the mesolimbic pathway originate in the ventral tegmental area (VTA) in the midbrain, and project to regions of the limbic system including the nucleus accumbens in the ventral striatum, amygdala, hypothalamus and medial prefrontal cortex[11,12]. Activation of this pathway is associated with various cognitive functions such as types of learning and reward-related processes[12,13]. Neurones of the mesocortical pathway also originate in the VTA and project to cortical areas including the orbitofrontal cortex, medial prefrontal cortex and anterior cingulate cortex[14]. This pathway regulates a number of cognitive and emotional processes including attention, working memory and decision-making[15,16]. The psychiatric disorder schizophrenia is associated with the dysregulation of both the mesolimbic and mesocortical pathways (detailed in **Chapter 1.3**)[17]. The tuberoinfundibular pathway originates in the anterior pituitary and projects to the arcuate nucleus of the hypothalamus where dopamine tonically inhibits prolactin secretion[18]. The endocrine disorder, hyperprolactinaemia, can therefore arise when the tuberoinfundibular pathway is inhibited. Dopamine also has several roles in the periphery including the modulation of cardiovascular and renal function, glucose homeostasis, and immune systems[4,19].

1.1.2 DOPAMINE RECEPTORS

Dopamine receptors are members of the largest subfamily of G protein-coupled receptors (GPCRs), the Class A (rhodopsin-like) receptors[20]. This GPCR subfamily contains several conserved structural characteristics including seven transmembrane α-helical domains (TM) arranged in a cylindrical bundle and linked by alternating intracellular (ICL) and extracellular (ECL) loop regions as well as an

extracellular amino terminus and an intracellular carboxyl terminus (**Fig. 1.2**)[6]. Several class A GPCRs, including all dopamine receptors, have an eighth helical domain that is anchored to the intracellular side of the membrane through palmitoylation[21]. The extracellular half of the TM bundle forms the orthosteric ligand binding site where dopamine binds. X-ray crystallography and cryo-EM structures of dopamine receptors in complex with both agonists and antagonists have shown that the orthosteric ligand pocket is highly conserved among dopamine receptors (DR1-5) with amino acids from TM3, TM5, TM6, TM7 and ECL2 involved in orthosteric ligand binding[22–25].

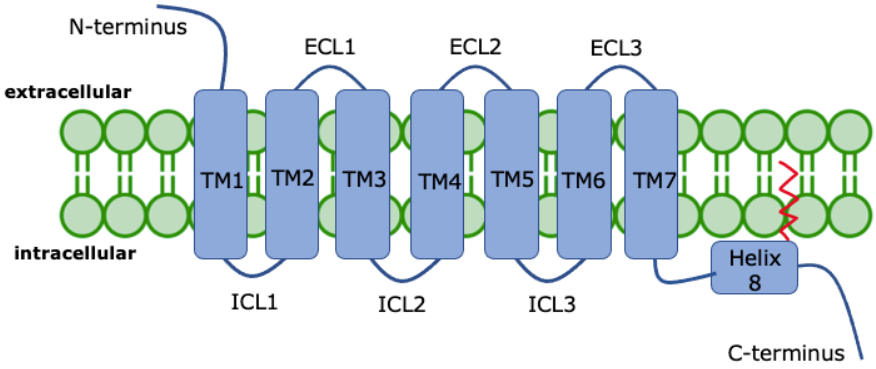

Figure. 1.2: General structure of a Class A GPCR.

The intracellular loops (ICL1-3), extracellular loops (ECL1-3), helical transmembrane domains (TM1-7), N(amino)-terminus and C(carboxyl)-terminus are shown. The C-terminus of class A GPCRs typically contain an eighth helix that is membrane-anchored through palmitoylation.

The binding of an agonist (activating ligand) to a Class A GPCR stabilises its active conformation by promoting the outward movement of the cytoplasmic ends of TM6 and to a lesser extent TM5, as well as an inward movement of the cytoplasmic end of TM7[26]. This results in the formation of a pocket within the cytoplasmic face of the TM bundle where effector proteins can bind[27]. GPCRs also contain several conserved and function-related motifs scattered within the intracellular half of the TM bundle[28]. The DRY motif, located at the intracellular end of TM3, stabilises the inactive receptor confirmation through a salt bridge termed an ionic lock[29]. A similar feature to this ionic lock forms between the TM7 sequence motif, NPxxY, and a tyrosine residue on TM5 via a hydrogen bond which instead is thought to stabilise the active receptor confirmation[27]. The CWxP motif within TM6 is also thought to stabilise active receptor confirmations by rearranging the TM6/7 interface between active and inactive states[30].

Heterotrimeric G proteins are known to bind to the pocket within the intracellular face of an activated GPCR[31]. These G proteins consist of three subunits: Gα, Gβ and Gγ. The Gα subunit consists of a Ras-like GTPase domain and α-helical domain[31]. Between these domains lies a binding site for guanine nucleotides. In contrast, the Gβ subunit contains a β-propellor domain comprising β-sheets[32]. The N-terminal of Gβ comprises an α-helix which interacts with an α-helix on the Gγ subunit through a tight coiled-coil interaction[32]. Thus, the Gβ and Gγ subunits function as a unit, Gβγ. The two domains of Gα interact with the Gβ propellor to form a trimeric protein[32]. Upon G protein-coupling to an activated GPCR, the α5 helix located on the C-terminal of Gα, extends into the intracellular core of the TM bundle[33]. The activated GPCR then acts as a guanine nucleotide exchange factor by promoting the exchange of guanosine diphosphate (GDP) for guanosine triphosphate (GTP) on the Gα subunit of the G protein[31]. This causes the activation and associated conformational change of the Gα subunit allowing its dissociation away from the Gβγ subunit and the receptor (**Fig. 1.3**). The GTP-bound Gα subunit and the Gβγ subunit are then able to independently activate downstream signalling cascades through the binding of intracellular effectors, namely, adenylyl cyclase (AC) and ion channels respectively[31]. The native GTPase activity of the Gα subunit allows its inactive GDP-bound state to

reform, promoting the formation of the heterotrimeric complex and allowing the G protein cycle to restart[34].

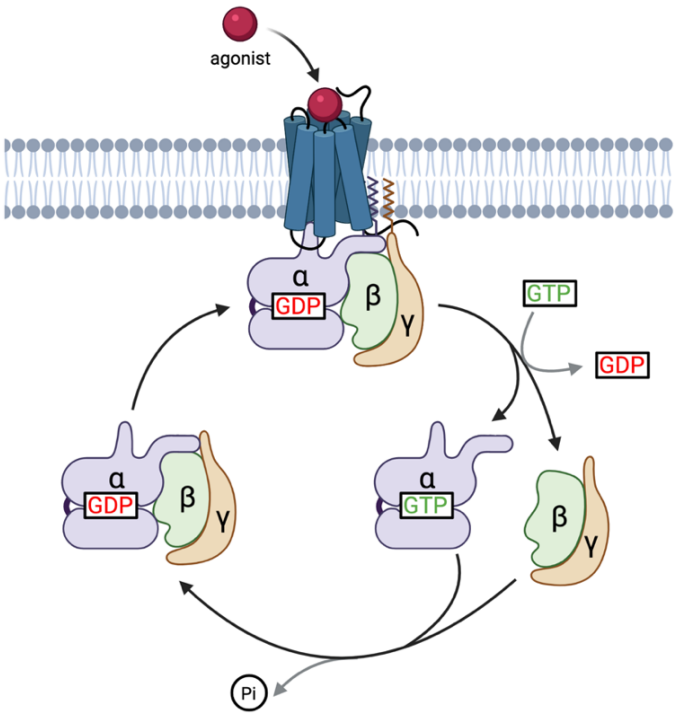

Figure 1.3: The G protein cycle.

Agonist binding promotes GPCR activation which allows a heterotrimeric G protein to bind to the receptor. The heterotrimeric G protein consists of a Gα subunit that binds guanine nucleotides and a Gβγ subunit. GPCR activation promotes a conformational change in the receptor which facilitates the exchange of GDP for GTP on the Gα subunit. This causes the G protein to dissociate from the receptor and also causes the dissociation of the G protein subunits which are now able to initiate downstream signalling cascades. Signalling is terminated when the inherent GTPase activity of the Gα subunit hydrolyses GTP to GDP. The heterotrimeric complex then reforms and couples to a GPCR allowing the cycle to begin again.

Dopamine receptors were originally proposed to exist as two separate populations termed D1R and D2R based on their ability to activate or inhibit AC, respectively[35,36]. Following the discovery of a further three dopamine receptors using genetic cloning approaches, the D1/D2R classification system was expanded into two classes based on the pharmacological, biochemical and structural properties of the receptors. The D1-like receptors (D1R, D5R) are located postsynaptically and couple to $G\alpha_{s/olf}$ proteins which activate AC and increase intracellular cyclic adenosine monophosphate (cAMP) levels[37,38]. The D2-like receptors (D2R, D3R, D4R) are located both pre- and postsynaptically and inhibit AC through coupling to $G\alpha_{i/o}$ proteins[39]. There is considerable homology within the structures of the two receptor classes with members of the D1-like class sharing 80% homology within their TM domains[4]. Within the TM domains of the D2-like class, the D2R and D3R share 75% identity and D2R and D4R share 53%[6]. The extracellular amino terminus is similar in length across all dopamine receptors however the carboxy terminus is around seven times longer for the D1-like receptors than the D2-like receptors. In addition, the D2-like receptors have longer ICL3 regions in comparison to the D1-like receptors which is common among GPCRs that couple to inhibitory G proteins[6]. The two receptor classes also show differences in their genetic structure with the D2-like receptors containing several introns allowing for alternatively spliced receptor variants and the D1-like receptors containing no introns in their coding regions[4].

1.2 DOPAMINE D2 RECEPTOR

1.2.1 BACKGROUND

Of all the dopamine receptors, the D2R is the most extensively investigated due to its clinical importance as the main pharmacological target in multiple neuropsychiatric diseases including schizophrenia and Parkinson's disease[37]. In the CNS, D2R is most highly expressed within the ventral striatum: in the olfactory tubercle and on medium spiny neurones (MSNs) in the nucleus accumbens[6]. There are also other areas of D2R enrichment throughout the brain including the substantia nigra pars compacta, amygdala, septum and cortical areas[4]. A complication in the study of D2R is the alternative splicing of the D2R gene resulting in two isoforms, a long (D2L) and short (D2S) isoform that differ by a 29-amino acid insert within ICL3 of D2L[40]. These isoforms have been shown to couple to distinct inhibitory G proteins which is most likely due to their structural differences within ICL3, a region involved in G protein-coupling[41,42]. Previous studies have shown that the deletion of D2L abolishes responses usually seen with postsynaptic striatal D2R activity including haloperidol (D2R antagonist)-induced catalepsy and the phosphorylation of a dopamine- and cAMP-regulated neuronal phosphoprotein (DARPP-32) selectively expressed in MSNs [43–45] . It has also been shown that the regulation of tyrosine hydroxylase phosphorylation in the dopaminergic nerve terminals is maintained in D2L knockout mice[45]. These studies suggest that the D2R isoforms have differing locations at the synapse with D2L being postsynaptic and D2S acting as a presynaptic autoreceptor. However, studies in which D2S and D2L expression is virally restored in D2R knockout mice have indicated that both isoforms can act as pre- or postsynaptic receptors[46]. In this thesis, D2L was used in all experiments with the exception of time-resolved fluorescence resonance energy transfer (TR-FRET) experiments in **Chapter 4.3.1** where D2S was used to determine the kinetic binding parameters of clozapine-Cy5.

1.2.2 D2R SIGNALLING AND REGULATION

D2R predominantly signals through coupling to the $G\alpha_{i/o}$ protein family which consists of the $G\alpha_{i1}$, $G\alpha_{i2}$, $G\alpha_{i3}$, $G\alpha_o$ and $G\alpha_z$ heterotrimeric G proteins[47,48]. **Figure 1.4** shows the cryo-EM structure of D2R in complex with $G\alpha_{i1}$ and the agonist, rotigotine. D2R agonists can stabilize differing receptor conformations that display differences in the degree of selectivity between members of the $G\alpha_{i/o}$ protein family[49,50]. However, a study that investigated the ability of GTP to decrease the affinity of dopamine for D2R, found that GTP was unable to regulate the binding affinity of dopamine to D2R in $G\alpha_o$-deficient mice[48]. This suggested that most of the effects of D2R within the brain were mediated by $G\alpha_o$ rather than $G\alpha_i$. Further *in vitro* studies investigating the loading of a non-hydrolysable form of GTP, GTPγS, onto different $G\alpha_{i/o}$ proteins upon receptor activation, found $G\alpha_o$ to be the most robustly activated by D2L[50,51]. Interestingly, a studying measuring agonist-induced G protein dissociation showed a more pronounced activation of $G\alpha_o$ by D2L in comparison to D2S[52]. There are differing enrichment levels of $G\alpha_{i/o}$ proteins in the striatum with an increased proportion of $G\alpha_o$ in the ventral striatum over the dorsal striatum causing a region-specific difference in dopamine sensitivity at the D2R[53]. The mesoaccumbal and nigrostriatal pathways project to the nucleus accumbens (ventral striatum) and dorsal striatum respectively, meaning these neuronal populations have differing D2R signalling sensitivities due to their differential coupling to $G\alpha_o$. This is relevant to drugs that target the D2R in terms of their *in vivo* efficacy within different brain regions.

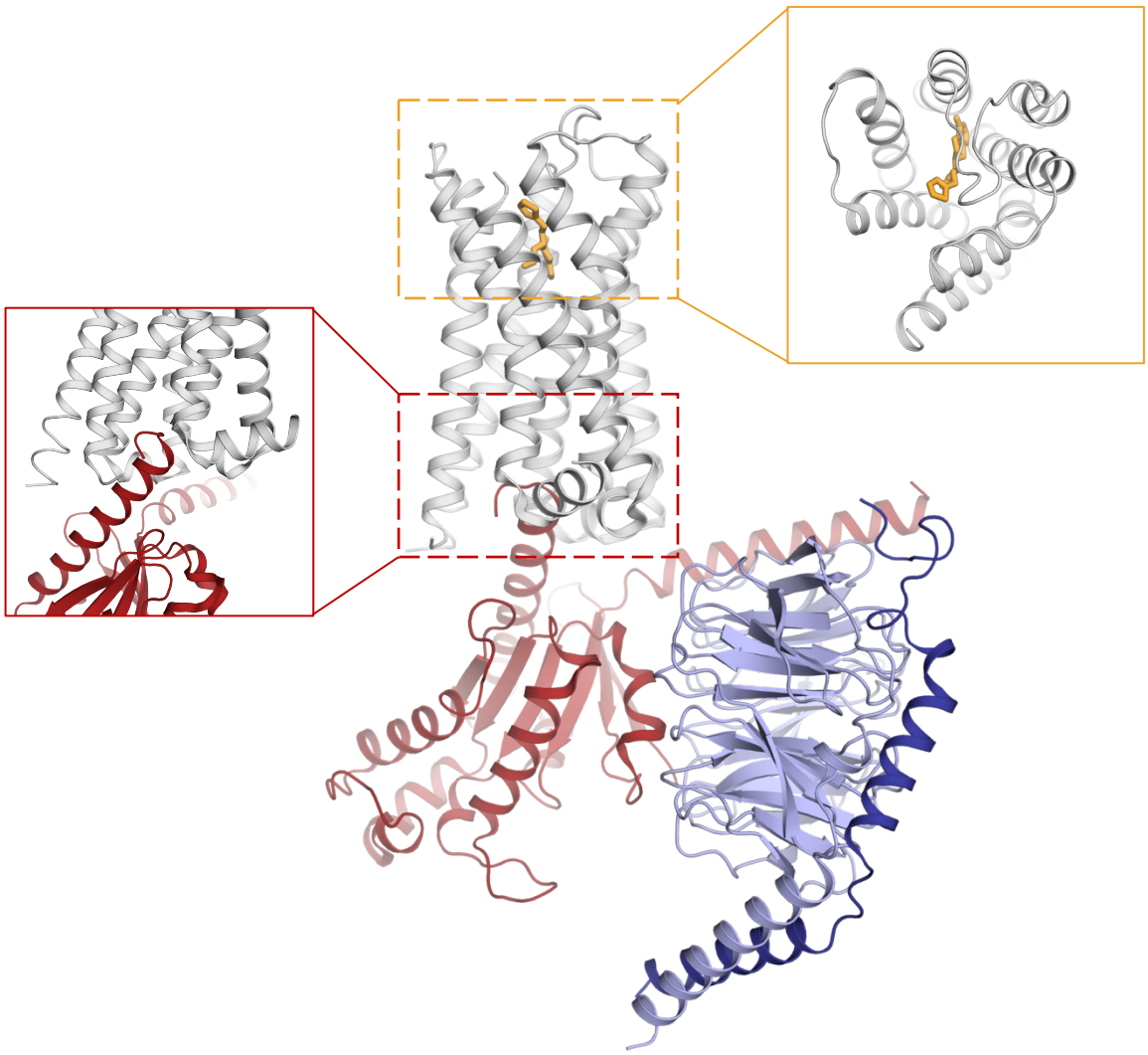

Figure 1.4: The cryo-EM structure of D2R in complex with $G\alpha_i$ and rotigotine.

The structure of an activated D2R (grey) bound to the agonist (yellow), rotigotine, and the heterotrimeric G protein, $G\alpha_{i1}\beta_1\gamma_2$ (PDB code: 8IRS). The $G\alpha_{i1}$ subunit is shown in red, the $G\beta_1$ subunit is shown in light blue, and the $G\gamma_2$ subunit is shown in dark blue. The red panel on the left shows the insertion of the α5 helix of the $G\alpha_{i1}$ subunit into the cytoplasmic pocket of D2R. The yellow panel on the right shows rotigotine bound to the orthosteric ligand binding pocket of D2R.

The coupling of D2R to $G\alpha_{i/o}$ proteins stimulates a range of downstream effects through the inhibition of AC including a decrease in the protein kinase A (PKA)-mediated phosphorylation of DARPP-32 and other PKA targets[15]. The decreased phosphorylation of DARPP-32 prevents its inhibition on protein-phosphatase 1, a regulator of the mitogen activated protein kinase pathway[54]. Other downstream signalling events following D2R activation are mediated by the Gβγ subunit including phospholipase C activation and L/N-type calcium channel inhibition which causes an increase and decrease of intracellular calcium levels respectively leading to the modulation of various calcium-regulated enzymes[4]. The Gβγ subunit also activates G protein-coupled inwardly-rectifying potassium channels (GIRKs) causing a decrease in intracellular potassium levels resulting in hyperpolarization and the inhibition of neuronal activity[15].

G protein-mediated D2R signalling is regulated by regulators of G protein signalling (RGS) and G protein-coupled receptor kinases (GRKs) by interfering with G protein activity or G protein-binding to the receptor[15]. These proteins prevent the hyper-activation of D2R signalling pathways through receptor desensitisation hence maintaining signal tone[55]. RGS proteins are intracellular proteins that bind directly to the Gα subunit and accelerate GTP hydrolysis to inactivate the G protein and terminate downstream signalling[56]. The RGS9-2 subtype is highly abundant in the striatum and is involved in the downregulation of G protein signalling following D2R activation[57,58]. GRK2 and GRK3 have been shown to phosphorylate D2R (both long and short isoforms) on ICL2/3 in response to agonist stimulation leading to the recruitment of β-arrestin2 which prevents G protein recruitment and signalling even in the presence of an agonist[59,60]. A study using a kinase 'dead' GRK2, GRK2 K220R, has shown that there is also a phosphorylation-independent mechanism of GRK2-mediated enhancement of β-arrestin2 recruitment to D2L which contradicts the canonical view of GPCR regulation based on studies of the β2-adrenergic receptor[61]. This may be due to the additional role of β-arrestin coupling to D2R outside of the attenuation of G protein signalling. β-arrestin-mediated signalling can occur following D2R activation through the formation of a signalling complex consisting of β-arrestin2, protein kinase B (Akt) and protein phosphatase 2A which ultimately inhibits

Glycogen synthase kinase-3 beta and the phosphoinositide 3-kinase/Akt pathway[62]. In addition, agonist-independent desensitization of D2L can also occur via the phosphorylation of ICL3 by protein kinase C (PKC) which prevents G protein coupling to the receptor[63].

1.2.3 D2R TRAFFICKING

The trafficking of D2R between the cell membrane and intracellular compartments is distinct from classical GPCR trafficking based on studies using β-adrenergic receptors. In this classical trafficking model, receptor activation promotes GRK-mediated receptor phosphorylation and the subsequent binding of β-arrestin which can interact with components of endocytic machinery like clathrin, adaptor protein-2 and dynamin to promote receptor internalization through clathrin-coated pits[64]. Acute homologous desensitisation occurs through the sequestration of receptor into endosomal compartments following agonist-induced internalization as the receptor is removed from the plasma membrane where it can be activated by extracellular stimuli[65]. Endocytic sorting then occurs where the receptor is either trafficked to the lysosome for degradation resulting in long-term receptor desensitisation, or the receptor is recycled back to the plasma membrane promoting its resensitisation where it can once again respond to extracellular signals[66].

In contrast, GRK-mediated receptor phosphorylation has been shown not to be required for the internalization of D2L but is instead thought to facilitate receptor recycling and resensitisation[61]. Heterologous desensitisation of D2R has also been shown to occur whereby the activation of different GPCRs promotes D2R internalization via a β-arrestin and dynamin-dependent pathway through the phosphorylation of multiple sites on the ICL3 of D2R by PKC that are distinct to the GRK phosphorylation sites[63,67]. There are also differences in the sensitivity of D2R to PKC-mediated phosphorylation between the splice variants with D2L showing reduced sensitivity compared to D2S due to the presence of a PKC pseudosubstrate site in the ICL3 insertion of D2L[68]. This may explain the different sensitivities seen

between the D2R isoforms in undergoing both homologous and heterologous desentisation through total internal reflection fluorescence (TIRF) and ELISA-based internalization studies where D2S was shown to be more readily internalized in comparison to D2L[69,70]. The differential desensitisation of the isoforms is particularly important *in vivo* where the isoforms have differing synaptic locations and signalling roles.

A further unique aspect of D2R trafficking is receptor sequestration into intracellular vesicles that are distinct from those that contain β-adrenoceptors and D1R[71,72]. It has been hypothesized that this difference may be caused by the segregation of structurally homologous receptors into separate vesicles[72]. Although the endocytosis of β-adrenoceptors and D1R has been well characterized as dynamin-dependent, conflicting studies have shown D2R sequestration as either dynamin-dependent[72,73] or dynamin-independent[71], possibly due to the use of either the short or long D2R isoform in these studies, respectively.

There is additional uncertainty around the fate of internalised D2R. It is generally thought that D2R is primarily targeted to degradation pathways following endocytosis via interaction with G protein-coupled receptor-associated sorting protein (GASP) and dysbindin, resulting in receptor downregulation[74,75]. However, several studies also show that varying amounts of both D2L and D2S are recycled back to the plasma membrane following internalization either through constitutive or dopamine-dependent recycling[61,71,76]. D2R function is dependent on the level of receptor expression at the plasma membrane and, because receptor recycling will have a large impact on this, a further understanding of this mechanism as well as the proportion of internalized D2R that is recycled is necessary.

Despite a high sequence homology between the D2R isoforms, they show differences in their anterograde trafficking to the cell surface following receptor synthesis in the ER[77]. Both isoforms are post-translationally modified in the Golgi apparatus through extracellular amino-terminal glycosylation[78]. However, D2L has been shown to be processed into its fully glycosylated form more slowly compared

to D2S [79]. In addition, a pulse-chase study showed 20% of D2L to be retained in post-ER compartments in a partially glycosylated form[79]. The internal retention of immature D2L is explained by the well characterised role of amino-terminal glycosylation in D2R trafficking through mutation studies[80]. It is interesting that there are notable differences in the amino terminal post-translational modifications between D2R isoforms despite their structural difference being located within an intracellular domain. This could be explained by the isoforms adopting different confirmations within intracellular compartments causing them to associate with differing proteins during post-translational modifications and anterograde trafficking to the cell surface [79].

1.3 SCHIZOPHRENIA

1.3.1 BACKGROUND

Schizophrenia is a chronic psychiatric disorder characterized by three groups of symptoms: positive (delusions, hallucinations), negative (social withdrawal, lack of motivation) and cognitive (impaired learning and attention)[81]. It is also associated with significant public health implications with a worldwide prevalence of just below 1%[82]. Negative and cognitive symptoms are the main predictor of functional disability in patients[83]. The precise cause of the disorder remains largely unknown, however, it is thought to be multifactorial with contributions from genetic factors and environmental influences. Although the risk factors are multiplicative, genetic factors appear the most potent with an increased lifetime risk of 6.5% in first degree relatives of patients as well as increased risk in certain ethnic groups[84]. Certain pre- or perinatal events like intrauterine viral exposure and obstetric complications may combine with other risk factors to facilitate the onset of schizophrenia[84]. Other late environmental and social influences include cannabis use, social isolation and urban living[85].

1.3.2 DOPAMINE HYPOTHESIS

The dopamine hypothesis of schizophrenia argues that the three altered domains seen in patients are predominantly caused by dysregulated dopaminergic signalling. This hypothesis underpins the treatment and ongoing investigation of schizophrenia and has been reconceptualized over time as research has advanced. The initial conception emerged from the discovery of antipsychotic drugs (APDs) in the 1950s which were found to treat the positive symptoms of schizophrenia[86]. Further evidence came from observations that amphetamine increased synaptic dopamine levels and symptoms of psychosis whereas reserpine depleted synaptic dopamine and proved effective at treating psychosis[87,88]. In the 1970s the clinical effectiveness of these APDs was shown to be directly correlated with their affinity for D2R through competition binding studies with [^{3}H] haloperidol[89,90]. This coined D2R

as the "antipsychotic receptor" and formed the hypothesis that schizophrenia is caused by excess dopamine signalling at D2R which explained why antipsychotics, which are antagonists at D2R (block receptor activation), conferred an improvement in positive symptoms[91]. This hypothesis was incompatible with later metabolite and imaging studies that showed that dopamine levels were not elevated throughout the brain. For example, it was demonstrated that schizophrenic patients had reduced blood flow and glucose metabolism in the prefrontal cortex compared to normal control subjects[92,93]. In addition, low levels of dopamine's major metabolite, homovanillic acid, were found in the cerebrospinal fluid of patients with schizophrenia suggesting that the hypofrontality seen in these previous studies was due to low frontal dopamine levels[94]. Frontal hypodopaminergia was proposed to be the cause of the negative symptoms of schizophrenia based on the similarities between these symptoms and the behaviours seen in animals and humans with lesions in the frontal cortex[95]. In addition, these frontal lobe lesions resulted in increased levels of dopamine and dopamine metabolites in the striatum which were then reduced following the application of dopamine agonists to prefrontal areas[96,97]. The dopamine hypothesis of schizophrenia was therefore reformulated to convey these region-specific changes in dopaminergic signalling; hypodopaminergia in the prefrontal cortex resulted in negative symptoms and led to hyperdopaminergia in subcortical regions resulting in positive symptoms[95].

This updated hypothesis was further supported by positron emission tomography (PET) and postmortem studies that found an increase in dopamine synthesis or storage in the midbrain of patients with schizophrenia[98]. However, a more recent imaging study found that amphetamine-induced presynaptic dopamine release was robustly decreased in most extrastriatal brain regions in patients with schizophrenia, including the prefrontal cortex and ventral midbrain[99]. Despite conflicting views on the hypodopaminergic areas of the brain in schizophrenic patients, there is a large body of evidence supporting hyperdopaminergia in the striatum of patients with schizophrenia. Several *in vivo* PET imaging studies using radiolabelled L-DOPA and amphetamine-induced dopamine release found elevated presynaptic dopamine synthesis and release in the striatum of schizophrenic patients

[100–104]. It was originally proposed that the specific site of hyperdopaminergia in the striatum was the nucleus accumbens (ventral striatum), therefore implicating an overactivity in the mesolimbic pathway as the cause of positive symptoms of schizophrenia. This was primarily based on the findings that APD injection into the nucleus accumbens abolished amphetamine-induced behaviour in rodents whereas APD injection into the caudate (dorsal striatum) showed no effect on these behaviours[105]. However, advances in PET cameras have allowed the distinction of functional subdivisions within the striatum[106]. Meta-analysis of studies investigating dopamine activity within these subdivisions found that dopaminergic function was elevated in dorsal regions of the striatum, in particular in the associative and sensorimotor regions, amongst individuals with schizophrenia[106,107]. These studies therefore reject the mesolimbic theory and define the dorsal striatum as the new locus of dopaminergic dysfunction in schizophrenic patients.

Importantly, changes in neurotransmitter systems that modulate dopaminergic signalling may also contribute to hyperdopaminergia in the striatum of schizophrenic patients. Reduced midbrain GABAergic transmission in schizophrenic patients has been hypothesised to cause a disinhibition of striatal dopamine signalling[108]. In fact, it has been shown that individuals with high psychosis risk display significantly reduced GABAA receptor binding in the striatum[109]. It has also been proposed that the glutamatergic signalling system may contribute to the symptoms of schizophrenia as antagonists of the glutamate receptor, NMDA, were found to induce schizophrenia-like symptoms[110].

1.4 ANTIPSYCHOTIC DRUGS

1.4.1 CLASSIFICATION

For all currently used APDs, the blockade of D2R is thought to be the pharmacological mechanism by which they are clinically effective against psychosis[111]. The first APD, chlorpromazine, stimulated the synthesis of several other early APDs including haloperidol and fluphenazine, all acting as D2R antagonists. Antagonists are defined as ligands that show no efficacy at a target receptor but can act to block the binding of other ligands e.g. endogenous dopamine[112]. Collectively, these early APDs are classified as first-generation antipsychotics (FGAs) and are also known as "typical" based on their propensity to cause extrapyramidal side effects (EPS) and hyperprolactinaemia[113]. These extrapyramidal effects encompass motor symptoms ranging from acute dystonia and parkinsonian symptoms, including tremor and bradykinesia, to more chronic and potentially irreversible symptoms like tardive dyskinesia (TD)[114]. These adverse effects arise as these drugs cannot distinguish between D2R in different brain regions, meaning excessive D2R blockade in the nigrostriatal pathway results in EPS and D2R blockade in the tuberoinfundibular pathway results in excess prolactin release[115,116]. PET imaging studies have demonstrated that a 60-80% occupancy of striatal D2R is required for the clinical efficacy of APDs[117]. However, for haloperidol, a D2R occupancy above 72% and 78% is associated with hyperprolactinaemia and EPS, respectively[117]. In addition, these drugs show little improvement of the negative and cognitive symptoms of schizophrenia[118].

The first approved atypical APD was clozapine which was termed "atypical" due to its reduced EPS risk in comparison to typical APDs[119]. Clozapine was also found to be efficacious in treating positive and negative symptoms in treatment-resistant schizophrenic patients who failed to respond to haloperidol after six weeks[120]. Clozapine remains the most efficacious APD and the drug of choice for treating refractory schizophrenia. However, it is underutilised in the clinic due to its several life-threatening side effects including severe neutropenia, myocarditis and seizures[121]. Consequently, several other atypical APDs, termed second generation

antipsychotics (SGAs), were generated with the aim of replicating clozapine's therapeutic profile without its associated risk. SGAs (e.g risperidone, olanzapine and quetiapine) are D2R and serotonin 2A receptor (5-HT2A) antagonists and generally show a reduced risk of EPS in comparison to FGAs[119]. A meta-analysis found all SGAs were associated with fewer extrapyramidal effects than the FGA, haloperidol[122]. However, it was also found that most SGAs were only as efficacious against positive symptoms as FGAs with the exception of clozapine, olanzapine, and risperidone that showed a modest increase in efficacy[122]. Although the atypical SGAs show an improved "on target" side effect profile, they are associated with metabolic side effects including weight gain, hyperlipidaemia and Type 2 diabetes mellitus due to off target interactions[123,124]. Although most FGAs and SGAs are thought of as neutral antagonists at D2R, some APDs have been shown to act as inverse agonists at both D2S and D2L through several *in vitro* assays including the inhibition of GTPγS binding[125], the stimulation of cAMP accumulation[126] and the inhibition of PLC activation[127]. Inverse agonists act to block constitutive receptor activity that exists in the absence of an agonist[112]. They therefore stabilize the inactive receptor confirmation resulting in 'negative efficacy'[112].

The more recent atypical APDs are termed third-generation antipsychotics (TGAs) and include aripiprazole, brexpiprazole and cariprazine. They act as weak partial agonists at the D2R meaning they have partial efficacy in relation to a full agonist at the D2R such as dopamine even at maximal receptor occupancy[113]. These APDs are thought to act as dopamine stabilisers by decreasing D2R signalling where there is an excess of dopamine e.g. in the dorsal striatum, whilst enhancing D2R signalling where there are low levels of endogenous dopamine e.g. in the frontal cortex[128]. In addition, their partial agonism at D2R avoids the complete blockade of D2R signalling resulting in a particularly low risk of EPS[129]. Unfortunately, clinical trials have demonstrated that atypical APDs (both SGAs and TGAs) do not show a significant improvement in the cognitive or negative symptoms of schizophrenia despite showing overall lower EPS risks in comparison to typical APDs[130,131].

All SGAs and TGAs are characterised as atypical despite showing variations in EPS risk, particularly in the incidence of TD and increased prolactin levels[132]. In addition, the SGAs risperidone and olanzapine show an increase in EPS risk with dose escalation[133]. Of all the atypical APDs, only clozapine can be considered truly atypical. Clozapine has the lowest EPS risk of all APDs that remains no different to placebo across the full dosage range[134]. Additionally, long-term clozapine treatment does not result in TD and does not cause an elevation in prolactin levels[134]. The precise molecular mechanism behind clozapine's unique therapeutic profile is yet to be fully understood.

1.4.2 THEORIES BEHIND THE ATYPICALITY OF APDS

Several pharmacological mechanisms have been proposed to account for the reduced EPS risk of atypical APDs. It was originally observed that APDs with better side effect profiles generally showed lower affinity at D2R[135,136]. Thus, it was hypothesised that differences in the binding kinetics between typical and atypical APDs at D2R accounted for their differing propensities to induce "on target" side effects including EPS and hyperprolactinaemia. This hypothesis was supported by studies associating APD atypicality with fast dissociation rates from both D2S and D2L[137,138]. From this the "fast-off" theory was born which proposed that the reduced side effect profile of atypical APDs is caused by their rapid dissociation from D2R[139]. In this model, atypical APDs rapidly dissociate from D2R leading to transient striatal D2R occupancy, resulting in surmountable antagonism as more receptors are available for binding by the transiently high local concentration of synaptic dopamine during phasic dopamine release. This results in decreased atypical APD D2R occupancy over time as dopamine outcompetes the atypical APD, leading to a reduced EPS risk. In contrast, the slower dissociation rate of typical APDs prevents dopamine binding to D2R thus causing prolonged D2R antagonism associated with adverse effects. Studies supporting this theory have successfully shown transient D2 occupancy with atypical APDs and sustained D2R occupancy with typical APDs[135,140]. The "fast-off" theory assumes that the association rates between APDs at D2R show

little variation meaning their affinity at D2R is predominantly determined by their dissociation rate. This assumption is based on previous work using radioligand dissociation experiments[141]. However, the association rates at D2R determined in this study were derived from D2R affinity and dissociation rates rather than direct measurements. Several studies have suggested that ligands with a high lipophilicity, like high-affinity D2R antagonists, show an accumulation in the membrane and subsequent rebinding to the receptor resulting in an underestimation of dissociation rates and a potentially increased receptor occupancy *in vivo*[142,143]. This is likely to have been a confounding factor in Kapur and Seeman's study on the dissociation rates of both typical and atypical APDs meaning the link between dissociation rates and atypicality may not be as clear as originally proposed. Moreover, some atypical APDs like olanzapine, risperidone, sertindole and ziprasidone show low EPS risks despite having a high affinity for D2R which suggests they should have slow D2R dissociation rates[144]. These APDs were later confirmed to dissociate slowly from D2L through direct measurements using a novel TR-FRET assay[145]. The "fast-off" theory, therefore, does not represent a general mechanism for atypicality of APDs.

Partial agonism of D2R has also been proposed to account for the atypicality of TGAs through the 'balancing' of dopaminergic dysregulation in differing brain regions depending on synaptic dopamine levels. The partial D2R agonist, aripiprazole, has been reported to act as an antagonist in areas of hyperdopaminergia and as an agonist in areas of hypodopaminergia[146]. Therefore, a partial D2R agonist should ideally allow enough dopaminergic signalling within the nigrostriatal and tuberoinfundibular pathways to avoid EPS and hyperprolactinemia, respectively[115]. However, TGAs are not solely partial agonists at D2R, for example, aripiprazole also displays partial agonism at some serotonin receptors (5-HT1A, 5-HT2C) and other dopamine receptors (D3R and D4R receptors) as well as antagonism at 5-HT2A receptors which may contribute to their reduced EPS risk[124].

A further theory to explain APD atypicality with respect to APD modulation of dopaminergic signalling is the idea of regionally selective APD binding. It has been

proposed that the selective binding of APDs to cortico-limbic areas confers APD atypicality through PET studies in humans[147–149]. These studies found a preferential occupancy of atypical APDs including amisulpiride, risperidone and clozapine, at temporal cortical D2R rather than striatal D2R. However, these findings have not been replicated for all atypical APDs and do not rule out the involvement of other brain regions (e.g. dorsal striatum).

It has also been proposed that APD atypicality may be due to selectivity for other receptors over D2R. The first of these theories was the "dopamine-serotonin antagonism" theory whereby a high ratio of the 5-HT2A to D2R blockade was associated with atypicality [150,151]. This was based on the finding that several SGAs showed higher affinities at 5-HT2A over D2R (e.g. clozapine and risperidone)[152]. Antagonism of 5-HT2A has been shown to increase dopaminergic transmission in the nigrostriatal pathway[153], thus reducing the EPS risk. However, there are several SGAs (e.g. amisulpride and remoxipride) that have a high affinity for D2R and low affinity for the 5-HT2A receptor and there are also FGAs (e.g. chlorpromazine and spiroperidol) that bind to the 5-HT2A receptor with a high affinity despite having a high EPS risk[151].

Kharkwal et al. recently showed that APD-induced catalepsy may be a result of D2R blockade on cholinergic interneurones (ChIs) through the use of transgenic mouse models in which the D2R was specifically knocked-out in ChIs[154]. D2R antagonism on ChIs results in an increase in acetylcholine (ACh) release[155]. The ACh-mediated activation of muscarinic M1 receptors (mAChRs) on D2R-expressing MSNs activates these neurones. Simultaneously, D2R antagonism on MSNs further activates these inhibitory neurones resulting in catalepsy[154]. Therefore, it was suggested that antagonism of M1 mAChR on MSNs may prevent the motor side effects seen with APD treatment. This is supported by the finding that clozapine has the lowest EPS risk of all clinically prescribed APDs as well as demonstrating antagonist effects at M1 mAChR[107]. However, other APDs with high EPS risks also have high affinity at M1 mAChR, most notably chlorpromazine[152]. Moreover, the

major metabolite of clozapine, *N*-desmethylclozapine, has been shown to act as an agonist at M1 mAChR[156].

Interestingly, glutamatergic modulation by APDs has also been proposed to account for their atypicality. *N*-methyl-D-aspartate receptor (NMDAR) antagonists, such as phencyclidine or ketamine, induce schizophrenia-like symptoms encompassing all three altered domains of schizophrenia[157]. Therefore, glutamatergic hypofunction has been proposed to contribute to the pathophysiology of schizophrenia. It has been suggested that glutamatergic hypofunction may precede dopamine dysregulation in schizophrenia and actually result in enhanced striatal dopamine responses based on findings from PET studies[158] and behavioural studies using a transgenic mice model where a subunit of AMPA glutamatergic receptors is knocked-out[159]. This may be explained by NMDAR hypofunction on cortical interneurones resulting in the disinhibition of cortical glutamatergic projections to the VTA leading to overactivity of dopaminergic pathways originating in the midbrain[160]. Although no atypical APDs demonstrate direct affinity for the *N*-methyl-D-aspartate receptor (NMDAR), it has been shown that some atypical APDs antagonize experimentally induced NMDAR hypofunction at both cellular and behavioural levels[115]. However, treatment with the typical APD, haloperidol, blocked ketamine-induced brain metabolic activation[161]. Therefore, glutamatergic modulation may not be limited to solely atypical APDs. Despite the emergence of multiple theories to explain the molecular mechanism of atypicality, there has yet to be a single mechanism that accounts for the improved side effect profile of every atypical APD.

1.4.3 ANTIPSYCHOTIC DRUG REBINDING AT D2R

Drug rebinding was initially identified in radioligand dissociation experiments where a slower decline in specific radioligand binding was seen using wash media lacking unlabelled ligand compared to when wash media with excess unlabelled ligand was used[162]. Therefore, it was thought that this difference in the time-wise

decline of specific radioligand binding could be explained by dissociated radioligand molecules binding again to their target receptors in the absence of a competing ligand. It was previously widely accepted that this rebinding effect was simply a matter of restoring a new mass action equilibrium between free and receptor-bound radioligand molecules, meaning rebinding should only be prevalent when a radioligand displays a very high affinity for its receptor[163,164]. However [^{3}H]-telmisartan and [^{3}H]-candesartan both showed considerable rebinding to the angiotensin II type 1 receptor (AT1) despite [^{3}H]-telmisartan demonstrating a lower affinity[165,166]. Furthermore, computer simulations of [^{3}H]-candesartan binding to AT1 following the mass action equilibrium model indicated that the free radioligand concentration in the well should have been 8 times higher than what was experimentally detected[165]. Thus, drug rebinding was proposed to describe a process whereby drug molecules consecutively bind to the same target receptor and/or nearby target receptors even when the concentration of drug in the bulk aqueous phase has dropped to insignificant levels, resulting in the local accumulation of drug near target receptors[162].

With respect to APD action at the D2R, modern assays allowed the direct measurements of association rates of APDs at D2L and D2S through TR-FRET and D2R-mediated potassium channel activation assays, respectively[143,145]. These studies revealed a high variability in D2R association rates among a large panel of APDs which disagreed with the previous widely held view that association rates are diffusion limited and therefore show little variability[141]. Sykes et al. examined the correlation between the kinetic parameters of several APDs and their propensity to cause excess prolactin release and EPS[145]. In support of the "fast-off" theory, they found that the dissociation rate correlated with hyperprolactinaemia where the slower dissociating ligands displayed a greater liability for prolactin elevation in schizophrenic patients. Interestingly, it was the association rate not the dissociation rate that correlated with the incidence of EPS[145]. APDs with faster association rates showed increased EPS risks which is inconsistent with the idea that it is solely the dissociation rate of APDs which drives the atypicality of these ligands. Thus, the "fast-on" hypothesis was formed which postulated that slow D2R association rates conferred APD atypicality. Fast

association rates of APDs at D2R were thought to drive APD rebinding to D2R within a diffusion limited synapse effectively causing insurmountable D2R antagonism (**Fig. 1.5**). The pre- and post-synaptic membranes of a synapse form barriers to free ligand diffusion effectively creating a compartment distinct from the surrounding bulk aqueous environment[162]. Accordingly, a ligand recently dissociated from D2R is likely to remain in close proximity to the membrane which increases the probability of a further binding event to the same or a nearby receptor[145]. This results in a high local concentration of ligand near the membrane leading to sustained D2R blockade and hence worse EPS risks.

The likelihood of a ligand rebinding to its target receptor was previously modelled by Vauquelin and Charlton[162]. In a well-mixed system, a ligand-receptor interaction can be described as below, whereby the effective forward reaction rate coefficient (k_f) equals k_{on} and the effective reverse reaction rate coefficient (k_r) equals k_{off}:

(1.1)

$$L + R \underset{k_-}{\overset{k_+}{\rightleftharpoons}} [L \ldots R] \underset{k_{-1}}{\overset{k_1}{\rightleftharpoons}} L.R$$

$$\approx L + R \underset{k_r}{\overset{k_f}{\rightleftharpoons}} L.R$$

Here, the free ligand is represented by L and the free receptor is represented by R. Once L and R are in close proximity, governed by the diffusion limited forward and reverse rate constants of k_+ and k_-, respectively, an encounter complex can form represented by [L…R][167]. Only then can the ligand-bound receptor complex (L.R) be formed, governed by the forward and reverse reaction rate constants of k_1 and k_{-1}, respectively.

However, the effective reaction rate coefficients are not strictly constants and can be influenced by biological factors. For example, when receptors are confined to a cell membrane rather than being uniformly distributed in solution, k_r is then related to k_{off} by a factor that depends on k_{on}, the number of free receptors available for binding (N), and the diffusion limited reverse rate (k_-) which itself is dependent on the geometry of the system and the ligand diffusion rate (D) [162]:

(1.2)

$$k_r = k_{off}/(1 + \frac{k_{on}N}{k_-})$$

Vauquelin and Charlton modelled k_- within a diffusion limited cylindrical synapse where, a, represents the cylinder radius and, $g_2(d/a)$, represents the dimensionless function of cylinder geometry[162]:

(1.3)

$$k_- = (D/a) \cdot g_2(d/a)$$

To further explore how k_{on} influences APD rebinding within a synapse, Sykes et al. estimated the effective rate of reversal of receptor blockade, k_r, for several APDs at D2R by accounting for both their association and dissociation rates in a more holistic model of receptor binding that mimicked the environment of a synapse (**equation 1.2 and 1.3**)[145]. This parameter was significantly correlated with the incidence of EPS and is likely to be better correlated to EPS than the association rate[145]. This is particularly the case when there are changes within the synaptic compartment such as increased receptor density which has been shown to increase drug rebinding and therefore increase the contribution of the association rate to receptor occupancy[145,168].

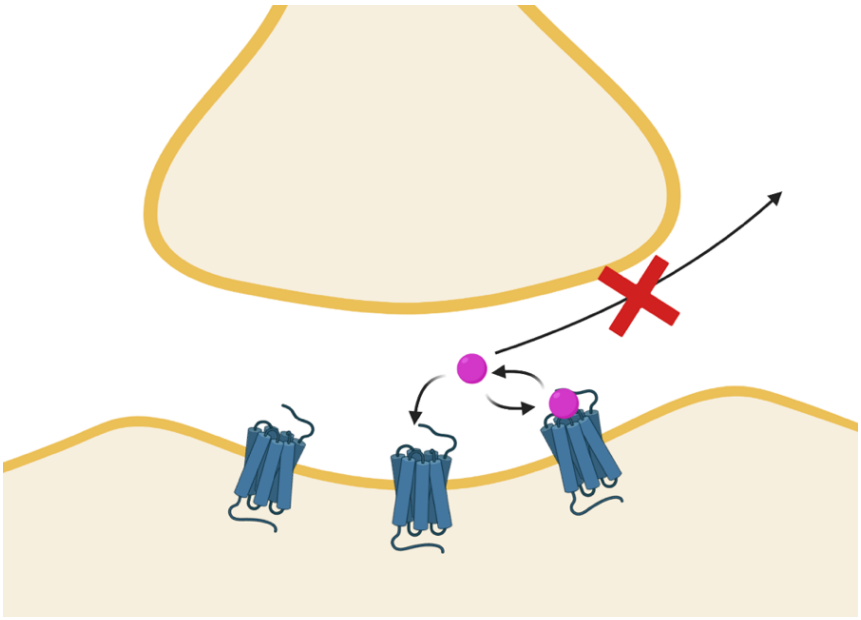

Figure 1.5: Antipsychotic drug rebinding to D2R in a synapse.

The synaptic compartment limits the diffusion of antipsychotic drug (pink) into the bulk aqueous environment surrounding the synapse. This increases the likelihood that an antipsychotic that has recently dissociated from D2R will rebind to the same or nearby receptor.

1.4.4 ANTIPSYCHOTIC-DRUG INDUCED D2R UPREGULATION

There have been conflicting findings regarding the density of D2R in the striatum of schizophrenic patients never treated with APDs in comparison to normal control subjects. PET studies performed on drug-naïve schizophrenic patients have shown both increased and decreased D2R using [^{11}C]methylspiperone and [^{11}C]raclopride[169–171]. However, it has been well established through animal studies as well as post-mortem and PET studies in humans that an upregulation of D2R occurs following long-term treatment with both typical and atypical APDs[172–174]. Despite the antagonistic nature of APDs, APD-induced D2R upregulation at the plasma membrane may result in increased dopaminergic signalling due to an increase in the available receptors for endogenous dopamine binding. Therefore APD-induced D2R upregulation may be linked to more hyperkinetic side effects within the EPS spectrum e.g. akathisia, characterised by motor restlessness, and TD, a potentially irreversible disorder characterised by involuntary orofacial movements[175]. Indeed, the upregulation of D2R has been implicated in TD as well as treatment-resistant schizophrenia making it a clinically important pharmacological property of APDs[176,177]. A recent study by Schrader et al. investigated the ability of several FGAs and SGAs to promote D2R (both D2L and D2S) upregulation at the plasma membrane by measuring the total and cell-surface expression of D2R following chronic drug treatment (24 hours) using biotinylation- and ELISA-based techniques[178]. Clozapine treatment caused the least D2R translocation to the cell membrane which may explain its superior efficacy in treating TD and treatment-resistant schizophrenic patients[120,179]. This unique property of clozapine showed no correlation with its affinity for D2R or its association and dissociation rate at D2R meaning the precise molecular mechanism behind this phenomenon remains unknown. The TGA, aripiprazole, increased D2R cell surface insertion and removal resulting in an overall weak enhancement of cell-surface D2R levels similar to that of clozapine[178]. The increased removal of cell-surface D2R mediated by aripiprazole is likely due to its partial agonism of D2R with respect to β-arrestin recruitment which increases D2R internalisation[180]. All other FGAs and SGAs significantly increased D2R upregulation in comparison to the vehicle[178]. In addition, colocalization experiments with D2R and

an ER marker, Sec61, suggested that the intracellular pool of D2R is localised to the ER[178]. This then raises the possibility that APDs act with different efficacies as pharmacological chaperones which are therapeutics that target a specific receptor and act as an intracellular scaffold to aid their correct folding allowing them to be trafficked out of the endoplasmic reticulum (ER) to the cell surface[178]. Pharmacological chaperones can rescue the expression of both mutant GPCRs and wild-type GPCRs that show inefficient folding and hence significant intracellular localisation[181]. Interestingly, D2L has been shown to contain a tri-arginine ER retention motif within ICL3 which may give rise to an intracellular pool of D2R within the ER[182]. It could be argued that an intracellular store of misfolded D2R may be an artifact of D2R overexpression in Human Embryonic Kidney (HEK) 293T cells. However, Schrader et al. found the differential actions of haloperidol and clozapine were preserved in pituitary derived MMQ cells with endogenous D2R expression levels[178].

APD-induced D2R upregulation has potential implications on D2R antagonism by APDs as an increase in D2R density within a synapse has been modelled to increase drug rebinding leading to prolonged D2R blockade[162]. This is particularly pertinent for typical APDs that are associated with enhanced D2R upregulation as well as high levels of D2R rebinding within the synapse driven by their fast association rates[145,178]. Therefore, these APDs may show particularly poor side effect profiles due to the additive effect of both processes.

1.5 AIMS OF THESIS

APDs that target D2R are the only effective pharmacological treatment for schizophrenia to date. The more recently developed APDs display a more favourable side effect profile where there is a reduced risk of EPS including acute and chronic motor disorders, but the molecular basis for this remains unclear. Recent studies have suggested that APD atypicality may be caused by reduced APD rebinding to D2R and a reduced efficacy for upregulating cell-surface D2R[145,178]. This thesis aims to experimentally validate the "fast-on" hypothesis by demonstrating differential APD rebinding *in vitro*, and further investigate the pharmacological chaperoning activity of APDs at the D2R in order to reveal differences in APD action that will enable the prediction of their side effect profiles.

Chapter 3 shows the optimisation of fluorescence correlation spectroscopy (FCS) settings to detect the fluorescent APDs, spiperone-d2 and clozapine-Cy5, in solution. In addition, the membrane expression and membrane dynamics of SNAP-D2R in a CHO tetracycline-inducible SNAP-D2R (long isoform) cell line is characterised using confocal imaging, FCS and a G protein activation bioluminescence resonance energy transfer (BRET)-based assay.

Following the optimisation and characterisation experiments performed in **Chapter 3**, the rebinding of APDs with differing kinetic profiles to D2R was explored in **Chapter 4**. Concentrations of spiperone-d2 and clozapine-Cy5 were measured in solution above CHO tetracycline-inducible SNAP-D2R cells using FCS**.** APD rebinding to D2R was examined through the formation concentration gradients of fluorescent APDs above D2R-expressing cells whereby a higher concentration of fluorescent APD near receptors is found in comparison to the bulk aqueous phase.

APD-induced changes in D2R (long isoform) localisation within a cell were investigated using a bystander BRET-based D2R trafficking assay in **Chapter 5**. In particular, the pharmacological chaperoning effects of APDs were investigated by monitoring D2R localisation at the ER and plasma membrane. Confocal imaging was

used as an auxiliary technique to investigate APD-induced changes in D2R upregulation to the plasma membrane.

Finally, **Chapter 6** shows the initial optimisation of the primary culture of striatal neurones from a SNAP-D2R mouse with the aim of investigating D2R expression levels and membrane dynamics in native cells using TIRF microscopy. In addition, establishing primary SNAP-D2R striatal cultures allows the effects of APD treatment on endogenously expressed D2R to be studied in more therapeutically relevant cells.

CHAPTER 2: MATERIALS AND METHODS

2.1 MATERIALS

Human Embryonic Kidney (HEK) 293T cells were used as a model cell line for the expression of recombinant proteins of interest. The Flp-In™ Chinese Hamster Ovary (CHO) parental cell line was purchased from Fisher Scientific (Loughborough, UK). This cell line was created by transfecting CHO cells with a pFRT/lacZeo vector and selecting cells for zeocin resistance. A zeocin-resistant clone with a single FRT site integrated at a transcriptionally active genomic locus was then chosen and amplified. This cell line can be further transfected with the pcDNA5/FRT expression vector, containing a gene of interest, and the pOG44 plasmid, which constitutively expresses Flp recombinase. This results in the targeted integration of the expression vector at the FRT site. This cell line can therefore be used to generate a stable cell line with homogenous expression levels of a gene of interest due to the integration of the expression vector at the same locus in every cell. The Flp-In™ CHO SNAP-D2S cell line was previously generated in-house using this Flp-In™ system. Here, the gene of interest is a D2S receptor with an N-terminal SNAP-tag (Promega, USA). The CHO tetracycline-inducible SNAP-D2R (long isoform) cell line was a kind gift from Jonathan Javitch. SNAP-D2L was cloned into a pcDNA5/TO expression vector before transfection into CHO cells. A stable cell clone was identified using hygromycin which was then expanded to generate the stable cell line.

All ligands were purchased from Sigma Aldrich (Gillingham, UK), made up to a stock concentration of 10 mM in dimethyl sulfoxide (DMSO) (Sigma Aldrich, UK) and stored at -20°C, with the exception of dopamine hydrochloride which was made up fresh on the day of assay. The fluorescent ligand, spiperone-d2 (part no. L0002RED), was purchased from Cisbio, Perkin Elmer (now Revvity (Cambridge, UK)). Clozapine-Cy5 was synthesized in the Biodiscovery Institute at the University of Nottingham by Shailesh Mistry. SNAP-Surface® Alexa Fluor® 488 was purchased from New England Biolabs (Hitchin, UK). SNAP-Surface® 549 and SNAP-Surface® Alexa Fluor® 647 were purchased from New England Biolabs (MA, USA). Janelia Fluor® 549i and Janelia Fluor® 646i were purchased from Tocris Bioscience (MN, USA). Cy5 NHS ester was purchased from Amersham Pharmacia Biosciences (Uppsala, Sweden) and ATTO 488

NHS ester was purchased from Sigma Aldrich (Gillingham, UK). Nano-Glo® furimazine substrate was obtained from Promega (WI, USA). SNAP-Lumi4-Tb and Tag-lite labelling medium were purchased from Revvity (Cambridge, UK). All N-terminally Venus tagged cell compartment markers were a generous gift from Nevin Lambert, Augusta University (GA, USA). Papain vials (PDS kit) and deoxyribonuclease I (DNase I) were purchased from Worthington Biochemical (NJ, USA).

Unless otherwise stated, all cell culture reagents and chemical stocks were purchased from Sigma Aldrich (Gillingham, UK). All cell culture glassware was purchased from Fisher Scientific (Loughborough, UK) with the exception of 10 cm cell culture dishes which were purchased from Grenier Bio-One (Stonehouse, UK). Various assay plates were used including white 96 well plates obtained from Grenier Bio-One (Stonehouse, UK), 384-well optiplates (LBS) obtained from Revvity (Cambridge, UK) and Nunc™ Lab-Tek™ chambered 8-well coverglass (No. 1.0 borosilicate glass bottom; 155411) obtained from Fisher Scientific (Loughborough, UK).

2.2 MOLECULAR BIOLOGY

2.2.1 TRANSFORMATION OF DNA INTO COMPETENT ESCHERICHIA COLI

In order to amplify plasmid DNA, they were first transformed into NEB® Turbo Competent *Escherichia coli* High Efficiency cells (New England Biolabs, UK). Cells were thawed on ice and 50 μl was added to two sterile 0.5 ml Eppendorf tubes to generate an 'active' and a 'control' transformation reaction. 1 μl DNA was added to the 'active' transformation reaction and both Eppendorf tubes were gently flicked before incubating on ice for 30 minutes. To facilitate the uptake of plasmid DNA into the cells, the tubes were subjected to a 30 second heat shock at 42°C before being incubated on ice again for 3 minutes. 500 μl of warmed LB broth (Lennox, 35 g/l) was then added to each tube using aseptic technique. Cells were then incubated in a shaking incubator for 1 hour at 37°C before being plated onto LB agar plates containing 100 μg/ml carbenicillin and left to grow overnight at 37°C. A successful transformation was indicated by the formation of colonies on the 'active' transformation reaction plate and a lack of colonies on the 'control' transformation reaction plate.

2.2.2 DNA PURIFICATION

Single colonies were picked from the 'active' transformation reaction plate and added to 5 ml LB broth with 100 μg/ml carbenicillin. These 'starter cultures' were then grown for 6 hours in a shaking incubator at 37°C before being transferred to a 500 ml conical flask containing 100 ml LB Broth with 100 μg/ml carbenicillin and again incubated at 37°C in a shaking incubator overnight. The following day, cells were pelleted by centrifugation at 5,000 g for 10 minutes at room temperature in 250 ml plastic bottles. The plasmid DNA was then extracted from the resulting cell pellets using the PureYield™ Plasmid Maxiprep protocol (Promega, UK). First, the cell pellets were resuspended in cell resuspension solution and transferred to a falcon tube prior to the addition of cell lysis solution. The tube was then inverted 5 times and left to incubate at room temperature for 3 minutes. Neutralisation solution was added, and

the tube was inverted 15 times to mix. The lysate was then centrifuged at 14,000 g for 20 minutes to precipitate the cell debris. The resulting supernatant containing plasmid DNA was loaded onto a clearing column stacked into a binding column and attached to a vacuum manifold (Promega, UK). Maximum vacuum was applied to allow the supernatant to pass through both columns, resulting in the binding of the plasmid DNA to the membrane of the silica-based binding column. Waste was collected into the vacuum pump for disposal and the clearing column was then removed and discarded. The binding column was next subjected to two wash steps assisted by vacuum to first remove endotoxins and then further contaminants using an ethanol-based column wash. The binding column membrane was then dried for 5 minutes by applying a vacuum to ensure the evaporation of excess ethanol. Finally, 1 ml of nuclease-free ddH_2O was added to the membrane and incubated for 1 minute before the elution of the plasmid DNA into a sterile 1.5 ml Eppendorf tube. DNA concentration and purity were then measured using a Nanodrop (Fisher Scientific, UK). This maxiprep procedure typically resulted in a DNA concentration of 150-1000 ng/μl and a ratio of absorbance at 260 nm:280 nm of 1.8-1.9, indicative of negligible levels of contamination with protein or RNA. DNA was then stored at -20°C.

2.3 CULTURE OF MODEL CELL LINES

2.3.1 PASSAGING

HEK 293T cells were cultured in Dulbecco's Modified Eagle Medium (DMEM) supplemented with 10% Foetal Bovine Serum (FBS). CHO cell lines were cultured in DMEM/F-12 supplemented with 10% FBS and 2 mM L-glutamine. The Flp-In™ CHO parental cell line was additionally supplemented with 100 μg/ml zeocin (Fisher Scientific, UK) whereas both the Flp-In™ CHO SNAP-D2R cell line and the CHO tetracycline-inducible SNAP-D2R cell line were supplemented with 200 μg/ml hygromycin B (Fisher Scientific, UK). All cells were grown in humidified incubators at 37°C and 5% CO_2.

The model HEK 293T and CHO cell lines were maintained in 75 cm^2 flasks and passaged at 70-90% confluency to ensure maximal cell viability. Growth media was removed before washing cells with Dulbecco's Phosphate Buffered Saline (D-PBS). Cells were then lifted from the flask using 1 ml of trypsin-EDTA solution (0.25%) and incubated at 37°C for 3 minutes to ensure that the adherent cells had detached from the flask. Cells were then resuspended in a total of 5 ml culture media before centrifugation at 1000 rpm for 3 minutes. The resulting pellet was suspended in 5 ml media before the addition to a new 75 cm^2 flask containing 12 ml culture media. Cells were passaged using split ratios of 1:2-1:20 depending on when they were required. Cells were counted prior to seeding in 10 cm dishes or Nunc™ Lab-Tek™ chambered coverglass 8-well plates using the Countess™ II automated cell counter (Fisher Scientific, UK) by loading 10 μl of a 1:1 ratio of suspended cells and trypan blue stain (Fisher Scientific, UK) onto Countess™ cell counting chamber slides (Fisher Scientific, UK).

2.3.2 FREEZING

To freeze CHO and HEK 293T cell lines, they were harvested and pelleted from 75 cm^2 flasks as previously described (**Chapter 2.3.1**). A cell pellet from a single 75

cm^2 flask was resuspended in 2 ml freezing media (FBS containing 10% (v/v) DMSO). The freezing media was sterile filtered prior to use using a 0.2 μm filter to remove any microbial contaminants. Cells were then divided into two cryovials (Fisher Scientific, UK) and placed into a Mr Frosty™ freezing container (Fisher Scientific, UK), and then into a -80°C freezer. This freezing container allowed the cells to cool slowly at a rate of 1°C/minute avoiding the formation of ice crystals inside the cell that could puncture the cell membrane leading to cell death. For longer-term storage, the cells were moved from the -80°C freezer after a minimum of 24 hours and into liquid nitrogen dewars.

To defrost cells, a cryovial was left to thaw before being added to 4 ml of culture media and then centrifuged at 1000 rpm for 3 minutes. The cell pellet was resuspended in 5 ml media and added to a 75 cm^2 flask containing 7 ml culture media. Once the cells recovered and were 70% – 90% confluent, they were passaged as normal.

2.4 PRIMARY NEURONAL CELL CULTURE

2.4.1 GLIA PREPARATION

To support the growth of primary striatal neurones, glia monolayers were prepared from P1-3 rat pups from a Charles River (Sprague Dawley) E15 rat. The protocol below describes the preparation of glia monolayers from one litter of rat pups (~ 6-8 pups). First, Earle's Balanced Salt Solution (EBSS) was added to a papain vial to achieve 20 U/ml enzyme activity. DNase I was made up to 1 U/μl using EBSS. ~ 5 ml of papain solution was prepared by adding DNase I and papain in a 1:20 ratio to a 25 ml dissociation vial (Thermo Fisher Scientific, USA). Next, ~ 15 ml of glia trituration media was prepared by adding 10% newborn calf serum (CBS) (Thermo Fisher Scientific, USA) and a 1:100 dilution of the previously prepared DNase I stock solution to Minimum Essential Media (MEM). The papain solution and glia trituration media were then perfused with humidified carbogen (95% oxygen and 5% CO_2) delivered through a 0.22 μm filter (Thermo Fisher Scientific, USA) and 20-gauge needle (BD, USA) for 30 minutes – 1 hour until a red colour was achieved indicative of the correct pH (7.2-7.4) for the survival of glia cells.

For the dissection of the rat pups, the pups were placed on ice until hypothermic (~ 10 mins) and then decapitated before their brains were removed and placed onto a circle of Sylgard™ (Dow Corning, USA), to act as a platform for dissection, within a Petri dish containing ice-cold D-PBS. Using a Fiber-Lite MI-LED A2 high intensity LED illuminator (Dolan-Jenner Industries, USA), fine forceps and a no. 10 scalpel (Feather, Thermo Fisher Scientific, USA), the cortices of rat pups were isolated and the meninges removed. To allow efficient digestion of tissue, the corticies were cut into smaller chunks and scored before being added to the papain solution which was then incubated at 37°C with carbogen perfusion for 10 minutes. 5 ml of glia trituration media was then added to rinse the tissue and stop enzyme digestion before the supernatant was removed. Trituration of the tissue was then carried out to break down the chunks of cortex to form an opalescent solution of dissociated cells. Up to five rounds of trituration were performed where 1 ml glia trituration media was used to triturate the cells 7 times before the tissue was left for

1 minute to settle and then the supernatant was removed and saved. The dissociated cells within the supernatant were then pelleted (0.5 g, 5 minutes) and resuspended in glia media (MEM supplemented with 10 % CBS, 100 U/ml penicillin-streptomycin and 5 μg/ml insulin dissolved in 20 mM HCl). Dissociated glia cells were counted using the Countess™ 3 automated cell counter (Thermo Fisher Scientific, USA) and diluted to a plating density of 1 x 10^6 cells/ml in glia media.

Prior to plating, 3 wax dots were drawn on the surface of each well of 12-well plates using an ImmEgde® wax histology pen (Vector Laboratories, USA) to allow separation between the glia monolayer and the later placed coverslip with adhered neuronal cells. This allowed for better media exchange throughout the well but also provided leverage so that coverslips could be more easily removed from wells with a minimised disruption to cells. After the wax dots were dry, the 12-well plates were poly-D-coated (50 μg/ml) and washed with D-PBS before being left to dry. Glia cells were then plated in these 12-well plates (Corning, Sigma Aldrich, USA) at a density of 400,000 cells/well. The plated cells were incubated in a humidified incubator (37°C, 5% CO_2) for 2 hours to allow the cells to adhere to the wells. After 2 hours, cells were washed twice with cold MEM (2 ml/well) and finally cold fed with glia media (2 ml/well) to help minimize the number of surviving neurones. Cells were then grown in a humidified incubator (37°C, 5% CO_2) until a monolayer of 70% confluence was formed. Mitotic cell division was then inhibited with the addition of 6.7 μg/ml 5-fluorodeoxyuridine (FDU) (Sigma Aldrich, USA) to maintain the confluency and viability of the cells. One litter of rat pups yielded around 6 x 12-well plates of glia which were used for neuronal cell culture at least 1 week after plating and for up to 4 weeks after plating.

2.4.2 NEURONAL PREPARATION ON COVERSLIPS

A transgenic SNAP-D2R mouse line previously generated by Mike Holsey (lab of Jonathan Javitch) was used to culture striatal neurones. C57BL6 x CBAF1 hybrid mice (B6CBAF1) were used to generate the SNAP-D2R transgenic mice. Using CRISPR-

Cas9 gene editing, a SNAP-tag construct was inserted directly upstream of the gene encoding D2R (mouse DRD2) through injection into a fertilised egg followed by implantation into a pseudo pregnant female mouse. The SNAP-tag construct was comprised of the following elements: rat metabotropic glutamate receptor 5 signal peptide (MFLLLILSVLLLKEDVRGSAQS) – linker (TR) – HA-tag (YPYDVPDYA) – linker (TRGSTGEFT) – SNAPf-tag (MDKDCEMKRTTLDSPLGKLELSGCEQGLHRIIFLGKGTSAADA VEVPAPAAVLGGPEPLMQATAWLNAYFHQPEAIEEFPVPALHHPVFQQESFTRQVLWKLLKV VKFGEVISYSHLAALAGNPAATAAVKTALSGNPVPILIPCHRVVQGDLDVGGYEGGLAVKEWLL AHEGHRLGKPGLG – linker (PAG). Mouse pups were then genotyped by PCR and the SNAP-tag insertion was validated using slice immunohistochemistry.

The day before the neuronal culture of homozygous SNAP-D2R mice, conditioned neuronal media was prepared by washing 2 x 12-well plates of glia (description of preparation in **Chapter 2.4.1**) twice with cold MEM before adding 2 ml/well of neuronal media (BrainBits NbActiv4 (Thermo Fisher Scientific, USA)) supplemented with 1% FBS (Thermo Fisher Scientific, US), 100 U/ml penicillin-streptomycin and 0.5 mM kynurenic acid (KA)). Papain solution was prepared as previously described for glia cells (**Chapter 2.4.1**), with the addition of 0.5 mM of the neuroprotective agent KA to inhibit the glutamate-induced death of neurones. In addition, only 2 ml of papain solution was needed as only the striata of ~ 6 mice from a single litter was digested. ~ 10 ml of neuronal trituration media (neuronal media with 10% FBS) was incubated at 37°C and perfused with carbogen for 30 minutes - 1 hour.

The SNAP-D2R mouse pups were prepared for dissection as previously described with rat pups (**Chapter 2.4.1**). Here, striatal dissection was performed by taking a thick cross section across the middle of the brain before shelling out the cortex to obtain both pieces of striatum either side of the midline. Care was taken to avoid the hippocampus and to remove any meninges before scoring the chunks of striatum. The subsequent digestion and trituration of striatal tissue followed the same protocol as for rat cortex tissue (**Chapter 2.4.1**). Following trituration of the striatal tissue, a solution of dissociated neuronal cells was formed. Cells were then

pelleted (0.5 g, 5 minutes), resuspended in neuronal media and counted before being diluted in neuronal media to a plating density of 1 x 10^6 cells/ml. 240 µl/ well of this cell suspension was plated into a 24-well plate (Corning, Sigma Aldrich, USA) that contained a 12 mm coverslip (Carolina Biological, USA) in each well. These coverslips were previously coated with 50 µg/ml poly-D-lysine, washed with D-PBS and then coated with 10 µg/ml laminin (Thermo Fisher Scientific, USA) before being washed again with D-PBS and allowed to dry. Neuronal cells were left to adhere to these coverslips for 2 hours in a humidified incubator (37°C, 5% CO_2). The coverslips were then transferred to the glia plates containing conditioned neuronal media. Using fine forceps, a single coverslip was gently placed on top of the wax dots in each well either face up, where the neurones were facing up into solution, or flipped face down, where the neurones were facing the glia monolayer (**Fig. 2.1**). Glia cell line-derived neurotrophic factor (GDNF) (Thermo Fisher Scientific, USA) was then added to wells (10 ng/ml) and 24 hours after plating, 6.7 mg/ml FDU was added to inhibit the growth of non-neuronal cells. Cells were incubated (37°C, 5% CO_2) for 10 days prior to staining and fixing with minimal observations under a microscope to minimise neuronal death.

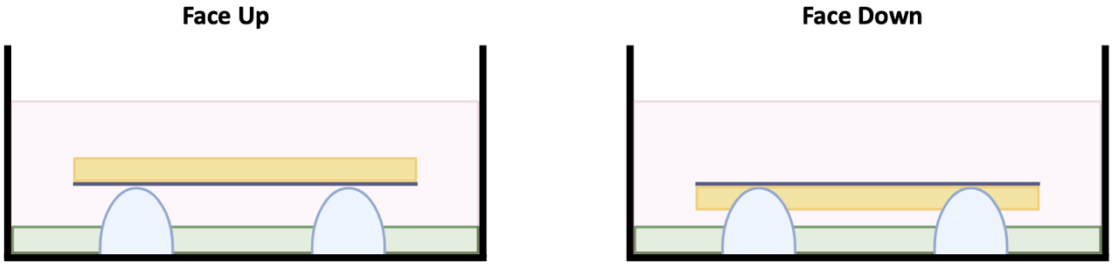

Figure 2.1: Schematic showing primary neuronal culture plating formats.
Wells of a 12-well plate containing a monolayer of glia cells (green) are shown with wax dots (blue hemispheres) acting as a platform for a coverslip with adhered neuronal cells (yellow) that is placed into the well either face up or face down. The wax dots ensure the coverslip is lifted above the glia cells to ensure all cells have access to the culture media.

After 10 days, coverslips were transferred to a 24-well plate containing cell impermeable SNAP-dyes (Janelia Fluor® 549i, Janelia Fluor® 646i, SNAP-Surface® Alexa Fluor® 549 and SNAP-Surface® Alexa Fluor® 647) made up in neuronal media at a range of concentrations (0.1 nM – 1 μM). All coverslips were placed in the SNAP-dye solutions with the neurones face up, irrespective of previous plating format, to allow optimal access of SNAP-dyes to the cells. Cells were incubated for 30 minutes (37°C, 5% CO_2) to allow labelling of the SNAP-tag. The coverslips were then washed with D-PBS before fixing with 4% paraformaldehyde (PFA) (Electron Microscopy Sciences, USA) and incubating for 10 minutes at room temperature. Cells were washed with D-PBS again before staining with 1 μM 4',6-diamidino-2-phenylindole (DAPI) (Thermo Fisher Scientific, USA) for 15 minutes at room temperature. Cells were washed with D-PBS for a final time and stored in D-BPS with 0.02% sodium azide (Ricca Chemical, USA) at 4°C using parafilm to minimize bacterial growth and evaporation.

In addition to striatal cultures from SNAP-D2R mice, wild type (WT) striatal cultures from B6CBAF1 mice were prepared using the same protocol as above as a negative control. As a positive control, CHO tetracycline-inducible SNAP-D2R cells were also seeded on 12 mm coverslips (Carolina Biological, USA) and SNAP-labelled. 20,000 cells were plated per coverslip and left to grow in a humidified incubator (37°C, 5% CO_2) for 3 days before the growth media was changed and supplemented with 1 μg/ml tetracycline for 24 hours. The following day cells were SNAP-labelled with 1 μM of each of the above SNAP-dyes made up in CHO growth media for 30 minutes (37°C, 5% CO_2). The coverslips were then fixed and DAPI-stained using the same protocol as for the striatal neurones above.

2.5 FUNCTIONAL ASSAYS

2.5.1 G PROTEIN ACTIVATION ASSAY

D2R-mediated G protein activation was measured using a bioluminescence resonance energy transfer (BRET) assay based on the dissociation of the $G_{\beta\gamma}$ subunits from the $G_{\alpha o}$ subunit (**Fig. 2.2**). CHO tetracycline-inducible SNAP-D2R cells were first plated in a 10 cm cell culture dish (~ 1.5 x 10^6 cells/dish) and grown in culture media overnight in a humidified incubator at 37°C and 5% CO_2. The next day, cells were transfected with DNA constructs using polyethylenimine (PEI) (Polysciences, USA) in a ratio of 1:6 total DNA to PEI. The following DNA constructs encoded in a pcDNA3.1 vector were first diluted in 250 μl of 150 mM sterile NaCl: 2 μg $G_{\alpha o}$, 1 μg masGRK3-ct-Rluc, 1 μg Venus1-155-$G_{\gamma 2}$ and 1 μg Venus156-239-$G_{\beta 1}$. The masGRK3-ct-Rluc construct encoded amino acids 495-688 of the carboxyl-terminus of a bovine GRK3, preceded by a myristic acid attachment peptide (mas; MGSSKSKTSNS), and fused to Rluc8[183]. A $G_{\beta\gamma}$-Venus protein was expressed through the transfection of the Venus1-155-$G_{\gamma 2}$ construct which encoded amino acids 1-155 of a venus protein fused to a GGSGGG linker and then to the amino-terminus of a human $G_{\gamma 2}$, and the Venus156-239-$G_{\beta 1}$ construct which encoded amino acids 156-239 of a venus protein fused to a GGSGGG linker and then to the amino-terminus of a human $G_{\beta 1}$[183]. PEI was next diluted by adding 30 μl into 220 μl of 150 mM sterile NaCl. The diluted PEI solution was then added to the diluted DNAs and vortexed for 3 seconds prior to a 10-minute incubation at room temperature to allow PEI/DNA complexes to form. Cell media was replaced and supplemented with 100 U/ml penicillin-streptomycin before the gentle addition of the complexes to cells. Cells were left to incubate for 24 hours at 37°C, 5% CO_2 in a humidified incubator. Cells were then harvested using 0.5 ml of trypsin-EDTA solution (0.25%) and left to incubate at 37°C for 3 minutes to ensure cells had detached. Cells were resuspended in 5 ml media before centrifugation at 1000 rpm for 3 minutes. The resulting pellet was suspended in a total of 10 ml media supplemented with tetracycline hydrochloride (1 ng/ml – 10 μg/ml). Cells were then replated in white 96-well plates (100 μl/well) and grown for a further 24 hours.

The following day, cells were washed once with D-PBS and incubated in fresh D-PBS (80 µl/well) for 30 minutes at 37°C. Five minutes prior to ligand addition, the Rluc substrate, coelenterazine h (NanoLight, USA), was added (10 µl/well at a final concentration of 5 µM) and incubated in a PHERAstar FS microplate reader (BMG LABTECH, UK) at 37°C. 10 µl of agonist or vehicle (D-PBS) was then added to wells using a multichannel pipette and the BRET signal was measured immediately and continuously over the next 10 minutes using the BRET1 plus filter which monitored the emission from Venus (505-535nm) and Rluc (445-475nm). The counts from the Venus acceptor were then divided by the Rluc donor to generate a BRET ratio. The resulting agonist-induced BRET ratios were then baseline-corrected by subtracting the BRET ratio from vehicle-treated cells. The baseline-corrected BRET ratios were finally normalized as a percentage of the response induced by the highest concentration of dopamine (10 µM).

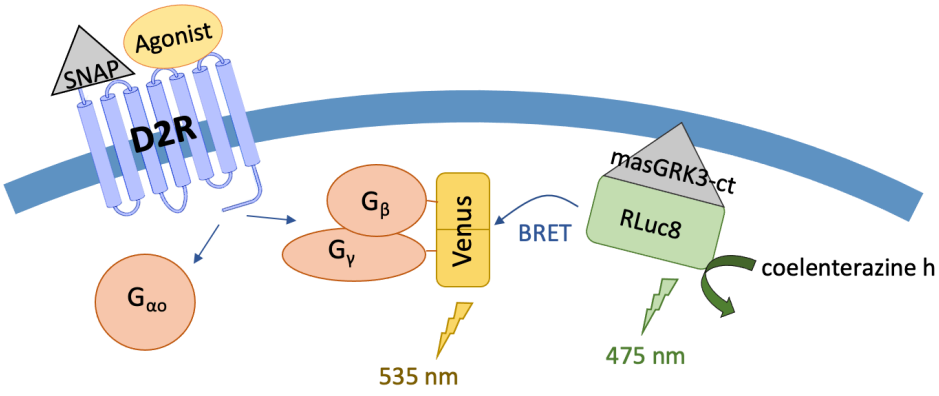

Figure 2.2: Schematic showing G protein activation assay.

CHO tetracycline-inducible SNAP-D2R cells were induced with 1 µg/ml tetracycline to allow SNAP-D2R expression on the cell membrane. Binding of an agonist to the SNAP-tagged D2R causes receptor activation leading to the dissociation of the $G_{\beta\gamma}$-Venus from the $G_{\alpha o}$ subunit. The membrane anchored masGRK3-ct-Rluc8 fusion protein can then bind the free $G_{\beta\gamma}$-Venus complex. In the presence of coelenterazine h, masGRK3-ct-Rluc8 emits light at 475 nm which can then excite the Venus tag of the dissociated $G_{\beta\gamma}$-Venus complex through bioluminescence resonance energy transfer (BRET) resulting in Venus emission at 535 nm.

2.5.2 BYSTANDER BRET-BASED TRAFFICKING ASSAY

This trafficking assay relies on bystander BRET to detect the localisation of D2R (long isoform)-Nanoluciferase (Nluc) in different cellular compartments using Venus-tagged cell compartment markers (**Fig. 2.3**). HEK 293T cells were plated in 10 cm dishes (~ 2 x 10^6 cells/ dish) and left to grow overnight in a humidified incubator at 37°C and 5% CO_2. Cells were then transfected using PEI in a ratio of 1:6 total DNA to PEI using the general transient transfection protocol previously described (**Chapter 2.5.1**). The following DNA constructs encoded in a pcDNA3.1 vector were transfected: 0.025 μg D2R-Nluc, 2 μg GRK2 or GRK2 K220R (kinase dead), 4 μg β-arrestin2 and 1 μg of one of the Venus-tagged cell compartment markers. These cell compartment markers comprised a Venus protein fused to the amino-terminus of fragments of KRas (25 amino acid C-terminal fragment) for the plasma membrane, Rab5 for the early endosomes, Rab7 for the lysosome, Rab11 for the recycling endosomes, Giantin for the Golgi apparatus and PTP1B for the ER, as previously described by Lan et al.[184]. Experiments were also performed with endogenous levels of GRK2 and β-arrestin2, therefore, these DNAs were not included in the DNA transfection mix and instead 6 μg of pcDNA3.1 was included to ensure that the total DNA transfected remained constant. PEI was then diluted by adding 42.15 μl into 207.85 μl of 150 mM sterile NaCl. The PEI was then added to the DNA transfection mix and the total combined 500 μl of PEI/DNA complexes were then added to the HEK 293T cells in a 10cm dish with fresh media supplemented with 100 U/ml penicillin-streptomycin. Transfected cells were incubated for 24 hours in a humidified incubator at 37°C and 5% CO_2. Prior to replating, white 96-well plates were coated with poly-D-lysine (20 μg/ml, 50 μl/well) for 30 minutes at room temperature. Plates were then washed with D-PBS and left to fully dry before use. To harvest the transfected cells, 10 ml of serum-free DMEM supplemented with 100 U/ml penicillin-streptomycin was used to lift the cells from 1.5 x 10 cm dishes before cells were replated into a single poly-D-lysine-coated white 96-well plate. 1.5 dishes of transfected cells were used to seed a single 96-well plate to compensate for the reduced cell growth seen with serum starving. The plated cells were then incubated

for 5 hours at 37°C and 5% CO_2 prior to ligand/vehicle addition (30 μl/well) followed by a further 24 hours of incubation prior to assay.

The next day, cells were washed once with 100 μl D-PBS and replaced with fresh D-PBS (60 μl/well). Ligand/vehicle (30 μl/well) was then added followed by 10 μl/well of the Nluc substrate, Nano-Glo® furimazine (1:1000 final assay dilution from manufacturer's stock). Experiments were also performed with a 4-hour washout where, 24 hours after drug/vehicle addition, cells were washed twice with 100 μl D-PBS, replaced with fresh D-PBS (90 μl/well) and incubated for 4 hours before the addition of 10 μl/well of the Nluc substrate. Washout experiments were only performed using the Venus-KRas and Venus-PTP1B cell compartment markers.

Once the Nluc substrate, Nano-Glo® furimazine, was added, cells were incubated in a PHERAstar FS plate reader for 15 minutes at 37°C before luminescence and fluorescence was measured using the BRET1 plus filter at 445-475nm (Nluc) and 505-535nm (Venus) respectively. The counts from the Venus acceptor were then divided by the Nluc donor to generate a BRET ratio. Data were presented as baseline-corrected BRET ratios by subtracting the mean BRET signal from vehicle (DMSO)-treated cells from the ligand-induced BRET signal.

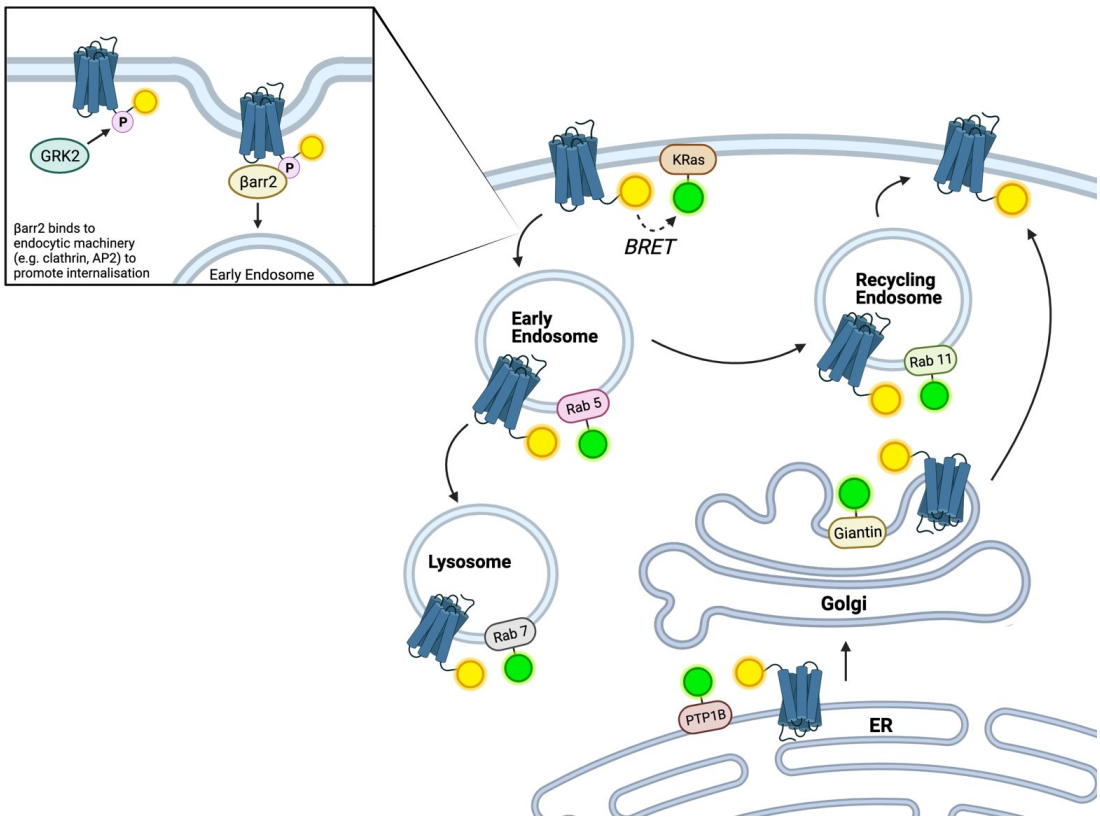

Figure 2.3: Schematic showing BRET trafficking assay.

The D2R (long isoform)-Nluc acts as the BRET donor with the C-terminal Nluc tag shown in yellow. The BRET acceptors are the various cell compartment markers tagged with a Venus protein (green). Localisation of D2R-Nluc was detected at: the cell membrane, using the Venus-KRas marker; the early endosome, using the Rab 5-Venus marker; the recycling endosome, using the Venus-Rab11 marker; the lysosome, using the Venus-Rab7 marker; the Golgi apparatus, using the Venus-Giantin marker; and the endoplasmic reticulum (ER), using the Venus-PTP1B marker. The magnified window above shows the involvement of GRK2 and β-arrestin2 in receptor internalisation and entry into the endosomal pathway.

2.6 BINDING ASSAYS

2.6.1 MEMBRANE PREPARATION

Membrane preparations were performed using both CHO tetracycline-inducible SNAP-D2R cells and FlpIn™ CHO SNAP-D2S cells grown in 175cm^2 flasks. At ~ 75% confluency, CHO tetracycline-inducible SNAP-D2R cells were induced with 1 μg/ml tetracycline. Once both cell lines reached ~ 90% confluency, cells were washed twice with 12 ml D-PBS and incubated with 12 ml of 100 nM SNAP-Lumi4-Tb reconstituted in Tag-lite labelling medium for 1 hour in a humidified incubator (37°C, 5% CO_2). Cells were washed again with 12 ml D-PBS to remove any unbound SNAP-Lumi4-Tb label and then harvested by scraping with 10ml D-PBS per flask. The harvested cells were collected by centrifugation (10 minutes, 1500 rpm) and the resulting cell pellet was frozen at -80°C.

The cell pellet was thawed on ice, resuspended in 15 ml D-PBS and homogenised on ice using an electrical homogenizer (Ika-Werk GmbH & Co. KG, Germany) (setting 4, 10 x 2 second bursts). The homogenised cells were then centrifuged for 30 minutes at 48,000 g at 4°C (Beckman Avanti J-251 Ultra- centrifuge, Beckman Coulter, UK). The supernatant was discarded, and the pellet was resuspended in 15 ml D-PBS before being centrifuged a second time (30 min, 48,000 g, 4°C). The resulting cell pellet was then resuspended in 6 ml D-PBS and further homogenised using a 10 ml glass homogeniser (20 passes, speed 10) (Ika-Werk GmbH & Co. KG, Germany) and BD precision glide 27-gauge needle to make the solution uniform. The protein concentration of the membrane solution was measured (**Chapter 2.6.2**) before being aliquoted and stored at −80°C until required.

2.6.2 PROTEIN CONCENTRATION DETERMINATION

The protein concentrations of membrane preparations were determined using the Pierce™ BCA (bicinchoninic acid) Protein Assay Kit (Fisher Scientific, UK) according to the manufacturer's instructions. This kit allows the colorimetric

detection and quantification of total protein in unknown samples. The reduction of Cu^{2+} to Cu^{+} mediated by peptide bonds under alkaline conditions, is detected by a working reagent containing BCA. Cu^{+} chelates with two molecules of BCA to form a purple complex which exhibits a strong absorbance at 562 nm[185]. The formation of this coloured complex is linear with increasing protein concentrations.

Bovine serum albumin (BSA) standards were first diluted in D-PBS to generate diluted BSA standards ranging from 0.25 mg/ml – 2 mg/ml. 25 μl of each standard was added, in duplicate, to a clear flat-bottom 96-well plate (Corning; Sigma Aldrich, UK) to generate a standard curve. The membrane prep was then diluted 1:1 in D-PBS before 25 μl of the neat sample and the diluted sample were added, in duplicate, to the plate. BCA working reagent was prepared by mixing BCA reagent A and BCA reagent B in a 50:1 ratio. 200 ul/well of this working reagent was then added to the plate and incubated at 37°C for 30 minutes. The absorbance at 562 nm was then measured using a PHERAstar FS plate reader (BMG LABTECH, UK). A standard curve was created by plotting the average measured absorbance values of the diluted BSA standards against their known concentrations. From this curve, the concentration of the membrane prep was interpolated from its average measured absorbance values.

2.6.3 ASSOCIATION KINETICS

A Time-Resolved Fluorescence Resonance Energy Transfer (TR-FRET) assay was used to determine the kinetic parameters, association (k_{on}) and dissociation (k_{off}) rates, of fluorescent APDs spiperone-d2 and clozapine-Cy5, at D2R. TR-FRET assays provide information on the interaction of two labelled proteins/molecules through the energy transfer between a donor and acceptor fluorophore which occurs when they are < 10 nm apart, when they have an emission and excitation spectral overlap, and when they are in a specific spatial orientation[186] (**Fig. 2.4**). TR-FRET assays also show high signal-to-noise ratios due to the long-lived emission of the lanthanide donor (e.g. terbium) meaning the emission signal from the acceptor can be measured after the background autofluorescence has decayed.

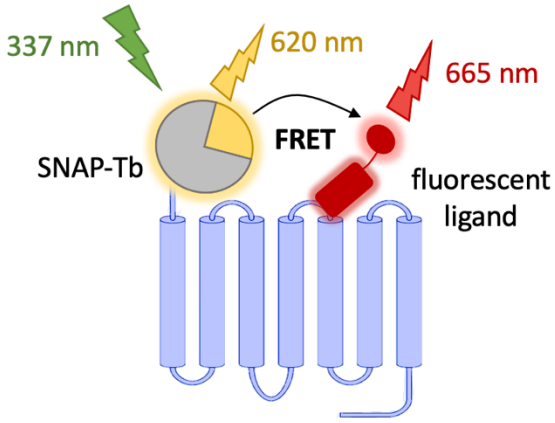

Figure 2.4: Schematic showing time-resolved fluorescence resonance energy transfer (TR-FRET) assay.

Upon 337 nm laser excitation, the terbium-labelled SNAP tag donor (SNAP-Tb) N-terminally tagged to the receptor emits light at 620 nm and transfers energy to the fluorescent ligand acceptor causing it to emit light at 665 nm.

All ligands were diluted in binding buffer: HEPES-buffered saline solution (HBSS) (H6648, Sigma-Aldrich, UK), 20 mM HEPES, 1% DMSO, 0.02% pluronic acid, 1 mg/ml glucose (pH 7.4). Cell membranes were also diluted in binding buffer supplemented with 100 μM Gpp(NH)p and 50 μg/ml saponin. Membrane concentrations of 1.5 μg/well or 1.0 μg/well were used, depending on the cell line, to achieve terbium counts of ~ 1,000/well. Increasing concentrations of 10 μl of spiperone-d2 or clozapine-Cy5 were added to a 384-well plate, in singlet, along with either 10 μl of binding buffer, to determine total binding, or 10 μl of haloperidol (10 μM), to determine non-specific binding. Ligands were incubated at 37°C for 10 minutes before the injection of cell membrane to initiate the binding reaction.

TR-FRET measurements were acquired on a PHERAstar FS plate reader (BMG LABTECH, UK) at 37°C. Cell membrane solution was primed onto the injection system and injected into wells at 400 μL/s (20 μl/well). The plate was then subjected to a single double orbital shake at 100 rpm before the first measurement cycle was initiated. The HTRF optic module, set at a focal height of 11.4 mm, excited the terbium label at 337 nm using 4 flashes/well every 4 seconds. The terbium donor emission signal (620 nm) and fluorescent ligand acceptor emission signal (655 nm) were collected, and Homogenous Time-Resolved Fluorescence (HTRF) ratios were obtained by dividing the acceptor signal by the donor signal and multiplying by 10,000. Specific HTRF ratios were then generated by subtracting the non-specific binding HTRF ratios from the total binding HTRF ratios for each fluorescent APD concentration per experiment.

2.7 FLUORESCENCE MICROSCOPY

2.7.1 LIVE CELL CONFOCAL IMAGING

2.7.1.1 Characterisation of SNAP-D2R expression

CHO tetracycline-inducible SNAP-D2R cells were prepared for FCS measurements as described in **Chapter 2.7.3**. Briefly, cells were harvested from a 75 cm^2 flask and seeded at 10,000 cells/well in Nunc™ Lab-Tek™ chambered 8-well coverglasses and grown for 48 hours before assay. SNAP-D2R expression was induced with 10 ng/ml – 100 ng/ml tetracycline for 24 hours, and cells were labelled with 100 nM SNAP-Surface® Alexa Fluor® 488. Prior to cell-based FCS measurements (**Chapter 2.7.3**), confocal images were acquired using sequential scanning with 488 nm excitation (2%) and 493-630 nm emission range, and 633 nm excitation (3%) and 638-759 nm emission range. The pinhole diameter was set to 1 Airy Unit and the gain and offset settings were maintained within each experiment. Transmitted light images were also obtained with the condenser in the 'H' phase. All images were acquired as 12-bit images with 1024 x 1024 pixels per frame and 4 averages.

2.7.1.2 APD-induced chaperoning of SNAP-D2R to the cell membrane

CHO tetracycline-inducible SNAP-D2R cells were harvested from a 75 cm^2 flask and counted as previously described (**Chapter 2.3.1**). Cells were then seeded at 20,000 cells/well in Nunc™ Lab-Tek™ chambered 8-well plate and incubated overnight in a humidified incubator (37°C, 5% CO_2). The next day, the media was exchanged and supplemented with 1 μg/ml tetracycline to induce receptor expression. After a further 24 hours, the media was again exchanged and supplemented with 10 μM ligand or vehicle (DMSO). Cells were then incubated for an additional 24 hours before SNAP-tag labelling by incubating cells (37°C, 5% CO_2) with 100 nM SNAP-Surface® Alexa Fluor® 488 made up in CHO growth media containing 10 μM ligand/vehicle to maintain ligand pressure. Cells were then washed twice with pre-warmed HBSS (sodium pyruvate ($C_3H_3NaO_3$) 2 mM, NaCl 145 mM, D-Glucose 5 mM, KCl 5 mM,

$MgSO_4.7H_2O$ 1 mM, HEPES 10 mM, $CaCl_2$ 1.3 mM, $NaHCO_3$ 1.5 mM, pH 7.4) and replaced with HBSS containing 10 μM ligand/vehicle. Washout experiments were also performed where cells were SNAP-labelled and imaged in the absence of ligand which meant that the ligand pressure was removed for ~ 45 minutes prior to and during imaging.

SNAP-labelled cells were then equilibrated at 24°C for 10 minutes prior to confocal image acquisition performed at 24°C on a Zeiss LSM880 microscope fitted with a 40x c-Apo water immersion objective (NA 1.2). Two images for each ligand or vehicle were acquired per experimental day using 488 nm excitation (Argon laser, 2%) and 493-630 nm emission range. The pinhole diameter was set to 1 Airy Unit and the gain and offset settings were adjusted to maintain signal within the linear range of the detector and were kept consistent within each experiment. Transmitted light images were also obtained with the condenser in the 'H' phase. All images were acquired as 12-bit images with 1024 x 1024 pixels per frame and 4 averages.

2.7.2 PRIMARY NEURONE IMAGING

Prior to imaging, fixed coverslips with neuronal cultures were mounted onto Diamond® white glass microscope slides (Globe Scientific, USA) using ProLong™ Gold Antifade reagent (Thermo Fisher Scientifc, USA). Images were acquired on a Leica SP8 Confocal Microscope using a 10x dry objective (NA 0.4) and sequential line scanning with laser excitation at 405 nm (2%) and, 561 nm (2%) or 633 nm (3%). Emission was collected using HyD detectors and the pinhole diameter was set to 1 Airy unit. For each channel, the gain was set to maximum and kept consistent between experiments. Images were taken for each SNAP dye and concentration used (as described in **Chapter 2.4.2**) with 1024 x 1024 pixels per frame and 2 line and frame averages. In addition, z-stacks were taken with digital zoom so that the field of view encompassed either a single or a few neurones (zoom 2-3, depending on the size of neurone and dendrite length). The equatorial position of the cell (in the z axis) was first marked by eye and z-stacks of 20 mm thick were acquired based on this

equatorial slice (2 mm step size, 11 steps). Fixed coverslips with CHO tetracycline-inducible SNAP-D2R cells were mounted and imaged as a positive control using the same protocol as described above for neuronal imaging.

2.7.3 FLUORESCENCE CORRELATION SPECTROSCOPY

Fluorescence correlation spectroscopy (FCS) settings for measurements of fluorescent ligands (spiperone-d2 and clozapine-Cy5) in solution were optimised at 24°C on a Zeiss LSM880 microscope fitted with a 40x c-Apo water immersion objective (NA 1.2). For these optimisation experiments, the FCS confocal volume was calibrated each experimental day using a 10 x 10 second and 1 x 60 second data collection of 10 nM Cy5-NHS ester (D= 3.16 x 10^{-10} m^2/s)[187]. The fluorescent ligands were made up in HBSS and their concentration and diffusion coefficients were determined over a range of added concentrations (10 - 40 nM) using several laser powers (5 - 30%) with and without 0.1% BSA. Here, the FCS detection volume was placed in solution at 200 μm above the glass and data were collected using 3 x 10s reads at each added concentration and laser power.

FCS experiments were also carried out using the Flp-In™ CHO parental cell line and the CHO tetracycline-inducible SNAP-D2R cell line. Cells from both cell lines were harvested from a 75 cm^2 flask and counted as previously described (**Chapter 2.3.1**). Cells were then seeded at 10,000 cells/well in Nunc™ Lab-Tek™ chambered coverglass 8-well plates and incubated for 48 hours in a humidified incubator (37°C, 5% CO_2). CHO tetracycline-inducible SNAP-D2R cells were induced with 10 ng/ml – 100 ng/ml tetracycline 24 hours after plating and left to incubate for a further 24 hours before assay.

On the day of assay, Flp-In™ CHO parental cells were washed twice with pre-warmed HBSS before being treated with fluorescent spiperone-d2 or clozapine-Cy5 for 2 hours at 37°C. CHO tetracycline-inducible SNAP-D2R cells were first SNAP-labelled with 100 nM SNAP-Surface® Alexa Fluor® 488 made up in CHO media for 30

minutes at 37°C and 5% CO_2. These cells were then washed twice in warmed HBSS followed by a longer wash of 10 minutes. CHO tetracycline-inducible SNAP-D2R cells were assayed either in the absence of fluorescent ligand (HBSS only) or following incubation with fluorescent spiperone-d2 or clozapine-Cy5 for 2 hours at 37°C. FCS experiments using CHO tetracycline-inducible SNAP-D2R cells were also performed with a 30 minute pre-incubation of 10 μM of irreversible D2R antagonist, phenoxybenzamine (PBZ), followed by the co-addition of spiperone-d2 and PBZ for 2 hours at 37°C.

After the staining and/or fluorescent ligand treatment of both cell lines, cells were equilibrated at 24°C for 10 minutes before confocal image acquisition (**Chapter 2.7.1**) and FCS measurements were performed at 24°C on a Zeiss LSM880 microscope fitted with a 40x c-Apo water immersion objective (NA 1.2). The FCS confocal volume was calibrated each experimental day using a 10 x 10 second and 1 x 60 second data collection of 10 nM Cy5-NHS ester (D= 3.16 x 10^{-10} m^2/s)[187] or 20 nM ATTO488 (D= 4.0 x 10^{-10} m^2/s)[188] solutions. The FCS measurement volume was positioned over cells in x and y using a live confocal image with 488 nm excitation and a 493-630 nm band pass emission filter (pinhole diameter set to 1 Airy Unit) (**Fig. 2.5A**).

For FCS reads of fluorescent ligands in solution above cells, the detection volume was positioned in z at the approximated upper cell membrane position by eye and then moved 2 μm above this position to ensure no membrane was present. FCS measurements were taken using 633 nm excitation with emission collected through a LP650 filter and the pinhole diameter set to 1 Airy Unit. Fluorescence intensity fluctuations were collected for 5 seconds between 8 μm – 200 μm above the glass in 1 μm, 5 μm, 10 μm and 50 μm increments using a laser power of ~ 1.91 kW/cm^2 (15 %) (**Fig. 2.5B**). These z-scan reads were taken above FlpIn™ CHO parental cells without D2R expression, cells with a range of SNAP-D2R expression at the cell surface and 'no cell' control measurements where the z-scan reads were above glass only (**Fig. 2.5C**). The 'no cell' z-scans were also started at 8 μm above the glass (2 μm above the average cell height of 6 μm) to be comparable to z-scans above cells.

FCS measurements were also taken at the upper cell membrane of CHO tetracycline-inducible SNAP-D2R cells. First, the measurement volume was positioned in z at the approximated upper cell membrane position by eye and then precisely positioned using an intensity z-scan ± 2 µm in 0.25 µm intervals with 488 nm laser excitation with a low laser power (0.01%) (**Fig. 2.5D**). FCS reads were taken of SNAP-D2R labelled with Alexa Fluor® 488 in the absence of fluorescent drug treatment. Here, fluorescent fluctuations were collected for 1 x 30 seconds using a 488 nm excitation at ~ 0.03 kW/cm^2 laser power (0.1%) through a 508-691nm band pass emission filter (pinhole diameter set to 1 Airy Unit). In addition, FCS reads of fluorescent ligand were taken at the upper cell membrane allowing the detection of ligand in solution immediately adjacent to the membrane and also the detection of ligand bound to the membrane (**Fig. 2.5E**). Here, fluorescent fluctuations were collected for 1 x 30 seconds using a 633nm excitation at ~ 0.01 kW/cm^2 (0.1%) through a LP650 filter and the pinhole diameter set to 1 Airy Unit.

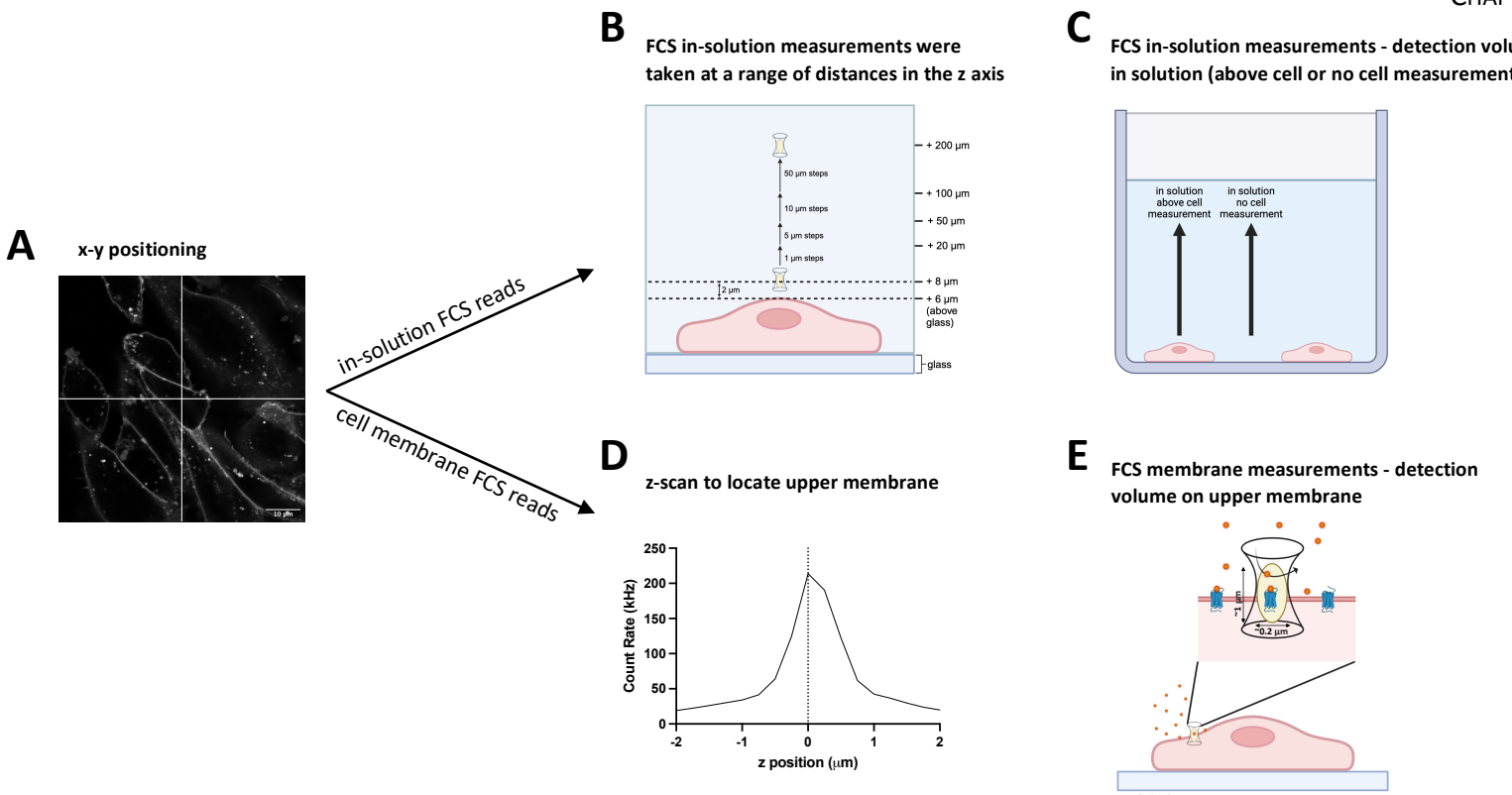

Figure 2.5: FCS experimental workflow of in-solution reads (top row – A, B & C) and cell membrane reads (bottom row- A, D & E).

(**A**) The FCS detection volume was positioned over cells in x and y using a live confocal image with a crosshair. (**B**) For in-solution FCS measurements, the detection volume was placed 8 µm above the glass in the z axis and moved in increasing increments of 1, 5, 10 and 50 µm steps up into solution from 8 µm – 200 µm above the glass. (**C**) Schematic representation of FCS measurements in solution. The detection volume was positioned in the x-y axis either above a cell (above cell measurement) or above the glass only (no cell measurement) within the same well of an 8-well chambered coverglass. (**D**) An intensity scan in z was performed ± 2 µm from the approximated upper membrane position to place the FCS detection volume precisely on the upper membrane. (**E**) Schematic representation of an FCS measurement on the upper membrane of a cell with fluorescent ligand present in solution and bound to the membrane. The excitation area (conical shape in black) and detection area (oval in yellow) of the FCS detection volume are shown.

2.8 DATA ANALYSIS

2.8.1 SOFTWARE

Functional and binding assay data were analysed using GraphPad Prism 10.1.1 (GraphPad Software, USA). Functional assay data are presented as mean ± standard error of the mean (SEM) whereas binding experiments were performed in singlet and are presented as a single experimental repeat representative of 3-5 individual experiments. Confocal images were collected using Zen Black 2012 (Zeiss, Germany) or Leica Application Suite X 5.2.2 (Leica Microsystems, Germany) for model cell lines and primary neuronal cultures, respectively. Images of CHO and HEK 293T model cell lines were processed and analysed using Zen Black 2012, whereas primary neuronal culture images were processed using Image J Fiji 2.14 (National Institutes of Health, USA). FCS data analysis and fitting were performed using Zen Black 2012 and are presented as mean ± SEM. A minimum of three FCS measurements either on the upper membrane of a cell or of a z-scan above a cell in solution were performed per experimental condition per day. All FCS data collected within one experimental day represents one n number. Figures were made either in BioRender (Toronto,Canada) or PowerPoint (Microsoft Corporation, USA).

2.8.2 STATISTICS

All statistical tests were performed using GraphPad Prism 10.1.1 with statistical significance defined as $P < 0.05$. Results from statistical tests are noted in figures and/or in the Results text where more specific details of the statistical tests can be found. Data normality was tested using the Shapiro-Wilk test and parametric statistical tests were only performed on data following a Gaussian distribution, except for parametric two-way analysis of variance (ANOVA) tests due to the lack of a non-parametric equivalent.

In all other cases, non-parametric tests were performed on non-normally distributed data.

2.8.2 FUNCTIONAL ASSAY ANALYSIS

Concentration response curves were fitted to a non-linear regression model:

(2.1)

$$y = \min + \left(\frac{max - min}{1 + 10^{(LogEC50 - x)}}\right)$$

Min and max represent the minimum and maximum values, respectively, of the curve. EC_{50} is the concentration of ligand required to produce half the maximal response (defined as the span of the curve (max-min)).

2.8.3 BINDING ASSAY ANALYSIS

Ligand binding of several concentrations of the fluorescent APDs, spiperone-d2 and clozapine-Cy5, was monitored over time. These time courses were fitted to a one-phase exponential association function:

(2.2)

$$binding = y_{max} \times (1 - e^{-k_{obs} \cdot t})$$

Equation 2.2 describes: the maximum response at infinite time, y_{max}; the observed association rate, K_{obs}; and time, t. In conjunction with **equation 2.2**, the kinetic parameters (association rate, k_{on}, and dissociation rate, k_{off}) of fluorescent APDs were determined by fitting association binding curves to a global non-linear regression model named 'Association kinetics – two or more conc. of hot'. This model utilises the following

relationship with k_{obs}:

(2.3)

$$k_{obs} = [\text{fluorescent ligand}] \times k_{on} + k_{off}$$

The global kinetic parameters, k_{off} and k_{on}, were then used to determine the binding affinities of the fluorescent APDs:

(2.4)

$$K_d = \frac{k_{off}}{k_{on}}$$

K_d is the equilibrium dissociation constant and represents the ligand concentration required to occupy 50% of receptors.

2.8.4 CONFOCAL IMAGE QUANTIFICATION

2.8.4.1 Characterisation of SNAP-D2R expression

SNAP-D2R expression of CHO tetracycline-inducible SNAP-D2R cells was quantified by drawing a region of interest (ROI) around the membrane of a cell on the transmitted light image, overlaying the fluorescence channel and measuring the mean intensity of 488 nm fluorescence within the ROI (**Fig. 2.6**).

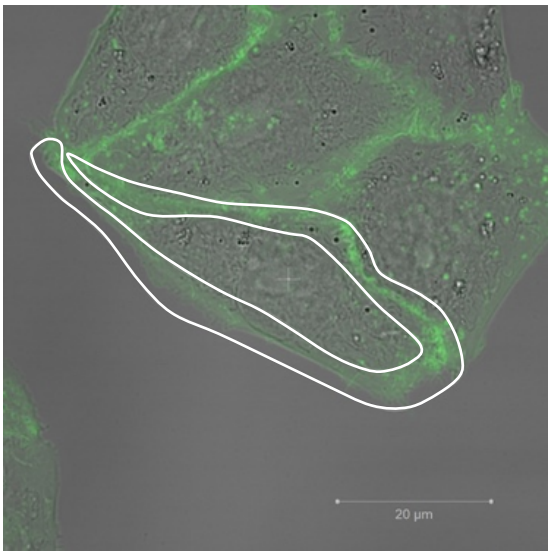

Figure 2.6: The drawing of an ROI to quantify SNAP-D2R expression.

On transmitted light images, a region of interest (ROI) shown in white was drawn around the membrane of SNAP-Surface® Alexa Fluor 488® -labelled CHO tetracycline-inducible SNAP-D2R cells. The fluorescent 488 nm channel was then overlayed allowing the measurement of the fluorescent SNAP-D2R signal (shown in green) at the membrane.

2.8.4.2 Imaging APD-induced chaperoning of SNAP-D2R to the cell membrane

CHO tetracycline-inducible SNAP-D2R cells were homogenous in size and morphology, meaning transmitted light images were easily thresholded to select only the cells and remove the background. First a region of interest (ROI) was drawn within the background (no cell area) on the transmitted light image. The 488 nm fluorescence channel was then overlayed and the mean fluorescence intensity within the ROI was measured. A threshold across the whole transmitted light image was then set based on this background fluorescent intensity to include all pixels with an intensity higher than the background (**Fig. 2.7**). This threshold value was kept consistent for all images acquired within one experimental day. The mean fluorescence intensity within the thresholded region of each image was then determined.

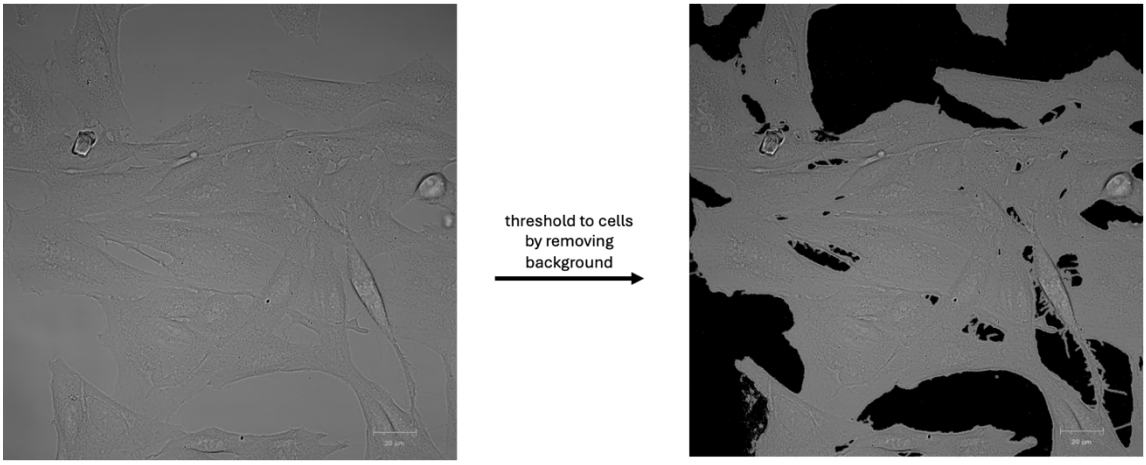

Figure 2.7: Threshold applied to quantify the fluorescent signal of labelled SNAP-D2R in CHO tetracycline-inducible SNAP-D2R cells.

Cells were treated with ligand/vehicle prior to labelling with SNAP-Surface® Alexa Fluor 488®. The 488 nm signal of SNAP-labelled SNAP-D2R was determined within cells by thresholding transmitted light images (example shown on the left) to select only the cells and to remove the background (shown in black) before overlaying the 488 nm fluorescent channel on top and measuring the mean fluorescence intensity within the grey selection area.

This thresholding method resulted in measuring the 488 nm intensity throughout whole cells rather than solely the fluorescent signal localised to the membrane. Unfortunately, due to the uniformity of the CHO tetracycline-inducible SNAP-D2R cells in the transmitted light image, the membrane could not be distinguished from the cytoplasm or other cellular compartments. However, SNAP-D2R was primarily localised at the membrane and showed a similar distribution within cells both with and without APD/vehicle treatment.

2.8.5 FCS ANALYSIS

FCS can detect the molecular dynamics of a fluorescent species within a defined detection volume (~ 0.2 fL, ~ 1 x 0.2 μm). As the fluorescent species diffuses through this detection volume, fluctuations in intensity are produced which can then be analysed using the normalised intensity autocorrelation function, G(τ), to determine the particle number, ligand concentration and diffusion coefficient of the fluorescent species (**Fig. 2.8A**). G(τ) compares the fluorescence intensity, δI, at a given time, t, first to the average fluorescence intensity, *I*, and then to the intensity of a fluctuation later at a given time later, δI(t + τ), before being normalised to the average intensity. This function is described as follows with angular brackets representing an ensemble average:

(2.5)

$$G(\tau) = 1 + \frac{\langle \delta I(\mathrm{t}) \cdot \delta I(\mathrm{t}+\tau) \rangle}{\langle I \rangle^2}$$

The algebraic form of G(τ) in relation to the 3D diffusion of a fluorescent species is shown below:

(2.6)

$$G(\tau) = 1 + \frac{A}{N} \cdot \sum_{i=1}^{m} \cdot f_i \cdot \left(1 + \frac{\tau}{\tau_{Di}}\right)^{-1} \cdot \left(1 + \frac{\tau}{S^2 \cdot \tau_{Di}}\right)^{-\frac{1}{2}}$$

where;

(2.7)

$$A = 1 + \frac{T}{1-T} \cdot e^{-\frac{\tau}{\tau_T}}$$

Here, f_i is the fraction of species, *i*, of a total, *m*, that have a dwell time of τ_{Di}. N describes the number of fluorescent particles in the detection volume. S is the structural parameter representing the ratio of the radial, ω_1, and vertical, ω_2, axes of the detection volume. A pre-exponential factor, A, was also included to account for the photophysics of the fluorophore where T is the percentage of molecules in the triplet state and τ_T is the lifetime of the triplet state. If the diffusion of a fluorescent species is limited to two-dimensional (2D) diffusion, such as a membrane receptor, $S \rightarrow \infty$ meaning **equation 2.6** simplifies to:

(2.8)

$$G(\tau) = 1 + \frac{A}{N} \cdot \sum_{i=1}^{m} \cdot f_i \cdot \left(1 + \frac{\tau}{\tau_{Di}}\right)^{-1}$$

Autocorrelation analysis applies the G(τ) function to every time point on the fluctuation intensity trace resulting in an autocorrelation curve which is then fit to an appropriate model. The half-decay of the fitted curve provides the average dwell time of the fluorescent species, τ_D, and the y axis intercept, G(0) provides the inverse of the average number of particles within the detection volume, N (**Fig. 2.8A**). From the dwell time of fluorescent species, the diffusion coefficient, D, was determined using the below equation:

(2.9)

$$\mathrm{D} = \frac{{\omega_1}^2}{4 \cdot \tau_\mathrm{D}}$$

In addition, the concentration (nM) of fluorescent species diffusing through a 3D Gaussian detection volume was determined with respect to N and the confocal detection volume, V_C, which was estimated as follows:

(2.10)

$$V_C = \pi^{\frac{3}{2}} \cdot \omega_1 \cdot \omega_2$$

Fluorescent particles limited to a 2D diffusion plane were expressed in particles per unit area, N/μm^2, based on the radius of the detection volume, ω_1.

The fluorescence intensity fluctuation traces were also analysed by photon counting histogram (PCH) analysis which analyses the traces with respect to their amplitude (**Fig. 2.8B**). The trace is divided into time bins and a frequency histogram is generated based on the number of photons per bin. The histogram deviates from a Poissonian distribution when the bin time used is less than the dwell time of the fluorescent species. This super-Poissonian deviation is then modelled to determine the average molecular brightness of the fluorescent species (photons per second per molecule), ε, and also the particle number, N.

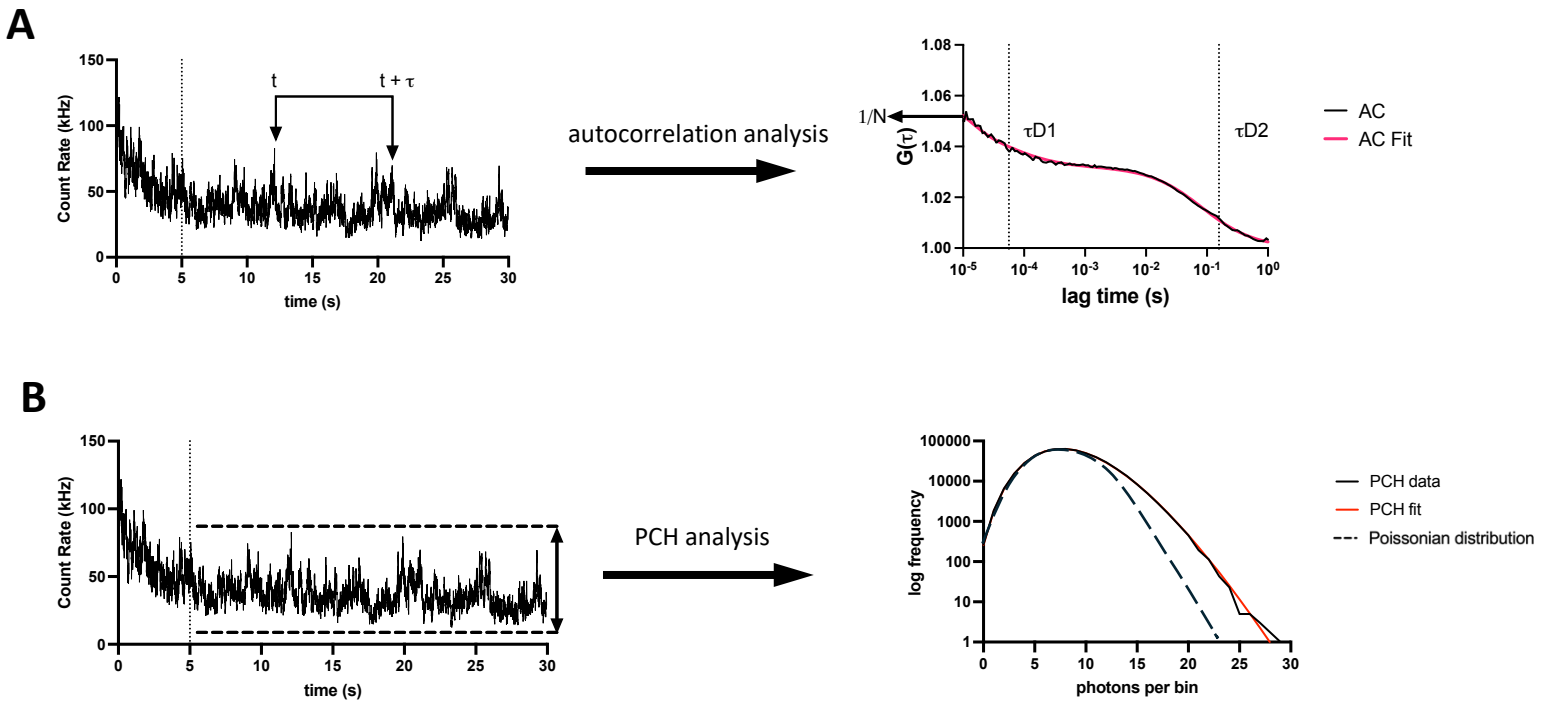

Figure 2.8: Autocorrelation analysis and PCH analysis of an intensity fluctuation trace derived from an FCS measurement.

An example fluctuation intensity trace is shown derived from an FCS measurement of a fluorescent ligand with the confocal detection volume placed on the upper membrane of a cell. (**A**) Autocorrelation analysis calculates the similarity of two time points, t and t + τ, on an intensity fluctuation trace over a range of τ values where τ represents the lag time, to generate an autocorrelation curve (AC) (in black). The AC curve is fitted to a model (in red) to derive the average dwell time of the fluorescent ligand in solution (τD1) and bound to the membrane (τD2). The inverse of the y-intercept provides the particle number (N) of the fluorescent species from which we can determine the particle number per square micron ($N/\mu m^2$) or the concentration (nM) of a fluorescent species bound to the membrane or in solution, respectively. (**B**) PCH analysis is performed on the same intensity fluctuation trace, but the trace is analysed with respect to the amplitude of the fluctuations (shown with arrow). The trace is portioned into time bins and the number of photons per bin counted to generate the frequency histogram shown. The analysed PCH data (in black) is fitted to a model (in red) allowing the molecular brightness (ε) and particle number (N) of the fluorescent species to be determined based on the deviation between the PCH fit and a Poissonian distribution (dotted line).

The confocal volume dimensions and structural parameter were determined each experimental day from the calibration measurements of Cy5-NHS ester or ATTO 488 solutions. Fluctuation intensity traces from these measurements were analysed using autocorrelation analysis (**equation 2.6**) and curves were fitted to a single 3D diffusion component model with a pre-exponential triplet state. The experimentally derived dwell times of the fluorescent species and their known diffusion speeds (Cy5-NHS ester; D= 3.16 x 10^{-10} m^2/s and ATTO488; D= 4.0 x 10^{-10} m^2/s)[188] were used to first determine ω_1. The experimentally derived structural parameter, S = ω_2/ω_1, was then used to determine ω_2.

FCS optimisation measurements of fluorescent spiperone-d2 and clozapine-Cy5 in solution were analysed using **equation 2.6** and the resulting autocorrelation curves were fitted to a model depicting a single, freely diffusing 3D component and a pre-exponential triplet state. The addition of 0.1% BSA into the fluorescent ligand solution required the introduction of a second 3D component representing the slower diffusing BSA-bound ligand.

Autocorrelation analysis of intensity fluctuation traces from FCS measurements of fluorescent spiperone-d2 or clozapine-Cy5 in aqueous solution above cells/glass were also analysed using **equation 2.6**. The resulting autocorrelation curves were fitted to a model depicting a single, freely diffusing 3D component and a pre-exponential triplet state. For FCS measurements where the confocal detection volume was positioned at the upper cell membrane, both freely diffusing ligand in the immediate local environment of the membrane and membrane-bound ligand was present in the detection volume as this volume spans both the lipid bilayer (5 nm) and the intra- and extracellular spaces adjacent to the membrane. Therefore, for all membrane reads the first 5 seconds of the fluctuation intensity trace was discarded prior to modelling as shown in **Figure 2.7** to compensate for bleaching of the fluorophore on slow moving membrane-bound species. For the FCS measurements of fluorescent spiperone-d2 or

clozapine-Cy5 at the cell membrane, a 2D diffusion component (component 2) representing membrane-bound ligand was introduced into the model in addition to a freely diffusing 3D component (component 1) and a pre-exponential triplet state (**equation 2.8**). Here, the dwell time of component 1 was limited to 50 μs – 70 μs based on the dwell time of both spiperone-d2 or clozapine-Cy5 freely diffusing in aqueous solution. To accurately determine the contribution of each component to the particle number, it was necessary to correct for the differing molecular brightness values of both ligands when in an aqueous or membrane-bound environment due to differences in quantum yield. PCH analysis was performed to determine the molecular brightness of both fluorescent ligands in an aqueous solution using a 1x 60 second read at ~ 0.01 kW/cm^2 laser power (633 nm, 0.1%) with the detection volume placed 200 μm above the glass. To determine the molecular brightness of the fluorescent ligands when bound to the membrane, the detection volume was placed on the upper membrane of CHO tetracycline-inducible cells that had been prepared as described in **Chapter 2.7.3**. However, after the 2-hour incubation with fluorescent drug, a 4 x volume wash with D-PBS was performed to remove as much free ligand in solution as possible, followed by a 1x 30 second read at ~ 0.01 kW/cm^2 laser power (633 nm, 0.1%). A 1 component PCH model was used for both ligands in both environments with a 40 μs bin time which is an appropriate time for the differing diffusion speeds of the ligands within both environments. In addition, the first-order correction was fixed at 0.6, based on Cy5 calibration data, to account for photons detected outside of a true Gaussian detection volume[189].

Autocorrelation curves of SNAP-Surface® Alexa Fluor® 488-labelled SNAP-D2R in the absence of fluorescent ligand were fitted to a model containing: a 3D component, limited to 20 μs – 80 μs dwell time representing free SNAP-label; a 2D component, representing the labelled receptor; and a pre-exponential triplet state. The fluctuation traces of SNAP-labelled SNAP-D2R were also analysed using PCH analysis to determine whether the measured population consisted of fluorescent species of a single brightness

(1 component) or multiple brightnesses (2 components)[190]. Here, a bin time of 100 μs and a first order correction of 0.6 was used.

CHAPTER 3: CHARACTERISATION OF FLUORESCENT LIGANDS IN SOLUTION AND SNAP-D2R ON THE MEMBRANE OF CHO TETRACYCLINE-INDUCIBLE SNAP-D2R CELLS USING FLUORESCENCE CORRELATION SPECTROSCOPY

3.1 INTRODUCTION

Fluorescence correlation spectroscopy (FCS) is an advanced spectroscopy technique that allows for the quantification of the molecular dynamics of a fluorescently labelled species within a small detection volume (~ 0.2 fL, ~ 1 x 0.2 μm)[191]. This defined detection volume is created by focusing a laser through a high numerical aperture objective to a diffraction limited spot with emission collected through a confocal pinhole[192]. As fluorescent species diffuse through this detection volume, fluorescence intensity fluctuations are generated. The self-similarity of the resulting fluorescence intensity fluctuation trace over time can then be analysed using autocorrelation analysis (detailed in **Chapter 2.8.5**) to provide information on the average number of fluorescent particles and their average dwell time within the detection volume, from which their concentration and diffusion coefficient can be calculated[193]. In addition, these fluctuations can be analysed with respect to their amplitude using PCH analysis (detailed in **Chapter 2.8.5**) where the fluctuation trace is divided into time bins and the number of photons per bin is counted generating a frequency histogram. The deviation of this histogram from a Poissonian distribution reveals the molecular brightness of a species which can be used to determine its stoichiometry[191]. Although FCS has single molecule sensitivity, it should be noted that it is not a single particle tracking technique as parameters are derived from ensemble averages[192].

FCS can be applied to a variety of biological systems including simple solutions of fluorescent molecules[194], cellular membranes[193,195] and even whole organisms[196]. FCS is a particularly powerful tool for investigating the properties of membrane proteins, including members of the GPCR family[197]. Information on the diffusion, density and oligomeric state of GPCRs within small areas of the membrane (~ 0.2 um^2) can be determined which in turn advances our understanding of GPCR regulation[198]. Furthermore, the spatial regulation of GPCRs has been shown to be important for functional signalling outcomes through compartmentalised signalling[199,200]. FCS is well suited to investigate GPCR dynamics within subcellular compartments due to its high

spatial and temporal resolution[191]. Another advantage of FCS is its high sensitivity at low concentrations, meaning GPCRs endogenously expressed at low levels in native cells can be investigated where traditional confocal imaging shows poor signal[189]. The lower limit of concentrations detectable using FCS whilst maintaining a reasonable signal-to-noise ratio, has been reported to be as low as 0.1 nM in cell-based measurements[191,192] and 1 pM in solution-based measurements[201]. On the other hand, high concentrations of fluorescent species may result in small fluctuations of intensity causing poor fitting of autocorrelation curves. Studies disagree on the upper limit of detectable concentrations using FCS with suggestions between 100 nM – 400 nM[191,192,202].

FCS has been used extensively to investigate the interactions of GPCRs with ligands through the identification of GPCR-ligand complexes[191]. Interestingly, several GPCRs including the β2-adrenoceptor[203], adenosine A1 and A3 receptors[204,205] and the histamine H1 receptor[206], have been shown to form different populations of GPCR-ligand complexes that show differing diffusion coefficients in the membrane. These differing GPCR-ligand populations show differences in their sensitivity to pertussis toxin[207] and ligand binding kinetics[1208] which suggests they may have distinct functional responses. It is therefore important to investigate ligand-induced changes in GPCR membrane dynamics to fully characterise the effect of ligand treatment on GPCR function. More recently, the effect of cell-surface β2-adrenoceptor expression on the distribution of a fluorescent derivative of propranolol in solution was investigated using FCS[209]. An uneven distribution of fluorescent ligand was seen in solution above cells expressing β2-adrenoceptor whereby there was a high local concentration immediately adjacent to the membrane in comparison to the bulk aqueous phase[209]. This suggests that in-solution measurements of ligands that target GPCRs are crucial to determine actual concentrations of ligand in the local environment of the receptor that may in turn affect estimations of drug affinity.

To investigate the distribution of fluorescent ligands above the dopamine D2 receptor (D2R) and how this is influenced by varying levels of D2R expression on cells

(**Chapter 4**), the FCS settings used to perform in-solution measurements of these fluorescent ligands (spiperone-d2 and clozapine-Cy5) were first optimised. In addition, we aimed to use FCS to quantify the variable SNAP-D2R (long isoform) expression that is attainable using the CHO tetracycline-inducible SNAP-D2R (long isoform) cell line used in **Chapter 4**.

3.2 CHAPTER 3 AIMS

The work described in Chapter 3 aimed to:

a) Optimise FCS settings to detect fluorescent ligands, spiperone-d2 and clozapine-Cy5, in solution;
b) Characterise the CHO tetracycline-inducible SNAP-D2R cell line for later use in FCS experiments.

3.3 RESULTS

3.3.1 OPTIMISATION OF FCS SETTINGS TO DETECT FLUORESCENT APDS IN SOLUTION

FCS was used to detect fluorescent APDs, spiperone-d2 and clozapine-Cy5, in solution (structures shown in **Fig. 3.1**). There are clear differences in the structure of these fluorescent APDs due to structural differences between spiperone and clozapine as well as differences in linker length and potentially the fluorophores. While the structure of the d2 fluorophore of spiperone-d2 remains undisclosed as it is a commercial compound, there is evidence that it may resemble a Cy5-like structure based on the molecular formula of the d1-amine dye derived from the synthesis of PPHT-d1 by Albizu et al.[210]. In addition, the optical profiles of spiperone-d2 and clozapine-Cy5 (sulfo-Cy5) showed similarities in their excitation and emission spectra and photophysical properties, particularly in the cis-trans isomerization effect observed in autocorrelation curves with lag times < 10 μs. The detection volume was placed in solution 200 μm above the glass before fluorescence fluctuations were recorded as described in **Chapter 2.7.3**. The fluorescence intensity fluctuation traces for both fluorescent ligands (**Fig. 3.2A**) were analysed using autocorrelation analysis resulting in monophasic curves which fit well to a single 3D component model with a pre-exponential triplet state to account for the photophysics of the fluorophore (described in **Chapter 2.7.3**) (**Fig. 3.2B**). The half decay of the autocorrelation curve fits for both spiperone-d2 and clozapine-Cy5, showed a single fluorescent component with a dwell time of ~ 60 μs, which was consistent across a range of added fluorescent ligand concentrations.

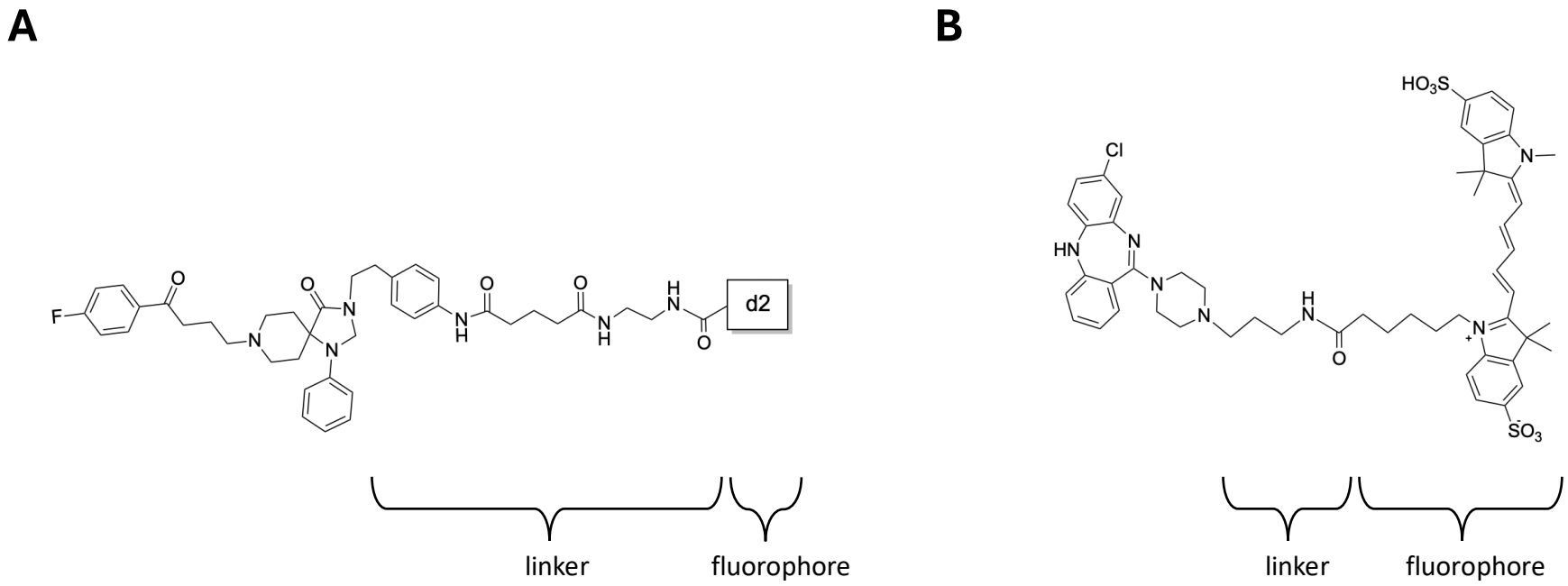

Figure 3.1: Structures of fluorescent APDs spiperone-d2 and clozapine-Cy5.

The estimated structure of spiperone-d2 (**A**) and the known structure of clozapine-Cy5 (**B**) are shown, with the linker and fluorophore regions labelled. Spiperone-d2 was purchased from Revvity whereas clozapine-Cy5 was synthesised in-house.

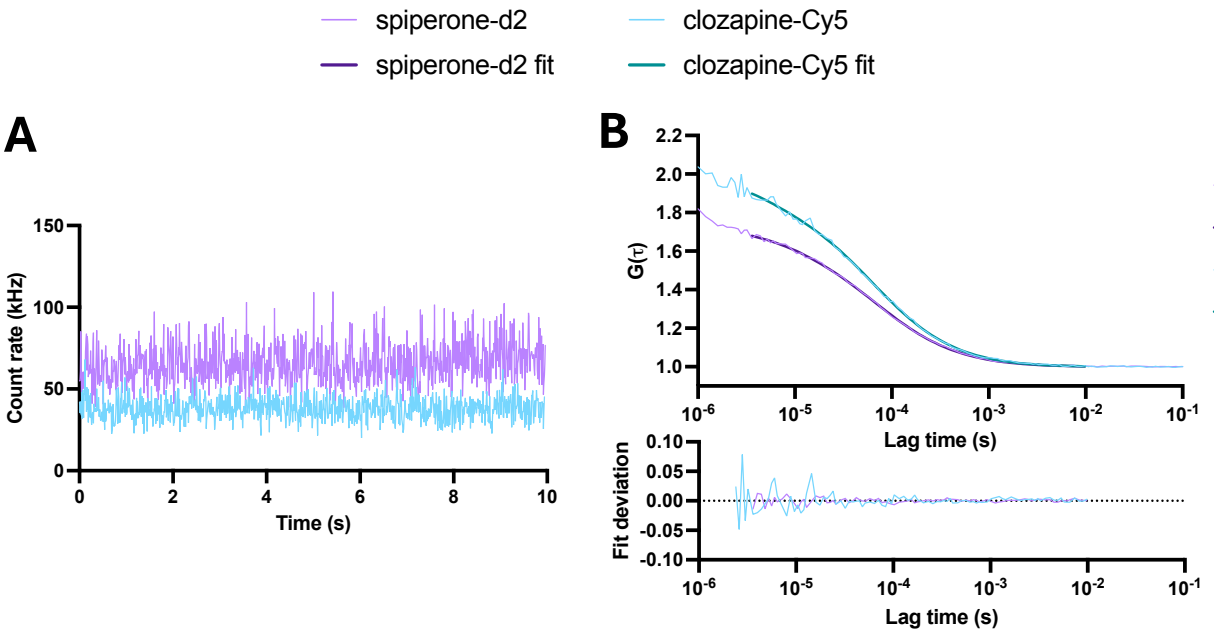

Figure 3.2: Representative fluorescence intensity fluctuation traces and autocorrelation curves from FCS measurements of fluorescent ligands in solution.

FCS measurements were taken of the fluorescent ligands, spiperone-d2 and clozapine-Cy5, in solution. Representative raw fluorescence intensity fluctuation traces (**A**) are shown. Autocorrelation analysis of these traces produced autocorrelation curves which were fitted to a single freely diffusing 3D component model (**B**). The deviation of the fit from the curve is also shown. An added concentration of 40 nM of each fluorescent ligand and a 633nm laser power of 15% was used.

To determine the optimal FCS settings for the detection of fluorescent ligands in solution, several parameters were investigated including the dynamic range for detection of ligand concentration and laser power. Interestingly, for both spiperone-d2 (**Fig 3.3A**) and clozapine-Cy5 (**Fig 3.3B**), the measured concentration of ligand was markedly lower than the nominally added concentration (up to ~ 11-fold) across all laser powers. Despite this, the added ligand concentration was significantly correlated with the measured concentration at each laser power for spiperone-d2 and at 15% laser power for clozapine-Cy5 (details of statistical test in **Table 3.1**).

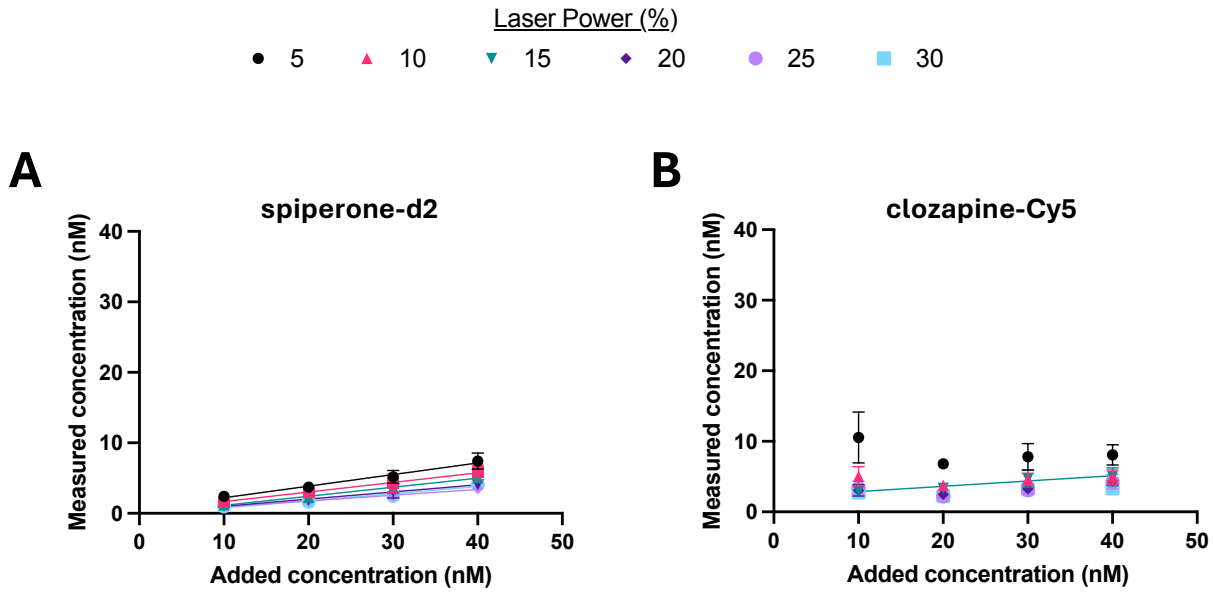

Figure 3.3: The correlation between the added concentration of fluorescent ligand and the measured concentration in solution using differing laser powers.

FCS was used to measure the concentration of spiperone-d2 (**A**) and clozapine-Cy5 (**B**) in solution over a range of added concentrations (10, 20, 30 and 40 nM). Autocorrelation curves were fitted to a single freely diffusing 3D component model. Data represent mean ± SEM of 4 independent experiments. Correlation between the added and measured concentration were assessed at each laser power using a two-tailed Pearson's correlation for both fluorescent ligands (details of statistical tests in **Table 3.1**). Where a correlation of statistical significance was observed ($P < 0.05$, two-tailed Pearson's correlation), a trend line was included but a linear relationship between the data is not assumed from the correlation analysis.

Table 3.1: Statistical results of the correlation between the added concentration of fluorescent ligand and the measured concentration in solution using differing laser powers.

FCS was used to measure the concentration of the fluorescent ligands, spiperone-d2 and clozapine-Cy5, in solution over a range of added concentrations using different laser powers as shown in **Figure 3.3**. Correlation between the added and measured concentration were assessed at each laser power using a two-tailed Pearson's correlation to allow the calculation of the correlation coefficient, r^2, for both fluorescent ligands; *P < 0.05, **P < 0.01, ***P < 0.001.

Laser power (%)	spiperone-d2		clozapine-Cy5	
	r^2	P	r^2	P
5	0.98	0.0083**	0.27	0.48
10	1.00	0.0009***	0.02	0.87
15	1.00	0.0017**	0.93	0.04*
20	0.99	0.0032**	0.58	0.24
25	0.99	0.0072**	0.26	0.49
30	0.96	0.023*	0.48	0.30

Next, the diffusion coefficients and counts per molecule (cpm) of the fluorescent ligands were investigated over a range of laser powers to find an optimal laser power that gave a strong signal (high enough cpm) without causing substantial bleaching demonstrated by an increased diffusion coefficient. The diffusion coefficients of spiperone-d2 and clozapine-Cy5 remained consistent across the range of laser powers tested (**Fig. 3.4A**). Indeed, only significant differences in the diffusion coefficient between laser powers were seen for spiperone-d2 between 5 % and 10 % laser power ($P < 0.05$, two-way ANOVA) and between 5 % and 15 % laser power ($P < 0.05$, two-way ANOVA). In addition, the diffusion coefficients appear similar between ligands (**Fig. 3.4A**). There were no significant differences in the diffusion coefficients between the fluorescent ligands at each laser power between each added concentration ($P > 0.05$, two-way ANOVA). As expected, the cpm increased with an increasing laser power for both fluorescent ligands irrespective of the added concentration (**Fig. 3.4B**). In addition, the cpm was mainly > 10 kHz for both fluorescent ligands at each added concentration across all laser powers which is considered an acceptable signal-to-noise level[211].

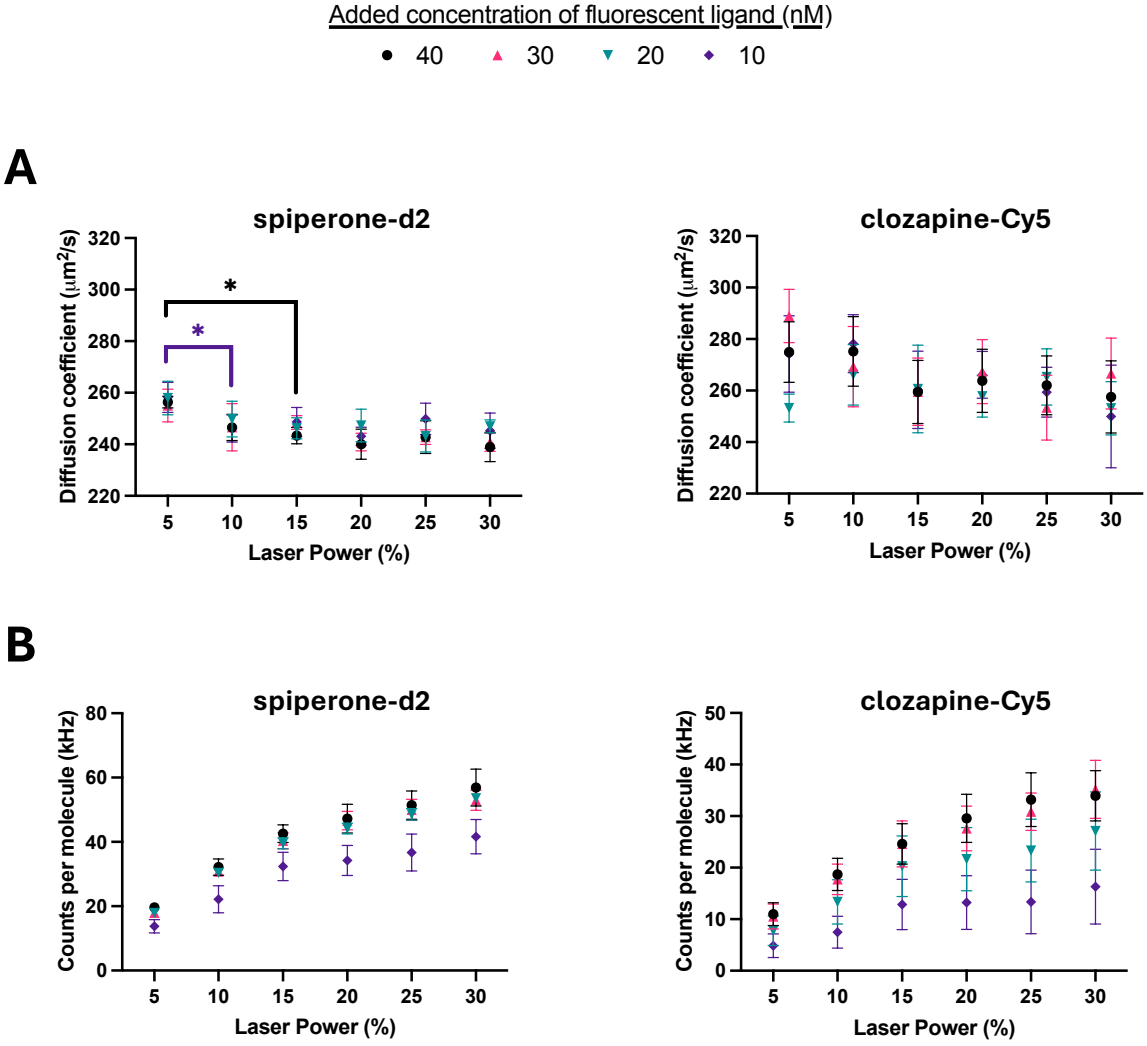

Figure 3.4: The diffusion coefficients and counts per molecule of fluorescent ligand in solution measured using differing laser powers over a range of added concentrations.

FCS was used to measure the diffusion coefficients (**A**) and counts per molecule (**B**) of spiperone-d2 and clozapine-Cy5 in solution over a range of added concentrations (10, 20, 30 and 40 nM). Autocorrelation curves were fitted to a single freely diffusing 3D component model. Data represent mean ± SEM of 4 independent experiments. A two-way ANOVA with Tukey's multiple comparison test was used to determine significant differences between the diffusion coefficients at each laser power for each added concentration of fluorescent ligand; * $P < 0.05$. Here, significance is shown in the colour corresponding to a particular added concentration of fluorescent ligand.

We hypothesised that the seemingly low concentration of fluorescent ligand in solution may be due to the binding of the ligand to sites on the chambered coverglass. To test this hypothesis, 0.1% bovine serum albumin (BSA) was added to the fluorescent ligand solutions of both spiperone-d2 and clozapine-Cy5. FCS measurements were then taken and the fluorescence intensity fluctuation traces for both fluorescent ligands (**Fig. 3.5A**) were analysed using autocorrelation analysis. The resulting autocorrelation curves were fitted with a two-component 3D model as described in **Chapter 2.8.5** (**Fig. 3.5B**). The first component of both fluorescent ligands showed a dwell time of ~ 60 μs, consistent with the dwell time of freely diffusing fluorescent ligand. For both fluorescent ligands, the second component showed a slower dwell time of ~ 400 μs, likely representing fluorescent ligand bound to BSA (60 kDa). This second component represented ~ 10% of the ligand population with the relative concentrations of component 1 and component 2 shown in **Figure 3.6**. Interestingly, the addition of BSA increased the measured concentration of fluorescent ligand unbound to BSA (component 1) in solution whereby the measured concentration was up to only ~ 1.5-fold lower than the added concentration for both ligands (**Fig 3.6A**&**B**). This suggests that a large proportion of both fluorescent ligands bind to non-specific sites on the chambered coverglass which are then displaced by BSA binding to these sites. As expected, for both component 1 and component 2 of both fluorescent ligands, there was a strong correlation between the added and measured concentration at each laser power (with the exception of component 2 of clozapine-Cy5 at a laser power of 20 %) (**Fig 3.6**) (details of statistical test in **Table 3.2**).

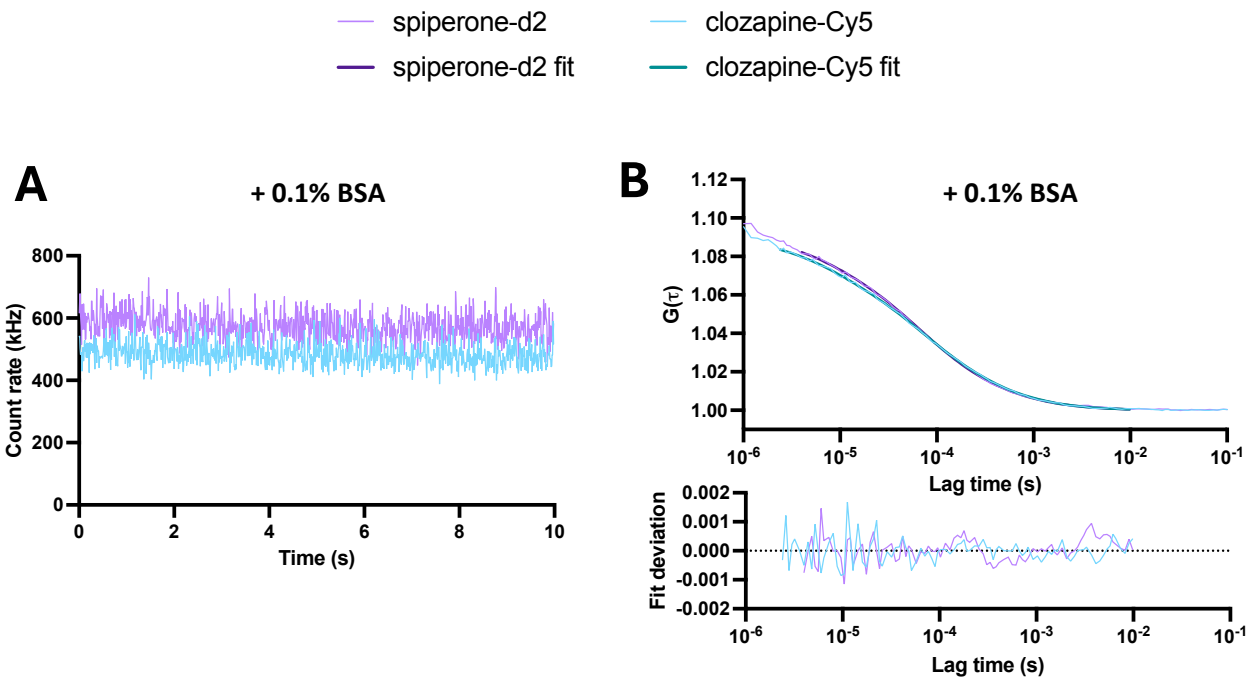

Figure 3.5: Representative fluorescence intensity fluctuation traces and autocorrelation curves from FCS measurements of fluorescent ligands in solution with 0.1% bovine serum albumin (BSA).

FCS measurements were taken of the fluorescent ligands, spiperone-d2 and clozapine-Cy5, in solution with 0.1% BSA. Representative raw fluorescence intensity fluctuation traces (**A**) are shown. Autocorrelation analysis of these traces produced autocorrelation curves which were fitted to a 2 x 3D component model (**B**). The deviation of the fit from the curve is also shown. An added concentration of 40 nM of each fluorescent ligand and a 633nm laser power of 15% was used.

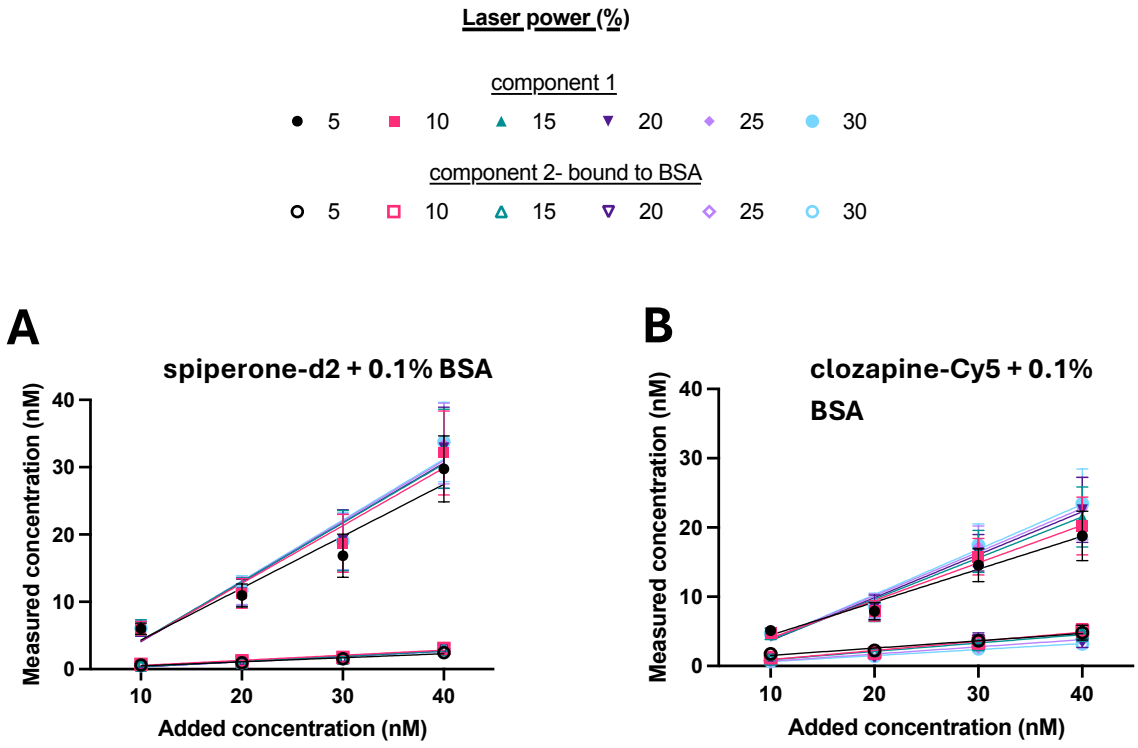

Figure 3.6: The correlation between the added concentration of fluorescent ligand with 0.1% bovine serum albumin (BSA) and the measured concentration in solution using differing laser powers.

FCS was used to measure the concentration of spiperone-d2 (**A**) and clozapine-Cy5 (**B**) in solution with 0.1% BSA. Autocorrelation curves were fitted to a 2 x 3D component model. Two distinct components were identified for both ligands based on their differing dwell times. For both fluorescent ligands, component 1 showed an average dwell time of ~ 60 µs whereas component 2, showed an average dwell time of ~ 400 µs, likely representing BSA-bound fluorescent ligand. The measured concentrations of the two components are shown for each ligand at various added concentrations using a range of laser powers. Data represent mean ± SEM of 4 independent experiments. Correlation between the added and measured concentration were assessed at each laser power using a two-tailed Pearson's correlation (statistical analysis results in **Table 3.2**). Where a correlation of statistical significance was observed ($P < 0.05$, two-tailed Pearson's correlation), a trend line was included but a linear relationship between the data is not assumed from the correlation analysis.

Table 3.2: Statistical results of the correlation between the added concentration of fluorescent ligand with 0.1% bovine serum albumin (BSA) and the measured concentration in solution using differing laser powers.

FCS was used to measure the concentration of the fluorescent ligands, spiperone-d2 and clozapine-Cy5, in solution with 0.1% BSA over a range of added concentrations using different laser powers as shown in **Figure 3.6**. Correlation between the added and measured concentration were assessed at each laser power using a two-tailed Pearson's correlation to allow the calculation of the correlation coefficient, r^2, for both fluorescent ligands; *P < 0.05, **P < 0.01.

Laser power (%)	spiperone-d2				clozapine-Cy5			
	component 1		component 2		component 1		component 2	
	r^2	P	r^2	P	r^2	P	r^2	P
5	0.94	0.028*	0.96	0.022*	0.98	0.011*	0.97	0.016*
10	0.95	0.023*	0.94	0.032*	0.98	0.012*	0.96	0.018*
15	0.95	0.023*	0.93	0.034*	0.97	0.014*	0.99	0.0067**
20	0.96	0.022*	0.91	0.045*	0.99	0.0075**	0.89	0.057
25	0.95	0.026*	0.91	0.046*	0.98	0.0083**	0.99	0.0034**
30	0.95	0.026*	0.95	0.025*	0.98	0.0089**	0.99	0.0030**

To determine the limits of what concentrations can be accurately measured with FCS, we used solutions of fluorescent Cy5 NHS ester. The added concentrations of 0.2 nM and 600 nM of Cy5 NHS ester were chosen based on previously reported limits of detection using FCS [191,192,202]. In addition, 0.2 nM and 600 nM of fluorescent antipsychotic drugs were required to be used in FCS experiments in **Chapter 4** to achieve the same levels of D2R occupancy due to their differing affinities at D2R. It was therefore necessary to see if these concentrations were first within the limits of detection using FCS. Fluorescence fluctuations of Cy5 NHS ester at both 0.2 nM and 600 nM were generated from FCS measurements at 15% laser power (**Fig. 3.7A**). Autocorrelation analysis of these fluctuations results in monophasic curves that were fitted with a single freely diffusing 3D component with a pre-exponential triplet state to account for the photophysics of Cy5 (**Fig. 3.7B**&**C**). The particle number within the FCS detection volume varied significantly between the two added concentrations of Cy5 NHS ester. The particle number was 0.12 and 182.41 for 0.2 nM and 600 nM of Cy5 NHS ester, respectively. This variation is demonstrated by the amplitude of the autocorrelation curves which is inversely proportional to the particle number (**Fig. 3.7B**&**C**). In addition, FCS measurements of both concentrations of Cy5 NHS ester showed a detectable signal demonstrated by a cpm of 20.72 and 17.26 for Cy5 NHS ester concentrations of 0.2 nM and 600 nM, respectively.

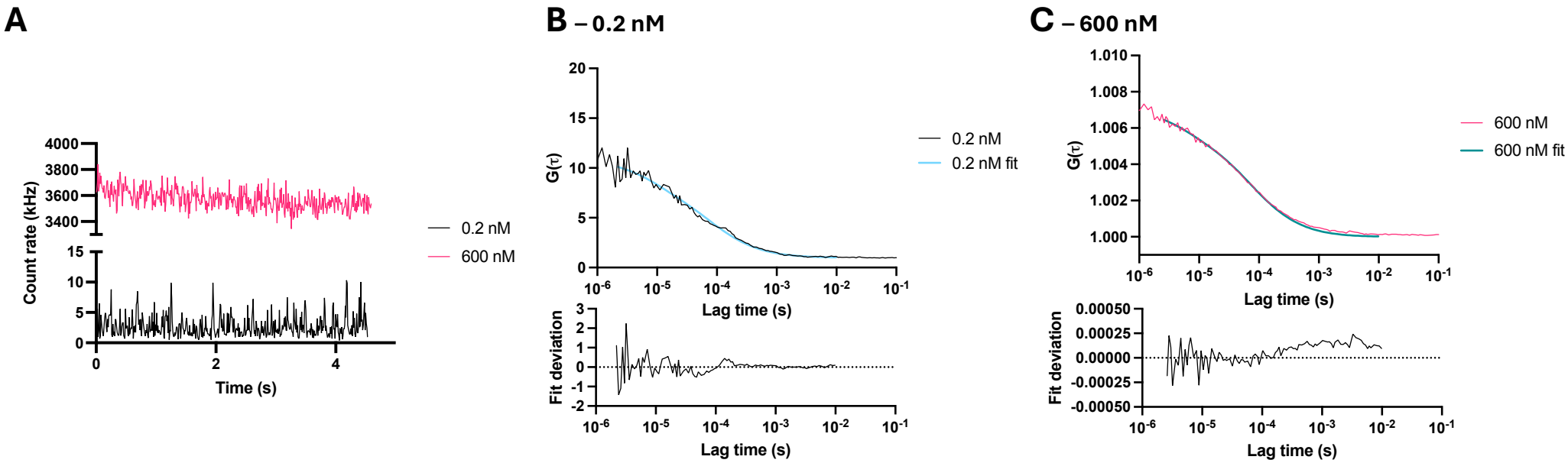

Figure 3.7: Representative fluorescence intensity fluctuation traces and autocorrelation curves from FCS measurements of Cy5 NHS ester in solution.

FCS measurements were taken of Cy5 NHS ester in solution at two different added concentrations, 0.2 nM and 600 nM. Representative raw fluorescence intensity fluctuation traces (**A**) are shown. Autocorrelation analysis of these traces produced autocorrelation curves which were fitted to a single freely diffusing 3D component model for 0.2 nM added concentration (**B**) and 600 nM added concentration (**C**). The deviation of the fit from the curve is also shown.

The measured concentrations of Cy5 NHS ester in solution were similar to their added concentrations at both 0.2 nM and 600 nM despite the 3,000-fold difference in these added concentrations (**Fig. 3.8**). In fact, the measured concentrations of Cy5 NHS ester were not significantly different to either added concentration ($P > 0.05$, Student's t-test). This therefore, indicates that a dynamic range of 0.2 – 600 nM was attainable with a fluorophore with this level of cpm.

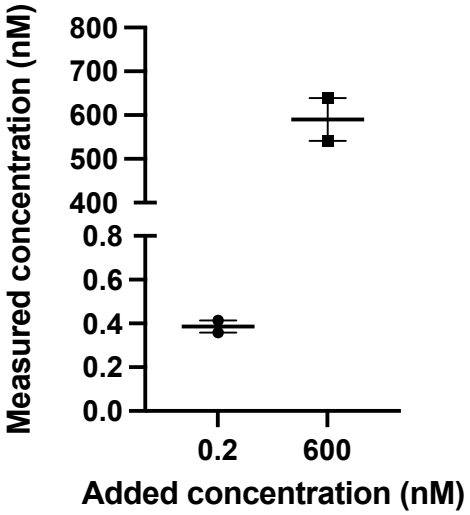

Figure 3.8: The measured concentration of Cy5 NHS ester in solution using fluorescence correlation spectroscopy.

Added concentrations of 0.2 nM or 600 nM of Cy5 NHS ester were measured in solution using fluorescence correlation spectroscopy. Autocorrelation analysis of fluorescent intensity traces produced autocorrelation curves which were fitted to a single freely diffusing 3D component model Data represent mean ± range of 2 measurements performed on the same experimental day.

3.3.2 CHARACTERISATION OF SNAP-D2R EXPRESSION IN CHO TETRACYCLINE-INDUCIBLE SNAP-D2R CELLS

The use of a CHO tetracycline-inducible SNAP-D2R (long isoform) cell line allowed the tetracycline-controlled transcription of SNAP-D2R, whereby SNAP-D2R expression was theoretically only induced following the addition of tetracycline. We first investigated the relationship between the concentration of tetracycline added to cells and the resulting levels of SNAP-D2R expression on the cell membrane using confocal microscopy. In general, cells labelled with membrane impermeable SNAP-Surface® Alexa Fluor 488® showed a SNAP-D2R signal predominantly restricted to the membrane with some small intracellular vesicles (**Fig. 3.9A**). Cells treated with 10 ng/ml tetracycline showed varying expression levels of SNAP-labelled SNAP-D2R at the membrane among cells within the same well (**Fig. 3.9A**). Interestingly, SNAP-D2R expression at the membrane appeared to be punctate, potentially indicating the formation of receptor clusters[212]. The mean fluorescence intensity at the membrane was determined by drawing a region of interest around the membrane of cells on a transmitted light image (described in detail in **Chapter 2.8.4**). The equivalent average pixel intensity in the fluorescence channel within this area provided a readout of the estimated relative expression of SNAP-D2R on the cell membrane. Using a range of tetracycline concentrations (10 ng/ml – 100 ng/ml), we showed CHO tetracycline-inducible SNAP-D2R cells displayed an extensive range of SNAP-D2R expression levels on the cell membrane (**Fig. 3.9B**). Based on the distribution of membrane fluorescence intensities across cells, cells were categorized as 'high-' (> 250 units of mean fluorescence intensity), 'low-' (50 < 250 units of mean fluorescence intensity) or 'non-expressing' (< 50 units of mean fluorescence intensity) SNAP-D2R cells (**Fig. 3.9B**).

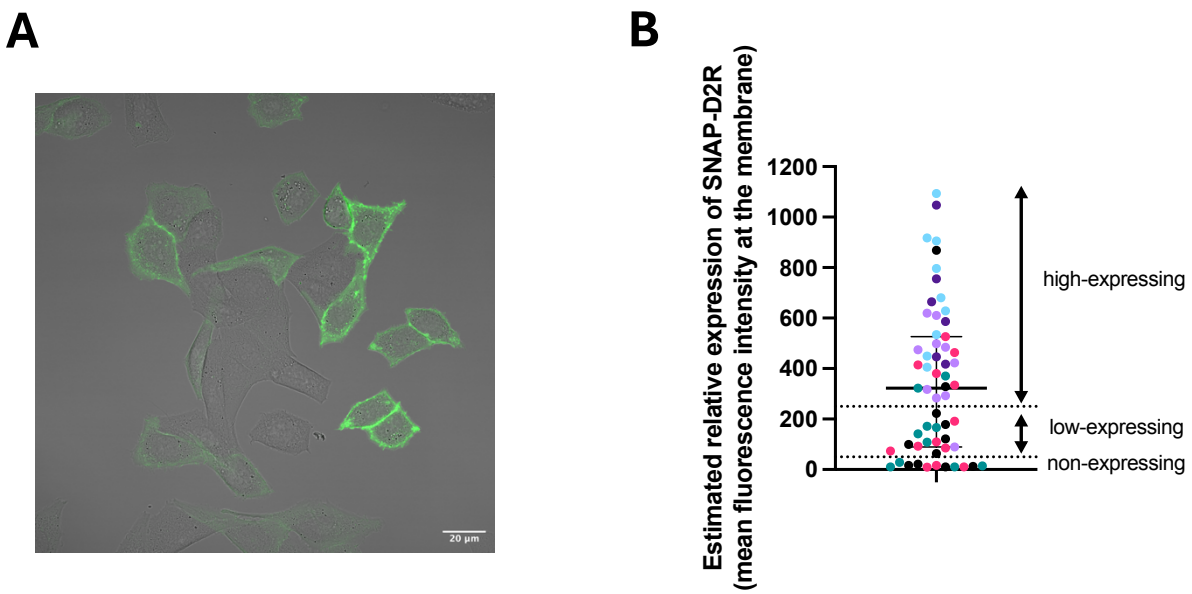

Figure 3.9: The variation of cell-surface SNAP-D2R expression among CHO tetracycline-inducible SNAP-D2R cells.

(**A**) Confocal image (overlayed transmitted light and 488 nm fluorescence channels) of CHO tetracycline-inducible SNAP-D2R (long isoform) cells treated with 10 ng/ml tetracycline for 24 hours before SNAP-labelling with SNAP-Surface® Alexa Fluor® 488. Cells in the same well displayed a range of SNAP-D2R expression on the membrane (shown in green). (**B**) The mean 488 nm intensity at the membrane of several cells as a readout of estimated SNAP-D2R expression. Each data point represents an individual cell with points of the same colour representing cell measurements collected on the same day over 7 independent experiments. The cells were characterized as high-‘ (> 250 units of mean fluorescence intensity), ‘low-‘ (50 < 250 units of mean fluorescence intensity) or ‘non-expressing’ (< 50 units of mean fluorescence intensity) SNAP-D2R cells based on their distribution as indicated.

To gain a more quantitative measure of SNAP-D2R expression in this inducible cell line, FCS reads were taken on the membrane of SNAP-labelled cells with a range of SNAP-D2R expression as described in **Chapter 2.7.3** and **Figure. 2.5**. Fluorescence intensity fluctuation traces were generated (**Fig. 3.10A**) which were analysed using autocorrelation analysis to produce autocorrelation curves (**Fig. 3.10B**). These curves were fitted with a 3D and 2D component model with a pre-exponential triplet state as described in **Chapter 2.8.5**. The 3D component comprised ~ 15 % of the total fluorescent population and showed dwell times consistent with free SNAP-Surface® Alexa Fluor® 488 label (dwell time τ_{D1}; 20 – 80 μs)[213]. The 2D component comprised ~ 85% of the population and was slower-diffusing (dwell time τ_{D2}; ~ 100 ms), representing the SNAP-labelled SNAP-D2R on the cell membrane. In addition, the fluorescence intensity fluctuation traces were analysed with respect to their amplitude using PCH analysis. The resulting PCH histograms were then fitted predominantly to a 1 component model (**Fig. 3.10B**), indicating a species of a single brightness.

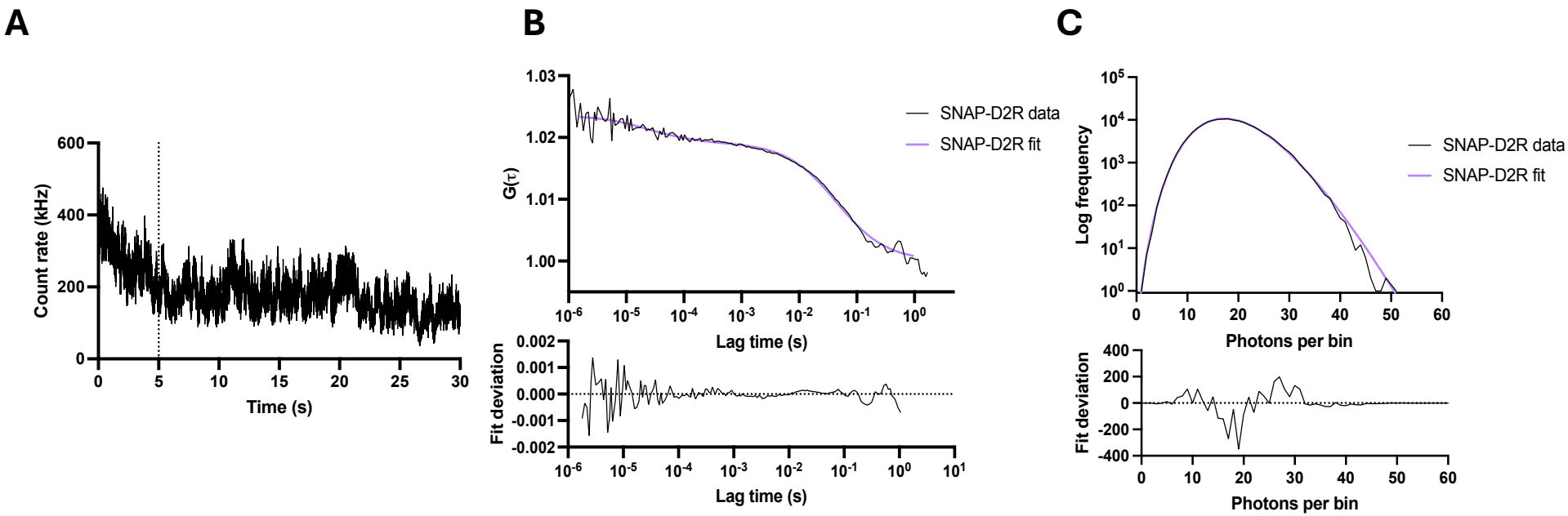

Figure 3.10: Representative fluorescence intensity fluctuation traces, autocorrelation curves and PCH histograms from FCS measurements of SNAP-labelled SNAP-D2R in CHO tetracycline-inducible SNAP-D2R cells.

CHO tetracycline-inducible SNAP-D2R (long isoform) cells were induced with 10 ng/ml – 100 ng/ml tetracycline for 24 hours prior to SNAP-labelling with SNAP-Surface® Alexa Fluor® 488. FCS measurements were then taken on the membrane of cells. Representative raw fluorescence intensity fluctuation traces are shown (**A**). Autocorrelation analysis of these traces produced autocorrelation curves which were fitted to a 3D and 2D component model (**B**). PCH analysis was also performed with a representative PCH histogram shown in (**C**) with a 1 component fit. The deviations of the fits from autocorrelation curves and PCH histograms is also shown.

FCS reads were taken on the membrane of cells following the measurement of their fluorescence intensity at the membrane as a readout of estimated SNAP-D2R expression as described above and in detail in **Chapter 2.8.4**. Autocorrelation analysis of fluctuation intensity traces derived from FCS measurements allowed the number of fluorescent particles per area of membrane to be determined. There was a strong correlation between the particle number per square micron of membrane and the mean fluorescence intensity at the membrane of the same SNAP-labelled CHO tetracycline-inducible SNAP-D2R cell (two-tailed Spearman's rank correlation; $r_s = 0.774$, $P < 0.0001$; **Fig. 3.11A**). This suggests that an increase in fluorescence intensity on the membrane is related to an increase in SNAP-D2R expression. In contrast, the diffusion coefficient of SNAP-D2R (derived from the dwell time) was not correlated with the mean fluorescence intensity at the membrane (two-tailed Pearson's correlation; $r^2 = 0.024$, $P = 0.353$; **Fig. 3.11B**), suggesting an increase in receptor density does not affect the two-dimensional diffusion of SNAP-D2R within the membrane. The diffusion coefficient of SNAP-D2R (0.115 ± 0.047 $\mu m^2/s$, n= 38 cells from 4 independent experiments) (**Fig. 3.12A**) was consistent with the diffusion coefficients of other SNAP-labelled GPCRs [187,189,213]. In addition, PCH analysis was performed to provide information on the oligomerization state of cell-surface SNAP-D2R through the determination of the average molecular brightness of SNAP-labelled SNAP-D2R (**Fig. 3.12B**). Of the fluctuation intensity traces for 38 cells measured over 4 independent experiments, 36 (94.7 %) fitted to a one component PCH model which suggests that the majority of the population exists as a species of a single brightness of 27,600 ± 1620 cpm/s. However, the traces of 2 cells (5.3 %) required the introduction of a second component into the PCH model due to a poor fit with a one component model at higher photons per bin values. Here, the second component was 169,000 ± 18,700 cpm/s which was ~ 6 times brighter than the first component (**Fig. 3.12B**). This suggests that on the minority of cells, SNAP-D2R may exist in oligomeric states or clusters[189,191].

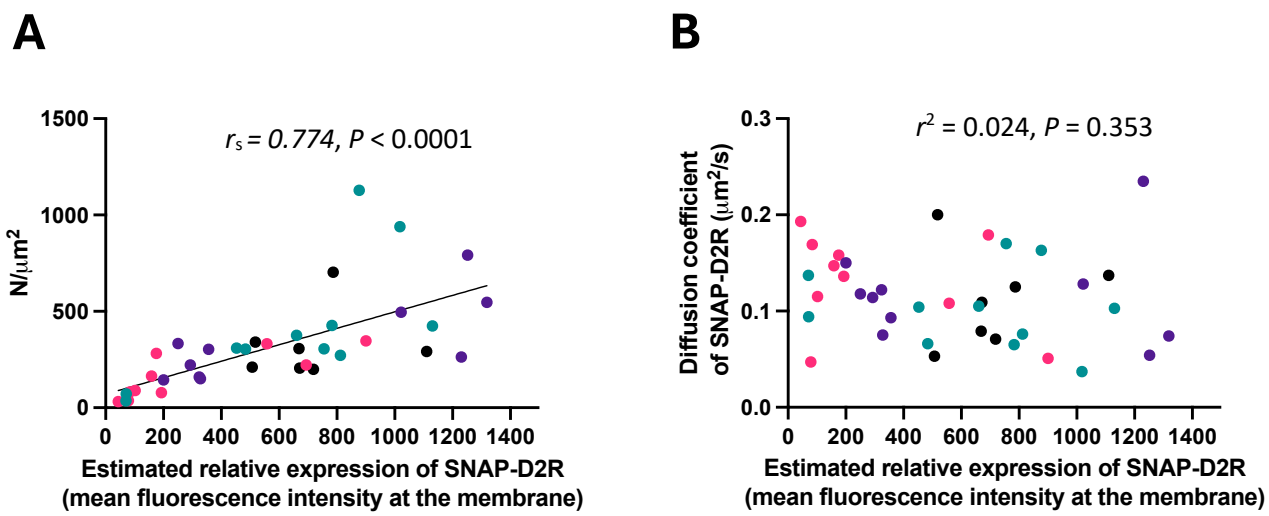

Figure 3.11: The correlation between cell-surface SNAP-D2R expression and the particle number or diffusion coefficient of SNAP-D2R in CHO tetracycline-inducible SNAP-D2R cells.

Variable SNAP-D2R expression was achieved through 24-hour induction of the CHO tetracycline-inducible SNAP-D2R (long isoform) cell line using 10 ng/ml – 100 ng/ml tetracycline. Cells were then labelled with SNAP-Surface® Alexa Fluor® 488 and the mean 488 nm intensity at the cell surface was recorded as an estimate of SNAP-D2R expression. Using fluorescence correlation spectroscopy (FCS), the average particle number per square micron (N/μm^2) at the membrane was determined and correlated with the estimated relative expression of SNAP-D2R (two-tailed Spearman's rank correlation; r_s = 0.774, P < 0.0001) (**A**). FCS was also used to determine the diffusion coefficient of SNAP-D2R which was correlated with the estimated relative expression of SNAP-D2R (two-tailed Pearson's correlation; r^2 = 0.024, P= 0.353) (**B**). Autocorrelation curves were fitted to a 3D and 2D component model. Where a correlation of statistical significance was observed (P < 0.05, two-tailed Pearson's correlation), a trend line was included but a linear relationship between the data is not assumed from the correlation analysis. Each data point represents an individual cell with points of the same colour representing cell measurements collected on the same day over 4 independent experiments.

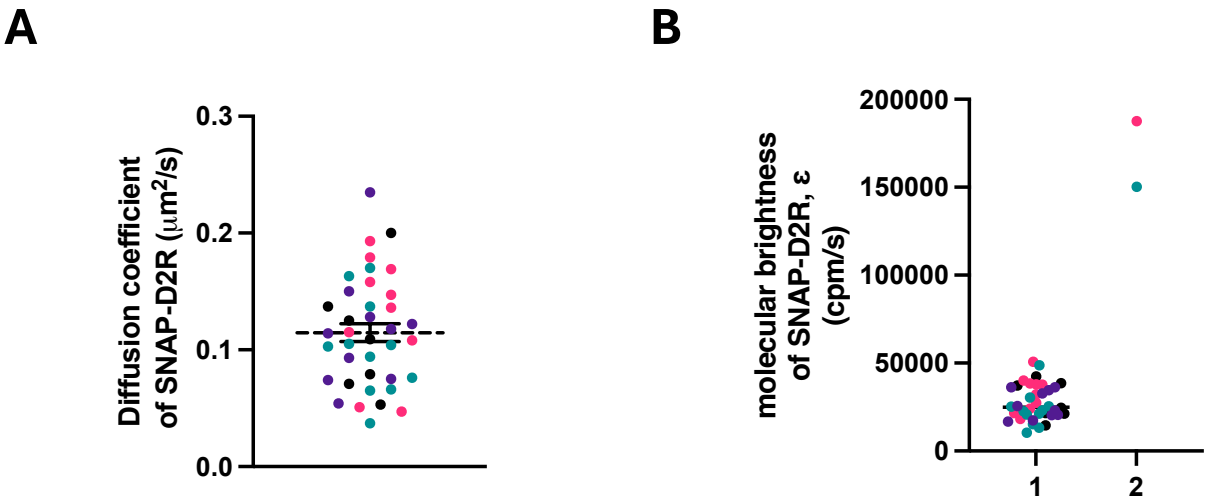

Figure 3.12: The diffusion coefficient and molecular brightness of SNAP-D2R in CHO tetracycline-inducible SNAP-D2R cells derived using fluorescence correlation spectroscopy.

SNAP-D2R expression was achieved through 24-hour induction of the CHO tetracycline-inducible SNAP-D2R (long isoform) cell line using 10 ng/ml – 100 ng/ml tetracycline. Cells were then labelled with SNAP-Surface® Alexa Fluor® 488 before fluorescence correlation spectroscopy (FCS) measurements were taken on the upper membrane. Resulting intensity fluctuation traces were then analysed by autocorrelation analysis to determine the diffusion coefficient of SNAP-D2R (**A**) and by PCH analysis to determine the average molecular brightness (ε) of SNAP-D2R (**B**). Each data point represents an individual cell with points of the same colour representing cell measurements collected on the same day over 4 independent experiments (n= 38 cells). Diffusion coefficient data (**A**) is plotted as mean (dotted line) ± SEM. Autocorrelation curves were fitted to a 3D and 2D component model. In (**B**), a one or two component PCH model was used with the first (1) and second (2) brightness values plotted. The brighter second component dictated by a two component PCH fit only represented a small percentage (5.26 %) of the total measured population.

3.3.3 SNAP-D2R ACTIVATION IN CHO TETRACYCLINE-INDUCIBLE SNAP-D2R CELLS

A BRET-based $G_{\alpha o}$ protein activation assay was used to investigate how varying levels of SNAP-D2R expression translated to a functional D2R-mediated response in CHO tetracycline-inducible SNAP-D2R cells (described in detail in **Chapter 2.5.1**). SNAP-D2R expression was induced for 24 hours using a range of tetracycline concentrations (0 ng/ml – 10,000 ng/ml) before treating the cells for 10 minutes with agonists (dopamine or quinpirole) and measuring $G_{\alpha o}$ protein activation. The maximal responses (R_{max}) induced by both agonists relative to 10 μM dopamine with 10,000 ng/ml tetracycline induction, increased with an increasing concentration of tetracycline (**Fig. 3.13**). The rank order of maximal responses induced by both agonists was the same: 10,000 ng/ml = 1,000 ng/ml = 100 ng /ml > 10 ng/ml > 1 ng/ml > 0 ng/ml tetracycline (**Table 3.3**). The rank order of relative potencies was the same for both agonists and followed the same order as that of the relative maximal responses (**Table 3.3**). Interestingly, for both agonists at 100 ng/ml tetracycline, $G_{\alpha o}$ protein activation seems to reach a ceiling whereby increasing the tetracycline concentration further does not result in an increase in $G_{\alpha o}$ protein activation (**Fig. 3.13**). In addition, increasing the tetracycline concentration beyond 100 ng/ml does not significantly increase the potencies of both agonists for inducing D2R-mediated $G_{\alpha o}$ protein activation (**Table 3.3**). This suggests that there is no further increase in receptor expression beyond 100 ng/ml tetracycline induction which would otherwise be shown through increased agonist potency demonstrated by left-shifted curves at higher tetracycline concentrations. The most variation in $G_{\alpha o}$ protein activation is seen with SNAP-D2R induction using 10 ng/ml tetracycline as indicated by wide error bars for both agonists (**Fig. 3.13**). Despite the relative maximal response induced by 1 ng/ml and 0 ng/ml tetracycline being significantly smaller than the relative maximal response at 10,000 ng/ml tetracycline for each agonist ($P < 0.05$, one-way ANOVA; **Table 3.3**), these low or absent concentrations of tetracycline still induced a $G_{\alpha o}$ protein activation response above the baseline which may suggest 'leaky' SNAP-D2R expression where a small amount of SNAP-D2R expression is still present in the absence of tetracycline (**Fig. 3.13**). Furthermore, at 1 ng/ml and 0 ng/ml tetracycline, the

potencies (pEC_{50}) of both agonists relative to 10 μM dopamine with 10,000 ng/ml tetracycline induction, were significantly lower than that at 10,000 ng/ml tetracycline (*P* < 0.001 for dopamine, and *P* < 0.0001 for quinpirole) (**Table 3.3**).

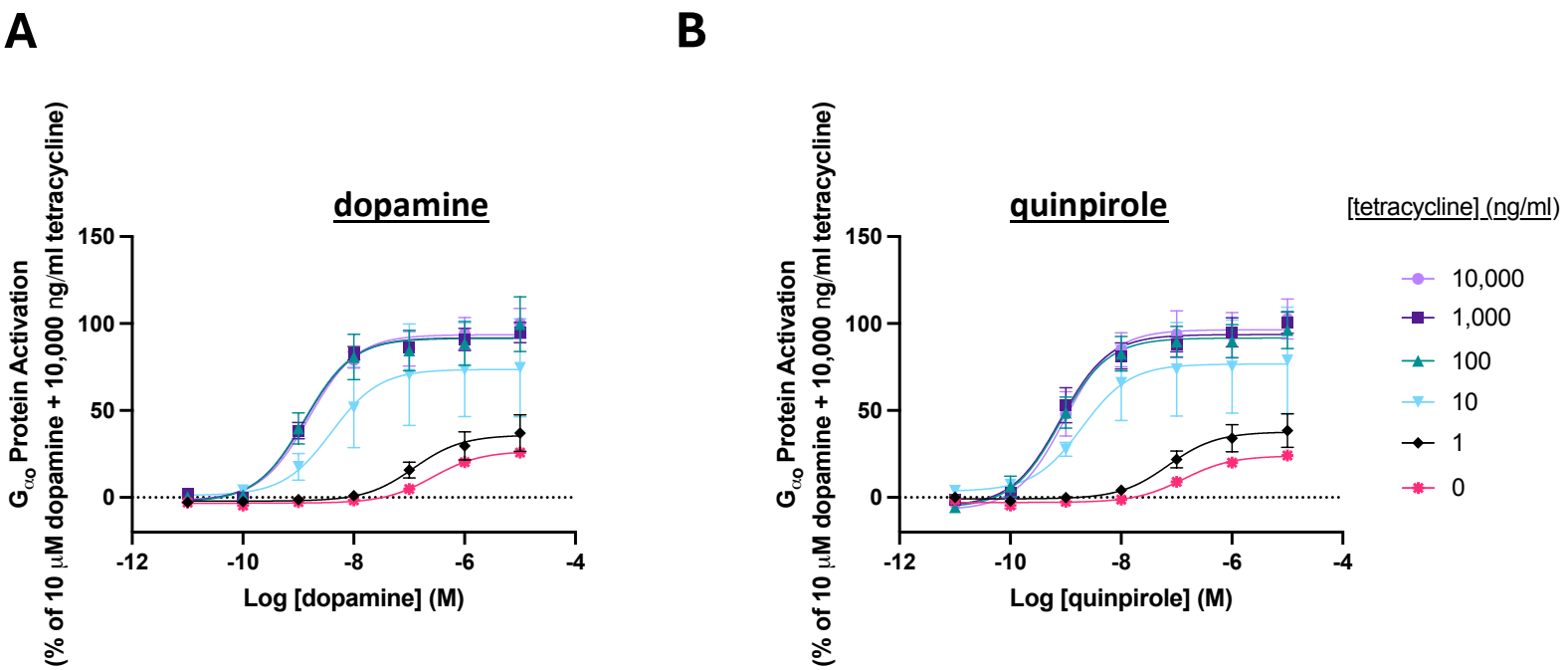

Figure 3.13: Concentration response curves showing agonist induced $G_{\alpha o}$ protein activation in CHO tetracycline-inducible SNAP-D2R (long isoform) cells following 24-hour induction with various concentrations of tetracycline.

SNAP-D2R mediated $G_{\alpha o}$ protein activation was measured in response to increasing concentration of dopamine (**A**) or quinpirole (**B**). Data are pooled (mean ± SEM) from 3 independent experiments performed in duplicate, normalised to the vehicle (0%) and to the response induced by 10 μM dopamine with 10,000 ng /ml tetracycline induction (100%).

Table 3.3: Potency and maximal effect estimates of agonist induced $G_{\alpha o}$ protein activation in CHO tetracycline-inducible SNAP-D2R (long isoform) cells following 24-hour induction with various concentrations of tetracycline.

SNAP-D2R mediated $G_{\alpha o}$ protein activation was measured in response to 10-minute treatment with dopamine or quinpirole. Pooled pEC_{50} (potency) values and R_{max} (maximal effect) values relative to the response induced by 10 μM dopamine with 10,000 ng/ml tetracycline induction, are shown. Data are pooled from 3 independent experiments conducted in duplicate and presented as mean ± SEM. One-way ANOVA with Dunnett's multiple comparison test was used to determine significant differences in $pEC_{50\ and}$ R_{max} values in comparison to 10,00 ng/ml tetracycline at each agonist; **P* < 0.05, ****P* < 0.001, *****P* < 0.0001.

[tetracycline] (ng/ml)	dopamine		quinpirole	
	pEC_{50}	**R_{max} (%)**	**pEC_{50}**	**R_{max} (%)**
10,000	8.81 ± 0.11	93.6 ± 2.9	9.02 ± 0.09	96.4 ± 2.5
1,000	8.88 ± 0.09	91.8 ± 2.2	9.10 ± 0.12	93.7 ± 3.0
100	8.90 ± 0.12	91.5 ± 3.0	9.10 ± 0.06	91.7 ± 1.5
10	8.41 ± 0.05	73.7 ± 1.1	8.71 ± 0.05	76.7 ± 0.9
1	6.92 ± 0.08***	35.9 ± 1.2*	7.15 ± 0.06****	37.7 ± 0.9*
0	6.58 ± 0.06***	26.6 ± 0.8*	6.88 ± 0.10****	23.9 ± 1.1*

3.4 DISCUSSION

In **Chapter 3**, we aimed to optimise FCS settings to measure fluorescent ligand concentrations in solution and to characterise the CHO tetracycline-inducible SNAP-D2R (long isoform) cell line. The fluorescent ligands, spiperone-d2 and clozapine-Cy5, and the CHO tetracycline-inducible SNAP-D2R cell line were used in FCS studies described in **Chapter 4** whereby antipsychotic drug rebinding at D2R was investigated.

FCS settings to measure fluorescent ligands in solution were optimised to determine the available dynamic range for measurable concentration as well as laser power. There was a notably low measured concentration in comparison to the added concentration of both spiperone-d2 and clozapine-Cy5 across a range of added ligand concentrations and laser powers. The addition of BSA resulted in an increase in the free fluorescent ligand concentration measured in solution likely due to BSA blocking non-specific sites on the coverglass. Despite this, we decided to perform FCS experiments in **Chapter 4** in the absence of BSA to avoid the use of more complicated models when fitting autocorrelation curves due to the presence of multiple components (BSA-bound ligand and free ligand). Furthermore, there may be brightness differences between BSA-bound ligand and free ligand which would complicate the quantification of their respective proportions of the total particle number. Therefore, in order to achieve a detectable signal, we chose an added concentration of 40 nM of both fluorescent ligands which resulted in ~ 5 nM measured concentration which is well within the range of detection capable using FCS[201]. In addition, according to our hypothesis that some fluorescent ligands may show increased rebinding to their target receptor depending on their kinetic properties (described in **Chapter 4**), the actual concentration of ligand near SNAP-D2R expressing cells may be markedly higher than 5 nM due to ligand rebinding resulting in a high local concentration of ligand near the target receptor.

From the fluorescent ligand optimisation experiments, a 633nm laser power of 15 % (~ 1.91 kW/cm^2) was chosen to be carried forward in future FCS studies. At this laser power a reasonable cpm (> 10 kHz)[211] was produced for FCS measurements of both

spiperone-d2 and clozapine-Cy5. No spot bleaching was seen at this laser power for either fluorescent ligand which would have been demonstrated by an increase in the diffusion coefficient. Furthermore, a similar laser power has been used in previous studies to measure fluorescent ligands in solution[207,209]. As previous studies have also suggested [191,192], we found 0.2 nM of Cy5 NHS ester to be comfortably measurable using FCS. The upper limit of detectable concentrations using FCS was thought to be at most 400 nM[202], however, we successfully demonstrated that concentrations of up to ~ 600 nM were able to be detected under our measurement conditions. This suggests that the concentration range that is detectable using FCS may be larger than previously reported further increasing its possible applications.

The initial characterisation of the CHO tetracycline-inducible SNAP-D2R cell line involved investigating the extent of the variability of cell-surface SNAP-D2R expression induced by varying concentrations of tetracycline. As expected, 24-hour receptor induction using a wide range of tetracycline concentrations resulted in a corresponding wide range of cell-surface SNAP-D2R expression. This variability in gene expression has been previously shown for tetracycline-inducible systems in HEK 293T cells[214–216]. FCS allowed the measurement of SNAP-D2R expression in a more quantitative manner through the determination of particle number per square area of membrane. This parameter was strongly correlated with the mean fluorescence intensity of SNAP-labelled SNAP-D2R at cell membranes validating this fluorescence readout within a region of interest at the membrane (described in **Chapter 2.8.4**) as an estimation of cell-surface SNAP-D2R expression.

FCS also showed that the dynamics of SNAP-D2R in terms of its diffusion coefficient at the membrane was consistent with other SNAP-labelled GPCRs[187,189,213] and was unaffected by increases in cell-surface SNAP-D2R expression. A recent study also demonstrated that a different GPCR, the M1 muscarinic acetylcholine receptor (M1R), showed no change in its diffusion coefficient when the receptor density on the membrane was increased[216]. Interestingly, in this study an increase in receptor

expression on the membrane resulted in an increase in receptor dimer formation in an expression-dependent manner[216], which has also been shown to occur with other GPCRs including the chemokine CXCR4 receptor[217]. Studies using oligomeric forms of GFP found that increasing the unit number of GFP resulted in slower diffusion coefficients due to an increase mass of the fluorescent particles passing through the FCS detection volume[218,219]. However, FCS cannot be used to identify dimers based on changes in diffusion coefficient alone as the diffusion speeds of two species must differ by at least a factor 1.6 to be resolved using FCS[220]. Therefore, only receptor oligomers containing a minimum of 6 receptors can be identified based on diffusion coefficients[221]. In this chapter we found through PCH analysis that for the majority of cells across a range of cell-surface SNAP-D2R expression levels, SNAP-D2R exists as a population of a single brightness which may explain why an increase in cell-surface SNAP-D2R expression did not affect its diffusion coefficient. A second component was detected in only 5.26 % of cells that was ~ 6-fold brighter than the first component which indicates the presence of higher-order oligomeric forms of SNAP-D2R[193]. It is important to note that in the absence of monomeric and dimeric controls we cannot establish the receptor number within either component[189,222]. It has been previously suggested that at high expression levels, D2S forms higher-order oligomers at the plasma membrane consisting of at least four receptors[223]. Receptor clustering leading to the formation of oligomers prior to internalisation via clathrin-coated pits has been reported for the μ-opioid receptor[213]. In addition, several other studies have used PCH analysis to show that other GPCRs also form oligomers, although predominantly homodimers, including the α1b-adrenoceptor, β2-adrenoceptor, serotonin 5-HT2A and 5-HT2C receptors, muscarinic acetylcholine M1 and M2 receptors, chemokine receptor CXCR4, and dopamine D1 receptor [189,216,217,221,224].

It is unlikely that the punctate expression of SNAP-D2R that was seen on the cell-surface of several CHO tetracycline-inducible SNAP-D2R cells reflects the presence of these higher-order SNAP-D2R oligomers given their small percentage in terms of the total receptor population. Instead, it may be the case that these brighter spots on the

cell surface represent membrane microdomains consisting of a cluster of D2Rs and lipids[225]. In support of this hypothesis, a study has shown neurokinin-1 receptors to exist in plasma membrane microdomains in a monomeric form despite the high concentration of receptors within these domains[226]. It has been shown that the majority of D2L (~ > 70 %) segregates into membrane microcompartments on the plasma membrane[227]. Moreover, D2R has been shown to organize in clusters on the membrane of neurones[228–230]. These clusters may allow the regulation of D2R signalling by providing discrete signalling sites enriched with D2R and signalling pathway components[225]. This is further supported by the finding of $G_{\alpha i}$ proteins within D2L-containing microcompartments[227].

Interestingly, a confocal image of 24-hour 10 ng/ml tetracycline induction of CHO tetracycline-inducible SNAP-D2R cells showed varied expression SNAP-D2R cell-surface expression among cells within the same well. This may have been reflected in D2R-mediated $G_{\alpha o}$ protein activation where 10 ng/ml tetracycline showed the most variation in agonist-induced $G_{\alpha o}$ protein activation demonstrated by wide error bars. Alternatively, this variation between experimental repeats in D2R-mediated $G_{\alpha o}$ protein activation using 100 ng/ml tetracycline, could be due to the binary nature of the tetracycline induction system with this concentration of tetracycline being around the threshold for receptor induction in this system[231]. In addition, the presence of a D2R-mediated $G_{\alpha o}$ protein activation ceiling (at 100 ng/ml tetracycline induction), has been demonstrated in other tetracycline-regulated systems and is reflective of a maximum cellular response possibly due to an absolute protein expression level limit or receptor reserve with signal amplification[232,233]. It is unlikely that there is a further increase in receptor expression induced by concentrations above 100 ng/ml tetracycline as both agonists do not show an increase in potency for D2R-mediated $G_{\alpha o}$ protein activation at these higher tetracycline concentrations. The low levels of $G_{\alpha o}$ protein activation seen with very low (1 ng/ml) and absent tetracycline concentrations is suggestive of 'leaky' SNAP-D2R and is a well characterised drawback of tetracycline-controlled gene expression[232,234]. More interestingly, these concentrations of tetracycline show a reduced potency for $G_{\alpha o}$

protein activation induced by both agonists in comparison to 10 μM dopamine with 10,000 ng/ml tetracycline induction. This could be caused by receptor reserve within this cell line where full receptor occupancy is not required to produce a maximal response. It has been shown in systems with receptor reserve that a decrease in receptor expression levels causes a decrease in agonist potency[235,236].

3.5 CONCLUSION

The measurement of the fluorescent antipsychotic drugs (APDs), spiperone-d2 clozapine-Cy5, in solution using FCS in the absence of BSA at 40 nM added concentration and at 15% laser power proved to be the optimal conditions for FCS experiments detailed in **Chapter 4** where the distribution of these ligands above D2R-expressing cells was investigated. In addition, the limits of detection in terms of measurable concentrations using FCS were determined for our system.

The CHO tetracycline-inducible SNAP-D2R (long isoform) cell line was shown to express variable levels of SNAP-D2R at the cell surface through induction with a range of tetracycline concentrations. This cell line is therefore especially suited to experimental applications such as FCS which requires low concentrations of labelled receptors to be able to accurately detect receptors diffusing through a small detection volume[237]. This cell line was therefore used in FCS studies in **Chapter 4** to determine the effect of the SNAP-D2R expression level at the cell surface on the distribution of fluorescent APDs above cells. In addition, the D2R-mediated $G_{\alpha o}$ protein activation seen in this cell line corresponded, on the whole, with the concentration of tetracycline added, demonstrating that the SNAP-D2R expressed in this cell line is functional.

CHAPTER 4: INVESTIGATING ANTIPSYCHOTIC DRUG REBINDING TO SNAP-D2R USING FLUORESCENCE CORRELATION SPECTROSCOPY

4.1 INTRODUCTION

Dopamine D2 receptor (D2R) antagonism is thought to be the pharmacological mechanism behind the clinical efficacy of antipsychotic drugs (APDs) in treating the positive symptoms of schizophrenia[111]. First-generation antipsychotics (FGAs) are referred to as "typical" based on their tendency to cause extrapyramidal side effects (EPS). These side effects encompass a variety of motor disorders that range from acute conditions, like acute dystonia, to more chronic conditions, like tardive dyskinesia[114]. EPS are thought to arise due to excessive antagonism of D2R in the nigrostriatal pathway[115]. Typical APDs generally have a high affinity for D2R which results in a small margin between D2R occupancy necessary for clinical efficacy and D2R occupancy associated with EPS[238]. It has been shown that 60% – 80% occupancy of D2R is required for typical APDs to induce a therapeutic response[239,240] but > 78% D2R occupancy has been associated with EPS[241,242]. Therefore, the overlap between desired and adverse D2R occupancy is largely unavoidable with FGAs.

In 1974, clozapine was first demonstrated to show efficacy in treating patients with psychosis who were unresponsive to APDs, in comparison to the prototype typical APD, chlorpromazine[243]. Clozapine has also shown greater efficacy in treating the negative symptoms of schizophrenia in comparison to FGAs[120,244]. Most promisingly, a large-scale double-blind study showed clozapine to have a lower EPS risk in comparison to chlorpromazine[120]. Unfortunately, clozapine is underutilised in clinic due to several "off-target" metabolic side effects including life-threatening agranulocytosis[121]. In an effort to generate APDs as efficacious as clozapine without the associated EPS risks of FGAs, second-generation APDs (SGAs) were developed. SGAs are termed as "atypical" as they are generally associated with a reduced EPS risk in comparison to FGAs, however, most SGAs are only as efficacious against both positive and negative symptoms as FGAs[122,245]. The superior side effect profile of SGAs may be due to their reduced affinity for D2R compared to FGAs, resulting in a lower D2R occupancy that is high enough for clinical efficacy without exceeding the threshold for inducing EPS[242,246]. Several

pharmacological mechanisms have been proposed to account for the reduced EPS risk of SGAs, including enhanced selectivity for the 5-HT2A receptor over D2R [151], fast dissociation rates at D2R [139], partial agonism at D2R[247] and regional selective binding to dopaminergic pathways projecting to cortico-limbic areas[115] (discussed in detail in **Chapter 1.4.2**). However, there has not been a single hypothesis that accounts for a general mechanism of atypicality across all clinically prescribed APDs.

Classically, association rates of APDs at D2R were thought to be diffusion limited and therefore show little variation [141]. Thus, differences in APD affinity at the D2R were thought to be based on their differing dissociation rates. Experiments that directly measure the binding kinetics of APDs have since shown that the association rates of APDs vary more than previously suggested[143,145]. Moreover, it was found that the association rates of APDs at D2L correlate with the incidence of EPS[145]. This correlation was proposed to be driven by APD rebinding within a diffusion limited synapse causing increased D2R blockade and therefore leading to higher EPS risk. Ligand rebinding describes the dissociation of a reversibly bound ligand from a receptor in a diffusion restricted system, followed by the consecutive binding to the same or nearby receptor [248]. This process therefore results in higher local concentrations of ligand proximal to the receptors in comparison to the bulk aqueous environment, which therefore leads to sustained receptor occupancy. According to the ligand rebinding model (detailed in **Chapter 1.4.3**), the overall effective reversal rate of a ligand dissociating from a receptor within a diffusion-restricted area is proportional to k_{off}, and also dependent on k_{on}, the diffusion rate of the ligand, the number of free receptors and the geometry of the restricted area[162]. Ligand rebinding is therefore known to be enhanced by fast ligand association rates, increased receptor densities and anatomical barriers to diffusion such as a synapse[145,162]. APDs with fast association rates at the D2R may be subject to this rebinding effect due to their action in the striatum where there is a high expression of D2R on medium spiny neurones[6]. Therefore, optimizing the association kinetics of APDs at D2R may improve their EPS risks.

However, the “fast-on” hypothesis for the molecular mechanism of atypicality has yet to be experimentally validated. Here, we aimed to show APD rebinding *in vitro* by revealing APD concentration gradients above D2R-expressing cells where there is a higher local concentration of APD immediately adjacent to the receptors on the cell surface in comparison to the bulk aqueous phase. We hypothesise that only APDs with fast association rates at the D2R would form these concentration gradients above D2R-expressing cells. We investigated the rebinding of two fluorescent APDs with differing binding kinetics, spiperone-d2 (fast association rate at D2R) and clozapine-Cy5 (slow association rate at D2R), by determining their concentration in the aqueous solution above D2R-expressing cells using fluorescence correlation spectroscopy (FCS).

4.2 CHAPTER 4 AIMS

The work described in Chapter 4 aimed to:

a) Characterise the binding kinetics of the fluorescent APDs, spiperone-d2 and clozapine-Cy5;
b) Investigate the distribution of the fluorescent APDs in solution above non-D2R-expressing and D2R-expressing cells;
c) Investigate the distribution of the fluorescent APDs both in solution immediately adjacent to the membrane of D2R-expressing cells and bound to the membrane of D2R-expressing cells.

4.3 RESULTS

4.3.1 CHARACTERISATION OF THE BINDING KINETICS OF FLUORESCENT APDS

To determine the influence of the association rate of APDs on their rebinding to D2R we used two fluorescent APDs, spiperone-d2 and clozapine-Cy5. These fluorescent APDs were chosen based on the differing binding kinetics of the non-fluorescent versions of these APDs used in clinic. The previously obtained binding kinetics revealed that spiperone displays a significantly faster association rate than clozapine (one-way ANOVA; $P < 0.0001$; ~ 39-fold) with no significant differences seen between their dissociation rates (one-way ANOVA; $P > 0.05$) despite spiperone showing a ~ 43-fold slower dissociation in comparison to clozapine: (spiperone, $k_{off} = 0.038 \pm 0.006$ min^{-1} and $k_{on} = 2.55 \pm 0.12 \times 10^9$ M^{-1} min^{-1}; clozapine, $k_{off} = 1.67 \pm 0.25$ min^{-1} and $k_{on} = 8.23 \pm 1.42 \times 10^7$ M^{-1} min^{-1})[145]. In addition, spiperone and clozapine show differing side effect profiles in patients with spiperone being associated with a high EPS risk and clozapine associated with a low EPS risk[145,249].

A time-resolved fluorescence resonance energy transfer (TR-FRET) assay (described in detail in **Chapter 2.6.3**) was used to determine if the differing binding kinetics of spiperone and clozapine were maintained in the fluorescent versions of these APDs: spiperone-d2 and clozapine-Cy5. The observed D2R association of each fluorescent APD at seven different concentrations was monitored over time (**Fig. 4.1A**). Plots of the observed association rate (K_{obs}) against the concentration of fluorescent APD demonstrated a linear relationship, indicating that the ligand-receptor interaction for both spiperone-d2 and clozapine-Cy5 followed the law of mass action (**Fig. 4.1B**). The ligand binding curves were fitted to a global non-linear regression model (detailed in C**hapter 2.8.3**) to determine the kinetic parameters (association rate, k_{on}; and dissociation rate, k_{off}) as well as the kinetically derived binding affinity of each fluorescent APD for D2R (**Table. 4.1**).

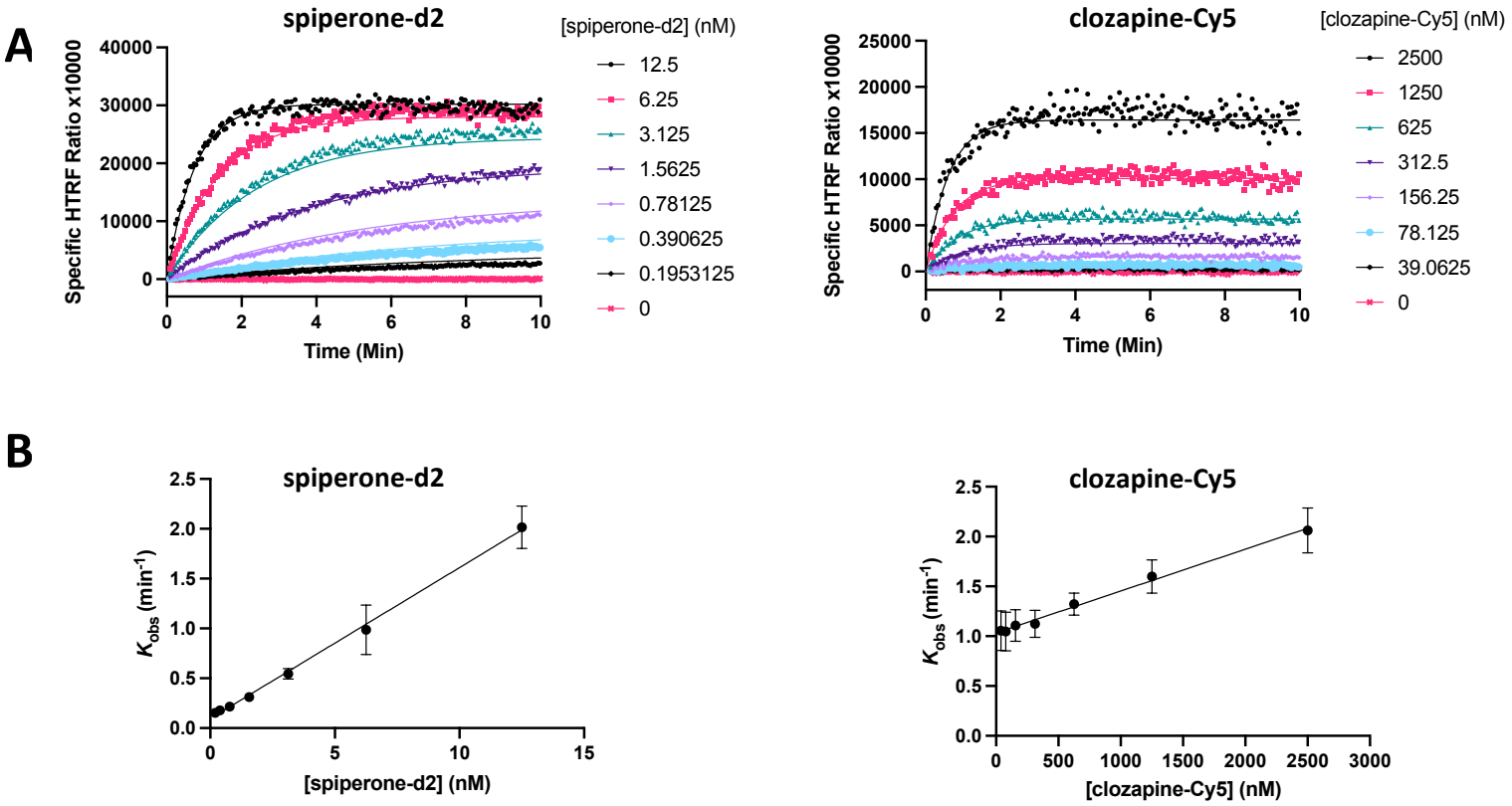

Figure 4.1: Determination of ligand binding kinetics of spiperone-d2 and clozapine-Cy5 at D2R using a time-resolved fluorescence resonance energy transfer assay.

(**A**) Representative association binding traces are shown for increasing concentrations of both spiperone-d2 and clozapine-Cy5 to D2L and D2S, respectively. Experiments were performed in singlet and are representative of 3 or 5 independent experiments for spiperone-d2 and clozapine-Cy5, respectively. (**B**) A one-phase exponential association model was used to fit binding traces to obtain the observed association rate (K_{obs}). Plots showing K_{obs} versus the concentration of spiperone-d2 or clozapine-Cy5 displayed a linear relationship. Data represent mean ± SEM of 3 or 5 independent experiments for spipeorne-d2 and clozapine-Cy5, respectively.

Table 4.1: Kinetic binding parameters of fluorescent antipsychotic drugs at D2R derived using a time-resolved fluorescence resonance transfer assay.

Data represent mean ± SEM from 3 or 5 experiments conducted in singlet for spiperone-d2 and clozapine-Cy5, respectively. The kinetically derived K_d is also shown.

	k_{off} (min^{-1})	k_{on} (M^{-1} min^{-1})	pK_d	K_d (nM)
spiperone-d2	0.13 ± 0.01	1.29 ± 0.15 x 10^8	9.00 ± 0.03	1.00
clozapine-Cy5	1.07 ± 0.10	4.00 ± 0.64 x 10^5	5.56 ± 0.06	2675

These data reveal that spiperone-d2 displays a significantly faster association rate (one-way ANOVA; $P < 0.0001$; ~ 300-fold) at the D2R as compared to clozapine-Cy5 along with a statistically similar dissociation rate (one-way ANOVA; $P > 0.05$) despite spiperone-d2 showing an ~ 8-fold slower dissociation rate in comparison to clozapine-Cy5. As such they represent suitable tool fluorescent compounds with which to investigate the influence of ligand binding kinetics on drug rebinding.

4.3.2 INVESTIGATION OF THE DISTRIBUTION OF FLUORESCENT APDS ABOVE NON-D2R-EXPRESSING CELLS

FCS was used as a tool to investigate the distribution of fluorescent APDs above D2R-expressing cells with the aim of providing experimental evidence of drug rebinding. We hypothesised that APDs with fast association rates at D2R are subject to rebinding which may appear as a drug concentration gradient where there is a high concentration of APD near D2R expressed on the cell surface, and a lower APD concentration in the bulk aqueous phase. The basis of FCS as an advanced spectroscopy technique is described in detail in **Chapter 3.1**. Briefly, FCS relies on the diffusion of fluorescent

particles in and out of a small detection volume created by a focussed laser beam[201]. Fluctuations in fluorescence intensity are recorded over time and analysed to determine several parameters including: the particle number per unit area of a fluorescent species diffusing in the 2D plane of a cell membrane (N/μm^2), the concentration of a fluorescent species in solution (nM), the diffusion coefficient of a fluorescent species (D, μm^2/s), and the molecular brightness of a fluorescent species (ε, cpm/s)[191]. The experimental FCS workflow used in this chapter is detailed in **Chapter 2.7.3**. In brief, we have used FCS to determine the concentrations of spiperone-d2 and clozapine-Cy5 in solution at varying distances above the upper membrane of cells. In addition, we have also investigated the concentrations of these fluorescent APDs bound to the membrane of cells.

First, the concentrations of the fluorescent APDs, spiperone-d2 or clozapine-Cy5, were measured in solution above CHO FlpIn parental cells without D2R expression to investigate the distribution of these fluorescent APDs in solution and whether this is affected by the presence of cells. Following the FCS measurement optimisation of these fluorescent APDs detailed in **Chapter 3.3**, a concentration of 40 nM of each fluorescent APD was chosen to be added to CHO FlpIn parental cells. This concentration was decided based on the actual measured concentration of fluorescent APDs in wells in the absence of cells and whether this measured concentration was in the detectable concentration range of FCS [201,250]. After 2 hours of 40 nM fluorescent APD incubation, above cell measurements and measurements in the absence of cells (above glass only) were taken in solution in the same well at a range of distances from 8 μm - 200 μm above the glass in varying increments in the z-axis (average cell height in this study ~ 6 μm). Fluorescence intensity fluctuations were collected for 5 seconds at each distance above the glass for both fluorescent APDs. Representative fluorescence intensity fluctuation traces at 9 μm, 35 μm and 100 μm above the glass are shown for spiperone-d2 (**Fig. 4.2**) and for clozapine-Cy5 (**Fig. 4.3**) for both above cell measurements and measurements in the absence of cells. The self-similarity of these traces over time was analysed using autocorrelation analysis (detailed in **Chapter 2.8.5**) which resulted in autocorrelation

curves that were fitted to a model depicting a single, freely diffusing 3D component and a pre-exponential to account for the fluorophore triplet state (representative curves shown in **Fig. 4.2** & **Fig.4.3**). As described in **Chapter 2.8.5**, the inverse of the y-intercept of this model provided the particle number (N) of the fluorescent species from which we determined the concentration (nM) of spiperone-d2 or clozapine-Cy5 in solution.

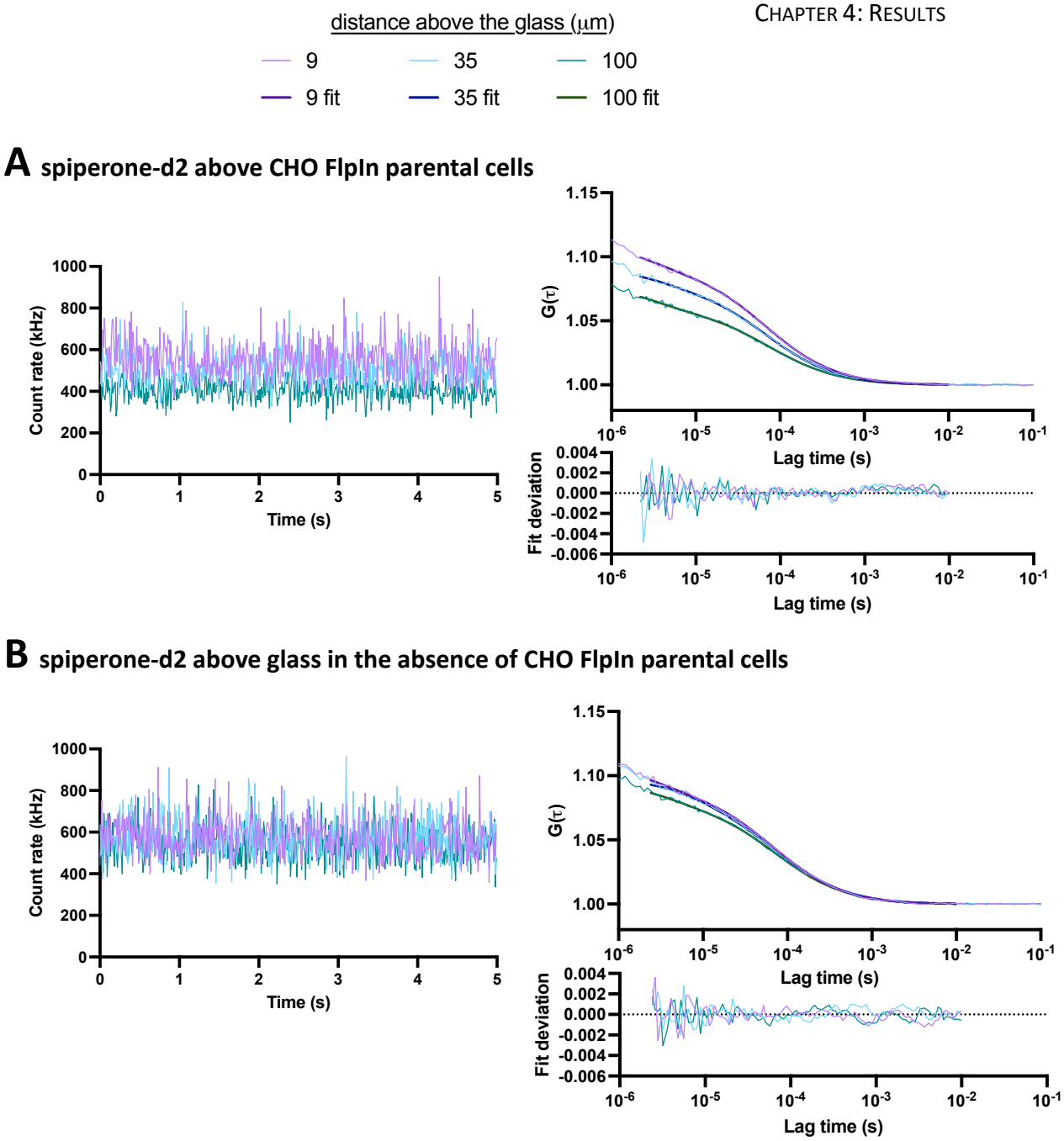

Figure 4.2: Representative fluorescence intensity fluctuation traces and autocorrelation curves from FCS measurements of spiperone-d2 in solution above CHO FlpIn parental cells at 9, 35 and 100 μm above the glass.

FCS measurements were taken of the fluorescent APD, spiperone-d2, at range of distances in solution in increasing increments in the z axis (8 μm – 200 μm above glass). Here, data from FCS measurements taken at 9 μm, 35 μm and 100 μm above the glass are shown. The FCS detection volume was placed in the x-y axis either above a single cell (above cell measurement) (**A**) or above glass in the absence of cells (**B**) within the same well. Representative raw fluorescence intensity fluctuation traces are shown on the left. Autocorrelation analysis of these traces produced autocorrelation curves (on the right) which were fitted to a single 3D component model. The deviation of the fit from the curve is also shown.

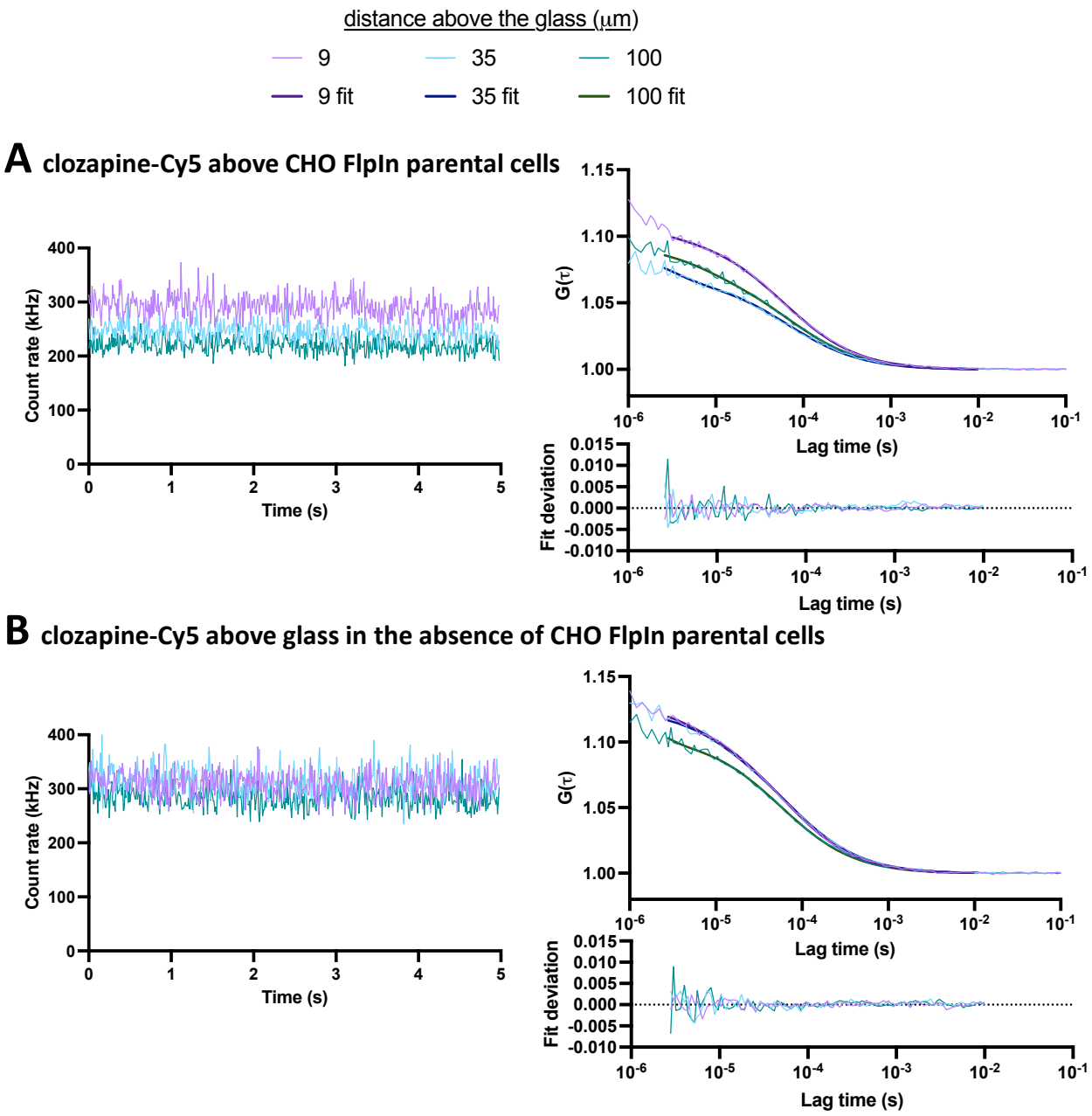

Figure 4.3: Representative fluorescence intensity fluctuation traces and autocorrelation curves from FCS measurements of clozapine-Cy5 in solution above CHO FlpIn parental cells at 9, 35 and 100 μm above the glass.

FCS measurements were taken of the fluorescent APD, clozapine-Cy5, at range of distances in solution in increasing increments in the z axis (8 μm – 200 μm above glass). Here, data from FCS measurements taken at 9 μm, 35 μm and 100 μm above the glass are shown. The FCS detection volume was placed in the x-y axis either above a single cell (above cell measurement) (**A**) or above glass in the absence of cells (**B**) within the same well. Representative raw fluorescence intensity fluctuation traces are shown on the left. Autocorrelation analysis of these traces produced autocorrelation curves (on the right) which were fitted to a single 3D component model. The deviation of the fit from the curve is also shown.

We showed that the measured concentrations of spiperone-d2 (**Fig. 4.4A**) and clozapine-Cy5 (**Fig. 4.4B**) in solution were similar to the added concentration of 40 nM across the range of distances measured (8 μm – 200 μm above glass). The measured concentrations of spiperone-d2 and clozapine-Cy5 were not significantly different to the added concentration of 40 nM at equivalent distances above glass for measurements in the presence and absence of a cell ($P > 0.05$, multiple t-tests). In addition, for both spiperone-d2 and clozapine-Cy5, there was no significant difference in the measured concentration of fluorescent APD between above cell measurements and measurements in the absence of cells at equivalent distances above glass ($P > 0.05$, two-way ANOVA). Therefore, there was an even distribution of both fluorescent APDs in solution within the well which was unaffected by the presence of a cell. Furthermore, the diffusion coefficients of spiperone-d2 were similar between above cell measurements and measurements in the absence of cells across the range of distances measured ($P > 0.05$, two-way ANOVA) (**Fig. 4.4C**). Interestingly, the diffusion coefficients of clozapine-Cy5 were significantly slower above cells in comparison to the measurements in the absence of cells at several distances between 10 μm – 60 μm above the glass ($P < 0.05$, two-way ANOVA) (**Fig. 4.4D**).

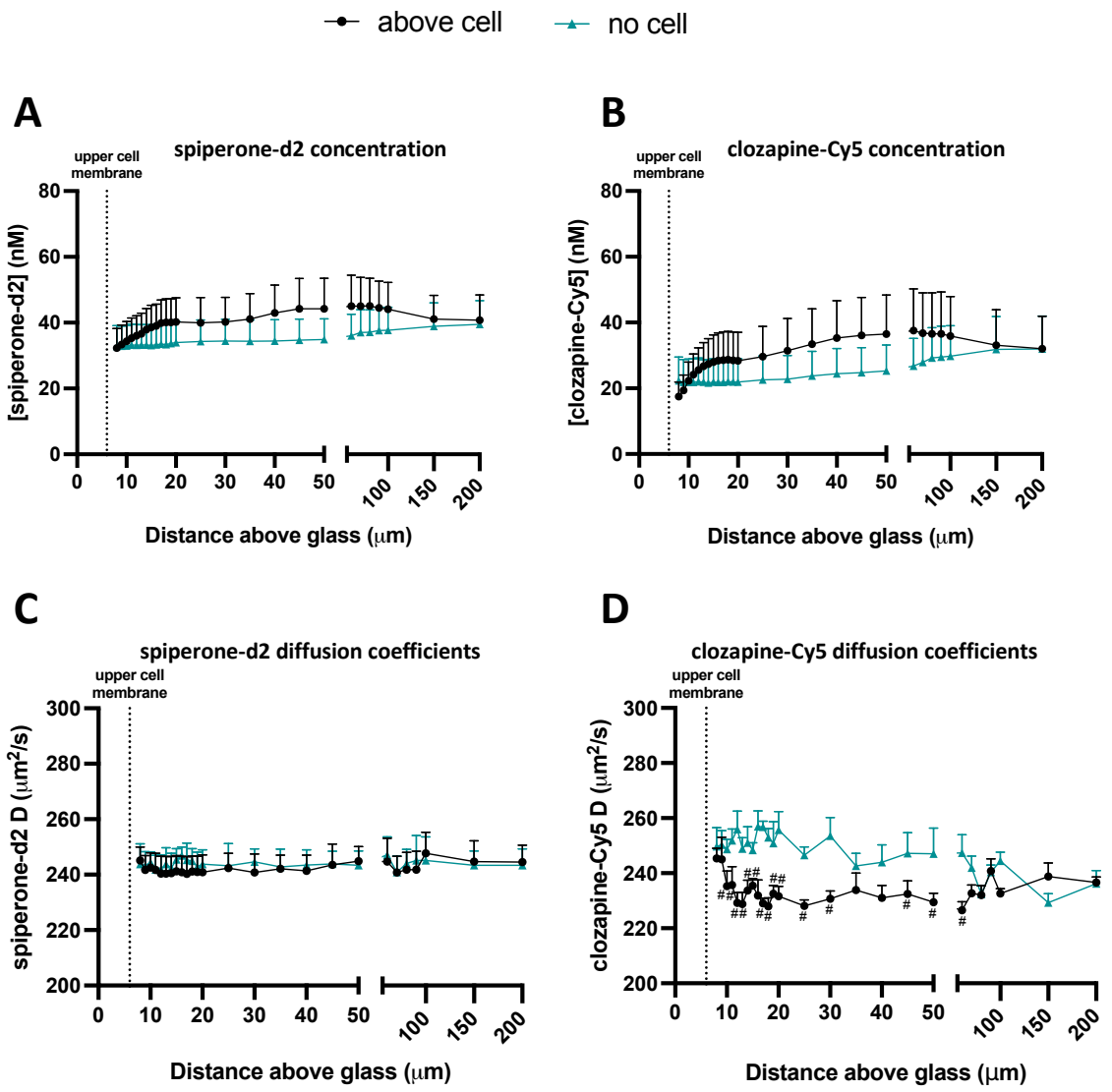

Figure 4.4: The concentrations and diffusion coefficients of spiperone-d2 and clozapine-Cy5 in solution above CHO FlpIn parental cells measured using FCS.

CHO FlpIn parental cells were plated in a chambered 8-well coverglass for 48 hours before 40 nM of either spiperone-d2 or clozapine-Cy5 was added to wells and incubated for 2 hours at 37 °C. FCS measurements were then taken at a range of distances in solution in increasing increments in the z axis (8 μm - 200 μm above glass). The FCS detection volume was placed in the x-y axis either above a single cell (above cell measurement, shown in black) or above glass (no cell measurement, shown in green) within the same well. Resulting autocorrelation curves were fitted to a single 3D component model. The measured concentration (**A** & **B**) and diffusion coefficients (**C** & **D**) are shown for spiperone-d2 and clozapine-Cy5. Data represent mean ± SEM of 5 independent experiments where 3 measurements were taken for each condition (above cell and no cell) per experimental day. No significant differences were found between the added concentration of 40 nM and the measured concentration of spiperone-d2 or

clozapine-Cy5 for above cell or no cell measurements at every distance measured ($P > 0.05$, multiple t-tests). In addition, no significant differences were found in the measured concentration of fluorescent ligand between the above cell and no cell measurements at equivalent distances above glass for both spiperone-d2 and clozapine-Cy5 ($P > 0.05$, two-way ANOVA; Tukey's multiple comparison test). Significant differences in the diffusion coefficients were only found for clozapine-Cy5, where $^{\#}$ denotes statistical significance ($P < 0.05$) for above cell measurements compared to no cell measurements at equivalent distances above the glass (two-way ANOVA, Tukey's multiple comparison test).

4.3.3 INVESTIGATION OF THE DISTRIBUTION OF SPIPERONE-D2 ABOVE D2R-EXPRESSING CELLS

To investigate the effect of SNAP-D2R (long isoform) expression on the concentration of spiperone-d2 above cells, spiperone-d2 was added to CHO tetracycline-inducible SNAP-D2R (long isoform) cells plated onto an 8-well chambered coverglass. A range of tetracycline concentrations (10 ng/ml -100 ng/ml) was added to cells for 24 hours which resulted in variable SNAP-D2R expression among cells within the same well. Cells were SNAP-labelled with SNAP-Surface® Alexa Fluor® 488 which allowed their characterisation as high-, low- or non-expressing SNAP-D2R cells based on the fluorescent SNAP-D2R signal on the membrane (detailed in **Chapter 3.3**). Following the measurement of SNAP-D2R expression on the membrane of a cell, fluorescent APD concentrations above the same cell were measured using FCS. This allowed the determination of the effect of SNAP-D2R cell-surface expression levels on the distribution of fluorescent APD in solution.

Initially, an added concentration of 40 nM of spiperone-d2 was chosen based on the FCS optimisation performed in **Chapter 3.3**. After a 2-hour incubation with spiperone-d2, above cell measurements or measurements in the absence of cells were taken in solution between 8 μm – 200 μm above glass as previously described for measurements using the CHO FlpIn parental cell line. Representative fluorescence intensity fluctuation traces at 9 μm, 35 μm and 100 μm above the glass are shown for above high-expressing SNAP-D2R cell measurements (**Fig. 4.5A**) and in the absence of cells (**Fig. 4.5B**). The resulting autocorrelation curves were fitted to a model depicting a single 3D component and a pre-exponential triplet state (**Fig. 4.5**). There were clear differences between the autocorrelation curves at various distances above the glass from measurements above high-expressing SNAP-D2R cells whereby the amplitude of the curve increased as the FCS detection volume was moved up into solution further away from the glass (**Fig. 4.5A**). However, for measurements in the absence of cells, the

autocorrelation curves at each distance above the glass showed similar amplitudes (**Fig. 4.5B**).

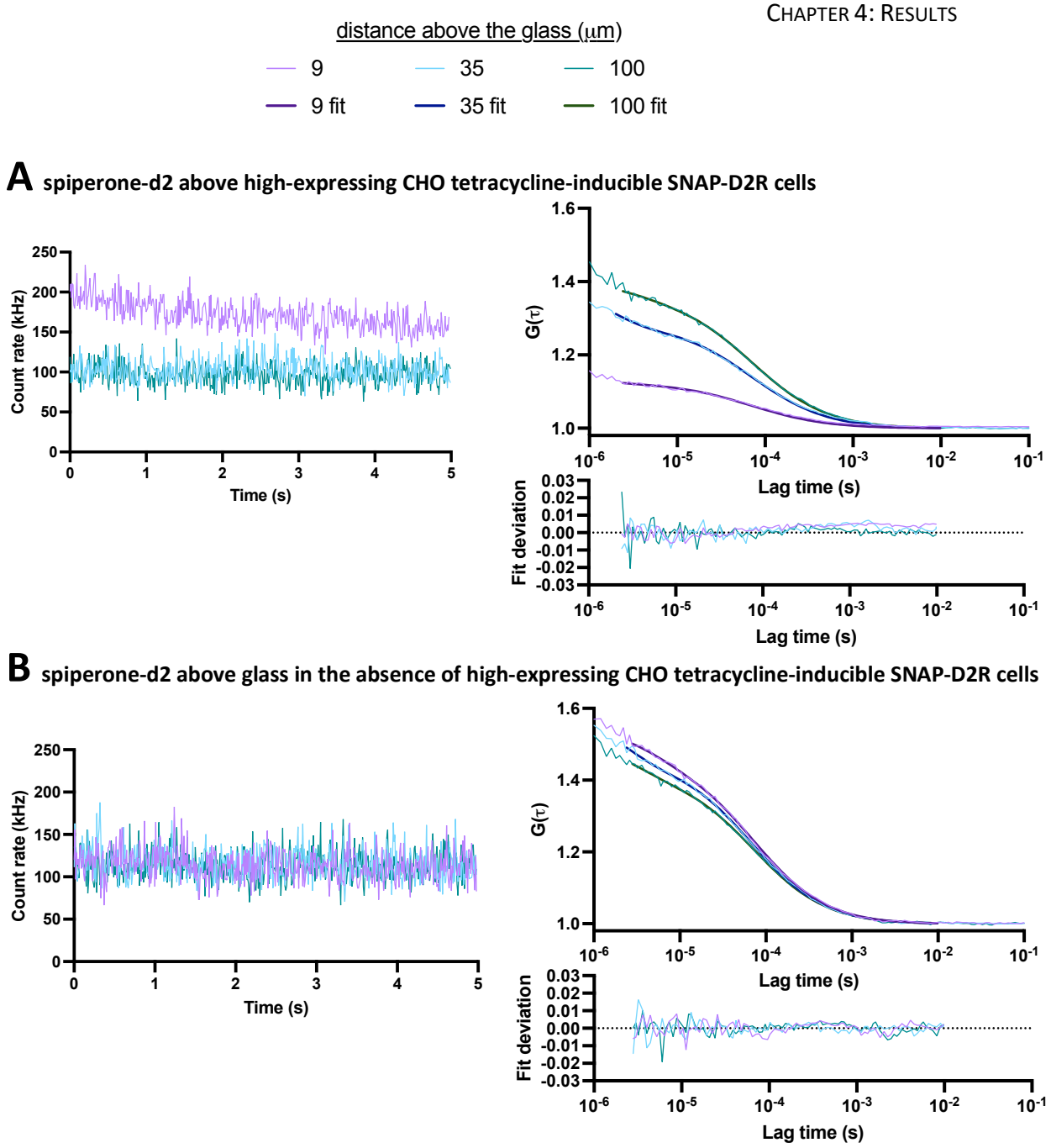

Figure 4.5: Representative fluorescence intensity fluctuation traces and autocorrelation curves from FCS measurements of spiperone-d2 in solution above high-expressing CHO tetracycline-inducible SNAP-D2R (long isoform) cells at 9, 35 and 100 μm above the glass.

FCS measurements were taken of the fluorescent APD, spiperone-d2, at range of distances in solution in increasing increments in the z axis (8 μm – 200 μm above glass). Here, data from FCS measurements taken at 9 μm, 35 μm and 100 μm above the glass are shown. The FCS detection volume was placed in the x-y axis either above a single cell (above cell measurement) (**A**) or above glass in the absence of cells (**B**) within the same well. Representative raw fluorescence intensity fluctuation traces are shown on the left. Autocorrelation analysis of these traces produced autocorrelation curves (on the right) which were fitted to a single 3D component model. The deviation of the fit from the curve is also shown.

Fold changes in spiperone-d2 concentrations were then calculated whereby spiperone-d2 concentrations for above cell measurements were divided by spiperone-d2 concentrations for measurements in the absence of cells at equivalent distances above the glass in the same well. These fold changes were calculated for measurements above high-, low- and non-expressing SNAP-D2R cells (**Fig. 4.6A**). There was a clear gradient in the fold change of spiperone-d2 concentration above high-expressing SNAP-D2R cells compared to measurements in the absence of cells (**Fig. 4.6A**). The fold change near the upper membrane (9 μm above glass; 1.99-fold ± 0.26, n=6) decreased as the detection volume was moved up into solution above the cells (200 μm above glass; 1.00-fold ± 0.03, n=6) such that at 200 μm above glass, the fold change above high-expressing SNAP-D2R cells was not statistically different to the fold change in the absence of a cell (0.99-fold ± 0.03, n=6) ($P > 0.05$, two-way ANOVA) . Between 8 μm – 14 μm above glass, the fold changes of spiperone-d2 were significantly higher than the fold change determined at the furthest distance measured (200 μm above glass) for high-expressing SNAP-D2R cells ($P < 0.05$, two-way ANOVA) (**Fig. 4.6A**). Interestingly, further away from the membrane at 30 μm above the glass, there was also a significant increase in the spiperone-d2 fold change in comparison to the fold change at the furthest distance measured for high-expressing SNAP-D2R cells ($P < 0.05$, two-way ANOVA) (**Fig. 4.6A**). For low- or non-expressing SNAP-D2R cells, no significant differences were found between the fold change at every distance measured compared to the furthest distance measured ($P > 0.05$, two-way ANOVA), suggesting that spiperone-d2 gradients were only formed above high-expressing SNAP-D2R cells. In addition, the fold changes in spiperone-d2 concentration above high-expressing SNAP-D2R cells compared to measurements in the absence of cells were significantly higher than those for low- and non-expressing SNAP-D2R cells between 8 μm – 12 μm above the glass ($P < 0.05$, two-way ANOVA) (**Fig. 4.6A**).

To further investigate whether the formation of spiperone-d2 gradients above high-expressing SNAP-D2R cells was dependent on SNAP-D2R expression, high-expressing SNAP-D2R cells were pre-incubated with 10 μM of the irreversible D2R

antagonist, phenoxybenzamine (PBZ), followed by the co-addition of 10 μM PBZ and 40 nM spiperone-d2 for 2 hours. PBZ pre-treatment reduced the concentrating effect of spiperone-d2 near the upper membrane of high-expressing SNAP-D2R cells (**Fig. 4.6B**). At 9 μm above the glass, the fold change of spiperone-d2 concentration above high-expressing SNAP-D2R cells compared to measurements in the absence of cells was significantly lower with PBZ treatment (1.22-fold ± 0.06, n=3) in comparison to without PBZ treatment (1.99-fold ± 0.26, n=6) ($P < 0.05$, two-way ANOVA).

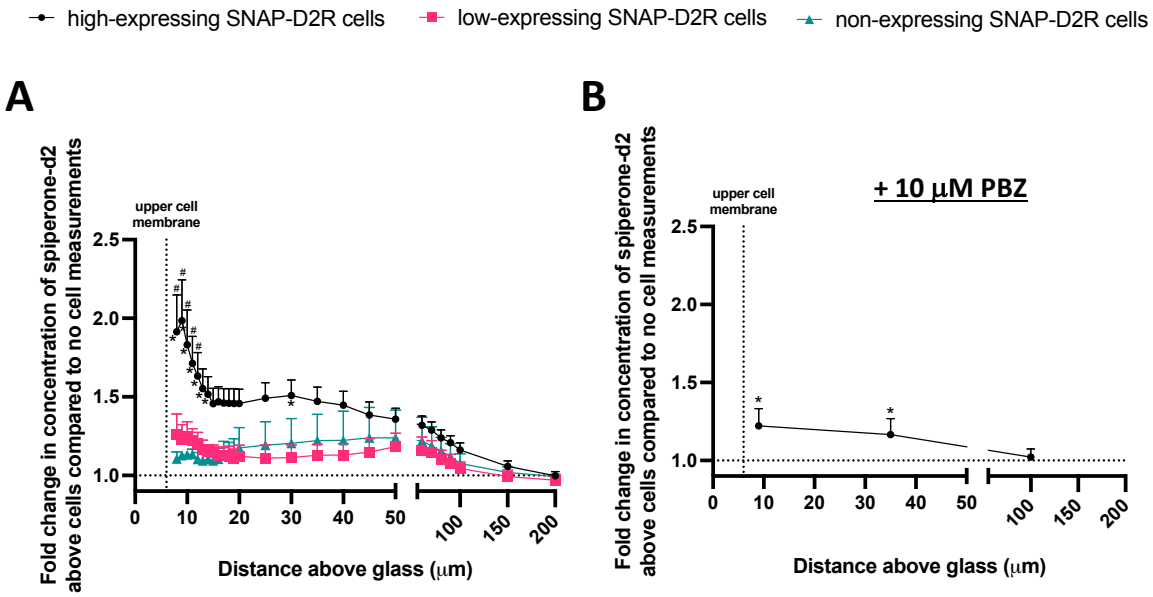

Figure 4.6: The fold change in the concentration of spiperone-d2 in solution above CHO tetracycline-inducible SNAP-D2R (long isoform) cells with a range of SNAP-D2R expression compared to no cell measurements across a range of distances (8 μm to 200 μm above glass).

Concentrations of spiperone-d2 were measured above SNAP-D2R-expressing cells SNAP-labelled with SNAP-Surface® Alexa Fluor® 488 using FCS. Resulting autocorrelation curves were fitted to a single 3D component model. Cells were categorized as high-, low- or non-expressing SNAP-D2R cells based on their fluorescent SNAP-D2R intensity at the membrane. A concentration of 40 nM spiperone-d2 was incubated for 2 hours at 37°C with (**B**) or without (**A**) phenoxybenzamine (PBZ) treatment (a 30-minute pre-incubation of 10 μM PBZ followed by the co-addition of 10 μM PBZ and 40 nM spiperone-d2). Data represent mean ± SEM of 3-6 independent experiments and * indicates statistical significance ($P < 0.05$) of the fold change measured at various distances above the glass compared to the fold change determined at the furthest distance measured for each category of SNAP-D2R expression with or without PBZ treatment (two-way ANOVA, Tukey's multiple comparisons test), whilst # denotes statistical significance ($P < 0.05$) of the fold change measured for high-expressing SNAP-D2R cells compared to the fold change for low- and non-expressing SNAP-D2R cells at equivalent distances above the glass (two-way ANOVA, Tukey's multiple comparison test).

Correlation analysis was used to illustrate the relationship between the level of cell-surface SNAP-D2R expression and the degree to which spiperone-d2 was concentrated above SNAP-D2R cells. Near the upper membrane of SNAP-D2R cells (9 μm above glass), there was a strong correlation between the SNAP-D2R expression of an individual cell and the fold change of spiperone-d2 concentration above that cell compared to measurements in the absence of cells (two-tailed Spearman's rank correlation, r_s = 0.80, P < 0.0001) (**Fig. 4.7A**). This correlation decreased as the FCS detection volume was moved up into the bulk aqueous phase away from cells (two-tailed Spearman's rank correlation: at 35 μm above glass; r_s = 0.51, P < 0.0001; at 100 μm above glass; r_s = 0.33, P = 0.0095) (**Fig. 4.7A**). Interestingly, the two-tailed Spearman's rank correlations at 9 μm, 35 μm and 100 μm above the glass were all statistically significant using a threshold of P < 0.05 (**Fig. 4.7A**). This is likely due to the assessment of a simple monotonic relationship using Spearman's rank correlation meaning the size of the effect is not accounted for due to data ranking.

PBZ treatment (a 30-minute pre-incubation of 10 μM PBZ prior to the co-addition of 10 μM PBZ and 40 nM spiperone-d2) abolished the strong correlation seen near the upper membrane at 9 μm above glass (two-tailed Spearman's rank correlation: r_s = 0.21, P = 0.28) (**Fig. 4.7B**). This suggests that the concentration gradient of spiperone-d2 above D2R-expressing cells was dependent on SNAP-D2R expression and the binding of spiperone-d2 to SNAP-D2R.

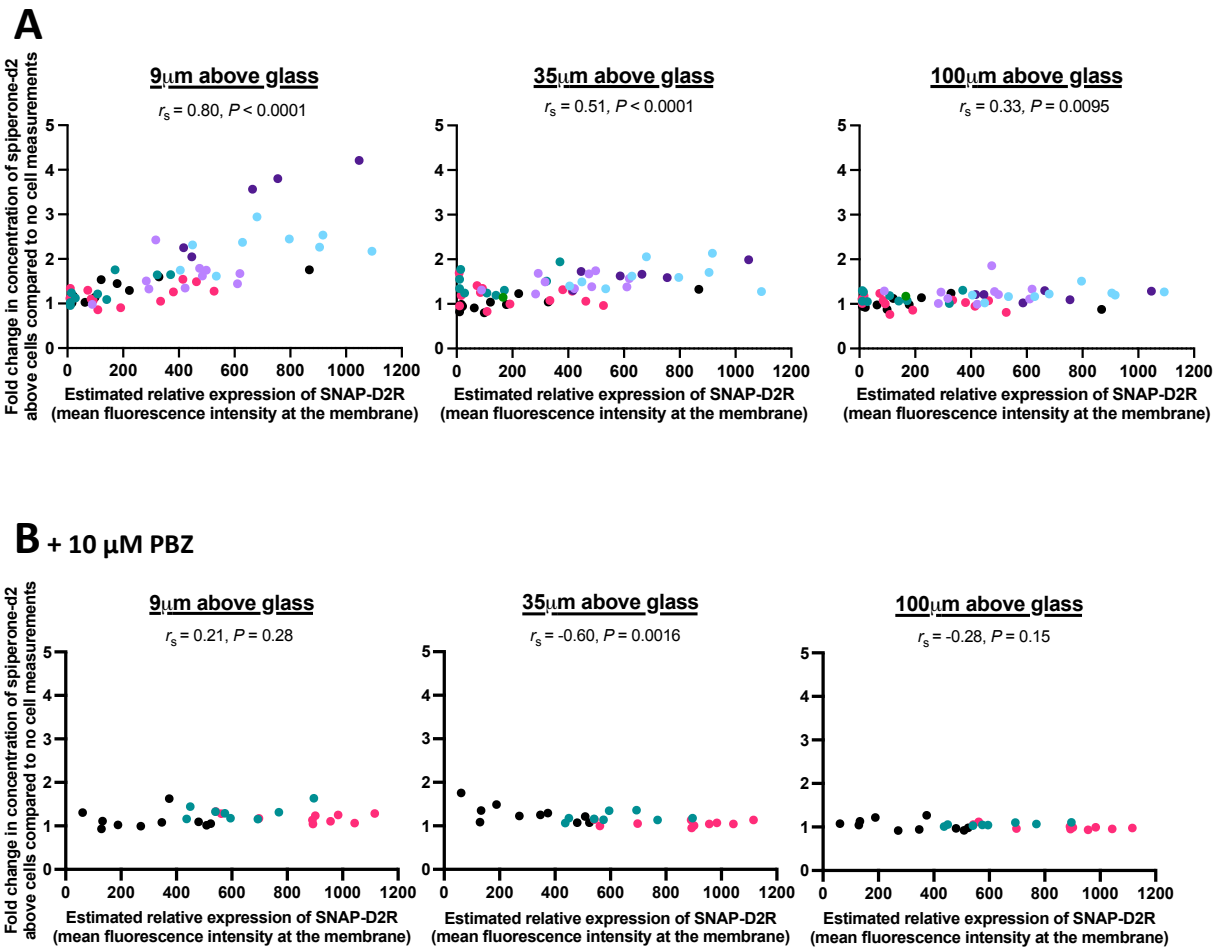

Figure 4.7: Correlation plots showing the relationship between the fold change in concentration of spiperone-d2 above CHO tetracycline-inducible SNAP-D2R (long isoform) cells compared to no cell measurements, and the cell-surface SNAP-D2R expression.

Cells were SNAP-labelled with SNAP-Surface® Alexa Fluor® 488 before the addition of 40 nM spiperone-d2 and incubated for 2 hours at 37°C with (**B**) or without (**A**) phenoxybenzamine (PBZ) treatment (a 30-minute pre-incubation of 10 μM PBZ before the co-addition of 10 μM PBZ and 40 nM spiperone-d2). FCS measurements were taken to determine the concentration of spiperone-d2 at specific distances above the glass. Resulting autocorrelation curves were fitted to a single 3D component model. The estimated relative expression of SNAP-D2R was determined by the mean fluorescence intensity of the SNAP-labelled SNAP-D2R on the cell membrane. Data points represent individual cell measurements from 3 – 7 independent experiments with measurements collected on the same day displayed in the same colour. Correlation between the two variables were assessed using a two-tailed Spearman's rank correlation allowing the calculation of the correlation coefficient, r_s.

We hypothesised that the formation of the spiperone-d2 concentration gradients above D2R-expressing cells was a result of spiperone-d2 rebinding to D2R, likely due to its fast association rate at the D2R. Therefore, we next investigated the distribution of clozapine-Cy5 above SNAP-D2R cells, a fluorescent APD with a ~ 300-fold slower association rate at D2R, to determine whether this rebinding effect is driven by differing association rates.

4.3.4 INVESTIGATION OF THE DISTRIBUTION OF CLOZAPINE-CY5 ABOVE D2R-EXPRESSING CELLS

We have proposed that the D2R expression-dependent concentration gradients above cells observed for spiperone-d2 was driven by drug rebinding. Therefore, we hypothesized that the rebinding effect would be less pronounced for the fluorescent APD, clozapine-Cy5, due to its ~ 300-fold slower association rate at D2R.

After a 2-hour incubation of CHO tetracycline-inducible SNAP-D2R cells with 40 nM clozapine-Cy5, above cell measurements or measurements in the absence of cells were taken in solution between 8 μm – 200 μm above glass as previously described. Representative fluorescence intensity fluctuation traces at 9 μm, 35 μm and 100 μm above the glass are shown for above high-expressing SNAP-D2R cell measurements (**Fig. 4.8A**) and in the absence of cells (**Fig. 4.8B**). Autocorrelation analysis of these traces resulted in autocorrelation curves that were fitted to a model depicting a single 3D component and a pre-exponential triplet state (**Fig. 4.8**). In contrast to spiperone-d2, autocorrelation curves for clozapine-Cy5 above high-expressing SNAP-D2R cells and in the absence of cells all showed similar amplitudes.

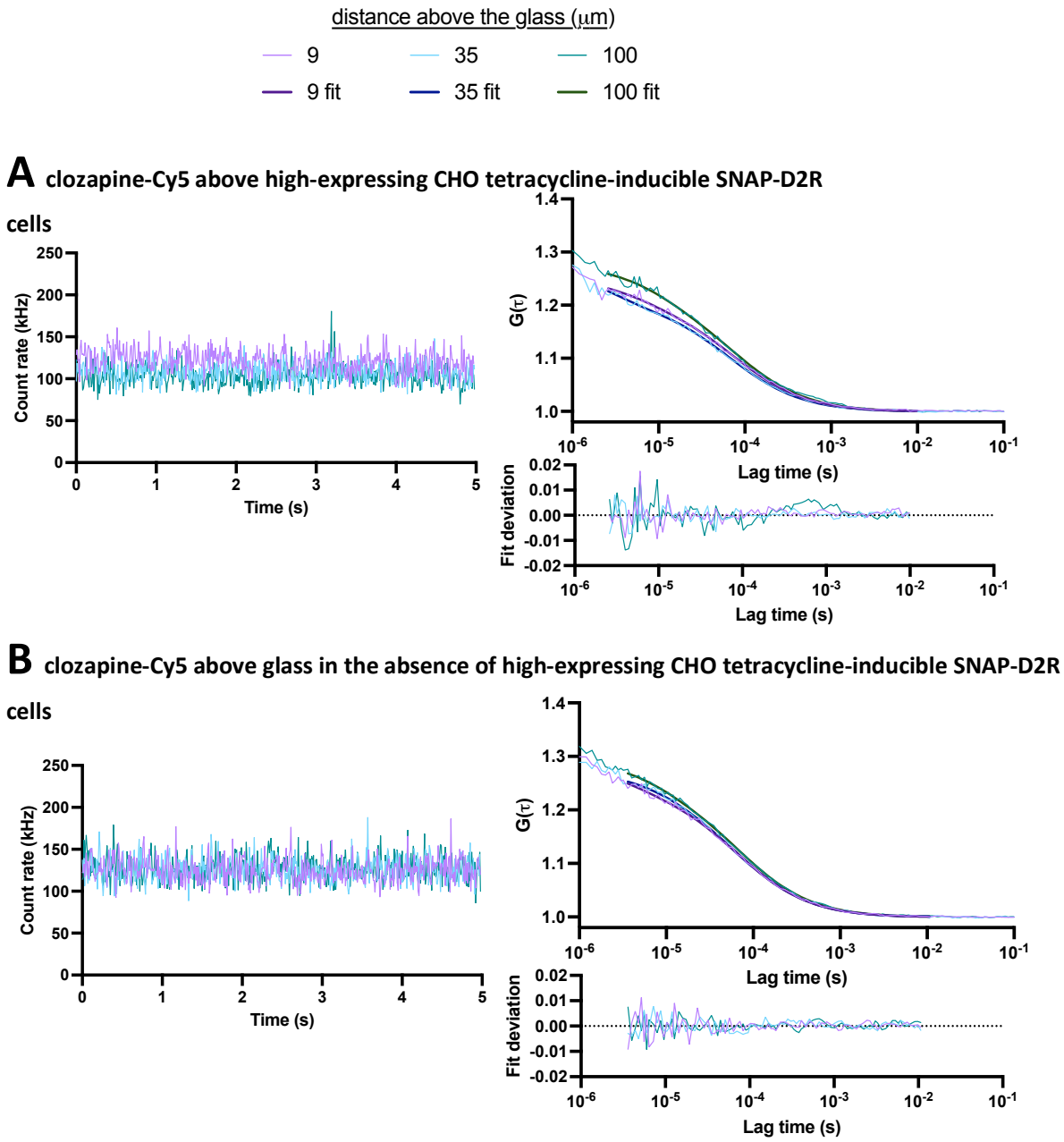

Figure 4.8: Representative fluorescence intensity fluctuation traces and autocorrelation curves from FCS measurements of clozapine-Cy5 in solution above high-expressing CHO tetracycline-inducible SNAP-D2R (long isoform) cells at 9, 35 and 100 μm above the glass.

FCS measurements were taken of the fluorescent APD, clozapine-Cy5, at range of distances in solution in increasing increments in the z axis (8 μm – 200 μm above glass). Here, data from FCS measurements taken at 9 μm, 35 μm and 100 μm above the glass are shown. The FCS detection volume was placed in the x-y axis either above a single cell (above cell measurement) (**A**) or above glass in the absence of cells (**B**) within the same well. Representative raw fluorescence intensity fluctuation traces are shown on the left. Autocorrelation analysis of these traces produced autocorrelation curves (on the right) which were fitted to a single 3D component model. The deviation of the fit from the curve is also shown.

Surprisingly, clozapine-Cy5 formed significant concentration gradients above high-, low- and even non-D2R-expressing cells (**Fig. 4.9A**). The fold changes in clozapine-Cy5 concentration above cells compared to measurements in the absence of cells were significantly higher at 8 μm – 40 μm, 10 μm – 12 μm and 12 μm – 26 μm above the glass for high-, low- and non-D2R-expressing cells, respectively, compared to the furthest distance measured (200 μm above glass) for each category of D2R expression ($P < 0.05$, two-way ANOVA). It should be noted that these clozapine-Cy5 concentration gradients near the cell surface were modest in comparison to those formed by spiperone-d2. Between 8 μm – 11 μm above the glass, the fold change of spiperone-d2 concentration was significantly higher than the fold change of clozapine-Cy5 concentration above high-expressing cells compared to measurements in the absence of cells ($P < 0.05$, two-way ANOVA). The peak fold change for spiperone-d2 above high-expressing SNAP-D2R cells was 1.99 ± 0.26 (n=6) at 9 μm above the glass whereas the peak fold change for clozapine-Cy5 was only 1.38 + 0.05 (n=4) at 10 μm above the glass (**Fig. 4.6A** & **Fig. 4.9A**). In addition, the concentration gradients formed by clozapine-Cy5 appear to be independent of receptor expression as at every distance measured above glass there was no significant difference between the fold change in clozapine-Cy5 concentration above high-expressing SNAP-D2R cells compared to the fold change above low- and non-expressing SNAP-D2R cells ($P > 0.05$, two-way ANOVA) (**Fig. 4.9A**).

Correlation analysis was also used to illustrate the relationship between the level of cell-surface SNAP-D2R expression and the degree to which clozapine-Cy5 was concentrated above SNAP-D2R cells. At 9 μm above the glass there was a significant correlation ($P < 0.05$) between the cell-surface SNAP-D2R expression and the fold change of clozapine-Cy5 above cells compared to measurements in the absence of cells (two-tailed Spearman's rank correlation, $r_s = 0.33$, $P = 0.035$) (**Fig. 4.9B**). However, this correlation was qualitatively weaker (~ 2.5-fold) in comparison to the correlation between the fold change of spiperone-d2 and SNAP-D2R expression at 9 μm above glass (spiperone-d2 treatment at 9 μm above glass, two-tailed Spearman's rank correlation; r_s

= 0.80, $P < 0.0001$). Interestingly, at 35 μm and 100 μm above the glass, there was a weak increase in the correlation between cell-surface SNAP-D2R expression and the fold change of clozapine-Cy5 above cells compared to measurements in the absence of cells in comparison to 9 μm above glass (two-tailed Spearman's rank correlation: 35 μm above glass; $r_s = 0.43$, $P = 0.0048$; and at 100 μm above glass; $r_s = 0.40$, $P = 0.0079$) (**Fig. 4.9B**). However, these correlations remained qualitatively weaker (~ 2-fold) in comparison to the strong correlation seen between the fold change of spiperone-d2 and SNAP-D2R expression at 9 μm above glass in **Figure 4.7A**. Furthermore, at 35 μm and 100 μm above the glass, the correlations between the fold change of both fluorescent APDs and SNAP-D2R expression appeared similar using a two-tailed Spearman's rank correlation: for spiperone-d2 at 35 μm above glass, $r_s = 0.51$, $P < 0.0001$ and for clozapine-Cy5 at 35 μm above glass, $r_s = 0.43$, $P = 0.0048$; for spiperone-d2 at 100 μm above glass, $r_s = 0.33$, $P = 0.0095$ and for clozapine-Cy5 at 100 μm above glass, $r_s = 0.40$, $P = 0.0079$).

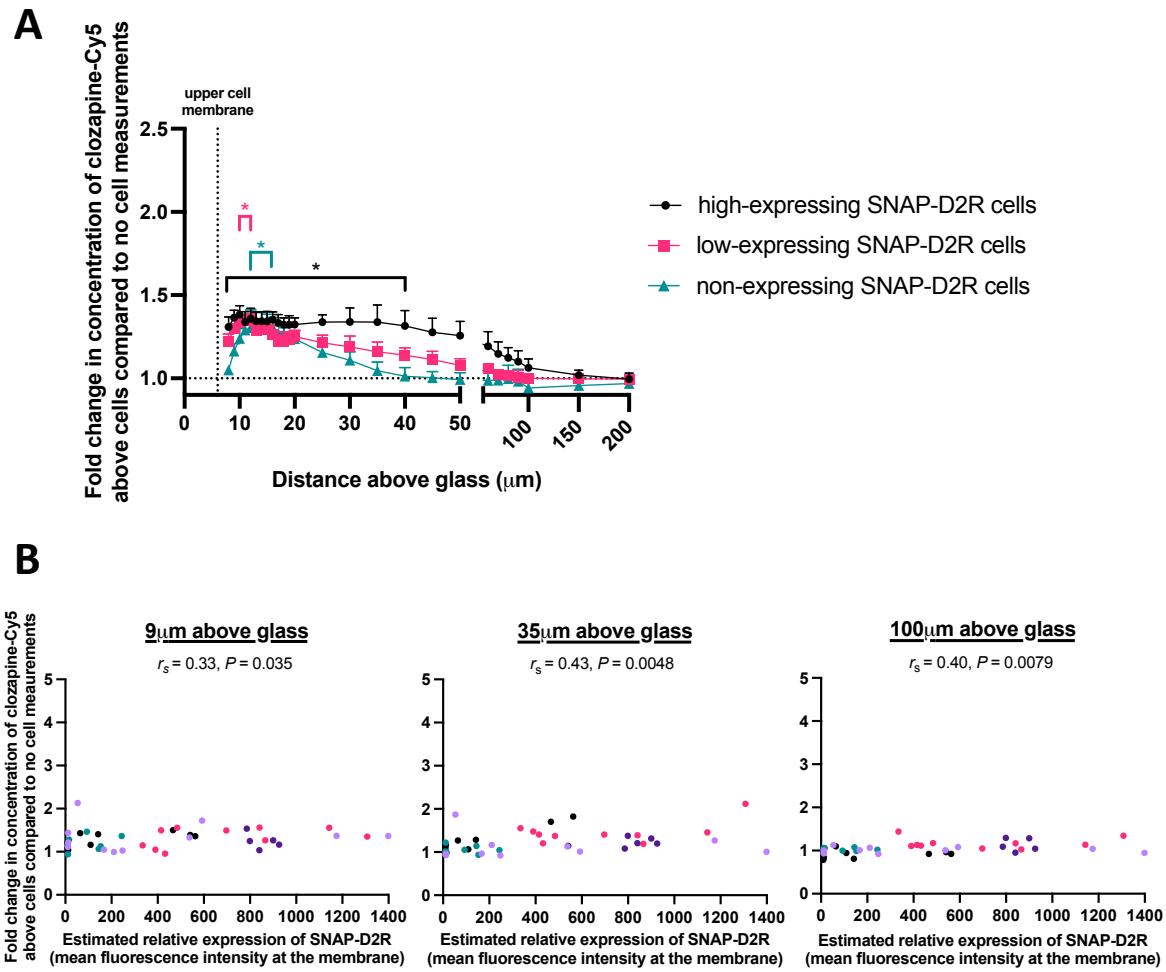

Figure 4.9: The investigation of the fold change in the concentration of clozapine-Cy5 in solution above CHO tetracycline-inducible SNAP-D2R (long isoform) cells compared to no cell measurements. Cells were SNAP-labelled with SNAP-Surface® Alexa Fluor® 488 before the addition of 40 nM clozapine-Cy5 and incubated for 2 hours at 37°C. FCS measurements were then taken to determine the concentration of clozapine-Cy5 at varying distances above the glass. Resulting autocorrelation curves were fitted to a single 3D component model. The estimated relative expression of SNAP-D2R was determined by the mean fluorescence intensity of the SNAP-labelled SNAP-D2R on the cell membrane. (**A**) The fold change in the concentration of clozapine-Cy5 above CHO tetracycline-inducible SNAP-D2R cells with a range of cell-surface SNAP-D2R expression compared to no cell measurements in solution across a range of distances (8 μm to 200 μm above glass). A concentration of 40 nM clozapine-Cy5 was added to cells and incubated for 2 hours at 37°C before measurements were taken. Data represent mean ± SEM of 3-4 independent experiments. The data points covered by the starred brackets [*] indicate statistical significance ($P < 0.05$) of difference in the fold change measured at various distances above the glass compared to the fold change determined at the furthest distance measured for each category of SNAP-D2R expression (two-way ANOVA, Tukey's multiple comparisons test). There was no statistical significance of the fold change above high-expressing SNAP-D2R cells compared to low- and non-expressing SNAP-D2R cells at every equivalent distance measured above the glass ($P > 0.05$; two-way ANOVA, Tukey's multiple comparisons test). (**B**) Correlation

plots showing the relationship between the fold change in concentration of clozapine-Cy5 above SNAP-labelled CHO tetracycline-inducible SNAP-D2R cells compared to no cell measurements, and the estimated cell-surface SNAP-D2R expression. Data points represent individual cell measurements which were taken over 4 independent experiments with points of the same colour representing measurements collected on the same day. Correlation between the two variables was assessed using a two-tailed Spearman's rank correlation allowing the calculation of the correlation coefficient, r_s.

4.3.5 INVESTIGATION OF THE DISTRIBUTION OF SPIPERONE-D2 AND CLOZAPINE-CY5 ABOVE D2R-EXPRESSING CELLS USING THE SAME FOLD-K_D ADDED CONCENTRATIONS

To test our hypothesis that APD rebinding is driven by fast association rates at the D2R, we first investigated the distribution of the fluorescent APDs, spiperone-d2 and clozapine-Cy5, above D2R-expressing cells using an added concentration of 40 nM of both ligands. This concentration was initially chosen based on data from the FCS optimisation measurements described in **Chapter 3.3**. However, the fluorescent APDs differ in their affinity for D2R by ~ 3,000-fold (spiperone-d2 pK_d = 9.00 ± 0.03 (n=3), clozapine-Cy5 pK_d = 5.56 ± 0.06 (n=5); **Table. 4.1**), meaning that the same added concentration of both fluorescent APDs would result in drastically different levels of receptor occupancy. Therefore, to ensure that the differing effects of spiperone-d2 and clozapine-Cy5 treatment we have observed were not driven by differing occupancy levels at D2R, we also investigated the rebinding of both fluorescent APDs at an added concentration of ~ 0.2 x K_d which we expect would result in ~ 17% receptor occupancy. The added concentrations of both fluorescent APDs at this fold-K_d (0.2 nM spiperone-d2 and 600 nM clozapine-Cy5) were on the edge of the dynamic range of FCS for detection of ligand concentration. However, we found both 0.2 nM and 600 nM concentrations of fluorescent ligand to be measurable using our FCS setup as described in **Chapter 3.3**.

Using an added concentration of 0.2 nM spiperone-d2, a clear gradient was seen above high-expressing SNAP-D2R cells (**Fig. 4.10**). Between 9 μm - 12 μm above the glass, the fold changes in spiperone-d2 concentration above high-expressing SNAP-D2R cells compared to measurements in the absence of cells were significantly higher than the fold change at the furthest distance measured (100 μm above the glass) ($P < 0.05$, two-way ANOVA) (**Fig. 4.10**). Most notably, there was a dramatic difference in the fold changes of spiperone-d2 concentration near the upper membrane of high-expressing SNAP-D2R cells compared to measurements in the absence of cells between the added concentrations of 0.2 nM and 40 nM spiperone-d2. The peak fold change for the added concentration of 0.2 nM spiperone-d2 was 139-fold ± 6.09 (n=3) at 9 μm above the glass,

whereas for the added concentration of 40 nM spiperone-d2, the peak fold change was 1.99-fold ± 0.26 (n=6) also at 9 μm above the glass. Furthermore, between 9 μm - 20 μm above the glass, the fold changes seen with an added concentration of 0.2 nM spiperone-d2 were significantly higher than those with an added concentration of 40 nM spiperone-d2 above high-expressing SNAP-D2R cells (with the exception of 19 μm above the glass where no significance was found) ($P < 0.05$, two-way ANOVA). The larger fold change near the upper membrane of high-expressing SNAP-D2R cells seen with a lower added concentration of spiperone-d2 may be due to a lower initial occupancy of receptors which has been shown to enhance rebinding due to the increased availability of free receptors for future binding events[162]. Furthermore, if the greater concentration gradient observed for spiperone-d2 as compared to clozapine-Cy5 when both used at a concentration of 40 nM was simply driven by receptor occupancy, we would have instead expected to see a lower fold change of spiperone-d2 concentration near the upper membrane of high-expressing SNAP-D2R cells for the lower added concentration of 0.2 nM spiperone-d2 in comparison to 40 nM spiperone-d2.

In contrast, a ~ 0.2 x K_d concentration of clozapine-Cy5 (600 nM) did not form concentration gradients above high-expressing SNAP-D2R cells (**Fig. 4.10**). There were no significant differences between the fold change in clozapine-Cy5 concentration above high-expressing SNAP-D2R cells compared to measurements in the absence of cells at every distance measured above the glass compared to the fold change at the furthest measured distance (100 μm above the glass) ($P > 0.05$, two-way ANOVA). Furthermore, between 9 μm – 15 μm above the glass, the fold changes in fluorescent APD concentration above high-expressing SNAP-D2R cells were significantly larger for an added concentration of 0.2 nM spiperone-d2 in comparison to an added concentration of 600 nM clozapine-Cy5 ($P < 0.05$, two-way ANOVA) (**Fig. 4.10**). Here, the peak fold change for an added concentration of 0.2 nM spiperone-d2 was 139-fold ± 6.09 (n=3) at 9 μm above the glass, whereas the fold change for an added concentration of 600 nM clozapine-Cy5 was only 1.48-fold ± 0.04 (n=3) at 9 μm above the glass. In addition, at 9

μm above the glass the fold change for an added concentration of 600 nM clozapine-Cy5 was not significantly different to that for an added concentration of 40 nM clozapine (1.36-fold ± 0.04 (n=3)) (P > 0.05, two-way ANOVA). This suggests that the rebinding effect near the upper membrane of high-expressing SNAP-D2R cells is negligible for clozapine-Cy5 in comparison to spiperone-d2 even at the same level of receptor occupancy.

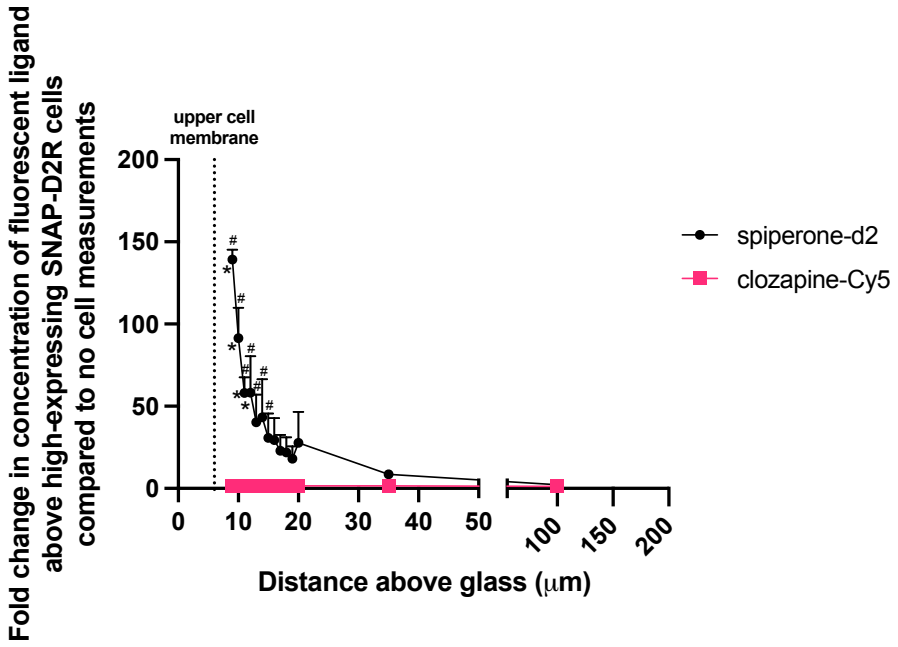

Figure 4.10: The fold change in the concentration of fluorescent APD above high-expressing CHO tetracycline-inducible SNAP-D2R (long isoform) cells compared to no cell measurements in solution across a range of distances (9 μm to 100 μm above glass).

A concentration of ~ 0.2 x K_d of spiperone-d2 (0.2 nM) or clozapine-red (600 nM) was added to high-expressing SNAP-D2R cells and incubated for 2 hours at 37°C before FCS measurements were taken. Resulting autocorrelation curves were fitted to a single 3D component model. Data represent mean ± SEM of 3 independent experiments. The data points indicated with * show statistical significance ($P < 0.05$) of the fold change measured at various distances above the glass compared to the fold change determined at the furthest distance measured (100 μm above the glass) for each fluorescent APD, whilst # denotes statistical significance ($P < 0.05$) between the fold change of spiperone-d2 and clozapine-Cy5 at equivalent distances above the glass (two-way ANOVA, Tukey's multiple comparison test).

4.3.6 INVESTIGATION OF THE CONCENTRATIONS OF SPIPERONE-D2 AND CLOZAPINE-CY5 IN SOLUTION IMMEDIATELY ADJACENT TO CELL-SURFACE SNAP-D2R AND BOUND TO THE CELL MEMBRANE

The positioning of the detection volume at 8 μm above the glass allowed the detection of fluorescent APD concentration in solution near the upper cell membrane (average cell height in this study ~ 6 μm). We also wanted to investigate whether the observed concentrating effects were more pronounced immediately adjacent to the receptor and whether the fluorescent APDs accumulate in the membrane. The FCS detection volume is ~ 1μm in height meaning its positioning on the upper cell membrane, which is ~ 5 nm in height, allows for ~ 0.5 μm of the extracellular environment above the membrane to be included in the detection volume (shown in **Chapter 2.7.3**). Therefore, FCS membrane reads allow for the detection of both the diffusion-limited membrane-bound fluorescent APDs and the fluorescent APDs in solution proximal to cell-surface SNAP-D2R. The fluorescent APDs within these different environments can be differentiated based on their differing diffusion speeds. To accurately simultaneously determine the concentrations of fluorescent APD in solution and bound to the membrane, it was necessary to account for any differences in molecular brightness when in an aqueous or membrane-bound environment due to differences in quantum yield. Differences in quantum yields between individual components of an autocorrelation curve can affect the determination of their concentrations due to their differential contribution to the overall amplitude of the fluorescence intensity trace. Therefore, FCS measurements were taken of both fluorescent APDs in solution as well as bound to the membrane using the same laser power to compare molecular brightness values (described in detail in **Chapter 2.8.5**) (**Fig. 4.11**). Here, the membrane FCS reads were performed following a 4 x volume fluorescent APD wash-off to try to remove as much of the free fluorescent APD in solution as possible. A brightness correction ratio (membrane-bound brightness/ brightness in aqueous solution) was calculated for spiperone-d2 and clozapine-Cy5 of 5.4 and 12.7, respectively (**Fig. 4.11**).

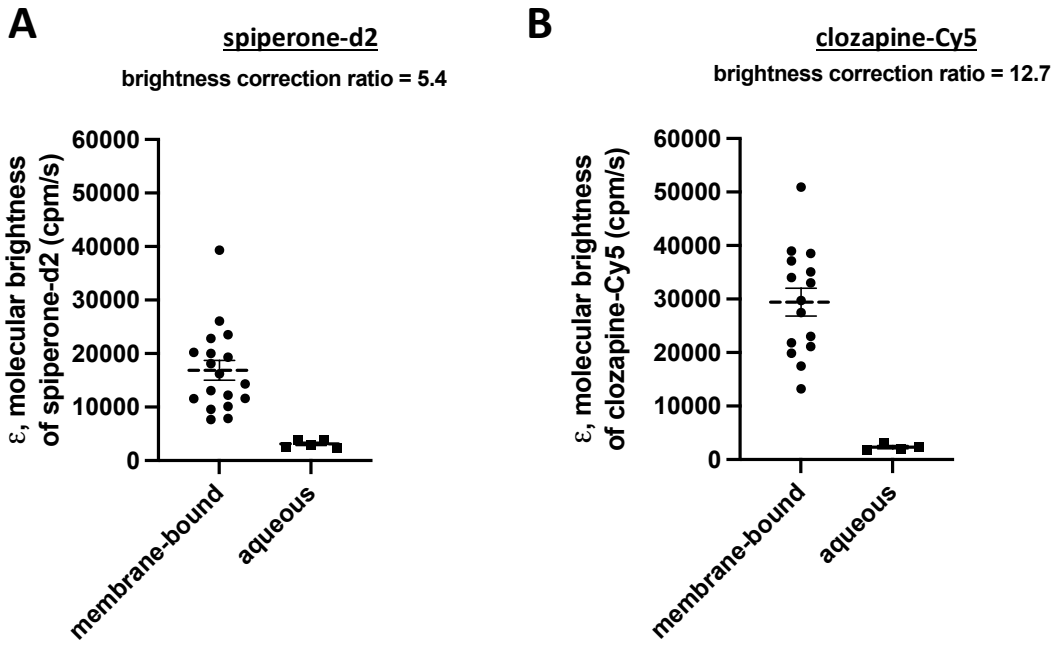

Figure 4.11: The molecular brightness of fluorescent APDs in an aqueous environment or bound to the membrane of CHO tetracycline-inducible SNAP-D2R cells.

Fluorescent APDs, spiperone-d2 (**A**) or clozapine-Cy5 (**B**), were added to either an empty well of an 8-well chambered coverglass for aqueous measurements, or to CHO tetracycline-inducible SNAP-D2R (long isoform) cells induced with 10 ng/ml –100 ng/ml tetracycline for 24 hours prior to experiment for membrane FCS measurements. Resulting fluorescence intensity fluctuation traces were analysed using PCH analysis and histograms were fit with a 1 component model for both membrane-bound and aqueous reads of both fluorescent APDs. An added concentration of 40 nM of both fluorescent APDs was used for aqueous or membrane-bound fluorescent APD measurements. For membrane-bound measurements, cells were first incubated with fluorescent APD for 2 hours followed by a 4 x volume wash-off to remove as much ligand in solution as possible. Aqueous fluorescent APD measurements were taken in solution at 200 μm above the glass in the absence on cells. Data is shown as mean ± SEM (dotted line) taken over 3-5 independent experiments. The brightness correction ratio (membrane-bound brightness / aqueous brightness) is shown for both fluorescent APDs.

With an added concentration of 40 nM, there was a ~ 7-fold increase in the measured concentration of spiperone-d2 in solution immediately adjacent to the upper cell membrane of cells with a high expression of SNAP-D2R, in comparison to the nominally added concentration of 40 nM (**Fig. 4.12A**). In addition, there was a strong correlation between the measured concentration of spiperone-d2 in solution immediately proximal to the membrane and the level of SNAP-D2R expression on the cell surface (two-tailed Pearson's correlation; r^2= 0.76, P < 0.0001) (**Fig. 4.12A**). This correlation was abolished with the 30-minute pre-treatment of 10 μM PBZ followed by the co-addition of 10 μM PBZ and 40 nM spiperone-d2 (two-tailed Pearson's correlation; r^2= 0.01, P = 0.61), demonstrating that the correlation is dependent on SNAP-D2R expression (**Fig. 4.12A**).

Contrastingly, the measured concentration of clozapine-Cy5 in solution immediately proximal to the membrane remained similar to the added concentration of 40 nM of clozapine-Cy5 across cells with a range of cell-surface SNAP-D2R expression (**Fig. 4.12A**). Indeed, there was no significant correlation between the cell-surface SNAP-D2R expression and the measured clozapine-Cy5 concentration in solution proximal to the upper membrane (two-tailed Pearson's correlation; r^2= 0.07, P = 0.29) (**Fig. 4.12A**). This is particularly interesting as further away from the upper membrane in solution at 9 μm, 35 μm and 100 μm above the glass, weak but still significant correlations were seen between the fold change in clozapine-Cy5 concentration above cells compared to measurements in the absence of cells and the level of cell-surface SNAP-D2R expression (**Fig. 4.12B**). The statistical significance of these weak correlations may be due to the ranked correlation test used at 9 μm, 35 μm and 100 μm above the glass due to the non-normal distribution of the data. Clearly, these slightly positive correlations do not affect the local concentration of clozapine-Cy5 immediately adjacent to SNAP-D2R on the cell membrane.

When an added concentration of 0.2 nM spiperone (~ 0.2 x K_d) was used, the measured concentration of spiperone-d2 in solution immediately proximal to the

membrane was ~ 100-fold higher than the nominally added concentration above even low-expressing SNAP-D2R cells (**Fig. 4.12B**). The measured concentration of spiperone-d2 increased to ~ 250-fold higher than the nominally added concentration of 0.2 nM above higher-expressing SNAP-D2R cells (**Fig. 4.12B**). Despite this, for the added concentration of 0.2 nM spiperone-d2, there was no correlation between the measured concentration of spiperone-d2 in solution within the local environment of the membrane and the cell-surface SNAP-D2R expression (two-tailed Spearman's rank correlation; r_s = 0.40, P = 0.071) (**Fig. 4.12B**). This could be a reflection of the rebinding effect reaching a ceiling at low SNAP-D2R expression due to the low initial receptor occupancy at the lower added concentration of 0.2 nM (spiperone-d2 pK_d = 9.00 ± 0.03, n=3; **Table. 4.1**). This low initial SNAP-D2R occupancy at 0.2 nM spiperone-d2 is likely to enhance ligand rebinding as there are a high number of unoccupied receptors available for rebinding spiperone-d2 once it has dissociated from a receptor[162]. In contrast, the higher added spiperone-d2 concentration of 40 nM is likely to result in high initial receptor occupancy at low levels of SNAP-D2R expression resulting in a less pronounced rebinding effect due to fewer unoccupied receptors available for rebinding. Therefore, as our data shows, with higher nominally added concentrations of spiperone-d2, an increase in cell-surface SNAP-D2R expression results in enhanced rebinding effects due to an increase in receptors available for rebinding.

In contrast, when the same fold-K_d concentration of clozapine-Cy5 was added (~ 0.2 x K_d, 600 nM), the measured concentration of clozapine-Cy5 immediately adjacent to the upper membrane was ~ 3-fold lower than the added concentration which highlights the absence of a concentrating effect above SNAP-D2R expressing cells for this fluorescent APD (**Fig. 4.12C**). In addition, there was no correlation between the measured concentration of clozapine-Cy5 within the local environment of the membrane and the SNAP-D2R expression on the cell surface (two-tailed Spearman's rank correlation; r_s= 0.02, P = 0.94) (**Fig. 4.12C**).

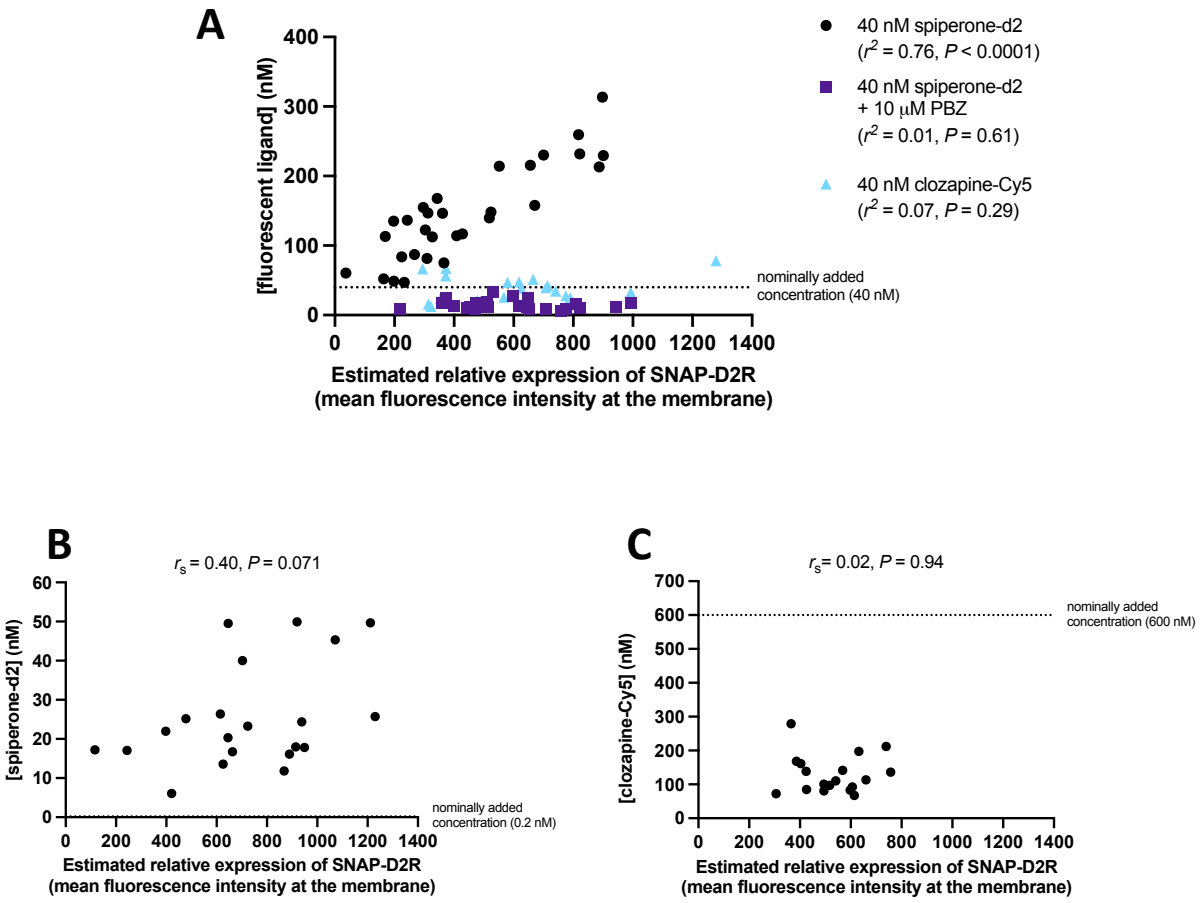

Figure 4.12: Correlation plots illustrating the relationship between the measured concentration of fluorescent APD in solution immediately adjacent to the membrane of CHO tetracycline-inducible SNAP-D2R (long isoform) cells, and the estimated cell-surface SNAP-D2R expression.

Cells were SNAP-labelled with SNAP-Surface® Alexa Fluor® 488 before the addition of 40 nM spiperone-d2 (with and without 10 μM phenoxybenzamine (PBZ) treatment) (**A**), 40 nM clozapine-Cy5 (**A**), 0.2 nM (~ 0.2 x K_d) spiperone-d2 (**B**), or 600 nM (~ 0.2 x K_d) clozapine-Cy5 (**C**). Cells were incubated for 2 hours at 37°C before measurements were taken at the upper membrane. Resulting autocorrelation curves were fit with a 2D and 3D component model. Here, only the concentrations of the 3D component are shown. Data points represent individual cell measurements which were taken over 3-5 independent experiments. Correlation between the two variables were assessed using either a two-tailed Pearson's correlation or a two-tailed Spearman's rank correlation allowing the calculation of the correlation coefficients, r^2 or r_s, respectively, depending on the normality of the data. A correlation of statistical significance was determined when $P < 0.05$ and is shown with a trend line.

As described in **Chapter 2.8.5**, membrane-based FCS reads of fluorescent APD resulted in autocorrelation curves from which the membrane-bound 2D component was distinguished from the freely diffusing 3D component based on its slower dwell time. This allowed the investigation of fluorescent APD accumulation in the membrane of CHO tetracycline-inducible SNAP-D2R cells in terms of the concentration of the 2D component. It should be noted that the membrane-bound 2D component may represent fluorescent APD bound to SNAP-D2R or bound non-specifically to other sites on the lipid bilayer. We found that treatment with either 40 nM or ~ 0.2 x K_d concentrations of both spiperone-d2 and clozapine-Cy5 resulted in low concentrations of membrane-bound fluorescent ligand in comparison to the concentration of free fluorescent ligand in solution immediately adjacent to the membrane (**Fig. 4.13**). Interestingly, only an added concentration of 40 nM of spiperone-d2 showed a significant correlation between its measured concentration bound to the membrane and the cell-surface expression of SNAP-D2R (two-tailed Pearson's correlation; r^2= 0.72, P < 0.0001) (**Fig. 4.13A**). This strong correlation was abolished with the pre-incubation of 10 μM PBZ followed by the co-addition of 10 μM PBZ and 40 nM spiperone-d2 (two-tailed Pearson's correlation; r^2= 0.0002, P = 0.96) (**Fig. 4.13A**). This suggests that the majority of spiperone-d2 (up to ~ 98% of total 2D component at high-expressing SNAP-D2R cells) may be binding to SNAP-D2R within the membrane rather than at non-specific sites on the membrane as spiperone-d2 membrane-binding was displaced by the irreversible antagonist, PBZ. Using an added concentration of 0.2 nM spiperone-d2, there was no significant correlation between its measured concentration bound to the membrane and the cell-surface expression of SNAP-D2R (two-tailed Pearson's correlation; r^2= 0.09, P = 0.18) (**Fig. 4.13B**). For both added concentrations of clozapine-Cy5 (40 nM and 600 nM), no correlation was seen between the measured clozapine-Cy5 concentration bound to the membrane and the cell-surface expression of SNAP-D2R (two-tailed Pearson's correlation; at 40 nM, r^2= 0.005, P = 0.76, **Fig. 4.13A**; at 600 nM, r^2= 0.01, P = 0.66, **Fig. 4.13B**).

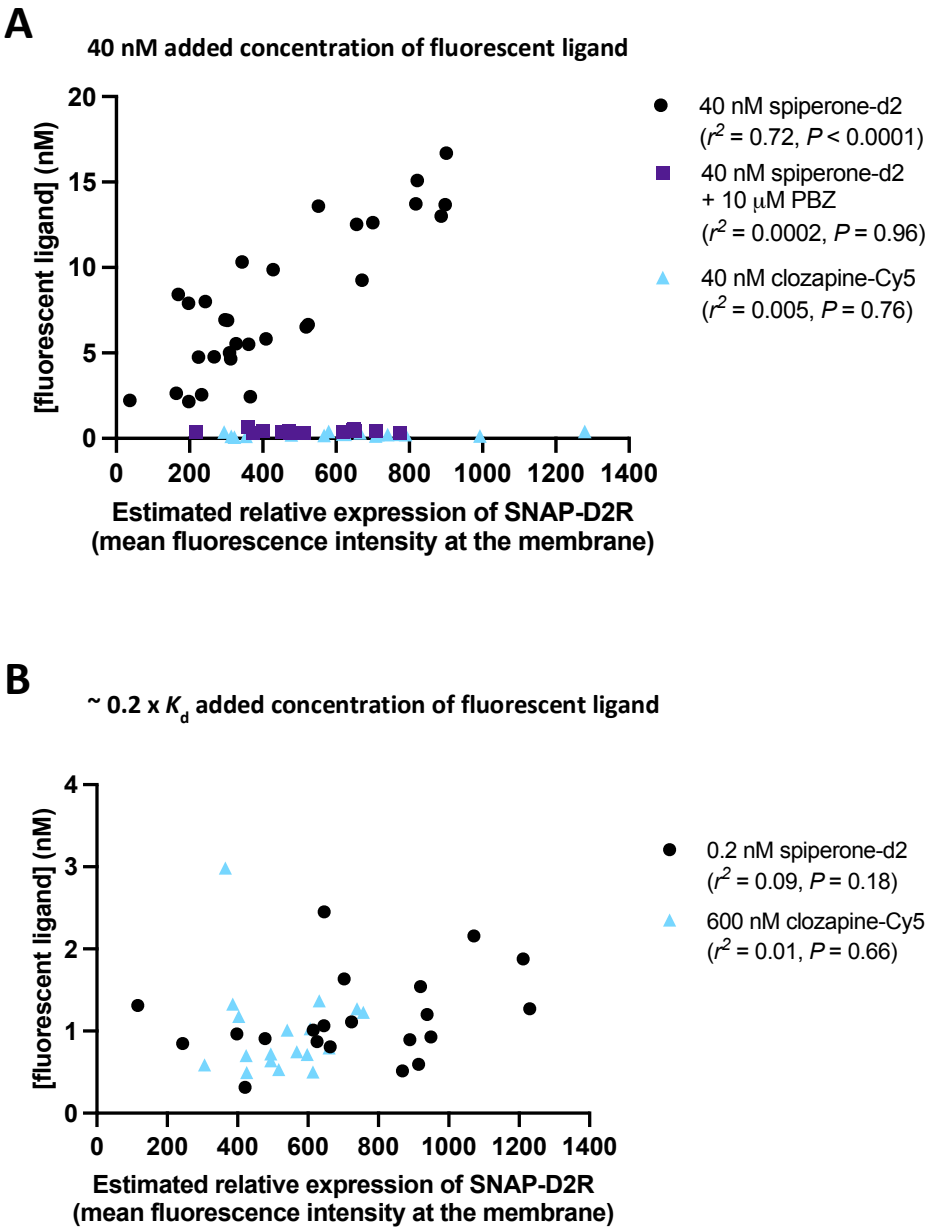

Figure 4.13: The correlation between the measured concentration of fluorescent ligand bound to the membrane of CHO tetracycline-inducible SNAP-D2R (long isoform) cells and the cell-surface expression of SNAP-D2R.

Cells were SNAP-labelled with SNAP-Surface® Alexa Fluor® 488 before the addition of 40 nM spiperone-d2 (with and without 10 μM phenoxybenzamine (PBZ) treatment) (**A**), 40 nM clozapine-Cy5 (**A**), 0.2 nM (~ 0.2 x K_d) spiperone-d2 (**B**), or 600 nM (~ 0.2 x K_d) clozapine-Cy5 (**B**). Cells were then incubated for 2 hours at 37°C before measurements were taken at the upper membrane. Resulting autocorrelation curves were fit with a 2D and 3D component model. Here, only the concentrations of the 2D component are shown. Data points represent individual cell measurements which were taken over 3-5 independent experiments. Correlation between the two variables were assessed using a two-tailed Pearson's correlation allowing the calculation of the correlation coefficient, r^2.

To further explore whether the membrane-bound component of each fluorescent APD represented fluorescent APD bound to SNAP-D2R or non-specifically bound to other sites on the membrane, we compared the diffusion coefficients of membrane-bound spiperone-d2 and clozapine-Cy5 with that of SNAP-labelled SNAP-D2R (derived in **Chapter 3.3**) (**Fig. 4.14**). The diffusion coefficients of both added concentrations of spiperone-d2 (40 nM and 0.2 nM) were not statistically different to the diffusion coefficient of SNAP-D2R ($P > 0.05$, one-way ANOVA) which suggests that spiperone-d2 in the membrane was primarily bound to SNAP-D2R. Treatment with the irreversible D2R antagonist PBZ (a 30-minute pre-incubation of 10 μM PBZ followed by the co-addition of 10 μM PBZ and 40 nM spiperone-d2), would have predominantly blocked spiperone-d2 binding to SNAP-D2R meaning spiperone-d2 bound to the membrane would be at non-specific sites. As expected, treatment with 40 nM spiperone-d2 and 10 μM PBZ showed a significantly faster spiperone-d2 diffusion coefficient in the membrane in comparison to SNAP-D2R ($P < 0.0001$, one-way ANOVA) (**Fig. 4.14**). This faster diffusion coefficient likely represents spiperone-d2 non-specifically bound to the membrane which would diffuse faster in comparison to receptor-bound spiperone-d2 due to its decreased mass. Interestingly, an added concentration of 40 nM clozapine-Cy5 showed a significantly faster diffusion coefficient in comparison to SNAP-D2R ($P < 0.0001$, one-way ANOVA) whereas an added concentration of 600 nM clozapine-Cy5 did not ($P > 0.05$, one-way ANOVA) (**Fig. 4.14**). This suggests that with the lower added concentration of 40 nM, clozapine-Cy5 bound to non-specific sites on the lipid bilayer whereas with the higher added concentration of 600 nM, clozapine-Cy5 showed specific binding to SNAP-D2R potentially due to a saturation of membrane sites. In agreement with this, an added concentration of 600 nM of clozapine-Cy5 showed a significantly higher concentration bound to the membrane in comparison to an added concentration of 40 nM (for 40 nM: 0.25 nM ± 0.03 (n=19 cells), and for 600 nM: 0.99 nM ± 0.14 (n= 18 cells)) ($P < 0.0001$; Student's t-test) (**Fig. 4.13**).

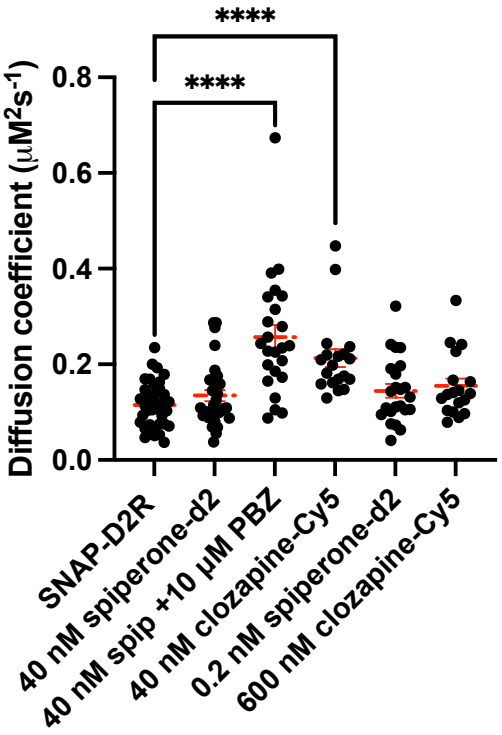

Figure 4.14 The diffusion coefficients of SNAP-D2R and fluorescent ligands in CHO tetracycline-inducible SNAP-D2R (long isoform) cell membranes.

Cells were SNAP-labelled with SNAP-Surface® Alexa Fluor® 488 before the addition of 40 nM spiperone-d2 (with and without 10 μM phenoxybenzamine (PBZ) treatment), 40 nM clozapine-Cy5, 0.2 nM (~ 0.2 x K_d) spiperone-d2, or 600 nM (~ 0.2 x K_d) clozapine-Cy5. Cells were then incubated for 2 hours at 37°C before FCS measurements were taken on the upper membrane. Resulting intensity fluctuation traces were then analysed by autocorrelation analysis to determine the diffusion coefficients of fluorescent ligands. FCS reads of SNAP-D2R were taken in the absence of fluorescent ligand. Autocorrelation curves were fitted to a 3D and 2D component model. Here, the diffusion coefficients of the 2D components are shown. Data points represent individual cell measurements which were taken over 3-5 independent experiments. Data is presented as mean ± SEM (shown in red). A one-way ANOVA with Dunnett's multiple comparison test was used to determine significant differences between the diffusion coefficient of each ligand in comparison to the diffusion coefficient of SNAP-D2R; ****$P < 0.0001$.

In addition, 633 nm fluorescence intensity scans across whole cells were used to investigate the membrane retention of fluorescent APDs. The membrane retention of high added concentrations of 300 nM and 600 nM of spiperone-d2 and clozapine-Cy5, respectively, was shown to be low (**Fig. 4.15**). As a comparison, a fluorescence intensity scan was performed across a high-expressing CHO tetracycline-inducible cell with 40 nM spiperone-d2 treatment where we have previously showed there to be relatively high concentrations of spiperone-d2 in solution immediately adjacent to the membrane (~ 7-fold higher than added concentration of 40 nM). Here, we can identify two peaks on the trace which represent higher concentrations of spiperone-d2 likely bound to the lower and upper cell membrane due to the presence of SNAP-D2R. In comparison, no clear membrane peaks are seen on the intensity scans of spiperone-d2 and clozapine-Cy5 across CHO FlpIn parental cells further suggesting that both fluorescent APDs show similarly low levels of non-specific binding to cell membranes (**Fig. 4.15**). Further evidence of both fluorescent APDs demonstrating low levels of membrane partitioning was seen in confocal images of cells treated with spiperone-d2 and clozapine-Cy5 (**Fig. 4.16**). There was minimal membrane or cytoplasmic retention of spiperone-d2 and clozapine-Cy5 in CHO FlpIn parental cells lacking D2R expression, whereas spiperone-d2 and clozapine-Cy5 were clearly bound to the membrane of SNAP-D2R expressing cells. There was a large overlap between the membrane SNAP-D2R signal and membrane fluorescent APD signal for both spiperone-d2 and clozapine-Cy5 as shown in the merged images, which suggests these ligands were specifically bound to D2R rather than to non-specific sites on the membrane (**Fig. 4.16**).

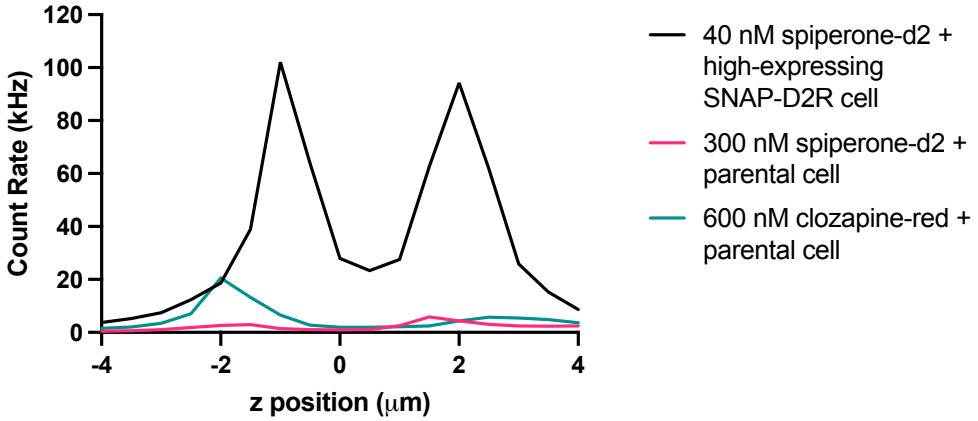

Figure 4.15: Fluorescence intensity z-scans of fluorescent APDs, spiperone-d2 and clozapine-Cy5, across CHO FlpIn parental cells and CHO tetracycline-inducible SNAP-D2R cells.

CHO tetracycline-inducible SNAP-D2R (long isoform) cells were induced with 1000 ng/ml tetracycline for 24 hours prior to the experiment to induce high levels of SNAP-D2R expression. CHO FlpIn parental cells were treated with 300 nM spiperone-d2 or 600 nM clozapine-Cy5 and CHO tetracycline-inducible SNAP-D2R cells were treated with 40 nM spiperone-d2 for 2 hours at 37°C before measurements were taken. The detection volume was placed over the nucleus of a cell in the x-y axis and in the z axis at approximately half of the height of the cell. A fluorescence intensity z-scan using 633 nm excitation was then performed ± 4μm in 0.5 μm intervals to identify the lower and upper membrane peaks. Data represent z-scans of individual cells.

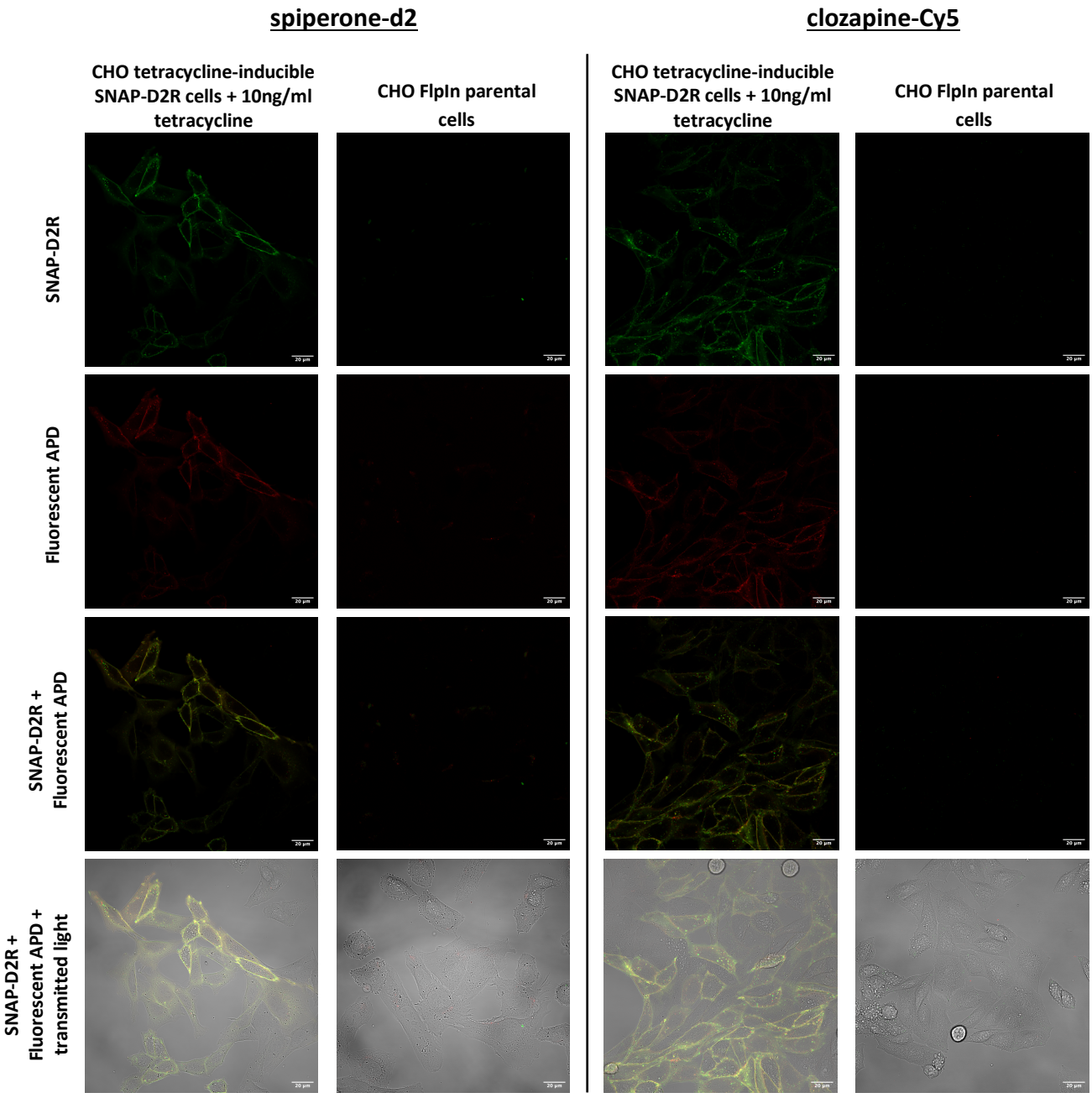

Figure 4.16: Confocal images of cells with or without SNAP-D2R (long isoform) expression treated with fluorescent APDs, spiperone-d2 and clozapine-Cy5.

CHO tetracycline-inducible SNAP-D2R (long isoform) cells were induced with 10 ng/ml tetracycline for 24 hours prior to the experiment. CHO tetracycline-inducible SNAP-D2R cells were labelled with SNAP-Surface® Alexa Fluor® 488 for 30 minutes at 37°C prior to fluorescent APD addition. Both CHO tetracycline-inducible SNAP-D2R cells and CHO FlpIn parental cells were treated with 40 nM spiperone-d2 or 40 nM clozapine-Cy5 for 2 hours at 37°C before confocal images were acquired using sequential scanning with excitation at 488 nm (SNAP-D2R channel) and 633 nm (fluorescent APD channel). Both single channel and merged fluorescence and transmitted light images are shown.

4.4 DISCUSSION

The negligible rebinding of some APDs to D2R, likely due to their slow D2R association rates[145], may be a molecular mechanism that contributes to their atypicality. To experimentally validate this hypothesis, we aimed to use FCS to investigate the distribution in solution of two fluorescent APDs with differing kinetic profiles above D2R-expressing cells. We hypothesised that rebinding would manifest as an APD concentration gradient whereby there is a higher concentration of fluorescent APD near the upper cell membrane of D2R-expressing cells in comparison to the bulk aqueous environment above cells. Interestingly, Gherbi et al. previously showed using FCS that a fluorescent derivative of propranolol formed larger concentration gradients above cells expressing propranolol's target receptor, β2-adrenoceptor, in comparison to cells lacking β2-adrenoceptor expression[209]. Above β2-adrenoceptor-expressing cells (at 2 μm above the membrane), the fluorescent propranolol concentration was up to ~ 25-fold higher than both the added concentration and the concentration measured in the bulk aqueous environment at 200 μm above the cell membrane[209].

Here, we showed that the fluorescent APD with a faster association rate by ~ 300-fold, spiperone-d2, formed concentration gradients that were dependent on the cell-surface expression of D2R (long isoform) whereas clozapine-Cy5 did not. At the same added concentration of fluorescent APD (40 nM), spiperone-d2 showed a significant concentrating effect above high-expressing D2R cells that was up to ~ 1.5 times larger than that seen for clozapine-Cy5. When an added concentration of ~ 0.2 x K_d was used for each fluorescent APD, resulting in similar levels of receptor occupancy, an even larger concentrating effect above high D2R-expressing cells of ~ 95-fold was seen for spiperone-d2 in comparison to clozapine-Cy5. Finally, the largest difference in the concentrating effect shown by these fluorescence APDs was seen immediately adjacent to the upper membrane of D2R-expressing cells (~ 0.5 μm above membrane) where spiperone-d2 concentrations were up to ~ 250-fold higher than the nominally added concentration whereas clozapine-Cy5 concentrations were ~ 3-fold lower than the nominally added

concentration. This suggests that clozapine-Cy5 showed negligible rebinding at D2R in comparison to spiperone-d2.

We first found that both fluorescent APDs were evenly distributed in solution above CHO FlpIn parental cells lacking D2R expression. This contrasts with a previous study that found a fluorescent propranolol derivative to form concentration gradients above CHO cells without expression of propranolol's target receptor, β2-adrenoceptor, whereby the ligand was at a higher concentration near the membrane cells in comparison to the bulk aqueous environment[209]. Interestingly, the diffusion coefficient of clozapine-Cy5 was slower above cells in comparison to measurements in the absence of cells, particularly within the first 50 μm above the glass. This is potentially a reflection of the inherent variability of the Brownian movement of molecules rather than an effect caused by the presence of cells lacking D2R expression, particularly as a similar variation in the diffusion coefficient of another fluorescent drug between above cell measurements and measurements in the absence of cells has also been reported[209].

Spiperone-d2 concentration gradients that were dependent on cell-surface SNAP-D2R expression, were next identified close to the upper membrane (between 8 μm – 14 μm above the glass) of D2R-expressing cells. The local higher concentrations of spiperone-d2 near D2R is indicative of rebinding and is supported by simulations which have found an increase in receptor expression to result in enhanced drug rebinding[162,251]. It is likely that in the minimally diffusion-restricted model system of a monolayer of cells within a solution-filled well used in this study, there was an unstirred layer above the cells that effectively created a diffusion-restricted reservoir which would explain why this rebinding effect near the upper cell membrane was possible. Indeed, unstirred layers of ~ 50 μm thick have been modelled to form above a monolayer of CHO cells through the identification of ligand diffusion delays[252]. Therefore, due to the diffusion-restricted nature of the environment close to cells, fluorescent APDs would be subject to rebinding in a manner dependent on the k_{on} and the number of D2R on the cell surface (rebinding model detailed in **Chapter 1.4.3**)[162].

In addition, receptor expression-dependent concentration gradients of fluorescent ligands near the upper membrane of cells have been previously reported with a fluorescent propranolol derivative at the β2-adrenoceptor[209]. Interestingly, a significant concentrating effect further away from high-expressing SNAP-D2R cells at 30 μm above the glass was seen with an added concentration of 40 nM spiperone-d2. This concentrating effect at 30 μm above the glass was absent when the lower added concentration of 0.2 nM spiperone-d2 was used, despite this lower added concentration resulting in a larger concentration gradient near the upper membrane of high SNAP-D2R expressing cells of up to ~ 70-fold in comparison to 40 nM spiperone-d2. Therefore, this concentrating effect at 30 μm above the glass is independent of the concentration gradient that forms closer to the upper cell membrane of D2R-expressing cells. Instead, it may be due to the variable presence of unstirred solution layers within a well representing a barrier to diffusion and resulting in an uneven concentration gradient from the upper cell membrane to the bulk aqueous environment[253]. Previous observations of unstirred layers in the bulk aqueous phase near a cell monolayer have also been reported[252,254]. The notably larger concentration gradient seen near the cell membrane of high-expressing SNAP-D2R cells with a lower added concentration of spiperone-d2 (0.2 nM compared to 40 nM) is likely due to the inverse relationship between drug rebinding and receptor occupancy levels. It has been shown that drug rebinding is enhanced at lower initial receptor occupancy levels and decreases as receptor occupancy increases[162,251].

Interestingly, in the immediate vicinity of SNAP-D2R receptors, spiperone-d2 showed the largest concentrating effect (up to ~ 250-fold higher concentration compared to the nominally added concentration of 0.2 nM) whereas the concentrating effect for clozapine-red was negligible with the same level of receptor occupancy (up to ~ 3-fold lower concentration compared to the nominally added concentration of 600 nM). This is unlikely to be due to differences in membrane retention as, despite high lipophilicity values of the non-fluorescent versions of the APDs[255,256], both fluorescent APDs at the same level of receptor occupancy showed similarly low concentrations

bound to the membrane in contrast to their measured concentrations in solution adjacent to the membrane. Further evidence that these fluorescent APDs show a lack of membrane partitioning was seen in confocal images which showed both spiperone-d2 and clozapine-Cy5 to demonstrate selective binding to the membrane of SNAP-D2R expressing cells only. This was a surprising finding as lipophilic drugs have been previously shown to integrate into the plasma membrane[257–259]. The hydrophilic nature of several fluorescent tags may prevent the membrane retention of these fluorescent APDs. Overall, it is more likely that the differences in the binding kinetics of these fluorescent APDs, particularly their association rate at D2R, are driving their differing concentrating effects above D2R-expressing cells. Furthermore, the fluorophores of spiperone-d2 and clozapine-Cy5 behave similarly in terms of their photophysics seen in intensity fluctuation traces (shown in **Chapter 3.3**) making it unlikely that differences in the fluorophores or linkers are driving the differences seen in their concentrating effect around SNAP-D2R.

It is important to note that we investigated fluorescent APD rebinding at SNAP-D2R in a simple *in vitro* system consisting of a monolayer of cells in a chambered plate. Here, the 3D diffusion of APDs was significantly less restricted than in the dense neuronal network of the striatum[260]. Drug rebinding phenomena are thought to be enhanced *in vivo*, particularly within a synapse where the pre- and post-synaptic membranes create barriers to drug diffusion into the bulk aqueous phase outside of the synapse[261]. Therefore, drug concentration within the synaptic compartment can remain high even when drug concentrations in the bulk aqueous phase have dropped to insignificant levels[162]. Thus, a high local concentration of drug forms around receptors expressed on synaptic membranes, enhancing drug rebinding[262]. In addition, biophysical models indicate that rebinding in a synapse can be further augmented by non-specific interactions with the postsynaptic membrane[167,263,264]. Rebinding of APDs with fast D2R association rates at D2R may therefore be even more pronounced *in vivo* compared to the significant rebinding effect we have demonstrated *in vitro* in the absence of a synapse.

It has been suggested that a dopaminergic synapse containing D2R may differ from a classical synapse where neurotransmitter release and reuptake are confined within the synapse. Instead, a volumetric dopamine transmission model has been proposed whereby dopamine diffusion dominates over its uptake leading to dopamine spillover beyond the limits of the synapse[265,266]. Striatal concentrations of dopamine of up to 1 μM have been modelled to diffuse up to ~ 2 μm away from the release site[265,267]. This dopaminergic transmission model is based on the predominantly extrasynaptic location of dopamine autoreceptors and DATs on dopaminergic neurones meaning that only dopamine outside the confines of the synaptic cleft can activate autoreceptors or be subject to reuptake [268–272]. However, the volumetric model is not wholly accepted due to studies showing D2R inhibitory post-synaptic currents to be rapidly and readily evoked providing high dopamine concentrations of $\geq$ 10 μM are reached which suggests that D2R autoreceptor activation occurs in a more localised manner than described in the volume transmission model[8,273].

We have demonstrated that in a minimally diffusion-restricted *in vitro* system, the rebinding of APDs with fast D2R association rates to D2R is driven by the level of SNAP-D2R expression on the cell surface, regardless of the level of SNAP-D2R expression on proximal cells. Therefore, even if the dopamine volume transmission model is assumed where the synapse is 'leaky' thereby allowing dopamine to diffuse out of the synaptic cleft, it seems likely that there will be significant APD rebinding *in vivo* providing there are high concentrations of D2R on the synaptic membrane. D2R is organised into dense nanoclusters (~ 10/μm^3) in the nucleus accumbens consisting of ~ 100 receptors per nanocluster[228]. Receptor nanoclusters are thought to be important for synaptic transmission and have been shown to form for several other receptors including NDMA receptors[274,275], dopamine D1 receptors[275], glycine receptors[274,276], GABA receptors[277] and nicotinic acetylcholine receptors[278]. Moreover, receptor clustering has been proposed to enhance rebinding as it is more likely for a dissociated drug to take part in a secondary binding event where there is a high local concentration of receptors[279]. This further supports the probable increased APD rebinding effect within the striatum of

patients in comparison to the already large concentrating effects above D2R-expressing cells seen *in vitro*.

We showed clozapine-Cy5 to have a low rebinding potential at D2R through negligible concentrating effects above D2R-expressing cells, likely driven by its slow association rate at D2R. As clozapine shows the lowest EPS risk out of all clinically used APDs, this finding supports the hypothesis that APDs that demonstrate low D2R rebinding could show better side-effect profiles. In fact, a previous study conducted a structure-kinetic relationship investigation that showed that structural modifications of the typical APD haloperidol resulted in compounds with a clozapine-like kinetic profile[280]. In addition, a recent study identified a highly selective D2R antagonist that showed a similar kinetic profile to clozapine (slow D2R association rate)[281]. This compound, along with clozapine, did not induce catalepsy in rodent models which may be suggestive of a low propensity to cause EPS in humans[281].

The differing rebinding potentials of drugs driven by differing binding kinetics also has wider implications beyond solely drug rebinding *in vivo*. Previous radioligand dissociation experiments identified potential [^{3}H]-spiperone rebinding to D2R through a difference in the decline of specific radioligand binding following radioligand wash out with or without an excess of unlabelled ligand in the wash media[282]. Similar instances of ligand rebinding in radioligand dissociation experiments were seen for antagonists targeting the AT1-type angiotensin II receptor and CB1-cannabinoid receptor[165,283]. This clearly illustrates the influence of the rebinding phenomenon on the *in vitro* measurements of equilibrium binding parameters such as affinity and potency which have driven drug discovery for decades. In *in vitro* assays, we assume the concentration of drug in the immediate vicinity of the receptor is the same as the added drug concentration, however, drug rebinding can cause significantly higher concentrations of drug around the receptor resulting in an overestimation of affinity and potency.

4.5 CONCLUSION

In this chapter, we showed that spiperone-d2 (fast association rate at D2R) forms concentration gradients above D2R (long isoform)-expressing cells that are dependent on D2R expression, whereas clozapine-Cy5 (slow association rate at D2R) does not. This concentrating effect was further enhanced for spiperone-d2 within the local extracellular environment proximal to the upper cell membrane. Here, using added fluorescent APDs concentrations resulting in the same receptor occupancy, spiperone-d2 concentrations were up to ~ 250-fold higher than the nominally added concentration whereas clozapine-Cy5 concentrations were ~ 3-fold lower than the nominally added concentration. These findings were suggestive of negligible clozapine-Cy5 rebinding in comparison to spiperone-d2 and provide evidence that optimizing the association kinetics of APDs at D2R may improve their EPS risks. The rebinding effects of APDs seen *in vitro* may be even more enhanced *in vivo* due to their action at diffusion-limited synapses as well as the high D2R density within these synapses. Furthermore, drug rebinding and the resulting higher drug concentrations near target receptors may influence affinity and potency measurements derived from *in vitro* assays. Drug rebinding therefore has broader implications on drug discovery and optimisation which fundamentally rely on these metrics.

CHAPTER 5: ANTIPSYCHOTIC DRUG-INDUCED TRAFFICKING OF D2R

5.1 INTRODUCTION

Antipsychotic drug (APD) use is associated with 'on-target' side effects termed extrapyramidal symptoms (EPS) which constitute a range of movement disorders. A wide variety of motor phenotypes with varying onsets are seen within the EPS spectrum. More acute onset disorders within EPS can develop within hours to days of starting APD treatment and include: Parkinsonism, characterised by Parkinsonian symptoms including muscle rigidity, tremor and bradykinesia; akathisia, characterised by motor restlessness; and acute dystonia, characterised by involuntary movements that vary from intermittent disturbances to maintained abnormal postures[175]. In contrast, later onset disorders within EPS can develop up to 6 months after starting treatment and include tardive dystonia, which presents similarly to acute dystonia but shows more sustained symptoms, and tardive dyskinesia (TD), the main late onset motor disorder within EPS predominantly characterised by involuntary orofacial movements[175,284]. The majority of the acute onset disorders within EPS can be somewhat alleviated with a reduction in APD dose or with the addition of anticholinergic agents or beta-adrenergic blockers that act to control muscle contractions[175]. Unfortunately, the later onset motor disorders prove more difficult to treat with no controlled studies regarding the treatment of tardive dystonia and no definitive treatment found for TD following the analysis of 45 clinical trials[175,285]. In addition, TD may be irreversible after discontinuation of the causative APD with one study finding only 13% of a cohort of 108 patients with TD showed complete resolution of TD symptoms after APD discontinuation[286]. There is therefore a large unmet clinical need to develop APDs that prevent the development of TD following chronic APD treatment.

The lack of an efficacious treatment for TD is likely due to its poorly understood pathophysiology. The most widely accepted theory behind TD pathogenesis is the dopamine hypersensitivity hypothesis which posits that in response to the chronic dopamine D2 receptor (D2R) blockade induced by APDs, there is an increase in D2R gene transcription and subsequently an increase in D2R at postsynaptic membranes of

medium spiny neurones in the striatum[287,288]. A higher expression of D2R results in dopamine hypersensitivity from an increased overall dopaminergic output causing disinhibition of the globus pallidus internus of the indirect pathway[289]. This weakens the inhibitory GABAergic projections to the thalamus resulting in overstimulation of motor outputs which manifests as a variety of hyperkinetic movements seen in TD[284]. There is direct evidence for this dopamine hypersensitivity theory in rats where chronic haloperidol treatment showed an increase in striatal D2R[290,291] accompanied by spontaneous hyperkinetic behaviours e.g. vacuous chewing movements[292–294]. However, the evidence to support this hypothesis is less clear in humans. It has been shown through PET imaging that chronic treatment of APDs with high D2R affinity in patients with schizophrenia results in a significant increase in striatal D2R binding compared to APD-naïve patients with schizophrenia[174]. Furthermore, in this study patients with the highest degree of D2R upregulation developed severe TD[174]. However, other PET imaging studies did not find an increase in D2R numbers within the striatum of patients with TD compared to patients without symptoms[295,296]. Further support for the dopamine hypersensitivity hypothesis is the common clinical observations in TD patients including the observation that an increased APD dose can temporarily alleviate symptoms of TD and that an abrupt withdrawal of APD can exacerbate TD[297]. In addition, the mechanism of action of recently approved VMAT-2 inhibitors for the treatment of TD is strong evidence in support of the dopamine hypersensitivity hypothesis[298]. VMAT-2 inhibition interferes with the cytosolic uptake and storage of dopamine into synaptic vesicles, increasing the enzyme-induced degradation of dopamine and subsequently decreasing the overall dopamine levels in the synaptic cleft[299]. There is therefore less dopaminergic signalling despite an increased number of striatal D2R in patients with TD, thereby reducing hyperkinetic symptoms. Moreover, this hypersensitivity effect has been well characterised for other receptors including the β2-adrenergic receptor, where hypersensitivity of endogenous ligands to the receptor occurs due to receptor upregulation as a compensatory mechanism for prolonged receptor blockade by beta-blocking agents[300–303]. It should be noted that this hypersensitivity and receptor

upregulation hypothesis does not explain why TD is often irreversible despite discontinuation of the offending APD, as in accordance with this theory, once the blockade of D2R is removed receptor numbers should decrease through receptor downregulation. It is possible that dopamine hypersensitivity may occur concurrently with other mechanisms to explain the pathogenesis of TD such as APD-induced damage to GABAergic neurones within the direct pathway[304].

Through several meta-analyses, it is clear that clozapine demonstrates the lowest EPS risks in comparison to first-generation (FGAs) and second-generation APDs (SGAs)[179,249,305]. In addition, several studies have found a reduction in TD symptoms when patients are switched to clozapine from a different APD[306,307]. It has been proposed that clozapine's superior side effect profile may be due to its low affinity at D2R, however, several other FGAs and SGAs that also have low D2R affinity show higher EPS risks than clozapine e.g. chlorpromazine and quietapine[145,249]. A recent study by Schrader and colleagues proposed a further mechanism behind clozapine's low EPS risk. They found that 'chronic' treatment (24 hours) with a panel of APDs including SGAs and FGAs resulted in the differential translocation of D2R (both D2L and D2S) to the cell surface[178]. They therefore suggested that APDs can act with different efficacies as pharmacological chaperones of D2R by acting as an intracellular scaffold to aid the correct folding of the receptor allowing it to be trafficked out of an intracellular store within the cell and to the cell surface[181].

Several studies examining the subcellular localisation of D2R in various model cell lines (CHO, HEK 293T, NG108-15, HeLa and COS-7) show D2R localisation at the plasma membrane as well as significant intracellular retention[58,227,308,309]. Interestingly, there are conflicting views as to the specific intracellular compartment where D2R is localised with both the ER[308] and the Golgi apparatus[309] being implicated. These studies also both suggest that the long D2R isoform, D2L, which contains a 29 amino acid insert in the third intracellular loop, shows increased intracellular retention within these compartments compared to the short D2S isoform[308–310]. This may be caused by the glycosylation

pattern on D2L that is indicative of poorly transported membrane proteins or possibly by the presence of a tri-arginine ER retention motif within the 29 amino acid insert of D2L[182]. Interestingly, extranuclear retention of D2R has also been seen within striatal neurones[58]. The inefficient trafficking of D2R out of the ER could represent a mechanism for the cell to modulate receptor sensitisation and D2R signal transduction[181].

It may be the case that some APDs show a higher affinity for D2L over D2S therefore explaining their superior D2R chaperoning ability given the intracellular retention of D2L. Nevertheless, both haloperidol and clozapine have a higher affinity for D2L over D2S[311] despite being shown to have a high and low efficacy for causing the upregulation of D2R at the cell surface, respectively[178]. Furthermore, several other GPCRs including the dopamine D4 receptor which is in the dopamine D2-like receptor family, have been shown to be rescued from the ER by pharmacological chaperones[181,312]. Of all APDs investigated by Schrader and colleagues, clozapine showed the lowest translocation of both D2L and D2S to the cell membrane which suggests its superior side effect profile may be caused by its low efficacy as a D2R chaperone[178]. As TD is associated with D2R upregulation, clozapine's low chaperoning ability of D2R may also explain why it is the only APD that has shown efficacy in treating TD[179,307].

Here, we have used a bystander BRET-based D2R trafficking assay to investigate the APD-induced trafficking of D2R (long isoform)-Nluc to various cellular compartments using Venus-tagged cell compartment markers: Venus-KRas (plasma membrane), Venus-Rab 5 (early endosome), Venus-Rab 11 (recycling endosome), Venus-Rab 7 (lysosome), Venus-Giantin (Golgi apparatus) and Venus-PTP1B (ER). We expect D2R-Nluc to primarily follow the classical GPCR trafficking model as described in **Chapter 1.3.3**. Briefly, classic GPCR trafficking is characterised by agonist-induced receptor activation promoting GRK- and β-arrestin-mediated internalisation into early endosomes. GPCRs can then be recycled back to the cell surface, promoting receptor resensitisation, or in the prolonged presence of agonist, the receptor is trafficked to late endosomes which combine with lysosomes resulting in receptor degradation and down-regulation[64]. The anterograde

transport of GPCRs begins in the ER where receptors are synthesized and folded before trafficking to Golgi apparatus where they may undergo post-translational modifications to attain a fully mature status before transport to the plasma membrane[313]. Using this D2R trafficking assay, we have investigated APDs with differing EPS risks to determine if differences in APD-induced D2R trafficking or chaperoning to the cell membrane can explain their varied side effect profiles, in particular with respect to the development of TD which has been associated with upregulation at the cell membrane[284]. As a complimentary technique, we also used confocal imaging to investigate the APD-induced changes in SNAP-D2R localisation within cells, primarily at the cell membrane.

5.2 CHAPTER 5 AIMS

The work described in Chapter 5 aimed to:

a) Validate a bystander BRET-based D2R trafficking assay to investigate the trafficking of D2R to the plasma membrane and other cellular compartments following chronic APD treatment;
b) Reveal differences in APD-induced D2R trafficking within the cell that could outline a potential mechanism for their varying EPS risks, in particular with respect to the development of TD;
c) Investigate the reversibility of APD-induced chaperoning of D2R to the plasma membrane following APD wash off to further investigate the pathophysiology of TD and its low reversibility rates.

5.3 RESULTS

5.3.1 VALIDATION OF D2R TRAFFICKING ASSAY USING REFERENCE AGONISTS

Previously in our group, the agonist-induced trafficking of D2R (long isoform) was investigated using only the plasma membrane and endosomal Venus-tagged markers (personal communication, A Keen). In these experiments, 0.25 μg of the donor, D2R-Nluc, was transfected along with 1 μg Venus-tagged compartment marker, 2 μg GRK2 and 4 μg β-arrestin2. Using the same DNA transfection ratio and the Venus-KRas plasma membrane marker, HEK 293T cells were transfected and treated with ropinirole for 24 hours. This resulted in a similar BRET response to that previously generated in our group (**Fig. 5.1**). Here, the ropinirole-induced decrease in the net BRET ratio (baseline-corrected to vehicle (DMSO)) represents a decrease in the proximity between D2R-Nluc and Venus-KRas which is indicative of agonist-induced internalisation resulting in less D2R-Nluc at the plasma membrane. It is well characterised that a low expression of the BRET donor in comparison to the acceptor is required to achieve high signal-to-noise ratios[314]. Therefore, to increase the assay window, a 10-fold decrease in BRET donor DNA, D2R-Nluc, was transfected (0.025 μg) which indeed showed a significant increase in the BRET signal of approximately 2-fold following treatment with ropinirole ($P < 0.0001$, unpaired t-test) (**Fig. 5.1**). As described in **Chapter 2.5.2**, 0.025 μg D2R-Nluc was then used in subsequent D2R trafficking experiments based on this increased BRET window for GRK2 and β-arrestin2 overexpression data.

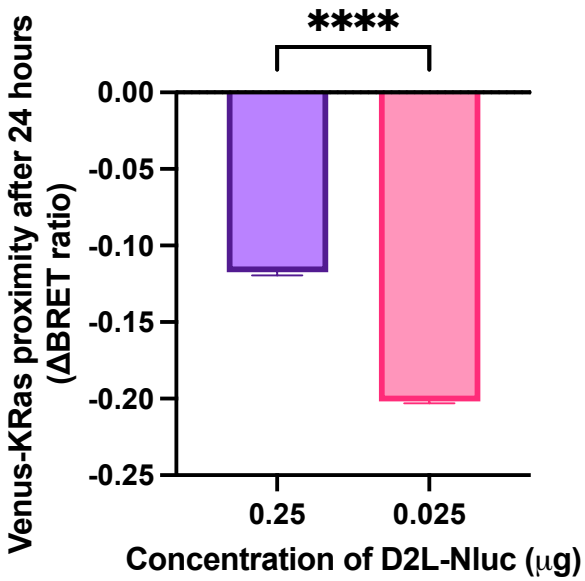

Figure 5.1: BRET window optimization of the D2R trafficking assay using the BRET donor, D2R-Nluc, and acceptor, Venus-KRas (plasma membrane marker).

HEK 293T cells were transfected with 0.25 µg or 0.025 µg D2R (long isoform)-Nluc, 1 µg Venus-KRas, 2 µg GRK2 and 4 µg β-arrestin2 and treated with 10 µM ropinirole for 24 hours prior to measurement. The ropinirole-induced BRET signal was corrected to the mean vehicle (DMSO) to give net BRET ratios. Pooled data (mean ± SEM) represent 3 individual experiments conducted in quadruplicate. Unpaired t-test was used to determine statistical significance between the different donor DNA amounts transfected; **** $P < 0.0001$.

The reference agonists ropinirole and dopamine were used to validate the bystander BRET-based assay as a tool to monitor D2R trafficking through various cell compartments following drug treatment. Ropinirole and dopamine have comparable affinity at D2R with pK_d values of 5.18 and 5.73, respectively[315]. However, ropinirole and dopamine have differing lipophilicities with clogP values (the calculated logarithmic values of their octanol-water partition coefficient using ChemDraw 20.1) of 2.80 and 0.17, respectively, and predicted Caco-2 permeabilities ($logP_{app}$ (cm/s); a measure of the permeability across Caco-2 cell monolayers as a prediction of *in vivo* absorption) of -4.57[316] and -5.03[317], respectively. D2R trafficking following 24 hours of ropinirole or dopamine treatment was first investigated at the plasma membrane using the Venus-KRas marker under endogenous levels of GRK2 and β-arrestin2 expression (in black; **Fig. 5.2**). Surprisingly, both ropinirole and dopamine showed a significant increase in D2R-Nluc translocation to the cell surface with respect to vehicle ($P < 0.0001$ and $P < 0.01$, respectively; unpaired t-test) rather than causing agonist-induced internalisation (shown as a decrease in the net BRET ratio). Overexpressing GRK2 and β-arrestin2 caused both agonists to show significant D2R-Nluc internalisation whereas overexpressing a dominant-negative kinase 'dead' mutant of GRK2, GRK2 K220R, and β-arrestin2 inhibits most of this internalisation (**Fig. 5.2**). Statistically significant differences were seen for each agonist between each of the three GRK2/GRK2 K220R and β-arrestin2 expression conditions ($P < 0.0001$, two-way ANOVA). In addition, for each GRK2/GRK2 K220R and β-arrestin2 expression condition, significant differences were seen between the two agonists for inducing D2R-Nluc trafficking towards or away from the cell membrane ($P < 0.0001$, two-way ANOVA) with dopamine inducing the greatest agonist-induced internalisation when GRK2 and β-arrestin2 is overexpressed (**Fig. 5.2**). Both agonists showed a similar overall pattern of D2R trafficking where the largest change in BRET over baseline was seen with overexpressed levels of GRK2 and β-arrestin2, followed by overexpressed levels of GRK2 K220R and β-arrestin2, and lastly endogenous levels of GRK2 and β-arrestin2.

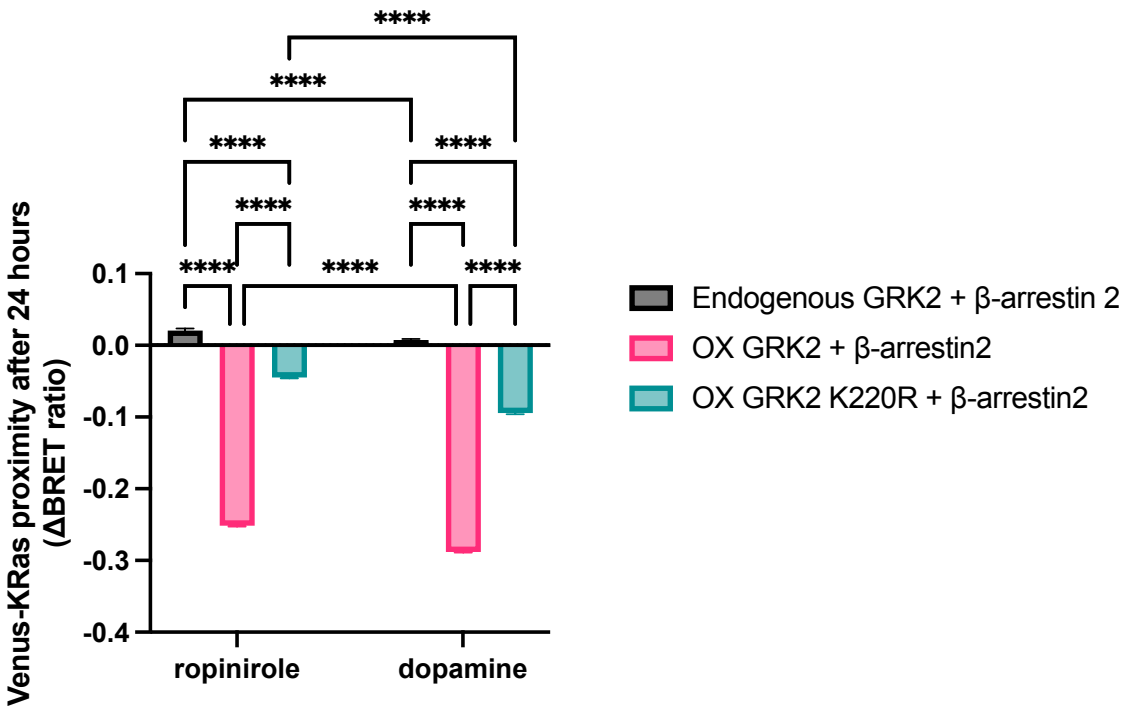

Figure 5.2: Trafficking of D2R (long isoform)-Nluc to the plasma membrane marker, Venus-KRas, in response to agonists with endogenous and overexpressed (OX) levels of GRK2/GRK2 K220R and β-arrestin2.

The agonist-induced change in BRET from baseline (DMSO) was measured following treatment with 10 µM ropinirole or dopamine for 24 hours. Pooled data (mean ± SEM) represent 3 individual experiments conducted with 14 replicates. Two-way ANOVA with Tukey's multiple comparison test was performed showing significant differences between the ligands as well as the GRK2/GRK2 K220R and β-arrestin2 expression conditions; ****$P < 0.0001$.

We next explored the agonist-induced D2R trafficking throughout the cell using further Venus-tagged cell compartment markers to validate the D2R trafficking assay through comparison to the current dogma on anterograde and retrograde cell-surface receptor trafficking within a cell. Following agonist-induced internalisation, receptors are initially sequestered into early endosomes and sorted to either the cell surface, via recycling endosomes, or to lysosomes, for degradation[318]. Twenty-four-hour treatment with both ropinirole and dopamine caused an increase in D2R-Nluc localisation at Venus-Rab5 positive early endosomes indicating agonist-induced endocytosis of D2R-Nluc (**Fig. 5.3A**). Dopamine treatment induced a significantly increased localisation of D2R-Nluc at Venus-Rab5 positive early endosomes at both GRK2 or GRK2 K220R and β-arrestin2 overexpression conditions in comparison to ropinirole treatment ($P < 0.0001$, two-way ANOVA) (**Fig. 5.3A**). This finding aligns with plasma membrane data where dopamine induced greater D2R-Nluc internalisation in comparison to ropinirole at these expression conditions. Both agonists also showed an increase in D2R-Nluc localisation at Venus-Rab11 positive recycling endosomes, indicative of agonist-induced receptor recycling and resensitisation at the plasma membrane (**Fig. 5.3B**). Dopamine treatment showed increased D2R-Nluc recycling in comparison to ropinirole ($P < 0.0001$ for all GRK2/GRK2 K220R and β-arrestin2 expression conditions, two-way ANOVA). The overall increase in the net BRET ratio following agonist treatment seen at these compartment markers aligned with the effect seen at the plasma membrane marker (**Fig. 5.2**): D2R-Nluc moved away from the plasma membrane following agonist-induced internalisation and entered the endosomal pathway. The effect on D2R-Nluc localisation at these endosomal compartments was also dependent on GRK2 and β-arrestin2 expression, following the same pattern seen at the plasma membrane whereby overexpression of GRK2 and β-arrestin2 enhanced agonist driven changes in BRET whereas overexpression of GRK2 K220R and β-arrestin2 causes a partial enhancement. For each ligand, there was a significant difference between each GRK2/GRK2 K220R and β-arrestin2 expression condition at each of these endosomal compartments ($P < 0.0001$, two-way ANOVA, not shown on **Fig. 5.3** for clarity). There was also an increase in D2R-Nluc localisation at

Venus-Rab7 positive lysosomes following ropinirole and dopamine treatment (other than under endogenous GRK2 and β-arrestin2 expression levels) which was expected following chronic agonist treatment (**Fig. 5.3C**). No statistically significant differences were found between ropinirole and dopamine treatment at each GRK2/GRK2 K220R and β-arrestin2 expression condition ($P > 0.05$, two-way ANOVA) (**Fig. 5.3C**).

Agonist treatment also affected D2R-Nluc localisation at the level of the ER and Golgi apparatus. Treatment with both agonists caused a decrease in D2R-Nluc localisation at the ER (**Fig. 5.3D**) and an overall increase in D2R-Nluc localisation at the Golgi apparatus (**Fig. 5.3E**). Ropinirole treatment induced a greater D2R-Nluc loss from the ER than dopamine ($P < 0.05$ for endogenous levels of GRK2 and β-arrestin2, $P < 0.0001$ for overexpressed levels of GRK2/GRK2 K220R and β-arrestin2; two-way ANOVA), which was also reflected at the Golgi apparatus ($P < 0.0001$ for all expression conditions, two-way ANOVA). At the ER, the effect on agonist-induced D2R-Nluc localisation was dependent on GRK2/GRK2 K220R and β-arrestin2 expression with significant differences seen between each GRK2/GRK2 K220R and β-arrestin2 expression condition for each ligand ($P < 0.0001$, two-way ANOVA, not shown on **Fig. 5.3** for clarity). At the Golgi apparatus, agonist-induced D2R-Nluc localisation was largely dependent on GRK2/GRK2 K220R and β-arrestin2 expression with significant differences seen between: endogenous and overexpressed GRK2 and β-arrestin2 levels ($P < 0.0001$ for ropinirole and $P < 0.001$ for dopamine; two-way ANOVA), endogenous and overexpressed GRK2 K220R and β-arrestin2 levels for ropinirole only ($P < 0.0001$; two-way ANOVA), and the two overexpression groups (GRK2 and β-arrestin2, and GRK2 K220R and β-arrestin2) ($P < 0.01$ for ropinirole and $P < 0.05$ for dopamine; two-way ANOVA) (not shown on **Fig. 5.3** for clarity).

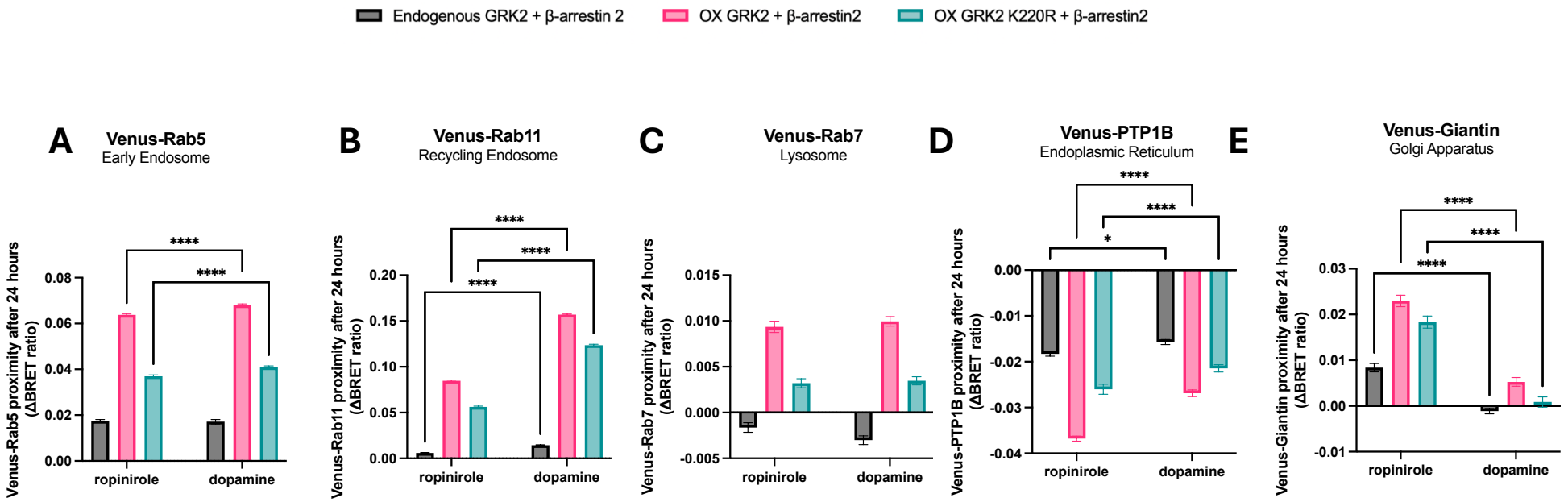

Figure 5.3: Trafficking of D2R-Nluc to various Venus-tagged compartment markers in response to agonists under endogenous and overexpressed (OX) levels of GRK2/GRK2 K220R and β-arrestin2.

Cells were treated with 10 μM ropinirole or dopamine for 24 hours before D2R (long isoform)-Nluc trafficking towards or away from (**A**) Venus-Rab5 positive early endosomes, (**B**) Venus-Rab11 positive recycling endosomes, (**C**) Venus-Rab7 positive lysosomes, (**D**) Venus-PTP1B positive endoplasmic reticulum and (**E**) Venus-Giantin positive Golgi apparatus was measured. The net BRET response was calculated by subtracting the mean vehicle (DMSO)-induced BRET signal from the agonist-induced BRET signal for each compartment marker. All data represent mean ± SEM from 3 separate experiments conducted with 14 replicates. Two-way ANOVA with Tukey's multiple comparison test was performed with significant differences between the ligands at each GRK2/GRK2 K220R and β-arrestin2 expression condition shown; **P* < 0.05, *****P* < 0.0001.

5.3.2 ANTIPSYCHOTIC DRUG-INDUCED D2R TRAFFICKING

The antipsychotic drugs (APDs) haloperidol, sulpiride and clozapine, were selected to investigate APD-induced changes in D2R-Nluc trafficking as they have previously shown a large, moderate and small efficacy, respectively, for causing D2R upregulation to the plasma membrane using a cell surface biotinylation assay[178]. Not only have these APDs been shown to have a range of efficacies for chaperoning D2R to the cell surface, but they also have varied EPS risks and lipophilicities (**Table 5.1**).

Table 5.1: Classification of antipsychotic drugs used in the BRET D2R trafficking assay.

Antipsychotic drug (APD) action, based on EPS odds ratios from a meta-analysis[249] are shown as well as their lipophilicities, shown as cLogP values (calculated using ChemDraw 20.1) and Caco-2 values (referenced). *APD has been shown as both atypical[249] and typical[319] in separate studies.

APD	Ligand Action	cLogP	Caco-2 ($logP_{app}$)
Haloperidol	Typical	3.77	-4.72[320]
Sulpiride*	Typical/Atypical	-0.0695	-6.16[321]
Clozapine	Atypical	3.36	-4.55[256]

Initially, 10 μM of each APD was used to investigate D2R-Nluc trafficking at the various Venus-tagged cell compartment markers under endogenous levels of GRK2 and β-arrestin2 expression. At Venus-KRas positive plasma membrane, all APDs induced a significant increase in D2R-Nluc localisation in comparison to vehicle (DMSO) ($P < 0.0001$, one-way ANOVA) (**Fig. 5.4A**). Haloperidol treatment showed the largest increase in D2R-Nluc localisation at the plasma membrane, followed by sulpiride and lastly clozapine with significant differences seen between all three APDs ($P < 0.0001$, one-way ANOVA) (**Fig. 5.4A**). This suggests that haloperidol has a greater efficacy in comparison to sulpiride and clozapine for acting as D2R pharmacological chaperone by binding to an intracellular pool of D2R and promoting the trafficking of D2R to the plasma membrane.

In the endosomal pathway (early endosomes (**Fig. 5.4B**) and recycling endosomes (**Fig. 5.4C**)), APD treatment caused an increase in D2R-Nluc localisation in comparison to vehicle (DMSO) treatment despite their action as antagonists ($P < 0.0001$, one-way ANOVA). At both endosomal compartments, haloperidol induced a significantly larger D2R-Nluc localisation in comparison to sulpiride ($P < 0.0001$; one-way ANOVA) whereas no significant difference was found in the APD-induced D2R-Nluc localisation between haloperidol and clozapine treatment ($P > 0.05$; one-way ANOVA). At Venus-Rab11 positive recycling endosomes (**Fig. 5.4C**), clozapine showed a larger D2R-Nluc translocation in comparison to sulpiride ($P < 0.0001$, one-way ANOVA). Interestingly, despite all APDs causing an increase in D2R-Nluc translocation to endosomal compartments, only haloperidol and sulpiride showed an increase in D2R-Nluc translocation to the lysosome in comparison to vehicle ($P < 0.0001$ for haloperidol and $P < 0.05$ for sulpiride, one-way ANOVA) (**Fig. 5.4D**). At the lysosome, haloperidol treatment showed the largest increase in D2R-Nluc localisation in comparison to sulpiride treatment ($P < 0.05$, one-way ANOVA) and to clozapine treatment ($P < 0.01$, one-way ANOVA) (**Fig. 5.4D**).

The ER is known to be an intracellular store of misfolded proteins, and therefore could be the cellular compartment from where APDs, particularly haloperidol and

sulpiride, are trafficking D2R-Nluc to the plasma membrane. Both haloperidol and sulpiride treatment caused a loss of D2R-Nluc from the ER in comparison to vehicle (DMSO) treatment demonstrating their action as pharmacological chaperones for D2R ($P < 0.0001$, one-way ANOVA) (**Fig. 5.4E**). Interestingly, sulpiride induced a significantly larger loss of D2R-Nluc from the ER in comparison to haloperidol ($P < 0.0001$, one-way ANOVA), despite sulpiride showing a reduced D2R-Nluc translocation to the plasma membrane in comparison to haloperidol. In contrast, clozapine treatment caused a significant increase in the localisation of D2R-Nluc at the ER in comparison to vehicle (DMSO) treatment ($P < 0.001$, one-way ANOVA) demonstrating its low efficacy as a D2R chaperone.

After cell surface proteins are successfully synthesized and folded in the ER, they are trafficked through the Golgi apparatus where they may undergo post-translational modifications before reaching the plasma membrane[322]. To further investigate the discrepancy between the rank order of APD efficacies for inducing D2R-Nluc upregulation at the plasma membrane and loss at the ER, D2R-Nluc trafficking was investigated at the Golgi apparatus (**Fig. 5.4F**). Here, haloperidol caused the largest increase in D2R-Nluc localisation in comparison to sulpiride and clozapine ($P < 0.0001$, one-way ANOVA) which aligned with plasma membrane data. Interestingly, clozapine showed a significantly larger increase in D2R-Nluc localisation at Venus-Giantin positive Golgi apparatus in comparison to sulpiride ($P < 0.001$, one-way ANOVA; **Fig. 5.4F**), despite clozapine treatment showing reduced D2R-Nluc translocation to the plasma membrane in comparison to sulpiride.

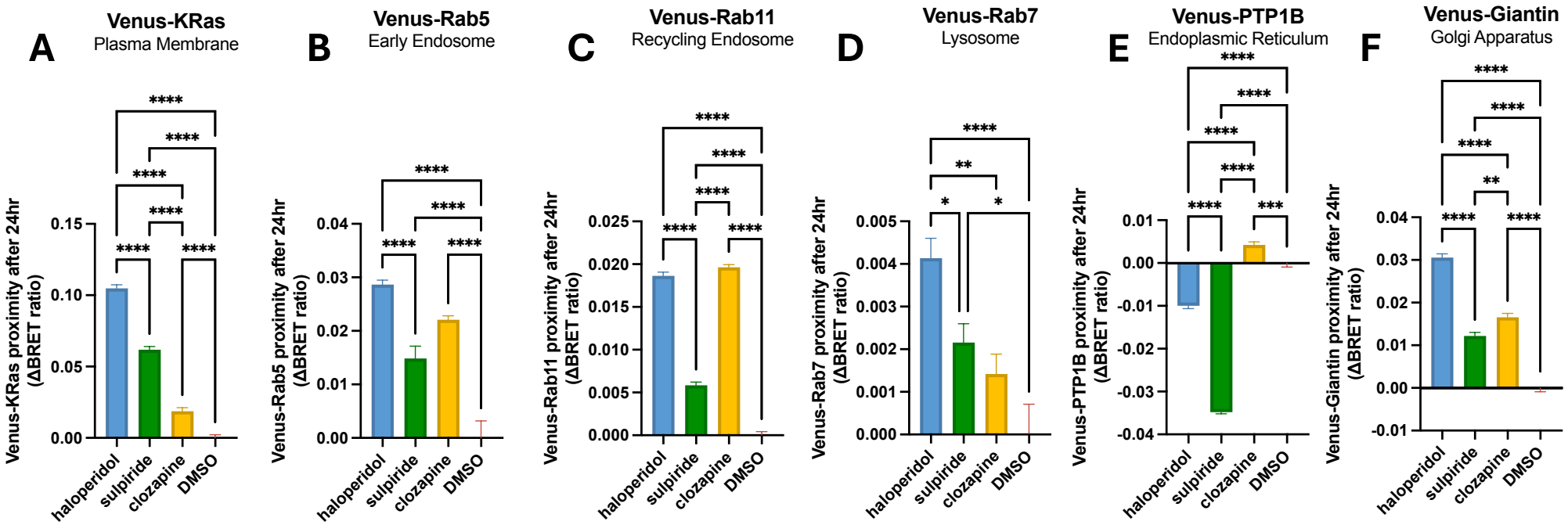

Figure 5.4: Trafficking of D2R-Nluc to various Venus-tagged compartment markers in response to antipsychotic drugs (APDs) under endogenous levels of GRK2 and β-arrestin2 expression.

HEK 293T cells were treated with 10 µM APD or vehicle (DMSO) for 24 hours before the D2R (long isoform)-Nluc trafficking towards or away from (**A**) Venus-KRas positive plasma membrane, (**B**) Venus-Rab5 positive early endosomes, (**C**) Venus-Rab11 positive recycling endosomes and (**D**) Venus-Rab7 positive lysosomes, (**E**) Venus-PTP1B positive endoplasmic reticulum and (**F**) Venus-Giantin positive Golgi Apparatus was measured. The APD-induced BRET signal was corrected to the mean vehicle (DMSO) response at each compartment marker. All data represent mean ± SEM from 3 separate experiments conducted with 14 replicates. Significant differences between ligands at each compartment were analysed using one-way ANOVA with Tukey's multiple comparison test; **P* < 0.05, ***P* < 0.01, ****P* < 0.001, *****P* < 0.0001.

As receptors are predominantly chaperoned out of the ER to the plasma membrane[181], the Venus-KRas (plasma membrane marker) and Venus-PTP1B (ER marker) were used to further explore the concentration-dependent chaperoning of D2R-Nluc by APDs under endogenous levels of GRK2 and β-arrestin2 expression. Concentration response curves were first produced to investigate D2R-Nluc trafficking to Venus-KRas positive plasma membrane following 24 hours of APD treatment (**Fig 5.5A**). Particularly for haloperidol and sulpiride, the curves seemed to be biphasic although a monophasic non-linear regression fit was preferred and shown on **Figure 5.5A**. For all three APDs, 10 μM was a saturating concentration which suggests that the differences in APD-induced D2R-Nluc localisation at the plasma membrane seen using a single APD concentration (10 μM) was not a result of differing receptor occupancy driven by their different D2R affinities (pK_d: haloperidol, 9.49; sulpiride, 7.87; clozapine, 7.69)[145]. The rank order of maximal responses (corrected to the mean vehicle (DMSO)-induced response) was: haloperidol > sulpiride > clozapine (**Table 5.2**, including statistical analysis) which aligned with single concentration data (10 μM) at Venus-KRas positive plasma membrane. In contrast, there were no significant differences in the potencies between any of the three APDS for causing D2R-Nluc translocation to the plasma membrane ($P > 0.05$, one-way ANOVA) (**Table 5.2**), despite differences in their affinities for D2R. There was therefore a disconnect between the affinity of APDs for D2R and their potency for chaperoning D2R to the cell surface. This was particularly the case for haloperidol which showed ~ 40-fold higher affinity compared to its potency. Interestingly, clozapine showed ~ 30-fold higher potency than affinity. However, clozapine's potency for chaperoning D2R-Nluc to the plasma membrane should be viewed with uncertainty as at high concentrations of clozapine, there was a negligible response in comparison to vehicle. It is likely that the lower response in comparison to vehicle seen with low added concentrations of clozapine, was driving clozapine data to be fitted by the non-linear regression model (**Fig 5.5A**).

Concentration response curves showing APD-induced translocation out of the ER also seemed to fit poorly to a monophasic non-linear regression model (**Fig 5.5B**). Instead, these curves appeared to be bell-shaped where at 10 μM, there was a reversal of the APD-induced loss of D2R-Nluc from the ER seen for haloperidol and clozapine and to a lesser extent for sulpiride (**Fig 5.5B**, highlighted by a box). The bell-shaped curves could not be properly defined as the reversal in APD-induced D2R-Nluc loss from the ER was only seen at a single concentration (10 μM). Therefore, curves were fitted to a monophasic non-linear regression model with the 10 μM data point excluded. The rank order of maximal responses corrected to vehicle (DMSO) was: sulpiride > haloperidol > clozapine (**Table 5.2**, including statistical analysis). This rank order also aligned with ER data using a single APD concentration (10 μM), however, did not reflect the rank order of efficacies at the plasma membrane. The rank order of potencies at the ER also significantly varied: haloperidol > sulpiride > clozapine (**Table 5.2**, including statistical analysis). Interestingly, the potencies of APDs for causing D2R-Nluc translocation from the ER more closely matched the affinities of the APDs for D2R (pK_d: haloperidol, 9.49; sulpiride, 7.87; clozapine, 7.69)[145] in comparison to the potencies at the plasma membrane. Overall, haloperidol and sulpride showed an enhanced D2R chaperoning activity in comparison to clozapine by inducing a D2R-Nluc loss at the ER and an increase at the plasma membrane whereas clozapine had a negligible effect on D2R-Nluc localisation at the plasma membrane.

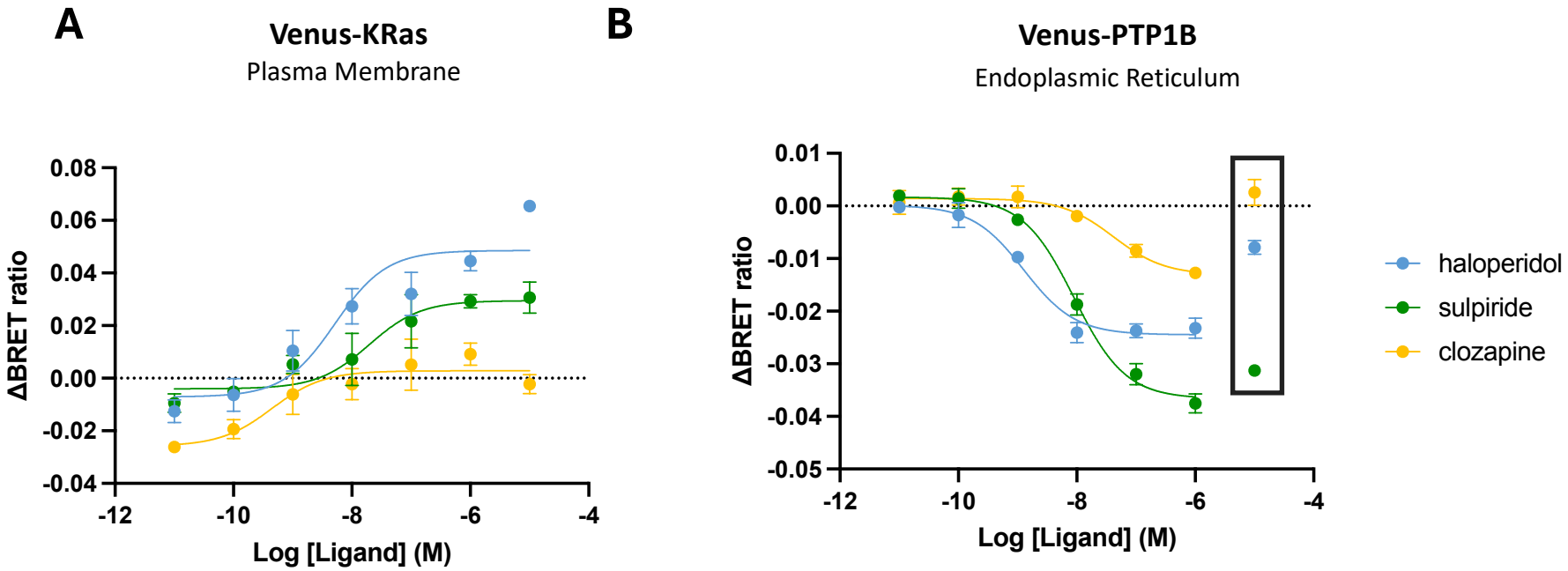

Figure 5.5: Concentration response curves showing D2R-Nluc trafficking at the plasma membrane and endoplasmic reticulum, following 24hr of antipsychotic drug treatment.

Bystander BRET was measured between D2R (long isoform)-Nluc and Venus-KRas positive plasma membrane (**A**) or Venus-PTP1B positive endoplasmic reticulum (**B**) in the presence of endogenous levels of GRK2 and β-arrestin2. Data are pooled (mean ± SEM) from 3-4 independent experiments conducted in quadruplicate. Data is presented as net BRET ratios corrected to the mean vehicle (DMSO) response at each concentration for each compartment marker. At Venus-PTP1B positive endoplasmic reticulum (**B**), data at 10 μM (highlighted in black box) did not fit the monophasic curve of the non-linear regression model so were therefore excluded from the fit.

Table 5.2: Potency and maximal effect estimates of D2R-Nluc trafficking at the plasma membrane and endoplasmic reticulum, following 24hr of antipsychotic drug treatment.

Bystander BRET was measured between D2R (long isoform)-Nluc and Venus-KRas (plasma membrane marker) or Venus-PTP1B (endoplasmic reticulum (ER) marker) in the presence of endogenous levels of GRK2 and β-arrestin2. Pooled pEC_{50} (potency) values and R_{max} (maximal effect) values of baseline-corrected data are shown. Data are pooled from 3-4 independent experiments conducted in quadruplicate and presented as mean ± SEM. One-way ANOVA with Dunnett's multiple comparison test was used to determine significant differences in $pEC_{50\ and}$ R_{max} values in comparison to haloperidol at each cellular compartment; **P* < 0.05, ***P* < 0.01, ****P* < 0.001, *****P* < 0.0001.

APD	Venus-KRas		Venus-PTP1B	
	pEC_{50}	R_{max} (Δ BRET)	pEC_{50}	R_{max}(Δ BRET)
Haloperidol	7.89 ± 0.70	0.055 ± 0.005	8.85 ± 0.09	-0.025 ± 0.001
Sulpiride	7.69 ± 0.51	0.031 ± 0.002*	8.02 ± 0.11**	-0.037 ± 0.001****
Clozapine	9.20 ± 0.31	0.003 ± 0.005***	7.31 ± 0.15****	-0.014 ± 0.001***

Confocal imaging was used as an auxiliary technique to investigate APD-induced changes in localisation of SNAP-D2R within cells. CHO tetracycline-inducible SNAP-D2R (long isoform) cells were first induced with a high concentration of tetracycline (1 μg/ml) followed by 24 hours of 10 μM APD addition. After APD/vehicle (DMSO) treatment, cells were labelled with SNAP-Surface® Alexa Fluor® 488 prior to the acquisition of live confocal images in the presence of APD/vehicle. From these confocal images, the general distribution of SNAP-labelled SNAP-D2R (in green) within the cell appeared consistent across all APD/vehicle conditions, with SNAP-D2R being primarily localised to the cell membrane rather than showing intracellular accumulation which would be indicated as bright spots within the cytoplasm[323] (**Fig. 5.6**). The most notable observation between the APD/vehicle conditions was an overall increased SNAP-D2R signal intensity for haloperidol treatment in comparison to clozapine (**Fig. 5.6**). Here, haloperidol treatment caused an increase in SNAP-D2R signal, primarily at the plasma membrane, which likely reflects an increased SNAP-D2R expression at the membrane as an increased SNAP-D2R fluorescent signal at the membrane was shown to correlate with an increased particle number using fluorescence correlation spectroscopy in **Chapter 3.3**.

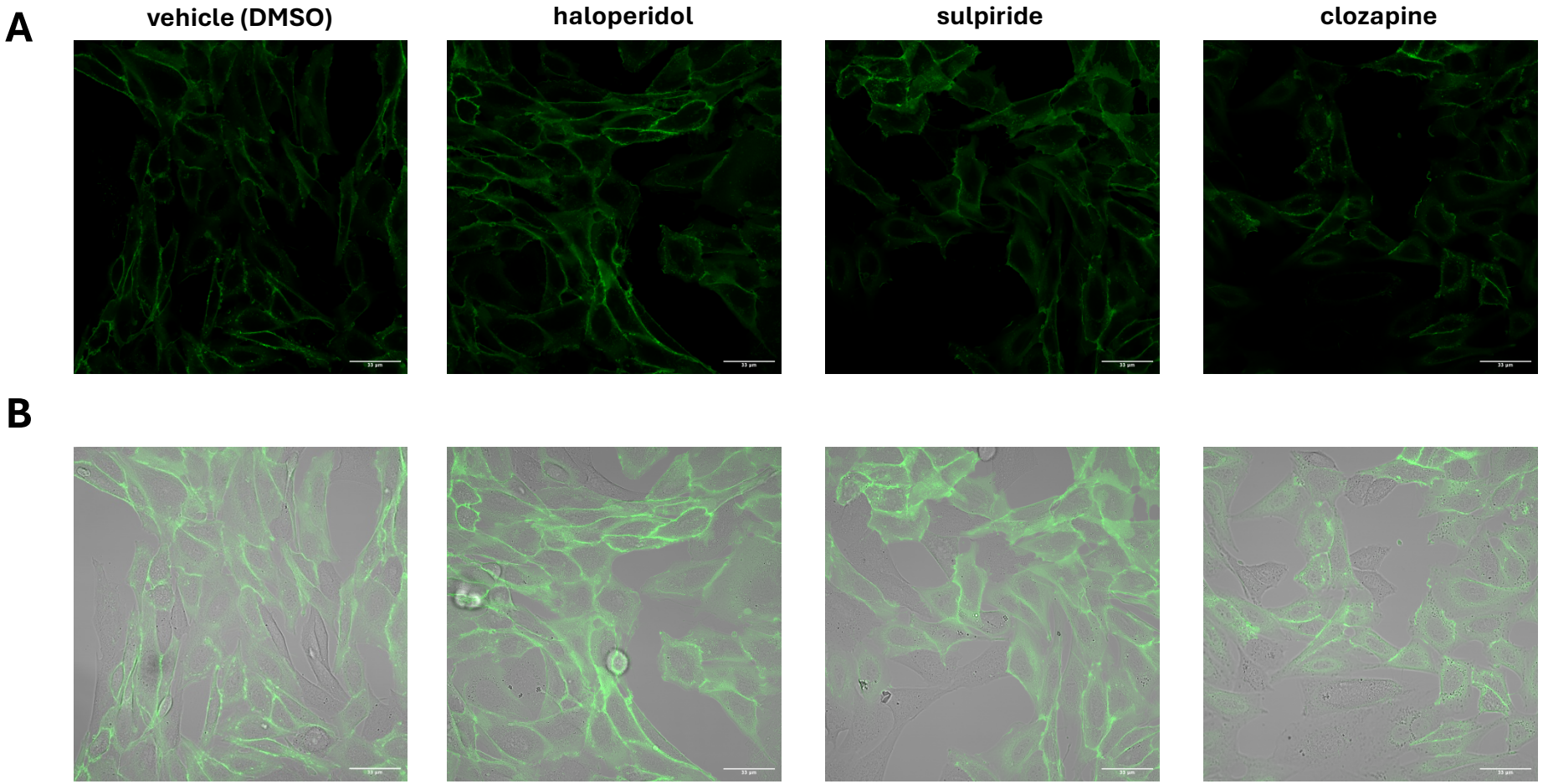

Figure 5.6: Confocal images showing antipsychotic drug-induced changes in SNAP-D2R localisation in CHO tetracycline-inducible SNAP-D2R cells.

CHO tetracycline-inducible SNAP-D2R (long isoform) cells were induced for 24 hours with 1 μg/ml tetracycline before 24 hours of antipsychotic drug (APD)/vehicle (DMSO) treatment. Cells were labelled with SNAP-Surface® Alexa Fluor® 488 prior to live confocal image acquisition in the presence of APD/vehicle. The 488 nm fluorescent channel is shown alone (**A**) and overlayed onto their respective transmitted light images (**B**). Images are representative of 3 independent experiments.

To gain a more quantitative comparison of the effect of differential APD treatment on D2R localisation in CHO tetracycline-inducible SNAP-D2R cells, the mean fluorescence intensity was measured within cells following the application of a threshold on confocal images to remove the background (as described in **Chapter 2.8.4**). This effectively provided a readout of the mean fluorescence intensity and therefore estimated SNAP-D2R expression at the plasma membrane due to the primary localisation of SNAP-D2R being at the plasma membrane. Interestingly, no significant differences were found in the estimated relative expression of SNAP-D2R in cells between each of the APD treatment conditions in comparison to vehicle (DMSO) ($P > 0.05$, one-way ANOVA) (**Fig. 5.7**). However, a significant difference in the SNAP-D2R expression was seen between haloperidol and clozapine treatment ($P < 0.01$, one-way ANOVA) (**Fig. 5.7**).

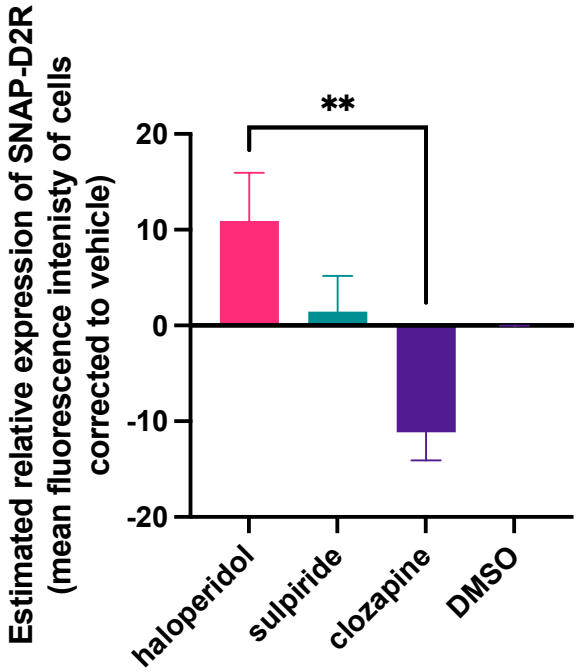

Figure 5.7: Antipsychotic drug-induced changes in estimated relative expression levels of SNAP-D2R within CHO tetracycline-inducible SNAP-D2R cells.

CHO tetracycline-inducible SNAP-D2R (long isoform) cells were induced for 24 hours with 1 μg/ml tetracycline before 24 hours of antipsychotic drug (APD)/vehicle (DMSO) treatment. Cells were labelled with SNAP-Surface® Alexa Fluor® 488 prior to live confocal image acquisition in the presence of APD/vehicle. A threshold was applied to confocal images to select only the cells and to remove the background before the 488 nm fluorescent intensity was measured within the resulting area. Data are corrected to vehicle and presented as mean ± SEM of three independent experiments with two images acquired per condition per experimental day. One-way ANOVA with Tukey's multiple comparison test was used to determine significant differences between each APD/vehicle condition; $^{**}P < 0.01$.

5.3.3 INVESTIGATING THE REVERSIBILITY OF ANTIPSYCHOTIC DRUG-INDUCED D2R CHAPERONING TO THE CELL SURFACE

The upregulation of D2R and hence enhanced dopaminergic signalling is associated with the development of TD[174]. TD shows low reversibility rates following the discontinuation of APDs which suggests that this receptor upregulation is a chronic response to APD treatment and may be irreversible[286]. To investigate the reversibility of D2R upregulation using the BRET D2R trafficking assay, we performed a 4-hour washout of APD after 24 hours of 10 μM APD treatment as described in **Chapter 2.5.2**. Concentration response curves investigating D2R-Nluc localisation at Venus-KRas positive plasma membrane and Venus-PTP1B positive ER were produced (**Fig. 5.8**). APD-induced BRET ratios were corrected to the mean vehicle (DMSO)-induced BRET signal at each concentration as in **Figure 5.5**.

At the plasma membrane, the rank order of APD-induced maximal responses (corrected to vehicle (DMSO)) followed the same overall order as without the washout: haloperidol > sulpiride = clozapine (**Table 5.3**). In addition, treatment with haloperidol or sulpiride followed by a 4-hour washout showed a significantly decreased D2R-Nluc localisation at the plasma membrane in comparison to haloperidol and sulpiride treatment without APD wash off, respectively ($P < 0.05$, one-way ANOVA; **Table 5.3**). By contrast, the 4-hour wash off did not significantly change the localisation of D2R-Nluc at the plasma membrane induced by clozapine ($P > 0.05$, one-way ANOVA; **Table 5.3**), with both wash conditions showing negligible clozapine-induced chaperoning effects of D2R-Nluc to the plasma membrane. Interestingly, a lower baseline relative to vehicle was seen following clozapine treatment without a 4-hour wash out in comparison to the wash condition (**Fig. 5.8A**). In addition, for APD-induced D2R-Nluc localisation at the plasma membrane there were no significant differences in the potencies (pEC_{50}) of the APDs with or without the 4-hour wash off, ($P > 0.05$, one-way ANOVA) (**Table 5.3**). However, with the washout step, the top of the non-linear regression curve for each APD was not consistently defined causing wide confidence intervals in their potencies. Finally, with a

4-hour APD wash off, haloperidol treatment no longer showed significant differences in D2R-Nluc localisation at the plasma membrane in comparison to sulpiride or clozapine treatment ($P > 0.05$, One-way ANOVA).

Concentration-response data produced at Venus-PT1B positive ER following haloperidol and clozapine treatment with a 4-hour APD washout (**Fig. 5.8B**) showed similar bell-shaped curves to data without APD washout. As previously seen with data without APD washout, there was only one data point (10 μM) that showed a reversal of the APD-induced D2R-Nluc loss from the ER (marked by box, **Fig. 5.8B**), meaning the bell-shaped curves were unable to be accurately fitted. Instead, a monophasic non-linear regression model was fitted to curves up to 1 μM as with the concentration-response curves without APD washout. It is important to note that 2/3 experimental repeats for haloperidol and clozapine, and only 1/3 experimental repeat for sulpiride fitted to the model as the tops of curves were unable to be consistently defined. Therefore, the potency and maximal response of sulpiride was unable to be determined. Surprisingly, at Venus-PTP1B positive ER, there were no significant differences in the maximal responses (corrected to vehicle (DMSO)) induced by haloperidol and clozapine with a 4-hour APD washout compared to the non-wash condition ($P > 0.05$, one-way ANOVA; **Table 5.3**). In addition, the pooled response of sulpiride at 1 μM (quoted in **Table 5.3**) with the 4-hour wash off was not significantly different to the maximal response induced by sulpiride without the APD wash off ($P > 0.05$, unpaired t-test). Although the potency of sulpiride was undetermined, there was a rightward shift in the curve of ~ 10-fold with the addition of the 4-hour wash off (**Fig. 5.8B**), suggesting a decrease in potency. In addition, data for haloperidol treatment with the 4-hour wash off was also rightward shifted by ~ 10-fold, despite haloperidol showing statistically similar potencies for D2R-Nluc translocation to the ER with or without the 4-hour washout ($P > 0.05$, one-way ANOVA, **Fig. 5.8B**). Finally, washing off clozapine did not cause a notable shift in the concentration response curve (**Fig. 5.8B**). Indeed, there was no significant difference in the potency of clozapine for causing D2R-Nluc translocation out of the ER between wash conditions ($P > 0.05$, one-way ANOVA, **Table 5.3**).

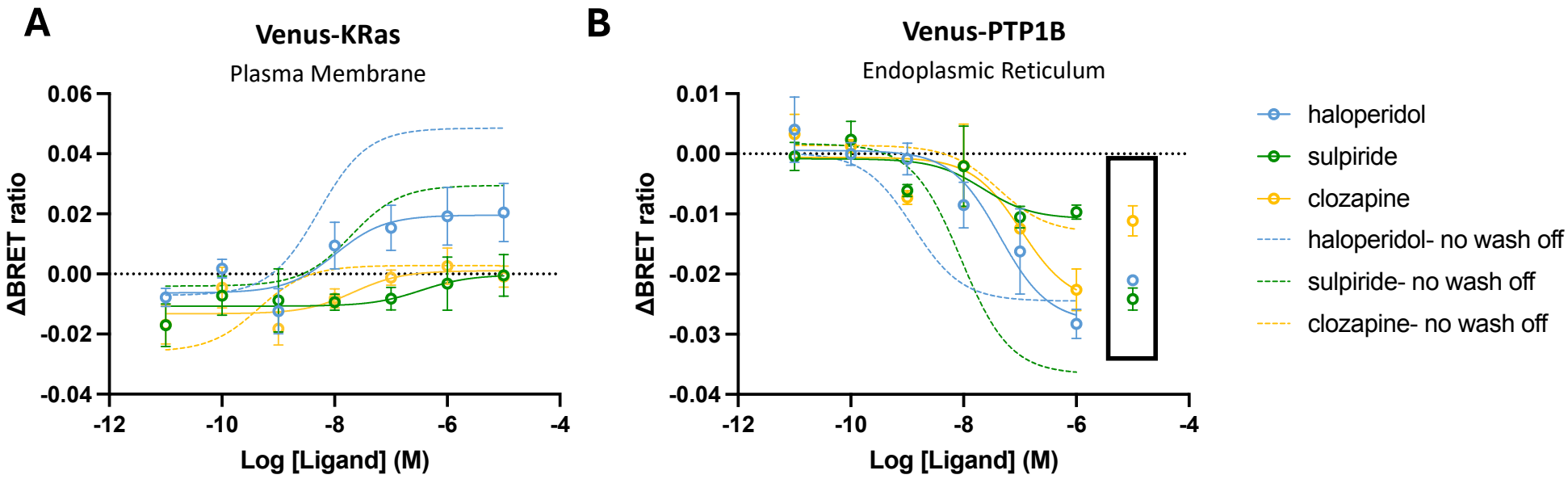

Figure 5.8: Concentration response curves showing D2R-Nluc trafficking at the plasma membrane and endoplasmic reticulum, following 24hr of antipsychotic drug (APD) treatment and a 4-hour APD wash off.

Bystander BRET was measured between D2R (long isoform)-Nluc and Venus-KRas (**A**) or Venus-PTP1B (**B**) in the presence of endogenous levels of GRK2 and β-arrestin2. Data are pooled (mean ± SEM) from 3-4 independent experiments conducted in quadruplicate. The APD-induced BRET signal was corrected to the mean vehicle (DMSO) response at each concentration for each compartment marker. Haloperidol, sulpiride and clozapine data without a 4-hour APD wash off is shown as dotted lines. At Venus-PTP1B positive endoplasmic reticulum (**B**), data at 10 μM (highlighted in black box) did not fit the monophasic curve of the non-linear regression model so were therefore excluded from the fit.

Table 5.3: Potency and maximal effect estimates of D2R-Nluc trafficking at the plasma membrane and endoplasmic reticulum, following 24hr of antipsychotic drug (APD) treatment and a 4-hour APD wash off.

Bystander BRET was measured between D2R (long isoform)-Nluc and Venus-KRas (plasma membrane marker) or Venus-PTP1B (endoplasmic reticulum (ER) marker) in the presence of endogenous levels of GRK2 and β-arrestin2. Pooled pEC_{50} (potency) values and R_{max} (maximal effect) values of baseline-corrected data are shown. Data are pooled from 3 independent experiments conducted in quadruplicate and presented as mean ± SEM. One-way ANOVA with Tukey's multiple comparison test was used to determine significant differences in $pEC_{50\ and}$ R_{max} values for each APD with and without the 4-hour wash off; **P* < 0.05. At Venus-PTP1B positive ER, both haloperidol and clozapine fitted the non-linear regression model for 2/3 experiments therefore R_{max} and pEC_{50} values are from only 2 experiments. At Venus-PTP1B positive ER, sulpiride only fitted the model for 1/3 experiments so the maximum response is quoted at 1 μM (#).

APD	Venus-KRas		Venus-PTP1B	
	pEC_{50}	**R_{max} (Δ BRET)**	**pEC_{50}**	**R_{max} (Δ BRET)**
Haloperidol	7.63 ± 0.52	0.020 ± 0.008*	8.12 ± 0.41	-0.026 ± 0.001
Sulpiride	7.97 ± 0.88	0.0003 ± 0.008*	-	-0.028#
Clozapine	7.58 ± 0.11	0.001 ± 0.004	7.94 ± 0.78	-0.018 ± 0.0005

Confocal imaging experiments were also performed where APD was washed off following the 24-hour incubation through SNAP-labelling and image acquisition in the absence of APD, meaning the APD pressure was removed from cells for a minimum of 45 minutes prior to imaging. The overall distribution of SNAP-D2R (long isoform) within cells remained similar to cells without APD wash off whereby SNAP-D2R was primarily localised to the plasma membrane irrespective of the APD/vehicle (DMSO) condition (**Fig. 5.9**). Even with this short APD wash off, the SNAP-labelled SNAP-D2R signal at the membrane appeared similar between all APD/vehicle (DMSO) conditions (**Fig. 5.9**). This suggests that the haloperidol-induced increase in SNAP-D2R expression at the cell-surface seen using confocal imaging (**Fig. 5.6**) and a BRET-based trafficking assay (**Fig. 5.5A**), is acutely reversible. Confocal images acquired with APD wash off were also analysed by measuring the mean fluorescence intensity within cells as described above for image analysis without APD wash off. Interestingly, the mean fluorescence intensity of cells treated with haloperidol prior to washing was no longer significantly different to that of clozapine ($P > 0.05$, one-way ANOVA; **Fig. 5.10**). In addition, there was no significant difference in the mean fluorescence intensity of cells following treatment with each APD in comparison to the vehicle (DMSO) ($P > 0.05$, one-way ANOVA; **Fig. 5.10**).

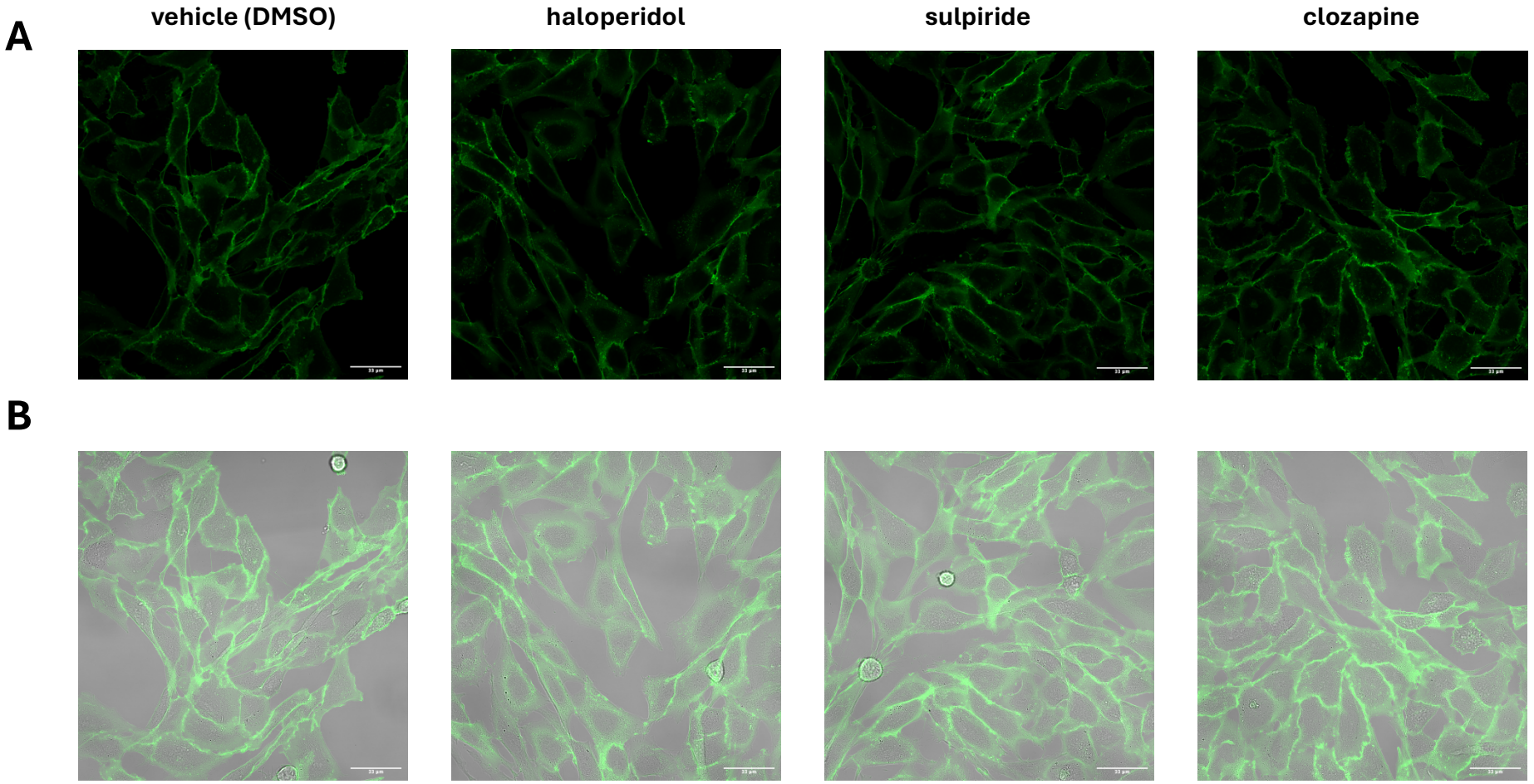

Figure 5.9: Confocal images showing antipsychotic drug-induced changes in SNAP-D2R localisation in CHO tetracycline-inducible SNAP-D2R cells following APD wash off.

CHO tetracycline-inducible SNAP-D2R (long isoform) cells were induced for 24 hours with 1 μg/ml tetracycline before 24 hours of antipsychotic drug (APD)/vehicle (DMSO) treatment. Cells were then labelled with SNAP-Surface® Alexa Fluor® 488 in the absence of APD prior to live confocal image acquisition again in the absence of APD. The 488 nm fluorescent channel is shown alone (**A**) and overlayed onto the respective transmitted light images (**B**). Images are representative of 2 independent experiments.

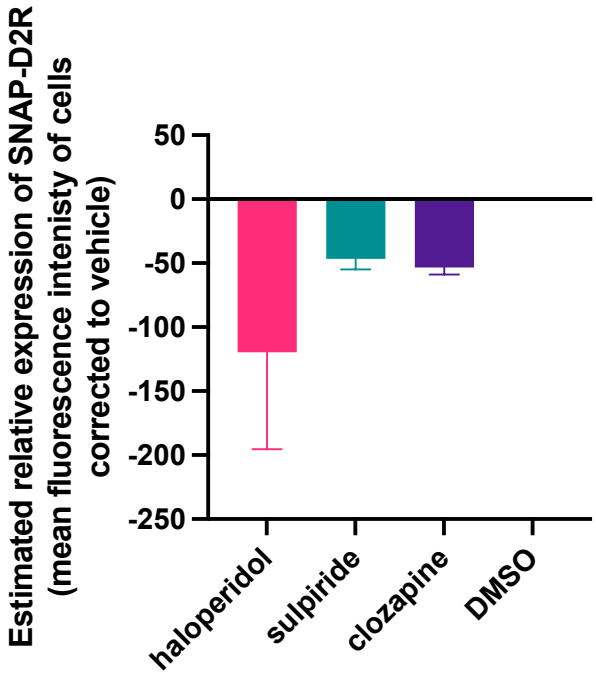

Figure 5.10: Antipsychotic drug-induced changes in estimated relative expression levels of SNAP-D2R within CHO tetracycline-inducible SNAP-D2R cells following APD wash off.

CHO tetracycline-inducible SNAP-D2R (long isoform) cells were induced for 24 hours with 1 μg/ml tetracycline before 24 hours of antipsychotic drug (APD)/vehicle (DMSO) treatment. Cells were labelled with SNAP-Surface® Alexa Fluor® 488 in the absence of APD prior to live confocal image acquisition again in the absence of APD. A threshold was applied to confocal images to select only the cells and to remove the background before the 488 nm fluorescence intensity was measured within the resulting area. Data are corrected to vehicle and presented as mean ± SEM of three independent experiments with two images acquired per condition per experimental day. One-way ANOVA with Tukey's multiple comparison test was used to determine significant differences between each APD/vehicle condition with no significant differences between each APD or vehicle condition found.

5.4 DISCUSSION

In this chapter, we aimed to use a BRET-based D2R trafficking assay and confocal imaging to reveal differences in the trafficking of D2R in cells following chronic treatment with APDs. Both experimental techniques clearly showed that haloperidol treatment resulted in the largest increase in the cell-surface expression of D2R compared to the other APDs tested. This may explain haloperidol's high EPS risk, particularly for TD which has been associated with increased D2R[174]. Clozapine treatment showed the lowest translocation of D2R to the cell membrane which may explain its low TD risk as well as its superior efficacy in treating TD [179,307]. Notably, the haloperidol-induced D2R upregulation at the cell surface was shown to be acutely reversible *in vitro*.

The BRET-based D2R trafficking assay described here relies on the use of marker proteins that are not passive markers. An overexpression of Rab proteins, in particular, may affect trafficking processes due to their role in vesicular transport through their action as GTPases[324]. In addition, due to the dynamic nature of vesicular trafficking, these Venus-tagged compartment marker proteins may not be exclusively localised to their respective compartments. However, extensive characterisation of their localisation has been carried out by several studies that have confirmed their localisation to be predominantly at their respective compartments through co-localisation imaging experiments with cell compartment stains [325–329]. Furthermore, confocal imaging experiments support data generated using the plasma membrane Venus-KRas marker.

To validate the BRET-based D2R trafficking assay, we first examined the ability of ropinirole and dopamine to change D2R-Nluc levels at the plasma membrane. Surprisingly, under endogenous expression levels of GRK2 and β-arrestin2 both agonists induced a significant increase in D2R-Nluc translocation to the plasma membrane over vehicle. This suggests an agonist-induced chaperoning effect where D2R-Nluc is trafficked out of the ER and to the plasma membrane via the Golgi apparatus. This apparent chaperoning activity of the agonists was unexpected as agonist treatment

classically results in receptor internalisation[64]. However, with the over expression of GRK2 and β-arrestin2, significant agonist-induced internalisation of D2R was seen fitting with the classical idea of agonist action at GPCRs. It may be the case that under endogenous levels of GRK2 and β-arrestin2 expression, the chaperoning effect of the agonists dominates over the internalisation effect whereas overexpressing GRK2 and β-arrestin2 shifts this equilibrium to internalisation. Furthermore, it has been shown that GRK2/β-arrestin2 can enhance the internalisation of GPCRs[330]. The kinase 'dead' GRK2, GRK2 K220R, and β-arrestin2 overexpression showed a partial inhibition of the agonist-induced internalisation seen with GRK2 and β-arrestin2 overexpression suggesting that a portion of D2R can internalise in a manner independent of GRK2 kinase activity. This agrees with literature that found D2L capable of undergoing internalisation in the absence of GRK2-mediated receptor phosphorylation[61]. More recently, it has been shown that GRK2 K220R enhances the efficacy of dopamine-induced β-arrestin2 recruitment at D2L, suggesting that there is a kinase-independent mechanism for the GRK2 enhancement of β-arrestin2 recruitment to D2L[331]. This may explain the enhanced D2R internalisation (D2R-Nluc loss from KRas-positive plasma membrane) seen with GRK2 K220R and β-arrestin2 overexpression in comparison to endogenous levels of GRK2 and β-arrestin2.

Overall, both agonists induced trafficking of D2R to the various cellular compartments in a manner that agrees with the classical agonist-induced GPCR trafficking model. Treatment with both agonists caused the internalisation of D2R-Nluc, as demonstrated by D2R-Nluc movement away from Venus-KRas positive plasma membrane and an increase in D2RL-Nluc translocation to Venus-Rab5 positive early endosomes. After chronic APD treatment (24 hours), an increased D2R-Nluc translocation to Venus-Rab7 positive lysosomes was seen potentially indicating agonist-induced long-term desensitisation of D2R. A study investigating D2S trafficking using D2R-Rluc8 and GFP2-Rab7 BRET pairs also showed dopamine and ropinirole-induced long term desensitisation of D2R as early as 1 hour following agonist treatment[332]. However, short-term desensitisation of D2R and receptor resensitisation through

receptor recycling back to the plasma membrane was still seen following 24 hours of agonist treatment through an increased D2R-Nluc translocation to Venus-Rab11 positive recycling endosomes.

At the ER, the agonists appeared to be acting as chaperones by causing D2R-Nluc translocation out of the ER resulting in a subsequent increase in D2R-Nluc translocation to the Golgi apparatus. However, this did not translate to increased D2R-Nluc expression at the plasma membrane in overexpressed levels of GRK2/GRK2 K220R and β-arrestin2 which suggests that the internalisation effect of the agonists overwhelms their chaperoning effect in these expression conditions. In addition, agonist action on D2R-Nluc translocation at the ER and Golgi apparatus may be a compensatory mechanism where D2R-Nluc is trafficked out of the ER and Golgi apparatus to replace lost D2R-Nluc following receptor downregulation. The cell surface replenishment of receptor from an intracellular pool of receptors within the Golgi apparatus in response to receptor downregulation has been previously reported for protease-activated receptors[333] and opioid receptors[334,335].

The differences between the agonists for inducing D2R translocation to the plasma membrane and lysosomes agree with a previous study which found ropinirole to cause significantly less D2S translocation away from the plasma membrane in comparison to dopamine and found no significant differences between ropinirole and dopamine-induced D2S trafficking at the lysosome (all with overexpressed levels of GRK2 and β-arrestin2)[332]. Interestingly, this study found no significant difference between ropinirole and dopamine-induced D2S translocation to early endosomes which disagrees with our data which showed ropinirole to cause significantly less D2R translocation to the early endosomes in comparison to dopamine. This may be explained by the use of different D2R isoforms within the studies. The differences in D2R trafficking seen between agonists is unlikely to be due to differences in affinity as they have similar reported affinity values at D2L[315]. Ropinirole and dopamine do show differing lipophilicities which may explain their differences in trafficking at intracellular

compartments. At the ER, dopamine showed a reduced chaperoning effect in comparison to ropinirole which may be due to its reduced lipophilicity meaning less dopamine is able to enter the cell to bind to and chaperone D2R from an intracellular pool. On the other hand, the agonists show similarly high Caco-2 membrane permeability values which has shown to be a better predictor of blood-brain barrier permeability in comparison to cLogP values[336]. Alternatively, dopamine may degrade faster than ropinirole thus resulting in a weaker D2R chaperoning capability at the same added concentration. It is known that dopamine quickly oxidises in solution at the neutral pH of HEK 293T growth media (pH of ~ 7.4) before ultimately degrading into reactive oxygen species[337]. In summary, the agonist-induced classical trafficking of D2R seen in the bystander BRET-based trafficking assay confirmed that the assay was able to successfully report trafficking of the D2R at various cellular compartments.

Next, APD-induced changes in D2R localisation within cells were investigated using the validated BRET D2R trafficking assay. The plasma membrane and ER are arguably the compartments of the most interest when examining the chaperoning ability of APDs. As seen in single concentration (10 μM) data as well as concentration response curves, haloperidol treatment caused the greatest translocation of D2R-Nluc to Venus-KRas positive plasma membrane followed by sulpiride and then clozapine, which agrees with previous findings[178]. These differences in efficacy for APD-mediated cell surface D2R upregulation cannot be explained by the differing lipophilicities of the APDs as clozapine showed the lowest efficacy despite having a similar lipophilicity to haloperidol (**Table 5.1**). It has also been shown that there is no correlation between membrane permeabilities and the ability of APDs to upregulate D2L to the cell surface[178]. In addition, the molecular basis of their differing chaperoning abilities cannot be explained by differences in affinity nor association or dissociation rates at D2L[145]. Interestingly, all APDs showed a statistically similar potency for causing D2R upregulation to the cell surface. This disagrees with a previous study that showed larger variations in potency between APDs for causing D2L cell surface upregulation and suggested that it is the cell permeability of APDs that influence their potency[178]. Furthermore, in this study the

potency of sulpiride and clozapine for trafficking D2R out of the ER was significantly lower than that of haloperidol despite haloperidol and clozapine having similar lipophilicity values. The idea that differences in D2R chaperoning could be explained by difference in APD lipophilicity is also flawed as all clinically approved APDs are formulated to cross the blood-brain barrier and therefore have high membrane permeabilities. Indeed, haloperidol and clozapine show high membrane permeability and sulpiride shows moderately high permeability in Caco-2 membrane permeability assays (**Table 5.1**) with permeability classification based on previous literature[336,338].

Interestingly, sulpiride induced a significantly larger loss of D2R from the ER compared to haloperidol which was not reflected at the cell membrane where haloperidol showed a greater D2R translocation compared to sulpiride. However, at the Golgi apparatus, the rank order of efficacy matched with plasma membrane data where haloperidol caused a greater increase in D2R localisation compared to sulpiride. This was surprising as GPCRs are known to be trafficked from the ER directly to the Golgi apparatus during anterograde trafficking[339]. The discrepancy between the rank order of APD efficacies at the ER versus the Golgi apparatus and plasma membrane could be driven by the fact that both haloperidol and clozapine, and to a much lesser extent sulpiride, show bell-shaped concentration response curves at the ER. There was an uptick in the data at 10 μM which was more pronounced for haloperidol and clozapine in comparison to sulpiride. This may indicate that over 24 hours, multiple cellular processes are affecting the changes of D2R levels in the ER and the combination of these processes may be different for different APDs. For example, as well as APD-mediated chaperoning of D2R out of the ER, it is possible that chronic haloperidol treatment may result in D2R synthesis within the ER to replace lost receptor following downregulation at the lysosome. This would then cause haloperidol treatment to show a reduced D2R loss from the ER as BRET between newly synthesized D2R-Nluc in the ER and the Venus-PTP1B marker would cause an increased signal. This is supported by haloperidol inducing a significantly larger translocation of D2R-Nluc to the lysosome in comparison to sulpiride and clozapine. Interestingly, clozapine treatment did not cause D2R loss from the ER but

increased D2R-Nluc localisation at the Golgi apparatus that was significantly larger than that induced by sulpiride. It also may be the case that haloperidol and sulpiride show improved chaperoning of D2R from the Golgi apparatus to the plasma membrane whereas clozapine is unable to chaperone D2R out of the Golgi apparatus as efficiently. In addition, the biphasic nature of concentration response curves of haloperidol and sulpiride-induced D2R-Nluc translocation to Venus-KRas positive plasma membrane may also be suggestive of interrelated dynamic processes contributing to the overall proximity of D2R-Nluc to Venus-KRas positive plasma membrane in a concentration-dependent manner.

It is known that pharmacological chaperones are able to rescue the expression of both mutant and wild-type GPCRs that show inefficient folding and hence significant intracellular localisation likely in the ER[181]. Therefore, it is possible that the differing chaperoning ability of APDs is due to their differing affinities for a misfolded or incomplete D2R that has an altered orthosteric binding site. This could explain why haloperidol's affinity for a wild-type D2R is ~ 40-fold higher that its potency for causing D2R translocation to the PM which may rely on lower affinity binding to an altered D2R within an intracellular compartment. However, haloperidol's potency for causing D2R translocation out of the ER is more similar to its affinity for WT D2R with only a ~ 4-fold difference. In addition, it could be argued that an intracellular store of misfolded D2R may be an artifact of D2R overexpression in HEK 293T cells. However, Schrader et al found the differential actions of haloperidol and clozapine were preserved in pituitary derived MMQ cells with endogenous D2R expression levels[178].

Further support of the D2R chaperoning capabilities of haloperidol was shown through confocal imaging of SNAP-D2R within CHO tetracycline-inducible SNAP-D2R (long isoform) cells. The SNAP-D2R localisation in this cell line was shown to be predominantly localised to the plasma membrane regardless of APD/vehicle treatment which contrasts with several studies that found significant intracellular retention of SNAP-D2L [58,227,308,309]. This could be due to differences in D2R labelling and image

acquisition between studies with samples in these studies all undergoing immunolabelling at 20°C prior to fixation in comparison to samples undergoing live SNAP-labelling at 37°C prior to live imaging in this study. However, it is known that lower temperatures reduce receptor internalisation and fixation ceases receptor internalisation[323,340]. SNAP-D2R localisation being largely restricted to the plasma membrane of CHO tetracycline-inducible cells meant that the measurement of the fluorescence of SNAP-labelled SNAP-D2R within cells provided an estimation of the level of SNAP-D2R expression on the cell surface. Haloperidol treatment showed the largest increase in SNAP-D2R upregulation at the plasma membrane, indicative of its action as a D2R chaperone[181]. Sulpiride and clozapine showed a moderate and small efficacy as a D2R chaperone, respectively, in comparison to haloperidol. However, each APD produced a change in SNAP-D2R expression at the cell surface that was not statistically different in comparison to vehicle (DMSO) treatment. The haloperidol-induced chaperoning effect of D2R seen in imaging experiments was therefore less pronounced in comparison to the chaperoning effect seen using a BRET-based D2R trafficking assay. This may be due to threshold technique used to analyse confocal images where the fluorescence intensity of SNAP-labelled SNAP-D2R was measured throughout the whole cell which may have resulted in other intracellular process affecting D2R distribution to be accounted for rather than solely measuring D2R translocation to the cell membrane. However, confocal imaging data clearly showed a significant difference between haloperidol and clozapine treatment in the APD-induced upregulation of SNAP-D2R at the membrane which aligns with BRET-based D2R trafficking data.

Overall, both imaging and BRET-based D2R trafficking data demonstrated the differential action of APDs as D2R chaperones may have therapeutic relevance particularly to tardive dyskinesia (TD), an antipsychotic-induced hyperkinetic movement disorder that is associated with an upregulation of D2R[288]. A recent meta-analysis showed TD risk to be particularly high with haloperidol treatment in comparison to clozapine treatment[179]. Furthermore, clozapine is the only APD that shows convincing

efficacy in patients with TD, possibly due to its uniquely low chaperoning activity of D2R[341].

All APDs induced an increase in D2R localisation to the endosomal compartments involved in classical trafficking (early endosomes and recycling endosomes) using the BRET-based D2R trafficking assay. This is surprising as internalisation and entry into the trafficking pathway is associated with agonist-induced receptor activation rather than inhibitory antagonist action at a receptor. However, this effect may be a result of normal membrane turnover rather than a ligand-receptor interaction-dependent mechanism. Alternatively, this effect may be caused by agonist-independent constitutive recycling of D2R. It has also been shown that clozapine and haloperidol act as full inverse agonists at D2R, inhibiting the receptor's constitutive activity, whereas sulpiride acts as a partial inverse agonist[342,343]. Therefore, as full inverse agonists, haloperidol and clozapine may be more likely to shift the equilibrium toward the inactive D2R state and prevent constitutive D2R recycling in comparison to sulpiride, resulting in increased D2R localisation at the plasma membrane. However, we saw an increased recycling of D2R following haloperidol and clozapine treatment in comparison to sulpiride and an increased D2R localisation at the plasma membrane following haloperidol treatment in comparison to clozapine treatment. Chaperoning effects of APDs therefore need to be distinguished from inverse agonism. We tried to investigate this using an ER to Golgi apparatus transport inhibitor (brefeldin-A), however, chronic treatment with this inhibitor after 24 hours led to cell death and with shorter APD treatment (8 hours), no APD-induced upregulation to the cell surface was seen. Alternatively, antipsychotic-induced entry of D2R into endosomal compartments may be explained by an overall increase in D2R at the plasma membrane following chronic APD treatment. If the D2R number is increased at the cell surface and the rate of internalisation or recycling is unaffected, there will still be an increase in D2R within these endosomal compartments. However, clozapine treatment causes an increase in D2R localisation at recycling endosomes that is significantly larger than that induced by haloperidol treatment, despite causing a negligible increase in D2R at the plasma membrane.

Notably, a 4-hour APD wash off following chronic treatment with each APD resulted in a reduced or negligible translocation of D2R-Nluc to the plasma membrane compared to the no wash condition, using the BRET-based D2R trafficking assay. This finding is further supported by imaging experiments that showed that the haloperidol-induced cell surface upregulation of D2R is reversed following an even shorter APD wash off period of at least 45 minutes. This suggests that once drug pressure is removed, D2R is downregulated and returns to normal levels at the plasma membrane. This disagrees with several animal studies that have shown that APD-induced upregulation in the striatum is prolonged even after the removal of the antipsychotic agent[177,344–346]. The differences in these findings could be explained by differences in experimental conditions such as the experimental model (model cell line versus animal model) and length of drug exposure. Here, the rapid reversal of APD-induced D2R cell surface upregulation in a model cell line brings the dopamine hypersensitivity hypothesis into question as they suggest that the irreversibility of EPS syndromes such as TD cannot be explained by a permanent upregulation of D2R even when the offending APD is discontinued. Furthermore, there is very little clinical evidence for the prolonged D2R upregulation in humans following the termination of the offending APD[347]. It is therefore possible that in humans this APD-induced D2R upregulation may be transient, and the irreversibility of TD may be caused by another mechanism that leads to dopamine supersensitivity within the striatum. For example, animal studies have shown that APDs can increase the proportion of D2R that is in a high affinity state which could lead to dopamine supersensitivity through endogenous dopamine binding[348]. It should be noted that despite the fact that most studies report TD remission rates below 25%[349–352] , in several of these studies patients continued with APD treatment to manage psychoses or as symptomatic treatment for TD meaning the true reversibility of symptoms is difficult to accurately determine.

At the ER, sulpiride treatment with a 4-hour washout generated right-shifted concentration response curves where the top of the curve was inconsistently defined (only defined on 1/3 experimental repeats) suggesting a decrease in potency compared

to the no washout condition. This suggests that a sufficient wash off was performed as a higher drug concentration was required to achieve a similar maximal effect. Furthermore, sulpiride has the lowest lipophilicity out of the three APDs suggesting it may be the most easily washed out. APD wash off did not significantly affect the potency or maximal responses of haloperidol or clozapine-induced D2R loss from the ER. However, this was not reflected at the plasma membrane where there was a significantly reduced D2R-Nluc localisation for haloperidol and sulpiride with APD washout. Therefore, investigation into D2R localisation at the Golgi apparatus within the anterograde pathway after APD wash off may account for these differences and provide a complete picture of anterograde trafficking.

It should be noted that the nature of the BRET trafficking assay, in terms of the use of different cell compartment markers, makes it difficult to make quantitative comparisons between the magnitude of the BRET response between cell compartments. In addition, it is difficult to clearly distinguish a chaperoning effect from other cellular processes, for example, changes in protein synthesis, cellular ATP levels and cell viability, all of which can affect protein trafficking within a cell[353–355]. Further controls would therefore be useful for these BRET trafficking experiments including: the investigation of more APD treatment timepoints; the use of the D2S isoform, which shows reduced intracellular retention in comparison to D2L[79] and therefore is likely to show reduced APD-induced chaperoning; and the use of other unrelated GPCRs that are amenable to rescue by pharmacological chaperones e.g. V2 vasopressin receptor mutants[356]. In addition, auxiliary experiments could be carried out including pulse chase studies where the SNAP-label on SNAP-D2R is blocked prior to APD incubation and SNAP-Surface® Alexa Fluor® 488 labelling is carried out following APD incubation to visualize solely the SNAP-D2R inserted into the membrane during APD treatment. Although, it would again be difficult to definitively establish whether the new SNAP-D2R at the cell surface appears as a result of APD-induced chaperoning of SNAP-D2R or as a consequence of normal protein turnover within the 24-hour APD incubation time. Western blot experiments could also be carried out before and after APD treatment to monitor the glycosylation

status of D2R. A larger population of fully glycosylated mature D2R following APD treatment could confirm their action as pharmacological chaperones of D2R by assisting in the full glycosylation of D2R hence allowing its translocation to the cell surface[79,80].

5.5 CONCLUSIONS

The overall chaperoning ability of APDs is demonstrated through D2R expression levels at the plasma membrane as chaperoning ultimately results in increased receptor expression at the cell surface[181]. Thus, APD-induced D2R (long isoform)-Nluc localisation at Venus-KRas positive plasma membrane using the BRET-based D2R trafficking assay, and confocal imaging experiments investigating the plasma membrane SNAP-D2R signal following chronic APD treatment were investigated. The order of efficacy for antipsychotic-induced D2R upregulation to the plasma membrane (haloperidol > sulpiride > clozapine) and hence their D2R chaperoning ability, correlate with the side-effect profiles of these antipsychotic drugs. This suggests that antipsychotics with low efficacy for D2R chaperoning may show improved EPS risks. Clozapine shows the lowest EPS risk among all antipsychotic drugs and is also the only APD that shows clear efficacy against TD symptoms[179,307]. These findings highlight D2R cell-surface upregulation as a potential mechanism behind clozapine's superior side effect profile. However, the irreversibility of TD once APD treatment is discontinued[286] cannot be explained by sustained D2R upregulation at the cell surface as an APD washout of at least 45 minutes reversed this upregulation. These data suggests that APD-induced D2R upregulation is not the sole mechanism behind the development of TD.

CHAPTER 6: PRIMARY CULTURE OF SNAP-D2R-EXPRESSING STRIATAL NEURONES

6.1 INTRODUCTION

Immortalised cell lines are commonly used in research as a model to study biological processes[357]. They are particularly useful to study a protein of interest in isolation through transfection, allowing mechanistic insights into protein regulation and function[358]. Further advantages of these model cell lines include their ease of use, an unlimited supply of cells and the circumvention of ethical concerns over the use of animal and human tissue[359]. It is also thought that model cell lines allow for the generation of reproducible results under the presumption that cells consist of a homogenous population. However, cell lines are also prone to genotypic and phenotypic variation over time, leading to the heterogeneity of cultures which can cause variability in data[360]. In addition, commonly used cell lines (e.g. HeLa, HEK 293T and CHO) are not best suited as a model for every cell type due to the complex nature of specialised cells. For example, neurones have a highly compartmentalised structure as well as unique features including multiple dendrites and an axon, that are not represented in these cell lines[361]. Furthermore, even immortalised neuronal cell lines, such as SH-SY5Y, are unlikely to recapitulate properties of neurones *in vivo* as they are often derived from tumorigenic tissue[362]. The cells of immortalised neuronal lines are also often limited to sparse and simple processes from their cell bodies meaning cell-to-cell synaptic transmission cannot be studied due to the absence of functional synapses[363]. Primary neuronal cultures prepared from fresh brain tissue are generally accepted as a better model to investigate biological processes in neurones[362,364]. However, primary neuronal culture has some disadvantages, not only in terms of the ethical considerations, but also the culturing itself is technically challenging and cells are less amenable to transfection[362]. Furthermore, the number of neurones from a single culture is limited and restricted to the development stage of the rodents used[362,365]. It is also important to note that all cells, regardless of the origin, acquire abnormal characteristics when cultured *in vitro*[363].

Arguably, a major disadvantage of primary neuronal culture is the unavoidable contamination of 'pure' neuronal cultures with other cell types (e.g. astrocytes and

oligodendrocytes) that exist in rodent brain tissue[362]. In fact, the presence of glia cells in culture is thought to be required to support the viability and functionality of neurones [365,366] meaning that neurones are often plated directly on top of a layer of glia feeder cells in a co-culture format[367,368]. This means that it is necessary to visually distinguish the neurones of interest from other cell types in culture which is often achieved with immunohistochemistry using cell-lineage specific markers[369,370]. However, this visualisation-based separation technique does not result in the physical separation of neurones which is helpful for more advanced experimental applications such as electrophysiology[371], western blot analysis[372] and advanced microscopy techniques[373].

Total internal reflection fluorescence (TIRF) microscopy is used to investigate the cell membrane dynamics and spatial distribution of membrane proteins including GPCRs[374], the largest family of proteins targeted by approved drugs[375]. TIRF microscopy requires cells of interest to be plated directly on a glass coverslip so that light can travel at a high incidence angle through the glass resulting in the excitation and detection of fluorophores within a thin optical slice (~ 100 nm) in the cell, near the coverslip[376]. This eliminates out of focus fluorescence that usually occurs with a larger excitation/detection area resulting in enhanced resolution hence allowing single particle detection[377]. The thin optical section achieved using TIRF microscopy also shows reduced photobleaching of fluorophores and increased cell viability during imaging in comparison to live confocal microscopy[377]. TIRF would therefore be a useful application to study receptors of interest expressed on native neuronal cells due to its high resolution and the fragile nature of cultured neurones.

Antagonism of the dopamine D2 receptor (D2R) expressed on medium spiny neurones (MSNs) in the striatum, is a common property of all clinically prescribed antipsychotic drugs (APDs) highlighting D2R as an important therapeutic target for disorders where psychosis is a primary symptom including schizophrenia and bipolar disorder[378]. APDs with poor side effect profiles have been shown to upregulate the cell-surface levels of D2R in CHO cells and pituitary-derived MMQ cells[178]. We have also

shown this to be the case in HEK 293T cells through a D2R trafficking BRET-based assay described in **Chapter 5**. A PET study has also shown *in vivo* evidence of APD-induced D2R upregulation in the striatum of patients with schizophrenia following chronic APD treatment[174]. It is therefore necessary to understand the organisation of endogenously expressed D2R in neurones at a cellular level and how this may be modulated by APDs to fully understand the pathophysiology of schizophrenia allowing for the development of better therapeutics with reduced side effects. We chose to use a SNAP-D2R mouse model for striatal culture (described in **Chapter 2.4.2**) which would allow for the visualisation of SNAP-D2R through SNAP-labelling and ultimately allow investigation of endogenously expressed D2R within MSNs of the striatum.

Here, we aimed to culture striatal MSNs in the absence of cortical neurones using a sandwich culture technique whereby MSNs are seeded onto a glass coverslip which is suspended above a glia feeder layer (described in detail in **Chapter 2.4.2**). We hypothesised that this neurone-glia sandwich culture format would allow a 'pure' culture of striatal neurones to be easily removed from the glia bed for subsequent experimentation. With this plating format, and the use of a SNAP-D2R transgenic mouse line, striatal neurones could be examined using TIRF to provide information on the D2R expression levels, diffusion and organisation of native D2R at the membrane of native cells.

6.2 CHAPTER 6 AIMS

The work described in Chapter 6 aimed to:

a) Optimise striatal neurone and glia sandwich protocol to maximise neuronal viability;
b) Optimise SNAP-labelling of SNAP-D2R striatal cultures.

6.3 RESULTS

6.3.1 OPTIMISATION OF STRIATAL NEURONE CULTURE PLATING

The final version of the protocol for the culture of SNAP-D2R-expressing striatal neurones described in **Chapter 2.4.1** and **Chapter 2.4.2**, was initially based on protocols from Banker et al. and Sulzer et al.[379,380]. These protocols were modified to achieve maximal neuronal cell viability in our hands which was determined by the percentage of live cells using a Countess™ II automated cell counter (Fisher Scientific, UK) following the trituration of striatal tissue. Neuronal viability was also assessed by the density and morphology of neuronal cells in culture through confocal imaging. Briefly, the resulting protocol involved the plating of dissociated striatal neurones on glass coverslips before their suspension above a bed of glia cells in glia-conditioned neuronal media. With each striatal culture, more experience in striatal dissection and trituration was gained, allowing the completion of these processes within 30 minutes which in turn had a positive effect on the number of surviving neurones per coverslip. The addition of DNase I into the trituration media also sped up the overall trituration time as tissue was less sticky due to reduced DNA build up in the sample from broken cells.

Two different sandwich formats were used as described in **Chapter 2.4.2**, whereby the coverslips with adhered striatal neurones were suspended above the glia bed either face up (neurones facing up into solution) or face down (neurones facing glia cells). Despite extensive variability in cell density between coverslips within the same culture and between different cultures, both face up and face down plating formats showed surviving neurones. Interestingly, both plating formats showed cells with neuronal morphology, where cells had processes, and cells with glia-like morphology, where cells had limited processes and increased cytoplasm around the nucleus[381] (**Fig. 6.1A**). The distribution of these cell types varied depending on the plating format. Face down plating showed a more uniform distribution of both neurones and glia across the coverslip whereas with face up plating, neurones and glia were primarily restricted to the edges of the coverslip. Interestingly, the middle of the coverslip of face up cultures

was mainly empty with areas of cell debris indicative of cell death. The cells in the middle of the coverslip in the face up format are more likely to die as they may be too far away from glia cells for their growth to be supported. Despite both face up and face down cultures being maintained in glia-conditioned media, it may be the case that there is a gradient of glia-released substances from the glia bed whereby these substances remain at a high concentration relatively local to glia cells and decrease in concentration significantly at the middle of the face up coverslip. This suggests that glia-conditioned media is not enough to support striatal neuronal development, and instead striatal neurones may require closer contact with glia cells. Finally, the length of time that striatal neurones were cultured prior to imaging was also optimised. Previous studies culturing striatal neurones used a culture period of 7 - 8 days before experimentation[382,383]. Here, at 7 days of culture there were a limited number of cells with processes and on those cells, the processes were sparse and short in length (**Fig 6.1B**). In contrast, a 10-day culture period resulted in striatal neurones with increased processes (**Fig 6.1C**) with some even showing a long singular process resembling an axon (**Fig 6.1D**). Therefore, a 10-day culture period was used to achieve a more developed neurone morphology that is more similar to neurones in *in vivo* brain tissue.

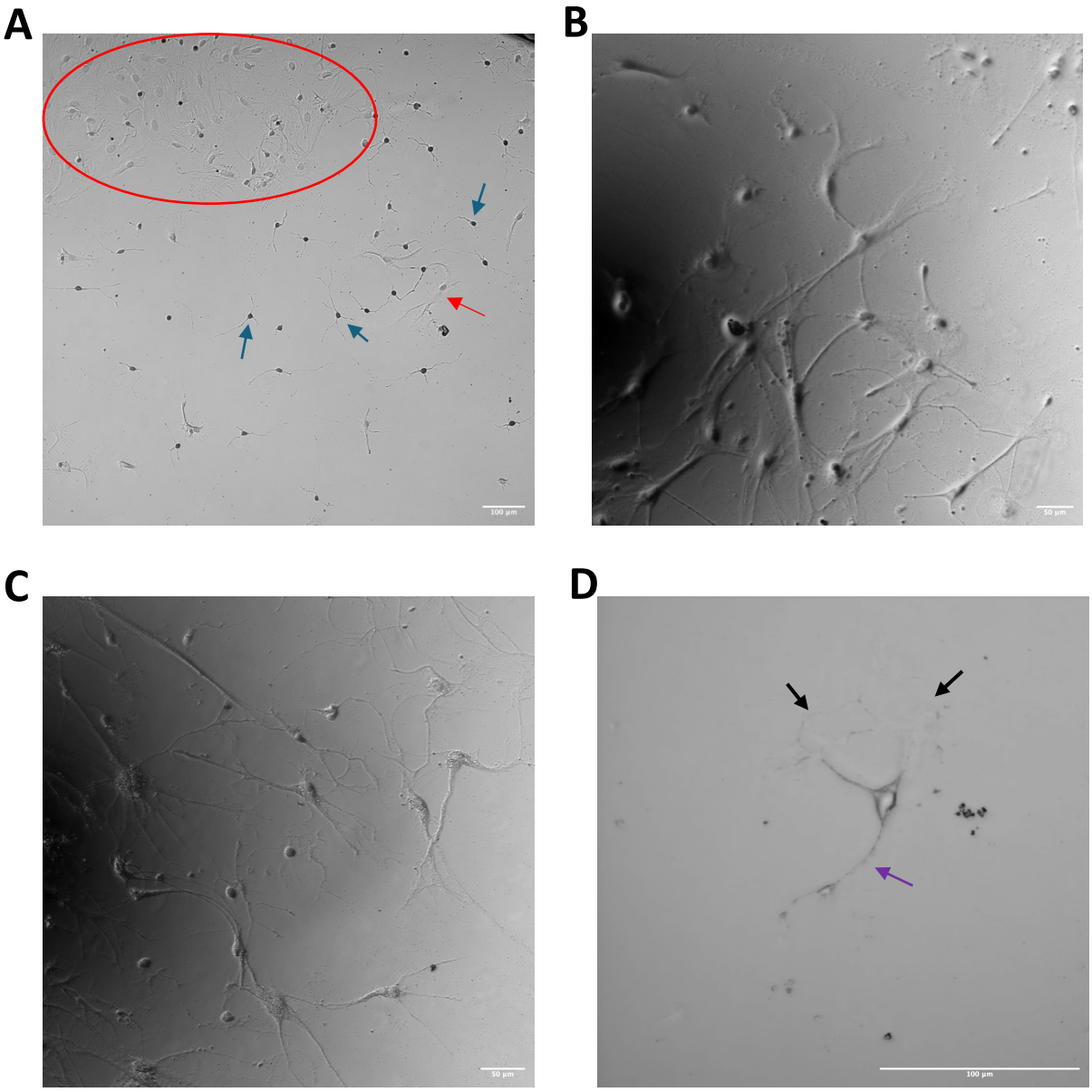

Figure 6.1: Transmitted light images of striatal neurone cultures on coverslips grown face down on a bed of glia.

(**A**) Cells with both glia-like morphology (examples circled in red or shown with red arrow) and neuronal-like morphology (examples shown with blue arrow) were present on coverslips seeded with striatal neurones. (**B**) A 7-day striatal neurone culture showing minimal neurone-like processes. (**C**) A 10-day striatal neurone culture with cells showing more extensive processes. (**D**) A zoomed-in image of a neurone from a 10-day striatal neurone culture exhibiting dendritic branching (black arrows) and an axon-like process (purple arrow).

6.3.2 OPTIMISATION OF THE SNAP-LABELLING OF SNAP-D2R-EXPRESSING STRIATAL NEURONES

As a positive control, CHO tetracycline-inducible SNAP-D2R (long isoform) cells were first induced with 1 μg/ml tetracycline for 24 hours before SNAP-labelling with 1 μM of various cell impermeable SNAP-dyes (Janelia Fluor® 549i, Janelia Fluor® 646i, SNAP-Surface® Alexa Fluor® 549 and SNAP-Surface® Alexa Fluor® 647). Positive SNAP-D2R staining was seen with each SNAP-dye with an arguably stronger signal from the yellow SNAP-dyes (exciting at 549 nm) (**Fig. 6.2A**) compared to the red SNAP-dyes (exciting at 646/647 nm) (**Fig. 6.2B**). This could be caused by differences in labelling efficiency, excitation/emission efficiency or quantum yield differences between the dyes[384].

SNAP-labelling of striatal cultures from both SNAP-D2R and WT mice was then performed using 100 nM of each SNAP-dye. Interestingly, cells with both neuronal-like and glia-like morphology showed positive SNAP-labelling with every dye used in both SNAP-D2R and WT striatal cultures (**Fig. 6.3**). Furthermore, the intensity of the SNAP-label signal in cells with a glia-like morphology was not visibly different to the intensity of the SNAP-label signal in neuronal cells. This suggested there was significant non-specific SNAP-labelling. Several steps were taken to troubleshoot this with an aim to improve the signal-to-noise ratio. First, SNAP-labelling with each SNAP-dye was investigated at lower concentrations of 10 nM, 1 nM and 0.1 nM, however, non-specific labelling was still observed at all three concentrations. Next, striatal neurones were pre-treated with 1 μM non-fluorescent SNAP-biotin (New England Biolabs, USA) for 30 minutes (37°C, 5% CO_2) prior to labelling with 10 nM, 1 nM or 0.1 nM of each SNAP-dye (**Fig. 6.4**). This pre-blocking step had no effect on the non-specific labelling of glia cells seen with each type of SNAP-dye and at every concentration (0.1 nM, 1 nM or 10 nM). In addition, an overnight wash-off of SNAP-dye post SNAP-labelling with 10 nM Janelia Fluor® 549i was carried out with and without a SNAP-biotin pre-treatment. This wash-off method did not show any improvement in the signal-to noise ratio. All images from

the above optimisation trials showed similar labelling to that in **Figure 6.3**, thus, not all images are shown as no further information is gained.

In addition, the SNAP-labelling of only rat glia using 10 nM of Janelia Fluor® 549i showed a positive SNAP-D2R signal (**Fig. 6.5**), further suggesting that the SNAP-label signal is indeed non-specific. Finally, a biotin-streptavidin affinity-based labelling technique was used to investigate a SNAP-D2R labelling method independent of small-molecule fluorescent dyes which may be non-specifically entering cells. Here, cells were treated with SNAP-biotin as described above before fixation, blocking and labelling with 20 nM Q dot streptavadin-565 (Thermo Fisher Scientific, USA) for 1 hour (**Fig. 6.6**). Again, this method showed no improvement in the specific SNAP-D2R signal.

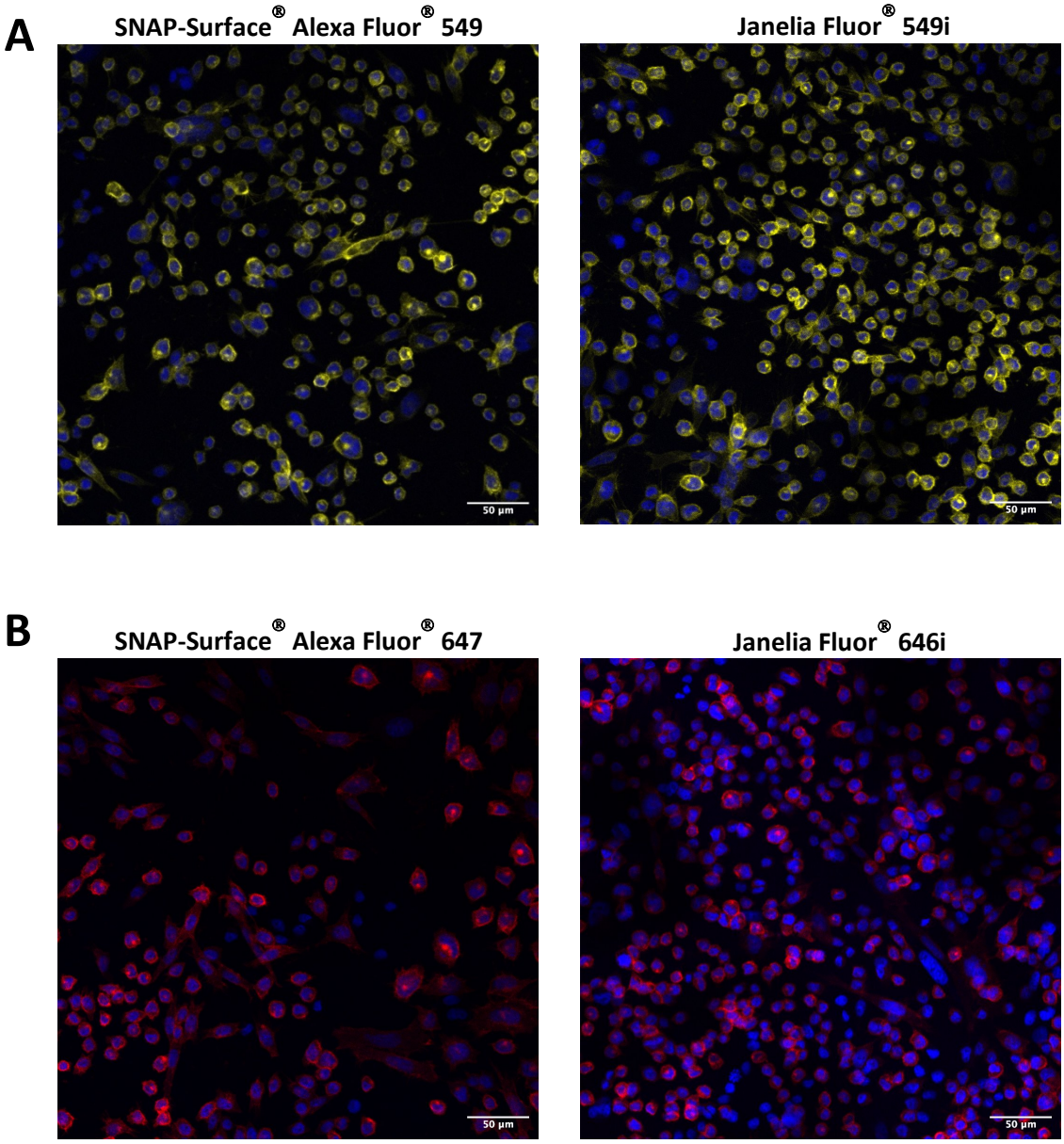

Figure 6.2: Confocal images of SNAP-labelled CHO tetracycline-inducible SNAP-D2R cells.

CHO tetracycline-inducible SNAP-D2R (long isoform) cells were induced with 1 µg/ml tetracycline for 24 hours prior to SNAP-labelling. Cells were then labelled with yellow (SNAP-Surface® Alexa Fluor® 549 and Janelia Fluor® 549i) (**A**) or red (SNAP-Surface® Alexa Fluor® 647 and Janelia Fluor® 646i) (**B**) cell impermeable SNAP-dyes. Cells were fixed and DAPI-stained (in blue) prior to image acquisition.

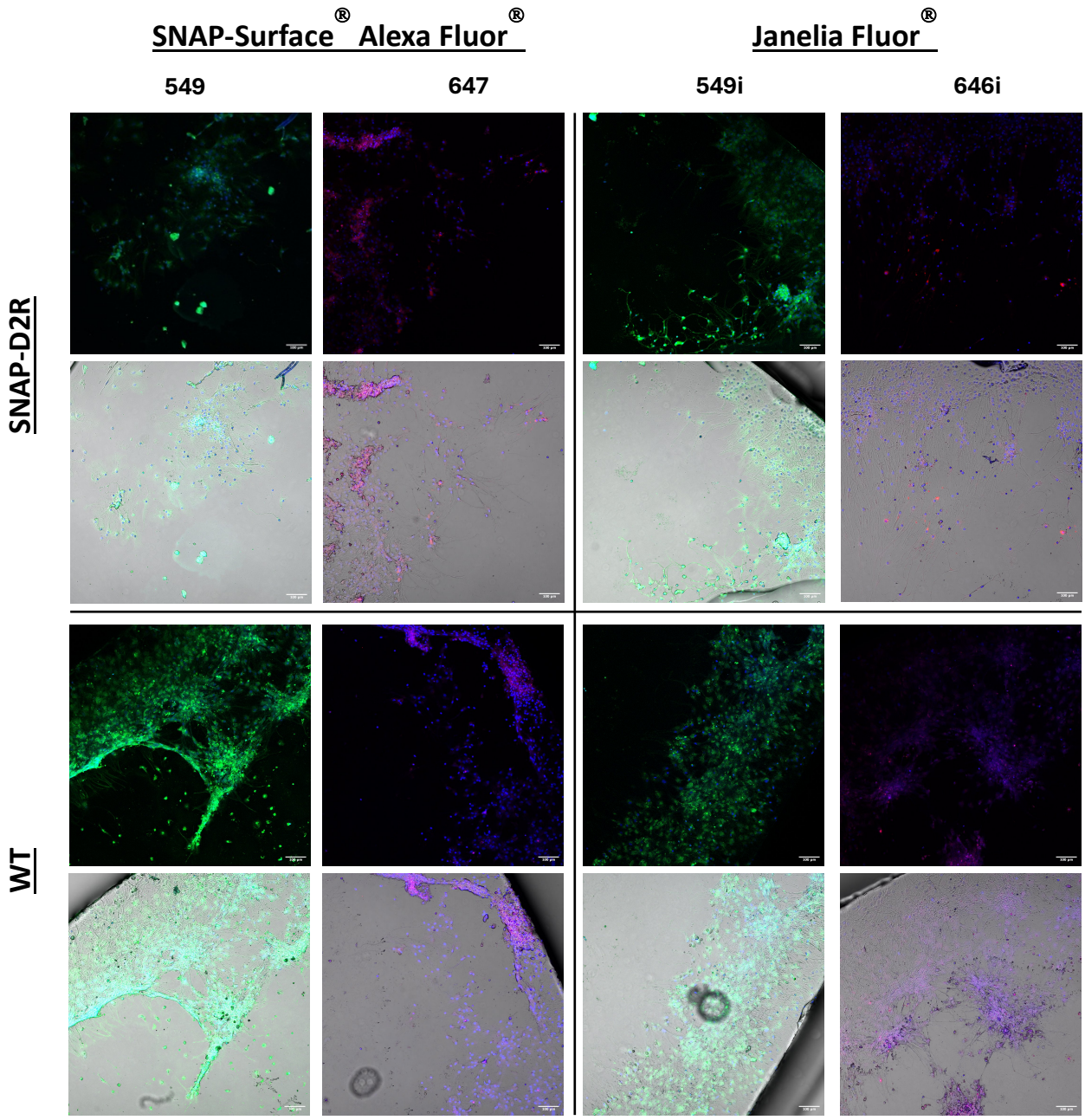

Figure 6.3: Confocal images of SNAP-labelled striatal cultures from SNAP-D2R and WT mice.

10-day striatal cultures of SNAP-D2R or WT mice were labelled with 100 nM of various cell impermeable SNAP-dyes: SNAP-Surface® Alexa Fluor® 549, SNAP-Surface® Alexa Fluor® 647, Janelia Fluor® 549i and Janelia Fluor® 646i. Cells were then fixed and DAPI-stained (in blue) prior to image acquisition. Fluorescence and transmitted light channels are shown.

A – 10 nM Janelia Fluor® 549i

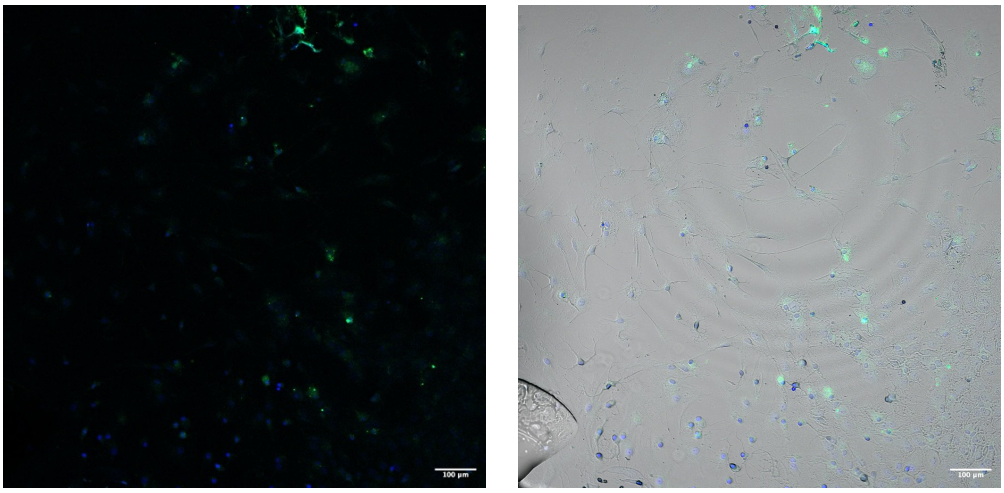

B – 1 μM SNAP-biotin + 10 nM Janelia Fluor® 549i

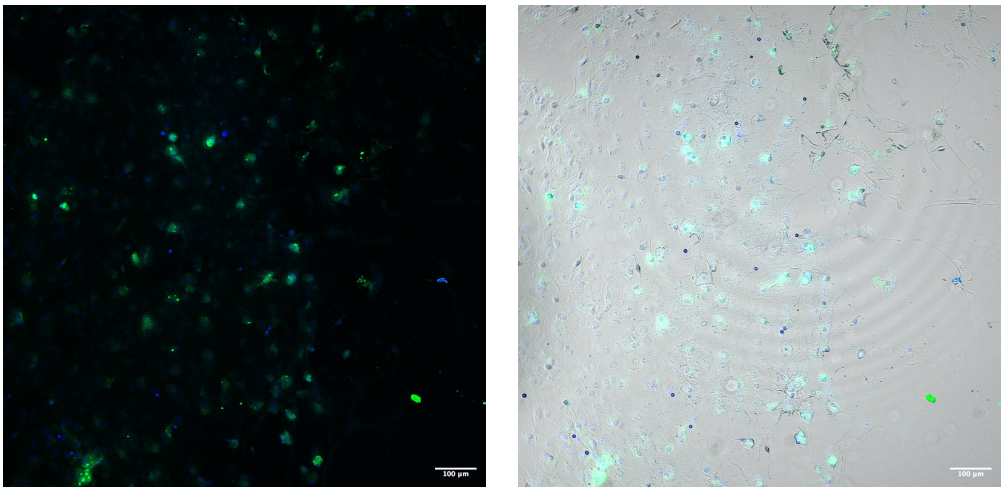

Figure 6.4: Effect of SNAP-biotin pre-treatment on the SNAP-labelling of striatal cultures from SNAP-D2R mice.

10-day striatal cultures of SNAP-D2R mice were labelled with 10 nM Janelia Fluor® 549i (in green) with (**B**) or without (**A**) a pre-treatment of 1 μM non-fluorescent SNAP-biotin. Cells were then fixed and DAPI-stained (in blue) prior to image acquisition. The fluorescence and transmitted light channels are shown.

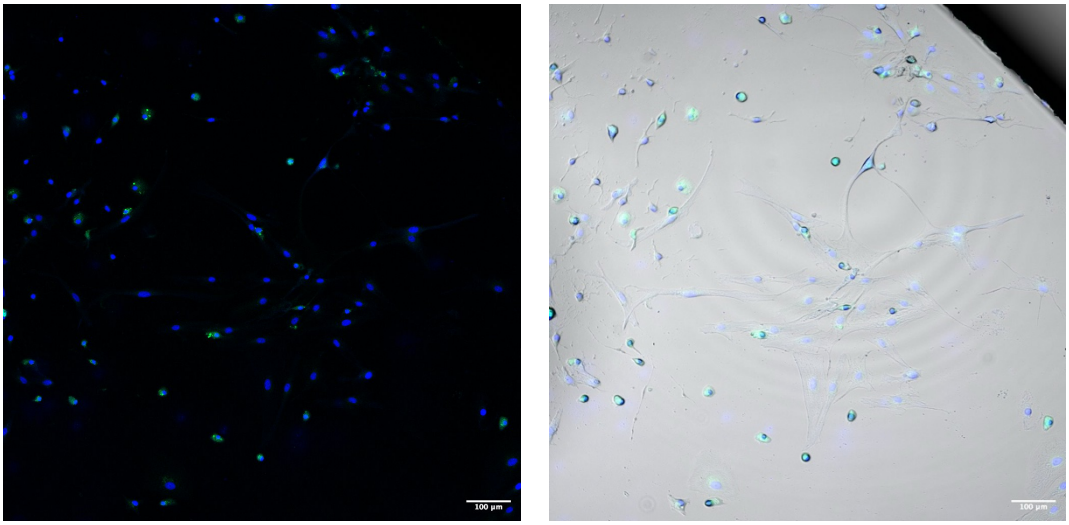

Figure 6.5: Confocal images of SNAP-labelled rat glia.

10-day cortical cultures of rat glia cells were labelled with 10 nM of Janelia Fluor® 549i. Cells were then fixed and DAPI-stained (in blue) prior to image acquisition. The fluorescence and transmitted light channels are shown.

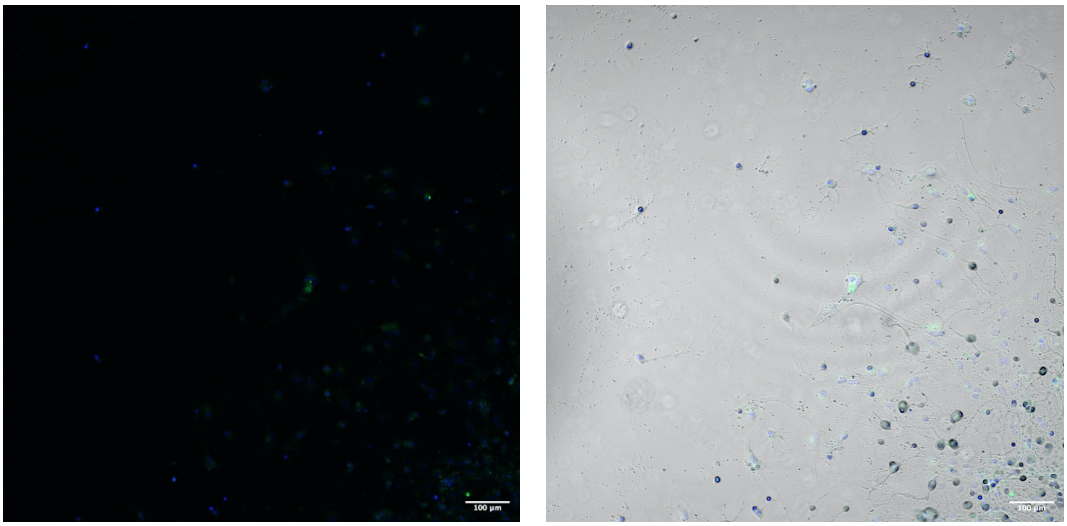

Figure 6.6: Confocal images of striatal cultures from SNAP-D2R mice labelled using a biotin-streptavidin affinity-based labelling technique.

10-day striatal cultures of SNAP-D2R mice were first labelled with 1 μM SNAP-biotin followed by 20 nM Q dot streptavadin-565. Cells were then fixed and DAPI-stained (in blue) prior to image acquisition. The fluorescence and transmitted light channels are shown.

6.4 DISCUSSION

Here, we have established a neurone-glia sandwich protocol whereby striatal neurones are cultured directly on a glass coverslip suspended above a bed of glia. This culture format allows the coverslip with adhered striatal neurones to be easily removed for investigation. This is advantageous as a 'pure' striatal culture does not require the identification and separation of neurones of interest from other cell types[369,370]. Furthermore, as neurones are directly adhered to the glass, more advanced experimental techniques than confocal imaging can be used, including TIRF microscopy which allows a single-molecule level of detection[385]. This level of resolution is crucial to investigate the spatiotemporal regulation of key proteins within neurones[386]. TIRF has been previously used to study the localisation of synaptic proteins moving along dendritic shafts of hippocampal neurones[386].

Several variations of neurone-glia sandwich plating formats have been previously developed using hippocampal neurones, cerebellar granule neurones and cortical neurones in an effort to generate 'pure' neuronal cultures that can be used for more advanced experimental applications[371,373,380,387,388]. Notably, there is a lack of a standardised *in vitro* protocol for the culture of D2R-expressing medium spiny neurones (MSNs) perhaps due to their difficultly to culture[389]. Historically, MSNs have been cultured as a mono-culture which has resulted in cells of simple neuronal morphology with a lack of dendritic spines, a well-defined characteristic of MSNs *in vivo*[390]. More recently, co-cultures of MSNs with cortical neurones have shown the retention of *in vivo* characteristics of MSNs including high densities of dendritic spines[389,391]. We were able to develop a striatal neurone and glia sandwich culture protocol that resulted in a removable coverslip with adhered viable striatal neurones, without the need for co-culture with cortical neurones or glia cells. Furthermore, following a 10-day culture period, neurones showed developed neuronal morphology using this plating technique.

Unfortunately, this culture technique did not result in completely 'pure' neuronal cultures meaning that there were cells with glia-like morphology present on the coverslip

as well as neurones. It is likely that the glia cells present on the coverslip were of mouse origin and were introduced through the dissection and trituration of striatal tissue which is known to contain several glia cell types to support neuronal development and function[392]. However, there were areas of the coverslip with solely neurones present that are directly adhered to the glass (**Fig. 6.1A**) meaning TIRF would still be applicable with this culture technique. Interestingly, there was significant neuronal cell death seen in the middle of face up coverslips suggesting that these cells may not have been close enough to the glia bed for their development to be supported.

Glia cells are known to secrete substances to support the development of neurones including brain derived neurotrophic factor (BDNF) which has been shown to specifically promote the survival and development of striatal neurones[393–395]. However, there is conflicting evidence as to whether the presence of glia cells in culture is required for neuronal development and functionality or whether this can be achieved with glia-conditioned media alone. For example, studies using hippocampal neurones found that the presence of glia cells in co-culture enhanced the number of synaptic contacts and spine density[396] as well as the transfection efficiency[397] in comparison to using glia-conditioned media alone. In contrast, aberrant cortical neurone firing was shown to be corrected using glia-conditioned media as well as control astrocytes[398]. In addition, MSNs co-cultured with cortical neurones showed viable and well-developed MSNs using glia-conditioned media alone[389,391]. This finding contrasts with our data from face up cultures that suggests that close contact with glia cells is required for the survival of striatal neurones despite the presence of glia-conditioned media within the well. The varied effects on neuronal development from the presence of glia cells or use of glia-conditioned media could be due to differing neuronal populations and variations in culture methods between studies.

To visualise the localisation of SNAP-D2R within striatal neurones, cultures were SNAP-labelled with a variety of cell impermeable SNAP-dyes (**Fig. 6.3**). Unfortunately, no SNAP-D2R signal was seen above the background despite several troubleshooting

attempts. There was SNAP-labelling of the same intensity for both glia cells and neuronal cells within SNAP-D2R striatal cultures. It is known that cultured glia cells do express D2R [399] which could explain their SNAP-labelling. However, extensive SNAP-labelling of both neuronal cells and glia cells were also seen in WT striatal cultures where no cells express a SNAP-tag. In addition, no difference in the extent of non-specific labelling was seen following SNAP-biotin pre-treatment. Together, this suggests that the SNAP-labelling seen in striatal cultures of SNAP-D2R mice is non-specific. Despite the cell membrane impermeability of the small-molecule SNAP-dyes, it may be the case that they are able to pass through primary cell membranes and be taken up into cells in a non-specific manner. This is supported by the finding that both neurones and astrocytes in culture show osmotic fragility and high membrane permeability[400].

SNAP-labelling followed by an overnight wash off step was carried out in an attempt to mimic the specific SNAP-D2R signal seen in coronal slices of SNAP-D2R mouse brains following *in vivo* SNAP-labelling (previously performed by members of the Javitch lab, Columbia University, USA). Presumably, the *in vivo* SNAP-labelling allows the enhanced clearance of SNAP-dye through physiological processes resulting in reduced background labelling. As the overnight wash off of SNAP-dye *in vitro* did not reduce the high background, it may be better to continue with *in vivo* SNAP-labelling and instead generate cultures from adult SNAP-D2R mice post SNAP-labelling. Although the culturing of neurones from adult mice is traditionally challenging[401], it is achievable as previous studies have successfully generated cultures of striatal neurones from adult mice[401,402].

6.5 CONCLUSION

A striatal neurone and glia sandwich culture technique was successfully optimised to allow the culture of striatal neurones from SNAP-D2R mice directly on a glass coverslip. These cultured striatal neurones retained *in vivo* neuronal characteristics including dendritic branching and axon formation suggesting normal neuronal morphology. Despite this, SNAP-labelling of these SNAP-D2R expressing striatal neurones did not result in a specific signal as glia cells were also labelled as well as both neuronal cells and glia cells in striatal cultures of WT mice. Several attempts were made to optimise this *in vitro* SNAP-labelling with the aim of improving the signal-to-noise ratio but to no avail. Therefore, the study of endogenously expressed D2R in native cells using TIRF microscopy could not be carried out. Immunohistochemistry of coronal slices of SNAP-D2R mice has shown a specific SNAP-D2R signal following the *in vivo* SNAP-labelling of SNAP-D2R mice. Thus, future work could involve culturing striatal neurones from adult SNAP-D2R mice post in vivo SNAP-labelling. These cultures could then be investigated using TIRF microscopy to reveal information on the organisation and diffusion of D2R in native cells.

CHAPTER 7: GENERAL DISCUSSION

7.1 GENERAL DISCUSSION

Dysregulated dopamine signalling at the D2R has been consistently implicated in the pathophysiology of schizophrenia (**Chapter 1.3.2**). In fact, all APDs that show clinical efficacy against the positive symptoms of schizophrenia are known to act as D2R antagonists[178]. Unfortunately, D2R antagonism is also associated with unwanted side effects termed, EPS. In addition to the unpleasant nature of the movement disorders within the EPS spectrum, their development may result in poor patient compliance and as a result poor treatment outcomes. Furthermore, some disorders within the EPS spectrum (e.g. TD) have been shown to be potentially irreversible[286], demonstrating the large unmet clinical need to develop APDs that are efficacious against psychosis without inducing EPS. Some APDs, most notably clozapine, show lower EPS risks. In an endeavour to explain the atypicality of APD action, a variety of molecular mechanisms have been proposed (**Chapter 1.4.2**). However, no single mechanism has sufficiently accounted for the typical or atypical nature of every APD. This thesis aimed to explore two promising molecular mechanisms to explain APD atypicality: (1) the reduced rebinding of atypical APDs to D2R resulting in surmountable D2R antagonism and (2) the low efficacy of atypical APDs as pharmacological chaperones of D2R resulting in reduced D2R upregulation to the cell surface. Using a variety of techniques including FCS, confocal imaging and BRET, we gained novel understanding into the differential rebinding of APDs *in vitro* and also expanded the current knowledge on APD-induced trafficking of D2R within a cell.

Chapter 3 optimised the FCS settings for in-solution reads of the fluorescent APDs, spiperone-d2 and clozapine-Cy5. In addition, the variable expression of SNAP-D2R in CHO tetracycline-inducible SNAP-D2R (long isoform) cells was characterised using confocal imaging and FCS. This then allowed the investigation of the concentration of these fluorescent APDs above cells with a range of SNAP-D2R expression levels through FCS experiments (detailed in **Chapter 4**). FCS was also used to investigate the membrane

dynamics of SNAP-D2R within CHO tetracycline-inducible SNAP-D2R cells which revealed information regarding the organisation of D2R on cell membranes.

Chapter 4 explored the rebinding of spiperone-d2 and clozapine-Cy5 above CHO tetracycline-inducible cells with a range of SNAP-D2R expression levels. FCS measurements in solution showed spiperone-d2 to form concentration gradients above cells that were dependent on the level of SNAP-D2R expression at the plasma membrane. Interestingly, clozapine-Cy5 did not form these concentration gradients indicating negligible levels of D2R rebinding in comparison to spiperone-d2.

Chapter 5 investigated the APD-induced trafficking of D2R (long isoform) to various cellular compartments using a bystander-based BRET trafficking assay and confocal imaging. Most notably, we found that APDs differentially trafficked D2R out of the ER and to the plasma membrane in a concentration-dependent manner. Therefore, APDs act with varying efficacies as D2R pharmacological chaperones. In addition, the APD-induced D2R upregulation at the plasma membrane was found to be acutely reversible *in vitro* which has implications on the mechanism of the irreversibility of TD.

Finally, **Chapter 6** showed the initial optimisation of a sandwich culture of primary SNAP-D2R-expressing striatal neurones. Although the visualisation of SNAP-D2R was unsuccessful, the optimised culture technique resulted in viable striatal neurones grown directly on a glass coverslip. This culturing technique has future applications such as neuronal preparation for TIRF microscopy which requires cells of interest to be directly adhered to glass.

An in-depth discussion of data can be found within the individual results chapters. In this chapter, general insights from results chapters will be discussed in the context of key biological questions regarding the molecular basis of APD atypicality.

7.1.1 CAN APD REBINDING IN VITRO PREDICT APD REBINDING IN VIVO?

Chapter 4 provides novel evidence of APD rebinding indicated by the formation of spiperone-d2 concentration gradients above D2R-expressing cells where there is a higher concentration of drug close to the receptors on the cell surface in comparison to the bulk aqueous environment further away from the cell. Interestingly, the fluorescent APD with a slower association rate at D2R, clozapine-Cy5, showed significantly reduced concentrating effects above D2R-expressing cells in comparison to spiperone-d2, which is indicative of negligible clozapine-Cy5 rebinding to D2R. This finding supports the recent "fast-on" hypothesis behind APD atypicality that posits that APDs with fast association rates at D2R, such as spiperone, show rebinding to D2R within a synapse resulting in high concentrations of drug within the synaptic cleft, subsequently causing prolonged D2R blockade and hence higher EPS risks[145].

Significant concentration gradients of spiperone-d2 were formed in a simple system with minimally restricted diffusion: a monolayer of D2R-expressing cells in a well. This suggests that an even greater rebinding effect may be seen *in vivo* due to the diffusion-restricted nature of neuronal networks and synaptic compartments of D2R-expressing MSNs. Here, synaptic membranes act as barriers to free diffusion meaning APD is maintained at a high concentration within the synaptic cleft, making it more likely for binding events at D2R on the synaptic membrane to take place. Furthermore, the density of endogenously expressed D2R on synaptic membranes may be higher than that on the membrane of the model cell line we used in rebinding studies. As discussed in **Chapter 4**, an increase in receptor density has been modelled to enhance rebinding[168]. In addition, the organisation of D2R on the synaptic membrane could impact rebinding. Interestingly, in **Chapter 3**, we showed that a small proportion of D2R exists as a brighter component which may indicate receptor clustering. D2R clustering has also been observed on the membrane of neurones[228–230] (discussed in **Chapter 3.4**). It is likely that increased APD rebinding occurs at these clusters due to a local increase in D2R expression. Overall, we predict that the significant rebinding effect of APDs to D2R seen

in vitro could be even more pronounced *in vivo*. Therefore, the actual concentrations of APD in the immediate vicinity of D2R receptors *in vivo* may be drastically higher than previously thought resulting in higher than desired D2R occupancy levels leading to poor side effect profiles.

APDs are dosed to achieve D2R occupancy levels within an often narrow therapeutic window where efficacy against psychosis is achieved without passing the threshold for EPS (**Chapter 1.4.1**). APD dosage is often based on affinity measurements at D2R from *in vitro* assays, where the rebinding effect has been previously unaccounted for potentially resulting in overestimation of affinity. More accurate measurements of drug concentrations in the immediate vicinity of target receptors could enable more accurate affinity estimates to in turn achieve receptor occupancy levels *in vivo* that are closer to the desired value. Therefore, prioritising the accurate measurement of affinity of both current and future APDs at D2R by accounting for this rebinding phenomenon could optimise APD dosing to achieve better side effect profiles. Furthermore, the D2R occupancy estimations of APDs are often taken from PET imaging studies using various APD radioligands[403]. These occupancy estimates are likely to be subjected to the same rebinding phenomenon seen in our *in vitro* studies and therefore may require re-interpretation based on the differing rebinding potentials of the APD radioligands used. Interestingly, a meta-analysis of PET studies found that atypical APDs showed increased D2R binding in the temporal cortex in comparison to typical APDs that showed D2R binding predominantly within the striatum[404]. It could be the case that APD rebinding underlies the differential labelling of brain regions seen with different APD radioligands.

7.1.2 COULD SEPARATE HYPOTHESISED MOLECULAR MECHANISMS BEHIND APD ATYPICALITY BE ADDITIVE?

We have demonstrated that typical APDs show increased D2R rebinding (**Chapter 4**) and an increased efficacy for acting as a D2R pharmacological chaperone by increasing D2R upregulation to the cell surface (**Chapter 5**). Therefore, these two pharmacological mechanisms may contribute to the high EPS risk seen with the majority of APDs. There is also a possibility that these separate mechanisms may be additive as we have shown that increased D2R expression at the cell surface enhances rebinding potentially leading to increased D2R blockade. Therefore, APDs that show high levels of rebinding, driven by fast D2R on rates, as well as high efficacies for D2R chaperoning may show particularly poor side effect profiles (**Fig. 7.1**).

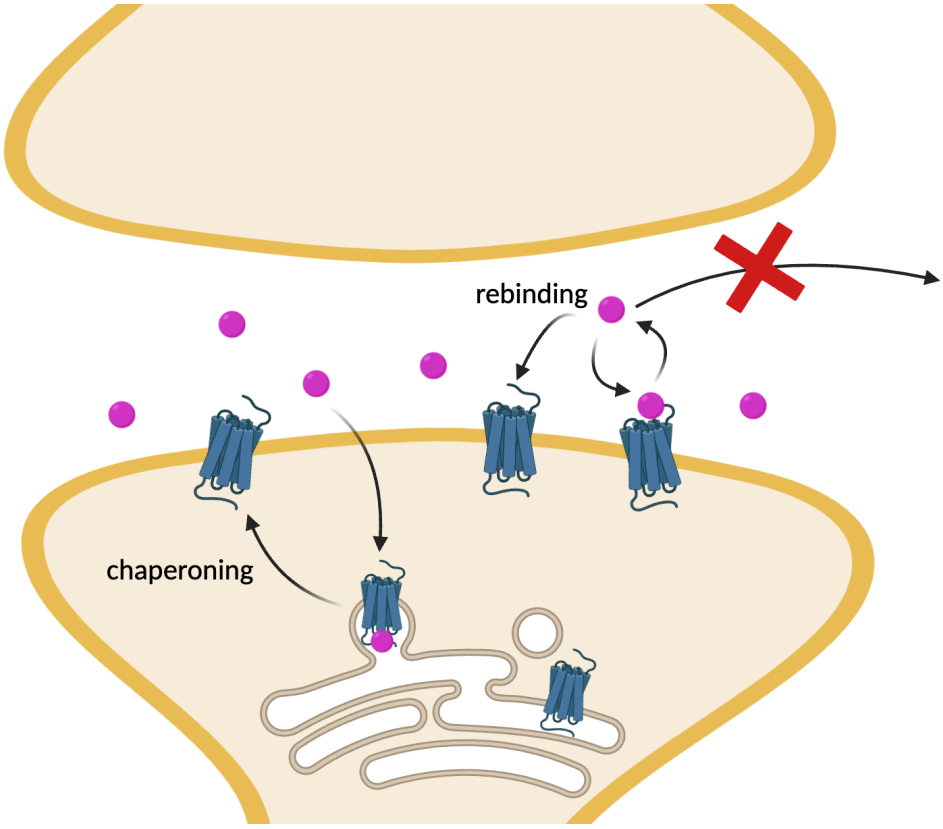

Figure 7.1: Schematic demonstrating the additive effects *in vivo* of antipsychotic drug rebinding to D2R and antipsychotic drug-induced D2R upregulation to the cell membrane.

Antipsychotic drugs (APDs) (shown in pink) may show particularly poor side effect profiles *in vivo* if they have both fast association rates at D2R (driving rebinding at D2R) and high efficacy for chaperoning D2R from the ER to the plasma membrane. The APD-mediated chaperoning of D2R (shown on left) results in an increased D2R expression on the cell surface. The diffusion-limiting synaptic membranes and increased D2R expression enhances APD rebinding to D2R within a synapse (shown on right). Overall, this results in an increased D2R blockade leading to high EPS risks.

The proposition that a single molecular mechanism may explain the atypicality of APDs excludes the possibility that atypicality may be caused by multiple interrelated mechanisms. It would be interesting to investigate the rebinding potential and chaperoning effects of a larger panel of APDs. This could then allow the meta-analysis of several APDs with respect to their 'fit' to all the proposed mechanisms of atypicality to establish whether there are common mechanisms that contribute to specific disorders within the EPS spectrum.

7.2 FUTURE DIRECTIONS

Using the FCS and BRET trafficking assay workflows optimised in this study, structure-activity relationship (SAR) studies could be carried out using analogues of a typical APD to determine what specific structural characteristics contribute to increased D2R rebinding and the pharmacological chaperoning of D2R. This could be carried out with haloperidol analogues generated in a previous structure-kinetic relationship study[280]. Interestingly, they showed that subtle structural modifications resulted in compounds that showed clozapine-like kinetic profiles (slower D2R association). We hypothesize that these particular analogues may show lower D2R rebinding and chaperoning potentials in future SAR studies. Therefore, these SAR studies would allow the prediction of APD side effect profiles based on the structural groups of the compound.

In **Chapter 6**, optimisation of primary culture of striatal neurones from SNAP-D2R mice was carried out with the aim to extend studies into cells of therapeutic relevance. Once the SNAP-labelling of these cultures is further optimised, FCS experiments (like those carried out in **Chapter 3**) could be carried out to investigate the membrane dynamics of endogenously expressed D2R. This would be particularly interesting given little is known about the absolute number of D2R expressed on MSNs. We could then compare the particle number of SNAP-D2R per squared micron with SNAP-D2R densities we determined on CHO tetracycline-inducible SNAP-D2R cells (**Chapter 3.3**) to determine if the rebinding effect seen within *in vitro* studies would be potentially greater *in vivo* based on increased D2R expression. In addition, we could examine the distribution of fluorescent APDs above SNAP-D2R-expressing striatal neurones using in-solution FCS measurements (as in **Chapter 4**) to see if concentration gradients indicative of rebinding are seen above native cells. These in-solution FCS experiments could also be performed in slice which may better recapitulate the dense neuronal network that is present *in vivo*. Furthermore, the advanced microscopy technique TIRF (discussed in **Chapter 6.1**) could be used to investigate SNAP-D2R membrane dynamics using single particle resolution.

These dynamics could then be assessed following treatment with APDs with differing EPS risks to determine whether APDs differentially affect D2R at the level of membrane organisation which may outline a novel molecular mechanism behind atypicality.

The pharmacological chaperoning activity of several APDs could also be investigated in primary striatal cultures from SNAP-D2R mice. Following chronic APD treatment and the SNAP-labelling of striatal neurones, the change of SNAP-D2R expression at the plasma membrane could be determined through increased fluorescence or particle number per square micron using confocal imaging techniques or FCS, respectively. In addition, co-localisation experiments could be performed following APD treatment with SNAP-labelled SNAP-D2R and cell membrane specific dyes (e.g CellMask™ (Fisher Scientific, UK)) or a fluorescently tagged CAAX motif. Co-localisation experiments have previously been successfully performed in neurones using dual-colour single molecule localisation microscopy[405].

However, if the SNAP-labelling of primary striatal neurones from SNAP-D2R mice continues to prove unsuccessful, it would be interesting to test whether acute neuronal cultures from adult mice are more susceptible to labelling. Better SNAP-labelling of these acute cultures could be due to increased neuronal maturity and potentially increased viability due to shorter culturing times. The SNAP labelling of SNAP-D2R mice was previously successful when carried out in live animals prior to the isolation of brain slices (personal communication with J. Javitch). This may be due to a reduced amount of SNAP-label reaching neurones, the increased clearance of SNAP label or the better viability of neuronal cells. Therefore, animals could undergo chronic treatment with different APDs before the administration of SNAP-label to the live animals prior to the investigation of D2R expression and localisation in slice.

A limitation of our study is the need for fluorescent APDs to investigate APD rebinding to D2R rather than using the clinically administered non-fluorescent versions of APDs. It would therefore be interesting to investigate the *in vivo* consequences of the rebinding of clinically used APDs. Zych and Ford have shown that dopaminergic neurones can be locally stimulated allowing dopamine release from a few varicosities[406]. This dopamine release onto nearby MSNs can be visualised using the genetically encoded dopamine indicator, dLight[406], meaning real concentrations of dopamine can be mapped onto local areas of MSNs (personal communication with C. Ford). In addition, inhibitory post synaptic currents (IPSCs) can be detected in specific areas of the MSN using patch clamp electrophysiology meaning we can determine the concentrations of dopamine required to illicit responses in neurones[406]. From experiments in **Chapter 4** that show the actual concentrations of fluorescent APDs above D2R-expressing cells, it would be interesting to treat MSNs with these concentrations of APD and determine if this alters the pattern of dopamine release onto the MSN and whether these concentrations of APD can then inhibit dopamine-induced IPSCs. We could therefore then see if the reported affinity of APDs match their *in vivo* efficacy based on their ability to inhibit IPSCs.

7.3 KEY CONCLUSIONS

In summary, this thesis explored two promising molecular mechanisms that have been proposed to explain the atypicality of APD action, using advanced microscopy techniques and BRET-based approaches. First, our data supported the recent "fast-on" hypothesis which posits that APD atypicality is driven by fast association rates of APDs at D2R. We provided novel experimental evidence of ligand rebinding through the detection of concentration gradients above cells that were dependent on cell-surface receptor expression. Moreover, we showed differential rebinding effects between APDs with different binding kinetics at D2R and different EPS risks. Our data also suggest wider reaching implications beyond solely APD rebinding as the rebinding phenomenon is likely to affect *in vitro* measurements of equilibrium binding parameters such as affinity and potency which have driven drug discovery for decades. Second, we gained further insight into the APD-induced translocation of D2R in a cell, particularly with respect to the APD-mediated pharmacological chaperoning of D2R from the ER to the cell membrane. Our data showed that APD-induced D2R upregulation to the cell surface is concentration-dependent and acutely reversible *in vitro*. This may therefore discount the APD-mediated chaperoning of D2R to the cell surface as the cause of the largely irreversible hyperkinetic disorder, TD. It is possible that the chaperoning activity of some APDs may enhance APD rebinding to D2R through an increase in cell-surface D2R, leading to worse side effect profiles. Overall, this thesis provided novel insights into the molecular basis of atypical APD action which could allow the easier prediction of side effect profiles of new APDs in the future.

REFERENCES

1. Carlsson, A., Lindqvist, M., Magnusson, T. & Waldeck, B. On the presence of 3-hydroxytyramine in brain. *Science (1979)* **127**, doi:10.1126/science.127.3296.471 (1958).

2. Montagu, K. A. Catechol Compounds in Rat Tissues and in Brains of Different Animals. *Nature* **180**, 244–245 (1957).

3. Carlsson, A., Lindqvist, M. & Magnusson, T. 3,4-Dihydroxyphenylalanine and 5-Hydroxytryptophan as Reserpine Antagonists. *Nature* **180**, 1200–1200 (1957).

4. Beaulieu, J.-M. & Gainetdinov, R. R. The Physiology, Signaling, and Pharmacology of Dopamine Receptors. *Pharmacol. Rev.* **63**, 182-217 (2011).

5. Daubner, S. C., Le, T. & Wang, S. Tyrosine hydroxylase and regulation of dopamine synthesis. *Arch. Biochem. Biophys.* **508**, 1–12 Preprint at https://doi.org/10.1016/j.abb.2010.12.017 (2011).

6. Missale, C., Russel Nash, S., Robinson, S. W., Jaber, M. & Caron, M. G. Dopamine receptors: From structure to function. *Physiol. Rev.* **78**, 189–225 Preprint at https://doi.org/10.1152/physrev.1998.78.1.189 (1998).

7. Meiser, J., Weindl, D. & Hiller, K. Complexity of dopamine metabolism. *Cell Commun. Signal.* **11**, 34 Preprint at https://doi.org/10.1186/1478-811X-11-34 (2013).

8. Ford, C. P. The role of D2-autoreceptors in regulating dopamine neuron activity and transmission. *Neuroscience* **282**, 13–22 Preprint at https://doi.org/10.1016/j.neuroscience.2014.01.025 (2014).

9. Bourdy, R. et al. Control of the nigrostriatal dopamine neuron activity and motor function by the tail of the ventral tegmental area. *Neuropsychopharmacology* **39**, 2788–2798 (2014).

10. Redgrave, P. et al. Goal-directed and habitual control in the basal ganglia: Implications for Parkinson's disease. *Nat. Rev. Neurosci.* **11**, 760–772 Preprint at https://doi.org/10.1038/nrn2915 (2010).

11. Luo, S. X. & Huang, E. J. Dopaminergic neurons and brain reward pathways: From neurogenesis to circuit assembly. *Am. J. Pathol.* **186**, 478–488 Preprint at https://doi.org/10.1016/j.ajpath.2015.09.023 (2016).

12. Helbing, C., Brocka, M., Scherf, T., Lippert, M. T. & Angenstein, F. The role of the mesolimbic dopamine system in the formation of blood-oxygen-level dependent

responses in the medial prefrontal/anterior cingulate cortex during high-frequency stimulation of the rat perforant pathway. *J. Cereb. Blood Flow Metab.* **36**, 2177–2193 (2016).

13. Alcaro, A., Huber, R. & Panksepp, J. Behavioral functions of the mesolimbic dopaminergic system: An affective neuroethological perspective. *Brain Res. Rev.* **56**, 283–321 (2007).

14. Boyle, C. C., Bower, J. E., Eisenberger, N. I. & Irwin, M. R. Stress to inflammation and anhedonia: Mechanistic insights from preclinical and clinical models. *Neurosci. Biobehav. Rev.* **152**, doi:10.1016/j.neubiorev.2023.105307 (2023).

15. Klein, M. O. et al. Dopamine: Functions, Signaling, and Association with Neurological Diseases. *Cell. Mol. Neurobiol.* **39**, 31–59 Preprint at https://doi.org/10.1007/s10571-018-0632-3 (2019).

16. Floresco, S. B. & Magyar, O. Mesocortical dopamine modulation of executive functions: beyond working memory. *Psychopharmacology* **188**, 567–585 (2006).

17. Konopaske, G. T. & Coyle, J. T. Schizophrenia. *Neurobiology of Brain Disorders: Biological Basis of Neurological and Psychiatric Disorders* 639–654 (Elsevier, 2015) doi:10.1016/B978-0-12-398270-4.00039-2.

18. Lyons, D. J., Hellysaz, A. & Broberger, C. Cellular/Molecular Prolactin Regulates Tuberoinfundibular Dopamine Neuron Discharge Pattern: Novel Feedback Control Mechanisms in the Lactotrophic Axis. *J. Neurosci.* **32**, 8074-8083 (2012).

19. Rubí, B. & Maechler, P. Minireview: New Roles for Peripheral Dopamine on Metabolic Control and Tumor Growth: Let's Seek the Balance. *Endocrinology* **151**, 5570–5581 (2010).

20. Rosenbaum, D. M., Rasmussen, S. G. F. & Kobilka, B. K. The structure and function of G-protein-coupled receptors. *Nature* **459**, 356–363 Preprint at https://doi.org/10.1038/nature08144 (2009).

21. Yang, H. S. et al. Role of Helix 8 in dopamine receptor signaling. *Biomol. Ther.* **27**, 514–521 (2019).

22. Chien, E. Y. T. et al. Structure of the human dopamine D3 receptor in complex with a D2/D3 selective antagonist. *Science (1979)* **330**, 1091–1095 (2010).

23. Wang, S. et al. D4 dopamine receptor high-resolution structures enable the discovery of selective agonists. *Science (1979)* **358**, 381–386 (2017).

24. Wang, S. et al. Structure of the D2 dopamine receptor bound to the atypical antipsychotic drug risperidone. *Nature* **555**, 269–273 (2018).

25. Zhuang, Y. et al. Structural insights into the human D1 and D2 dopamine receptor signaling complexes. *Cell* **184**, 931-942 (2021).

26. Xu, P. et al. Structures of the human dopamine D3 receptor-Gi complexes. *Mol. Cell* **81**, 1147-1159 (2021).

27. Manglik, A. & Kruse, A. C. Structural Basis for G Protein-Coupled Receptor Activation. *Biochemistry* **56**, 5628–5634 (2017).

28. Zhou, Q. et al. Common activation mechanism of class A GPCRs. *Elife* **8**, doi:10.7554/eLife.50279 (2019).

29. Buckley, S. J. et al. Evaluating conserved domains and motifs of decapod gonadotropin-releasing hormone G protein-coupled receptor superfamily. *Front. Endocrinol.* **15**, doi:10.3389/fendo.2024.1348465 (2024).

30. Olivella, M., Caltabiano, G. & Cordomí, A. The role of Cysteine 6.47 in class A GPCRs. *BMC Struct. Biol.* **13**, doi:10.1186/1472-6807-13-3 (2013).

31. Weis, W. I. & Kobilka, B. K. The Molecular Basis of G Protein–Coupled Receptor Activation. *Annu. Rev. Biochem.* **87**, 897–919 (2018).

32. Syrovatkina, V., Alegre, K. O., Dey, R. & Huang, X.-Y. Regulation, Signaling, and Physiological Functions of G-Proteins. *J Mol Biol* **428**, 3850–3868 (2016).

33. Oldham, W. M. & Hamm, H. E. Heterotrimeric G protein activation by G-protein-coupled receptors. *Nat. Rev. Mol. Cell. Biol.* **9**, 60–71 (2008).

34. McCudden, C. R., Hains, M. D., Kimple, R. J., Siderovski, D. P. & Willard, F. S. G-protein signaling: Back to the future. *Cell. Mol.Life Sci.* **62**, 551–577 Preprint at https://doi.org/10.1007/s00018-004-4462-3 (2005).

35. Spano, P. F., Govoni, S. & Trabucchi, M. Studies on the pharmacological properties of dopamine receptors in various areas of the central nervous system. *Adv. Biochem. Psychopharmacol.* **19**, 155–165 (1978).

36. Kebabian, J. W. & Calne, D. B. Multiple receptors for dopamine. *Nature* **277**, 93–96 Preprint at https://doi.org/10.1038/277093a0 (1979).

37. Beaulieu, J. M., Espinoza, S. & Gainetdinov, R. R. Dopamine receptors - IUPHAR review 13. *Br. J. Pharmacol.* **172**, 1–23 (2015).

38. Lud Cadet, J., Jayanthi, S., T. McCoy, M., Beauvais, G. & Sheng Cai, N. Dopamine D1 Receptors, Regulation of Gene Expression in the Brain, and Neurodegeneration. *CNS Neurol. Disord. Drug Targets* **9**, 526–538 (2010).

39. De Mei, C., Ramos, M., Iitaka, C. & Borrelli, E. Getting specialized: presynaptic and postsynaptic dopamine D2 receptors. *Curr. Opin. Pharmacol.* **9**, 53–58 Preprint at https://doi.org/10.1016/j.coph.2008.12.002 (2009).

40. Gallo, E. F. Disentangling the diverse roles of dopamine D2 receptors in striatal function and behavior. *Neurochem. Int.* **125**, 35–46 Preprint at https://doi.org/10.1016/j.neuint.2019.01.022 (2019).

41. Guiramand, J., Montmayeur, J. P., Ceraline, J., Bhatia, M. & Borrelli, E. Alternative splicing of the dopamine D2 receptor directs specificity of coupling to G-proteins. *J. Biol. Chem.* **270**, 7354–7358 (1995).

42. O'Dowd, B. F. et al. Site-directed mutagenesis of the cytoplasmic domains of the human β2-adrenergic receptor. Localization of regions involved in G protein-receptor coupling. *J. Biol. Chem.* **263**, 15985–15992 (1988).

43. Usiello, A. et al. Distinct functions of the two isoforms of dopamine D2 receptors. *Nature* **408**, 199–203 (2000).

44. Wang, Y. et al. Dopamine D2 long receptor-deficient mice display alterations in striatum-dependent functions. *J. Neurosci.* **20**, 8305–8314 (2000).

45. Lindgren, N. et al. Distinct roles of dopamine D2L and D2S receptor isoforms in the regulation of protein phosphorylation at presynaptic and postsynaptic sites. *Proc. Natl. Acad. Sci.* **100**, 4305–4309 (2003).

46. Neve, K. A. et al. Normalizing dopamine D2 receptor-mediated responses in D2 null mutant mice by virus-mediated receptor restoration: Comparing D2L and D2S. *Neuroscience* **248**, 479–487 (2013).

47. Obadiah, J. et al. Adenylyl cyclase interaction with the D2 dopamine receptor family; differential coupling to Gi, Gz, and Gs. *Cell.l Mol. Neurobiol.* **19**, 653–664 (1999).

48. Jiang, M., Spicher, K., Boulay, G., Wang, Y. & Birnbaumer, L. Most central nervous system D2 dopamine receptors are coupled to their effectors by Go. *Proc. Natl. Acad. Sci.* **98**, 3577–3582 (2001).

49. Cordeaux, Y., Nickolls, S. A., Flood, L. A., Graber, S. G. & Strange, P. G. Agonist regulation of D2 dopamine receptor/G protein interaction. Evidence for agonist selection of G protein subtype. *J. Biol. Chem.* **276**, 28667–28675 (2001).

50. Gazi, L., Nickolls, S. A. & Strange, P. G. Functional coupling of the human dopamine D 2 receptor with Gα i1, Gα i2, Gα i3 and Gα o G proteins: Evidence for agonist regulation of G protein selectivity. *Br. J. Pharmacol.* **138**, 775–786 (2003).

51. Lane, J. R., Powney, B., Wise, A., Rees, S. & Milligan, G. Protean agonism at the dopamine D2 receptor: (S)-3-(3-hydroxyphenyl)-N-propylpiperidine is an agonist for activation of Go1 but an antagonist/inverse agonist for Gi1, G i2, and Gi3. *Mol. Pharmacol.* **71**, 1349–1359 (2007).

52. Reiner-Link, D., Madsen, J. S., Gloriam, D. E., Bräuner-Osborne, H. & Hauser, A. S. Differential G protein activation by the long and short isoforms of the dopamine D 2 receptor. *Br. J. Pharmacol.* doi:10.1111/bph.16388 (2024).

53. Marcott, P. F. et al. Regional Heterogeneity of D2-Receptor Signaling in the Dorsal Striatum and Nucleus Accumbens. *Neuron* **98**, 575-587.e4 (2018).

54. Svenningsson, P. et al. DARPP-32: An Integrator of Neurotransmission. *Annu. Rev. Pharmacol. Toxicol.* **44**, 269–296 Preprint at https://doi.org/10.1146/annurev.pharmtox.44.101802.121415 (2004).

55. Gainetdinov, R. R., Premont, R. T., Bohn, L. M., Lefkowitz, R. J. & Caron, M. G. Desensitization of G protein-coupled receptors and neuronal functions. *Annu. Rev. Neurosci.* **27**, 107–144 Preprint at https://doi.org/10.1146/annurev.neuro.27.070203.144206 (2004).

56. Hollinger, S. & Hepler, J. R. Cellular regulation of RGS proteins: Modulators and integrators of G protein signaling. *Pharmacol. Rev.* **54,** 527–559 Preprint at https://doi.org/10.1124/pr.54.3.527 (2002).

57. Seeman, P., Ko, F., Jack, E., Greenstein, R. & Dean, B. Consistent with dopamine supersensitivity, RGS9 expression is diminished in the amphetamine-treated animal model of schizophrenia and in postmortem schizophrenia brain. *Synapse* **61**, 303–309 (2007).

58. Kovoor, A. et al. D2 dopamine receptors colocalize regulator of G-protein signaling 9-2 (RGS9-2) via the RGS9 DEP domain, and RGS9 knock-out mice develop dyskinesias associated with dopamine pathways. *J. Neurosci.* **25**, 2157–2165 (2005).

59. Boyd, K. N. & Mailman, R. B. Dopamine receptor signaling and current and future antipsychotic drugs. *Handb. Exp. Pharmacol.* **212**, 53–86 Preprint at https://doi.org/10.1007/978-3-642-25761-2_3 (2012).

60. Cho, D. et al. Agonist-induced endocytosis and receptor phosphorylation mediate resensitization of dopamine D2 receptors. *Mol. Endocrinol.* **24**, 574–586 (2010).

61. Namkung, Y., Dipace, C., Javitch, J. A. & Sibley, D. R. G protein-coupled receptor kinase-mediated phosphorylation regulates post-endocytic trafficking of the D2 dopamine receptor. *J. Biol. Chem.* **284**, 15038–15051 (2009).

62. Beaulieu, J. M. et al. An Akt/β-arrestin 2/PP2A signaling complex mediates dopaminergic neurotransmission and behavior. *Cell* **122**, 261–273 (2005).

63. Namkung, Y. & Sibley, D. R. Protein kinase C mediates phosphorylation, desensitization, and trafficking of the D2 dopamine receptor. *J. Biol. Chem.* **279**, 49533–49541 (2004).

64. Moore, C. A. C., Milano, S. K. & Benovic, J. L. Regulation of receptor trafficking by GRKs and arrestins. *Annu. Rev. Physiol.* **69**, 451–482 Preprint at https://doi.org/10.1146/annurev.physiol.69.022405.154712 (2007).

65. Rajagopal, S. & Shenoy, S. K. GPCR desensitization: Acute and prolonged phases. *Cell. Signal.* **41**, 9–16 (2018).

66. Hanyaloglu, A. C. & Von Zastrow, M. Regulation of GPCRs by endocytic membrane trafficking and its potential implications. *Annu. Rev. Pharmacol. Toxicol.* **48**, 537–568 Preprint at https://doi.org/10.1146/annurev.pharmtox.48.113006.094830 (2008).

67. Hosey, M. M. What molecular events underlie heterologous desensitization? Focus on "Receptor phosphorylation does not mediate cross talk between muscarinic M 3 and bradykinin B 2 receptors". *Am. J. Physiol. Cell Physiol.* **277**, C856–C858 (1999).

68. Morris, S. J. et al. Differential desensitization of dopamine D2 receptor isoforms by protein kinase C: The importance of receptor phosphorylation and pseudosubstrate sites. *Eur. J. Pharmacol.* **577**, 44–53 (2007).

69. Tabor, A., Möller, D., Hübner, H., Kornhuber, J. & Gmeiner, P. Visualization of ligand-induced dopamine D2S and D2L receptor internalization by TIRF microscopy. *Sci. Rep.* **7**, doi:10.1038/s41598-017-11436-1 (2017).

70. Thibault, D., Albert, P. R., Pineyro, G. & Trudeau, L.-É. Neurotensin Triggers Dopamine D2 Receptor Desensitization through a Protein Kinase C and β-Arrestin1-dependent Mechanism. *J. Biol. Chem.* **286**, 9174–9184 (2011).

71. Vickery, R. G. & Von Zastrow, M. Distinct dynamin-dependent and -independent mechanisms target structurally homologous dopamine receptors to different endocytic membranes. *J. Cell Biol.* **144**, 31–43 (1999).

72. Kim, K. M. et al. Differential Regulation of the Dopamine D2 and D3 Receptors by G Protein-coupled Receptor Kinases and β-Arrestins. *J. Biol. Chem.* **276**, 37409–37414 (2001).

73. Iwata, K., Ito, K., Fukuzaki, A., Inaki, K. & Haga, T. Dynamin and Rab5 regulate GRK2-dependent internalization of dopamine D2 receptors. *Eur. J. Biochem.* **263**, 596–602 (1999).

74. Bartlett, S. E. et al. Dopamine responsiveness is regulated by targeted sorting of D2 receptors. *Proc. Natl. Acad. Sci.* **102**, 11521–11526 (2005).

75. Marley, A. & Von Zastrow, M. Dysbindin promotes the post-endocytic sorting of G protein-coupled receptors to lysosomes. *PLoS One* **5**, doi:10.1371/journal.pone.0009325 (2010).

76. Li, Y. et al. Identification of two functionally distinct endosomal recycling pathways for dopamine D 2 receptor. *J. Neurosci.* **32**, 7178–7190 (2012).

77. Dal Toso, R. et al. The dopamine D2 receptor: two molecular forms generated by alternative splicing. *EMBO J.* **8**, 4025–4034 (1989).

78. Min, C. et al. N-linked Glycosylation on the N-terminus of the dopamine D2 and D3 receptors determines receptor association with specific microdomains in the plasma membrane. *Biochim. Biophys. Acta, Mol. Cell Res.* **1853**, 41–51 (2015).

79. Fishburn, C. S., Elazar, Z. & Fuchs, S. Differential glycosylation and intracellular trafficking for the long and short isoforms of the D2 dopamine receptor. *J. Biol. Chem.* **270**, 29819–29824 (1995).

80. Cho, D. et al. The N-terminal region of the dopamine D 2 receptor, a rhodopsin-like GPCR, regulates correct integration into the plasma membrane and endocytic routes. *Br. J. Pharmacol.* **166**, 659–675 (2012).

81. Patel, K. R., Cherian, J., Gohil, K. & Atkinson, D. Schizophrenia: Overview and treatment options. *P and T* **39**, 638–645 (2014).

82. Kahn, R. S. et al. Schizophrenia. *Nat. Rev. Dis. Primers* **1**, 1–23 (2015).

83. Correll, C. U. & Schooler, N. R. Negative symptoms in schizophrenia: A review and clinical guide for recognition, assessment, and treatment. *Neuropsychiatr. Dis. Treat.* **16,** 519–534 Preprint at https://doi.org/10.2147/NDT.S225643 (2020).

84. Picchioni, M. M. & Murray, R. M. Schizophrenia. *BMJ* **335**, 91–95 Preprint at https://doi.org/10.1136/bmj.39227.616447.BE (2007).

85. Boydell, J., van Os, J., McKenzie, K. & Murray, R. M. The association of inequality with the incidence of schizophrenia - An ecological study. *Soc. Psychiatry Psychiatr. Epidemiol*. **39**, 597–599 (2004).

86. Delay, J., Deniker, P. & Harl, J. M. Therapeutic use in psychiatry of phenothiazine of central elective action (4560 RP). *Ann. Med. Psychol*. **110**, 112–117 (1952).

87. Carlsson, A., Lindqvist, M. & Magnusson, T. 3,4-Dihydroxyphenylalanine and 5-hydroxytryptophan as reserpine antagonists. *Nature* **180**, 1200 Preprint at https://doi.org/10.1038/1801200a0 (1957).

88. Angrist, B. M., Schweitzer, J. W., Friedhoff, A. J. & Gershon, S. Investigation of p-methoxyamphetamine excretion in amphetamine induced psychosis. *Nature* **225**, 651–652 (1970).

89. Creese, I., Burt, D. R. & Snyder, S. H. Dopamine receptor binding predicts clinical and pharmacological potencies of antischizophrenic drugs. *Science (1979)* **192**, 481–483 (1976).

90. Seeman, P., Lee, T., Chau-Wong, M. & Wong, K. Antipsychotic drug doses and neuroleptic/dopamine receptors. *Nature* **261**, 717–719 (1976).

91. Snyder, S. H. The dopamine hypothesis of schizophrenia: focus on the dopamine receptor. *Am. J. Psychiatry* **133**, 197–202 (1976).

92. Ingvar, D. H. & Franzén, G. Abnormalities of cerebral blood flow distribution in patients with chronic schizophrenia. *Acta. Psychiatr. Scand*. **50**, 425–462 (1974).

93. Buchsbaum, M. S. et al. Cerebral Glucography with Positron Tomography: Use in Normal Subjects and in Patients with Schizophrenia. *Arch. Gen. Psychiatry* **39**, 251–259 (1982).

94. Lindström, L. H. Low HVA and normal 5HIAA CSF levels in drug-free schizophrenic patients compared to healthy volunteers: Correlations to symptomatology and family history. *Psychiatry Res.* **14**, 265–273 (1985).

95. Davis, K. L., Kahn, R. S., Ko, G. & Davidson, M. Dopamine in schizophrenia: A review and reconceptualization. *Am. J. Psychiatry* **148**, 1474–1486 (1991).

96. Scatton, B., Worms, P., Lloyd, K. G. & Bartholini, G. Cortical modulation of striatal function. *Brain Res*. **232**, 331–343 (1982).

97. Pycock, C. J., Kerwin, R. W. & Carter, C. J. Effect of lesion of cortical dopamine terminals on subcortical dopamine receptors in rats. *Nature* **286**, 74–77 (1980).

98. Howes, O. D. et al. Midbrain dopamine function in schizophrenia and depression: a post-mortem and positron emission tomographic imaging study. *Brain* **136**, 3242–3251 (2013).

99. Slifstein, M. et al. Deficits in Prefrontal Cortical and Extrastriatal Dopamine Release in Schizophrenia. *JAMA Psychiatry* **72**, 316-324 (2015).

100. Laruelle, M. & Abi-Dargham, A. Dopamine as the wind of the psychotic fire: new evidence from brain imaging studies. *J. Psychopharmacol*. **13**, 358–371 (1999).

101. Lindström, L. H. et al. Increased dopamine synthesis rate in medial prefrontal cortex and striatum in schizophrenia indicated by L-(β-11C) DOPA and PET. *Biol. Psychiatry* **46**, 681–688 (1999).

102. McGowan, S., Lawrence, A. D., Sales, T., Quested, D. & Grasby, P. Presynaptic Dopaminergic Dysfunction in Schizophrenia: A Positron Emission Tomographic [18F]Fluorodopa Study. *Arch. Gen. Psychiatry* **61**, 134–142 (2004).

103. Howes, O. D. & Kapur, S. The dopamine hypothesis of schizophrenia: Version III - The final common pathway. *Schizophr. Bull.* **35**, 549–562 Preprint at https://doi.org/10.1093/schbul/sbp006 (2009).

104. Howes, O. D. et al. The Nature of Dopamine Dysfunction in Schizophrenia and What This Means for Treatment. *Arch. Gen. Psychiatry* **69**, 776-786 (2012).

105. Pijnenburg, A. J. J., Honig, W. M. M. & Van Rossum, J. M. Inhibition of d-amphetamine-induced locomotor activity by injection of haloperidol into the nucleus accumbens of the rat. *Psychopharmacologia* **41**, 87–95 (1975).

106. McCutcheon, R., Beck, K., Jauhar, S. & Howes, O. D. Defining the Locus of Dopaminergic Dysfunction in Schizophrenia: A Meta-analysis and Test of the Mesolimbic Hypothesis. *Schizophr. Bull.* **44**, 1301–1311 (2018).

107. McCutcheon, R. A., Abi-Dargham, A. & Howes, O. D. Schizophrenia, Dopamine and the Striatum: From Biology to Symptoms. *Trends Neurosci.* **42**, 205–220 (2019).

108. Purves-Tyson, T. D., Brown, A. M., Weissleder, C., Rothmond, D. A. & Shannon Weickert, C. Reductions in midbrain GABAergic and dopamine neuron markers are linked in schizophrenia. *Mol. Brain* **14**, doi:10.1186/s13041-021-00805-7 (2021).

109. Kang, J. I. et al. Reduced Binding Potential of GABA-A/Benzodiazepine Receptors in Individuals at Ultra-high Risk for Psychosis: An [18F]-Fluoroflumazenil Positron Emission Tomography Study. *Schizophr. Bull.* **40**, 548-557 (2014).

110. Farber, N. B. The NMDA Receptor Hypofunction Model of Psychosis. *Ann. N Y Acad. Sci.* **1003**, 119–130 (2003).

111. Roth, B. L., Sheffer, D. J. & Kroeze, W. K. Magic shotguns versus magic bullets: Selectively non-selective drugs for mood disorders and schizophrenia. *Nat. Rev. Drug Discov*. **3**, 353–359 Preprint at https://doi.org/10.1038/nrd1346 (2004).

112. Kenakin, T. & Williams, M. Defining and characterizing drug/compound function. *Biochem. Pharmacol.* **87**, 40–63 (2014).

113. Li, P., L. Snyder, G. & E. Vanover, K. Dopamine Targeting Drugs for the Treatment of Schizophrenia: Past, Present and Future. *Curr. Top. Med. Chem.* **16**, 3385–3403 (2016).

114. Miller, D. D. et al. Extrapyramidal side-effects of antipsychotics in a randomised trial. *Br. J. Psychiatry* **193**, 279–288 (2008).

115. Miyamoto, S., Miyake, N., Jarskog, L. F., Fleischhacker, W. W. & Lieberman, J. A. Pharmacological treatment of schizophrenia: A critical review of the pharmacology and clinical effects of current and future therapeutic agents. *Mol. Psychiatry* **17**, 1206–1227 (2012).

116. Caron, M. G. et al. Dopaminergic receptors in the anterior pituitary gland. Correlation of [3H]dihydroergocryptine binding with the dopaminergic control of prolactin release. *JBC* **253**, 2244–2253 (1978).

117. Kapur, S., Zipursky, R., Jones, C., Remington, G. & Houle, S. Relationship between dopamine D2 occupancy, clinical response, and side effects: A double-blind PET study of first-episode schizophrenia. *Am. J. Psychiatry* **157**, 514–520 (2000).

118. Stępnicki, P., Kondej, M. & Kaczor, A. A. Current concepts and treatments of schizophrenia. *Molecules* **23**, 2087 Preprint at https://doi.org/10.3390/molecules23082087 (2018).

119. Gardner, D. M., Baldessarini, R. J. & Waraich, P. Modern antipsychotic drugs: A critical overview. *CMAJ* **172**, 1703–1711 Preprint at https://doi.org/10.1503/cmaj.1041064 (2005).

120. Kane, J., Honigfeld, G., Singer, J. & Meltzer, H. Clozapine for the Treatment-Resistant Schizophrenic: A Double-blind Comparison With Chlorpromazine. *Arch. Gen. Psychiatry* **45**, 789–796 (1988).

121. Nucifora, F. C., Mihaljevic, M., Lee, B. J. & Sawa, A. Clozapine as a Model for Antipsychotic Development. *Neurotherapeutics* **14**, 750–761 (2017).

122. Leucht, S. et al. Second-generation versus first-generation antipsychotic drugs for schizophrenia: a meta-analysis. *The Lancet* **373**, 31–41 (2009).

123. Michelsen, J. W. & Meyer, J. M. Cardiovascular effects of antipsychotics. *Expert Rev. Neurother.* **7**, 829–839 Preprint at https://doi.org/10.1586/14737175.7.7.829 (2007).

124. Meltzer, H. Y. & Massey, B. W. The role of serotonin receptors in the action of atypical antipsychotic drugs. *Curr. Opin. Pharmacol.* **11**, 59–67 Preprint at https://doi.org/10.1016/j.coph.2011.02.007 (2011).

125. Malmberg, Mikaels & Mohell, N. Agonist and inverse agonist activity at the dopamine D3 receptor measured by guanosine 5'--gamma-thio-triphosphate--35S- binding. *J. Pharmacol. Exp. Ther.* **285**, 119–126 (1998).

126. Hall, D. A. & Strange, P. G. Evidence that antipsychotic drugs are inverse agonists at D 2 dopamine receptors. *Br. J. Pharmacol.* **121**, 731–736 (1997).

127. Wurch, T., Boutet-Robinet, E. A., Palmier, C., Colpaert, F. C. & Pauwels, P. J. Constitutive Coupling of a Chimeric Dopamine D 2 /α 1 B Receptor to the Phospholipase C Pathway: Inverse Agonism to Silent Antagonism by Neuroleptic Drugs. *J. Pharmacol. Exp. Ther.* **304**, 380–390 (2003).

128. Mailman, R. & Murthy, V. Third Generation Antipsychotic Drugs: Partial Agonism or Receptor Functional Selectivity? *Curr. Pharm. Des.* **16**, 488–501 (2010).

129. Gründer, G., Carlsson, A. & Wong, D. F. Mechanism of new antipsychotic medications: Occupancy is not just antagonism. *Arch. Gen. Psychiatry* **60**, 974–977 Preprint at https://doi.org/10.1001/archpsyc.60.10.974 (2003).

130. Davidson, M. et al. Cognitive Effects of Antipsychotic Drugs in First-Episode Schizophrenia and Schizophreniform Disorder: A Randomized, Open-Label Clinical Trial (EUFEST). *Am. J. Psychiatry* **166**, 675–682 (2009).

131. Keefe, R. S. E. Neurocognitive Effects of Antipsychotic Medications in Patients With Chronic Schizophrenia in the CATIE Trial. *Arch. Gen. Psychiatry* **64**, 633-647 (2007).

132. Correll, C. U., Leucht, S. & Kane, J. M. Lower risk for tardive dyskinesia associated with second-generation antipsychotics: a systematic review of 1-year studies. *Am. J. Psychiatry* **161**, 414–425 (2004).

133. Farah, A. Atypicality of Atypical Antipsychotics. Prim Care Companion *J. Clin. Psychiatry* **7**, 268-274 (2005).

134. Goldstein, J. M. The new generation of antipsychotic drugs : how atypical are they ? *Int. J. of Neuropsychopharmacol.* **3**, 339–349 (2000).

135. Burki, H. R. Effects of fluperlapine on dopaminergic systems in rat brain. *Psychopharmacology* **89**, 77–84 (1986).

136. Seeman, P., Corbettand, R. & Van Tol, H. H. M. Atypical neuroleptics have low affinity for dopamine D2 receptors or are selective for D4 receptors. *Neuropsychopharmacology* **16**, 93–110 Preprint at https://doi.org/10.1016/S0893-133X(96)00187-X (1997).

137. Seeman, P. & Tallerico, T. Antipsychotic drugs which elicit little or no Parkinsonism bind more loosely than dopamine to brain D2 receptors, yet occupy high levels of these receptors. *Mol. Psychiatry* **3**, 123–134 (1998).

138. Seeman, P. & Tallerico, T. Rapid release of antipsychotic drugs from dopamine D2 receptors: An explanation for low receptor occupancy and early clinical relapse upon withdrawal of clozapine or quetiapine. *Am. J. Psychiatry* **156**, 876–884 (1999).

139. Kapur, S. & Seeman, P. Does fast dissociation from the dopamine D2 receptor explain the action of atypical antipsychotics?: A new hypothesis. *Am. J. Psychiatry* **158**, 360–369 Preprint at https://doi.org/10.1176/appi.ajp.158.3.360 (2001).

140. Saller, C. F. & Salama, A. I. Seroquel: biochemical profile of a potential atypical antipsychotic. *Psychopharmacology* **112**, 285–292 (1993).

141. Kapur, S. & Seeman, P. Antipsychotic agents differ in how fast they come off the dopamine D2 receptors. Implications for atypical antipsychotic action. *J. Psychiatry Neurosci.* **25**, 161–166 (2000).

142. Packeu, A., Wennerberg, M., Balendran, A. & Vauquelin, G. Estimation of the dissociation rate of unlabelled ligand-receptor complexes by a 'two-step' competition binding approach. Br. J. Pharmacol. **161**, 1311–1328 (2010).

143. Sahlholm, K. et al. The fast-off hypothesis revisited: A functional kinetic study of antipsychotic antagonism of the dopamine D2 receptor. *Eur. Neuropsychopharmacol.* **26**, 467–476 (2016).

144. Meltzer, H. Y. Update on typical and atypical antipsychotic drugs. Ann. Rev. Med. **64**, 393–406 Preprint at https://doi.org/10.1146/annurev-med-050911-161504 (2013).

145. Sykes, D. A. et al. Extrapyramidal side effects of antipsychotics are linked to their association kinetics at dopamine D2 receptors. *Nat. Commun.* **8**, 1–11 (2017).

146. Lieberman, J. A. Dopamine Partial Agonists. *CNS Drugs* **18**, 251–267 (2004).

147. Kessler, R. M. et al. Occupancy of Striatal and Extrastriatal Dopamine D2 Receptors by Clozapine and Quetiapine. *Neuropsychopharmacology* **31**, 1991–2001 (2006).

148. Bressan, R. A. et al. Optimizing Limbic Selective D2/D3 Receptor Occupancy by Risperidone: A [123I]-Epidepride SPET Study. *J. Clin. Psychopharmacol.* **23**, 5–14 (2003).

149. Bressan, R. A. et al. Is Regionally Selective D 2 /D 3 Dopamine Occupancy Sufficient for Atypical Antipsychotic Effect? An In Vivo Quantitative [123 I]Epidepride SPET Study of Amisulpride-Treated Patients. *Am. J. Psychiatry* **160**, 1413–1420 (2003).

150. Janssen, P. A. et al. Pharmacology of risperidone (R 64 766), a new antipsychotic with serotonin-S2 and dopamine-D2 antagonistic properties. *J. Pharmacol. Exp. Ther.* **244**, 685–93 (1988).

151. Meltzer, H. Y., Li, Z., Kaneda, Y. & Ichikawa, J. Serotonin receptors: Their key role in drugs to treat schizophrenia. *Prog. Neuropsychopharmacol. Biol. Psychiatry* **27**, 1159–1172 (2003).

152. Kusumi, I., Boku, S. & Takahashi, Y. Psychopharmacology of atypical antipsychotic drugs: From the receptor binding profile to neuroprotection and neurogenesis. *Psychiatry Clin. Neurosci.* **69**, 243–258 (2015).

153. Nikolaus, S. et al. Serotonergic Modulation of Nigrostriatal and Mesolimbic Dopamine and Motor/Exploratory Behaviors in the Rat. *Front. Neurosci.* **15**, doi: 10.3389/fnins.2021.682398 (2021).

154. Kharkwal, G. et al. Parkinsonism Driven by Antipsychotics Originates from Dopaminergic Control of Striatal Cholinergic Interneurons. *Neuron* **91**, 67–78 (2016).

155. Bertran-Gonzalez, J., Chieng, B. C., Laurent, V., Valjent, E. & Balleine, B. W. Striatal Cholinergic Interneurons Display Activity-Related Phosphorylation of Ribosomal Protein S6. *PLoS One* **7**, doi:10.1371/journal.pone.0053195 (2012).

156. Sur, C. et al. N-desmethylclozapine, an allosteric agonist at muscarinic 1 receptor, potentiates N-methyl-D-aspartate receptor activity. *Proc. Natl. Acad. Sci. U S A* **100**, 13674–13679 (2003).

157. Krystal, J. H. Subanesthetic Effects of the Noncompetitive NMDA Antagonist, Ketamine, in Humans. *Arch. Gen. Psychiatry* **51**, 199-214 (1994).

158. Kokkinou, M., Ashok, A. H. & Howes, O. D. The effects of ketamine on dopaminergic function: meta-analysis and review of the implications for neuropsychiatric disorders. *Mol. Psychiatry* **23**, 59–69 (2018).

159. Panayi, M. C. et al. Glutamatergic dysfunction leads to a hyper-dopaminergic phenotype through deficits in short-term habituation: a mechanism for aberrant salience. *Mol. Psychiatry* **28**, 579–587 (2023).

160. Ellaithy, A., Younkin, J., González-Maeso, J. & Logothetis, D. E. Positive allosteric modulators of metabotropic glutamate 2 receptors in schizophrenia treatment. *Trends Neurosci.* **38**, 506–516 (2015).

161. Duncan, G. E., Miyamoto, S. & Lieberman, J. A. Chronic Administration of Haloperidol and Olanzapine Attenuates Ketamine-Induced Brain Metabolic Activation. *J. Pharmacol. Exp.* **305**, 999–1005 (2003).

162. Vauquelin, G. & Charlton, S. J. Long-lasting target binding and rebinding as mechanisms to prolong in vivo drug action. *Br. J. Pharmacol.* **161**, 488–508 Preprint at https://doi.org/10.1111/j.1476-5381.2010.00936.x (2010).

163. Limbird, L. E. *Cell Surface Receptors: A Short Course on Theory and Methods.* (Springer US, 1996). doi:10.1007/978-1-4613-1255-0.

164. Sutter, A., Riopelle, R. J., Harris-Warrick, R. M. & Shooter, E. M. Nerve growth factor receptors. Characterization of two distinct classes of binding sites on chick embryo sensory ganglia cells. *J. Biol. Chem.* **254**, 5972–82 (1979).

165. Fierens, F., Vanderheyden, P. M. L., De Backer, J.-P. & Vauquelin, G. Binding of the antagonist [3H]candesartan to angiotensin II AT1 receptor-tranfected Chinese hamster ovary cells. *Eur. J. Pharmacol.* **367**, 413–422 (1999).

166. Le, M. T., Pugsley, M. K., Vauquelin, G. & Van Liefde, I. Molecular characterisation of the interactions between olmesartan and telmisartan and the human angiotensin II AT 1 receptor. *Br. J. Pharmacol.* **151**, 952–962 (2007).

167. Delisi, C. The effect of cell size and receptor density on ligand-receptor reaction rate constants. *Mol. Immunol.* **18**, 507–511 (1981).

168. Vauquelin, G. Rebinding: Or why drugs may act longer in vivo than expected from their in vitro target residence time. *Expert Opin. Drug Discov.* **5**, 927–941 (2010).

169. Farde, L. et al. D2 Dopamine Receptors in Neuroleptic-Naive Schizophrenic Patients: A Positron Emission Tomography Study with [11C]Raclopride. *Arch. Gen. Psychiatry* **47**, 213–219 (1990).

170. Nordstrom, A. L., Farde, L., Eriksson, L. & Halldin, C. No elevated D2 dopamine receptors in neuroleptic-naive schizophrenic patients revealed by positron emission tomography and [11C]N-methylspiperone. *Psychiatry Res. Neuroimaging* **61**, 67–83 (1995).

171. Wong, D. F. et al. Quantification of neuroreceptors in the living human brain: IV. Effect of aging and elevations of D2-like receptors in schizophrenia and bipolar illness. *J. Cereb. Blood Flow Metab.* **17**, 331–342 (1997).

172. Burt, D. R., Creese, I. A. N. & Snyder, S. H. Antischizophrenic drugs: Chronic treatment elevates dopamine receptor binding in brain. *Science (1979)* **196**, 326–328 (1977).

173. Lee, T., Seeman, P., Tourtellotte, W. W., Farley, I. J. & Hornykeiwicz, O. Binding of 3H-neuroleptics and 3H-apomorphine in schizophrenic brains. *Nature* **274**, 897–900 Preprint at https://doi.org/10.1038/274897a0 (1978).

174. Silvestri, S. et al. Increased dopamine D2 receptor binding after long-term treatment with antipsychotics in humans: a clinical PET study. *Psychopharmacology* **152**, 174–180 (2000).

175. Mathews, M. et al. Antipsychotic-Induced Movement Disorders: Evaluation and Treatment. *Psychiatry* **2**, 36-41 (2005).

176. Seeman, P. Tardive dyskinesia, dopamine receptors, and neuroleptic damage to cell membranes. *J. Clin. Psychopharmacol.* **8**, 3S-9S (1988).

177. Samaha, A. N., Seeman, P., Stewart, J., Rajabi, H. & Kapur, S. 'Breakthrough' dopamine supersensitivity during ongoing antipsychotic treatment leads to treatment failure over time. *J. Neurosci.* **27**, 2979–2986 (2007).

178. Schrader, J. M. et al. The differential actions of clozapine and other antipsychotic drugs on the translocation of dopamine D2 receptors to the cell surface. *J. Biol. Chem.* **294**, 5604–5615 (2019).

179. Carbon, M., Kane, J. M., Leucht, S. & Correll, C. U. Tardive dyskinesia risk with first- and second-generation antipsychotics in comparative randomized controlled trials: a meta-analysis. *World J. Psychiatry* **17**, 330–340 (2018).

180. Allen, J. A. et al. Discovery of β-arrestin-biased dopamine D 2 ligands for probing signal transduction pathways essential for antipsychotic efficacy. *Proc. Natl. Acad. Sci. U S A* **108**, 18488–18493 (2011).

181. Tao, Y. X. & Conn, P. M. Chaperoning G Protein-Coupled Receptors: From Cell Biology to Therapeutics. *Endocr. Rev.* **35**, 602–647 (2014).

182. Cokan, K. B. et al. Critical impact of different conserved endoplasmic retention motifs and dopamine receptor interacting proteins (Drips) on intracellular localization and trafficking of the d2 dopamine receptor (D2-r) isoforms. *Biomolecules* **10**, 1–18 Preprint at https://doi.org/10.3390/biom10101355 (2020).

183. Hollins, B., Kuravi, S., Digby, G. J. & Lambert, N. A. The c-terminus of GRK3 indicates rapid dissociation of G protein heterotrimers. *Cell Signal.* **21**, 1015–1021 (2009).

184. Lan, T. H., Liu, Q., Li, C., Wu, G. & Lambert, N. A. Sensitive and High Resolution Localization and Tracking of Membrane Proteins in Live Cells with BRET. *Traffic.* **13**, 1450–1456 (2012).

185. Smith, P. K. et al. Measurement of protein using bicinchoninic acid. *Anal. Biochem.* **150**, 76–85 (1985).

186. Shrestha, D., Jenei, A., Nagy, P., Vereb, G. & Szöllősi, J. Understanding FRET as a Research Tool for Cellular Studies. *Int. J. Mol. Sci.* **16**, 6718-6756 (2015).

187. Briddon, S. J. et al. Quantitative analysis of the formation and diffusion of A 1-adenosine receptor-antagonist complexes in single living cells. *Proc. Natl. Acad. Sci. U S A* **101**, 4673–4678 (2004).

188. Ayling, L. J. et al. Adenylyl cyclase AC8 directly controls its micro-environment by recruiting the actin cytoskeleton in a cholesterol-rich milieu. *J. Cell. Sci.* **125**, 869–886 (2012).

189. Goulding, J. et al. The use of fluorescence correlation spectroscopy to monitor cell surface β2-adrenoceptors at low expression levels in human embryonic stem cell-derived cardiomyocytes and fibroblasts. *FASEB Journal* **35**, doi:10.1096/fj.202002268R (2021).

190. Huang, B., Perroud, T. D. & Zare, R. N. Photon Counting Histogram: One-Photon Excitation. *ChemPhysChem* **5**, 1523–1531 (2004).

191. Briddon, S. J., Kilpatrick, L. E. & Hill, S. J. Studying GPCR Pharmacology in Membrane Microdomains: Fluorescence Correlation Spectroscopy Comes of Age. *Trends Pharmacol. Sci.* **39**, 158–174 (2018).

192. Kilpatrick, L. E. & Hill, S. J. The use of fluorescence correlation spectroscopy to characterise the molecular mobility of G protein-coupled receptors in membrane microdomains: an update. *Biochem. Soc. Trans.* **49**, 1547–1554 (2021).

193. Kilpatrick, L. E. & Hill, S. J. The use of fluorescence correlation spectroscopy to characterize the molecular mobility of fluorescently labelled G protein-coupled receptors. *Biochem. Soc. Trans.* **44**, 624–629 (2016).

194. Zhulou, W. et al. Principles of fluorescence correlation spectroscopy applied to studies of biomolecular liquid–liquid phase separation. *Biophys. Rep.* **8**, 100–118 (2022).

195. Betaneli, V., Mücksch, J. & Schwille, P. Fluorescence Correlation Spectroscopy to Examine Protein–Lipid Interactions in Membranes. *Methods Mol. Biol.* 415–447, doi:10.1007/978-1-4939-9512-7_18 (2019).

196. Dawes, M. L., Soeller, C. & Scholpp, S. Studying molecular interactions in the intact organism: fluorescence correlation spectroscopy in the living zebrafish embryo. *Histochem. Cell. Biol.* **154**, 507–519 (2020).

197. Hauser, A. S., Attwood, M. M., Rask-Andersen, M., Schiöth, H. B. & Gloriam, D. E. Trends in GPCR drug discovery: new agents, targets and indications. *Nat. Rev. Drug Discov.* **16**, 829–842 (2017).

198. Hill, S. J. & Watson, S. P. Fluorescence Approaches Unravel Spatial and Temporal Aspects of GPCR Organisation, Location, and Intracellular Signalling. *Trends Pharmacol. Sci.* **39**, 91–92 (2018).

199. Lohse, M. J. & Hofmann, K. P. Spatial and Temporal Aspects of Signaling by G-Protein–Coupled Receptors. *Mol. Pharmacol.* **88**, 572–578 (2015).

200. Ellisdon, A. M. & Halls, M. L. Compartmentalization of GPCR signalling controls unique cellular responses. *Biochem. Soc. Trans.* **44**, 562–567 (2016).

201. Yu, L. et al. A Comprehensive Review of Fluorescence Correlation Spectroscopy. *Front. Phys.* **9**, 1–21 (2021).

202. Briddon, S. J. & Hill, S. J. Pharmacology under the microscope: the use of fluorescence correlation spectroscopy to determine the properties of ligand–receptor complexes. *Trends Pharmacol. Sci.* **28**, 637–645 (2007).

203. Hegener, O. et al. Dynamics of β 2 -Adrenergic Receptor−Ligand Complexes on Living Cells. *Biochemistry* **43**, 6190–6199 (2004).

204. Corriden, R., Kilpatrick, L. E., Kellam, B., Briddon, S. J. & Hill, S. J. Kinetic analysis of antagonist-occupied adenosine-A 3 receptors within membrane microdomains of

individual cells provides evidence of receptor dimerization and allosterism. *FASEB J.* **28**, 4211–4222 (2014).

205. Middleton, R. J. et al. New Fluorescent Adenosine A 1 -Receptor Agonists That Allow Quantification of Ligand−Receptor Interactions in Microdomains of Single Living Cells. *J. Med. Chem.* **50**, 782–793 (2007).

206. Rose, R. H., Briddon, S. J. & Hill, S. J. A novel fluorescent histamine H 1 receptor antagonist demonstrates the advantage of using fluorescence correlation spectroscopy to study the binding of lipophilic ligands. *Br. J. Pharmacol.* **165**, 1789–1800 (2012).

207. Cordeaux, Y., Briddon, S. J., Alexander, S. P. H., Kellam, B. & Hill, S. J. Agonist-occupied A 3 adenosine receptors exist within heterogeneous complexes in membrane microdomains of individual living cells. *FASEB J.* **22**, 850–860 (2008).

208. Pramanik, A. & Rigler, R. Ligand-Receptor Interactions in the Membrane of Cultured Cells Monitored by Fluorescence Correlation Spectroscopy. Biol. Chem. **382**, 371-378 (2001).

209. Gherbi, K., Briddon, S. J. & Charlton, S. J. Micro-pharmacokinetics: Quantifying local drug concentration at live cell membranes. *Sci. Rep.* **8**, 1–9 (2018).

210. Albizu, L. et al. Time-resolved FRET between GPCR ligands reveals oligomers in native tissues. *Nat. Chem. Biol.* **6**, 587–594 (2010).

211. Altan-Bonnet, N. & Altan-Bonnet, G. Fluorescence Correlation Spectroscopy in Living Cells: A Practical Approach. *Curr. Protoc. Cell Biol.* **45**, doi: 10.1002/0471143030.cb0424s45 (2009).

212. Biener, G., Stoneman, M. R. & Raicu, V. Fluorescence intensity fluctuation analysis of receptor oligomerization in membrane domains. *Biophys. J.* **120**, 3028–3039 (2021).

213. Gondin, A. B., Halls, M. L., Canals, M. & Briddon, S. J. GRK mediates μ-opioid receptor plasma membrane reorganization. *Front. Mol. Neurosci.* **12**, doi:10.3389/fnmol.2019.00104 (2019).

214. Reeves, P. J., Kim, J.-M. & Khorana, H. G. Structure and function in rhodopsin: A tetracycline-inducible system in stable mammalian cell lines for high-level expression of opsin mutants. *Proc. Natl. Acad. Sci.* **99**, 13413–13418 (2002).

215. Jiang, W. et al. Tetracycline-regulated Gene Expression Mediated by a Novel Chimeric Repressor That Recruits Histone Deacetylases in Mammalian Cells. *J. Biol. Chem.* **276**, 45168–45174 (2001).

216. Zhou, X. et al. Diffusion and Oligomerization States of the Muscarinic M 1 Receptor in Live Cells–The Impact of Ligands and Membrane Disruptors. *J. Phys. Chem. B* **128**, 4354–4366 (2024).

217. Işbilir, A. et al. Advanced fluorescence microscopy reveals disruption of dynamic CXCR4 dimerization by subpocket-specific inverse agonists. *Proc. Natl. Acad. Sci.* **117**, 29144–29154 (2020).

218. Kitamura, A. & Kinjo, M. Determination of diffusion coefficients in live cells using fluorescence recovery after photobleaching with wide-field fluorescence microscopy. *Biophys. Physicobiol.* **15**, 1–7 (2018).

219. Pack, C., Saito, K., Tamura, M. & Kinjo, M. Microenvironment and Effect of Energy Depletion in the Nucleus Analyzed by Mobility of Multiple Oligomeric EGFPs. *Biophys. J.* **91**, 3921–3936 (2006).

220. Meseth, U., Wohland, T., Rigler, R. & Vogel, H. Resolution of Fluorescence Correlation Measurements. Biophys. J. **76**, 1619–1631 (1999).

221. Herrick-Davis, K., Grinde, E., Cowan, A. & Mazurkiewicz, J. E. Fluorescence Correlation Spectroscopy Analysis of Serotonin, Adrenergic, Muscarinic, and Dopamine Receptor Dimerization: The Oligomer Number Puzzle. *Mol. Pharmacol.* **84**, 630–642 (2013).

222. Herrick-Davis, K., Grinde, E., Lindsley, T., Cowan, A. & Mazurkiewicz, J. E. Oligomer Size of the Serotonin 5-Hydroxytryptamine 2C (5-HT2C) Receptor Revealed by Fluorescence Correlation Spectroscopy with Photon Counting Histogram Analysis. *J. Biol. Chem.* **287**, 23604–23614 (2012).

223. Guo, W. et al. Dopamine D2 receptors form higher order oligomers at physiological expression levels. *EMBO J.* **27**, 2293–2304 (2008).

224. Scarselli, M., Annibale, P. & Radenovic, A. Cell Type-specific β2-Adrenergic Receptor Clusters Identified Using Photoactivated Localization Microscopy Are Not Lipid Raft Related, but Depend on Actin Cytoskeleton Integrity. *J. Biol. Chem.* **287**, 16768–16780 (2012).

225. Laude, A. J. & Prior, I. A. Plasma membrane microdomains: Organization, function and trafficking (Review). *Mol. Membr. Biol.* **21**, 193–205 (2004).

226. Meyer, B. H. et al. FRET imaging reveals that functional neurokinin-1 receptors are monomeric and reside in membrane microdomains of live cells. *Proc. Natl. Acad. Sci.* **103**, 2138–2143 (2006).

227. Sharma, M., Celver, J., Octeau, J. C. & Kovoor, A. Plasma Membrane Compartmentalization of D2 Dopamine Receptors. *J. Biol. Chem.* **288**, 12554–12568 (2013).

228. Onishi, T., Sakamoto, H., Namiki, S. & Hirose, K. The Altered Supramolecular Structure of Dopamine D2 Receptors in Disc1-deficient Mice. *Sci. Rep.* **8**, doi: 10.1038/s41598-018-20090-0 (2018).

229. Lebowitz, J. J. et al. Subcellular localization of D2 receptors in the murine substantia nigra. *Brain Struct. Funct.* **227**, 925–941 (2022).

230. Gantz, S. C. et al. Distinct regulation of dopamine D2S and D2L autoreceptor signaling by calcium. *Elife* **4**, doi: 10.7554/eLife.09358 (2015).

231. Gossen, M. & Bujard, H. Tight control of gene expression in mammalian cells by tetracycline-responsive promoters. *Proc. Natl. Acad. Sci.* **89**, 5547–5551 (1992).

232. Barberis, M. & Verbruggen, P. Quantitative Systems Biology to decipher design principles of a dynamic cell cycle network: the “Maximum Allowable mammalian Trade–Off–Weight” (MAmTOW). *NPJ Syst. Biol. Appl.* **3**, doi:10.1038/s41540-017-0028-x (2017).

233. Cox, R. S., Surette, M. G. & Elowitz, M. B. Programming gene expression with combinatorial promoters. *Mol. Syst. Biol.* **3**, doi:10.1038/msb4100187 (2007).

234. Costello, A. et al. Leaky Expression of the TET-On System Hinders Control of Endogenous miRNA Abundance. *Biotechnol. J.* **14**, doi:10.1002/biot.201800219 (2019).

235. Johansson, B. et al. Hyperalgesia, anxiety, and decreased hypoxic neuroprotection in mice lacking the adenosine A 1 receptor. *Proc. Natl. Acad. Sci.* **98**, 9407–9412 (2001).

236. Fredholm, B. B. Adenosine receptors as drug targets. *Exp. Cell Res.* **316**, 1284–1288 (2010).

237. Tian, Y., Martinez, M. M. & Pappas, D. Fluorescence Correlation Spectroscopy: A Review of Biochemical and Microfluidic Applications. *Appl. Spectrosc.* **65**, 115–124 (2011).

238. Siafis, S. et al. Antipsychotic dose, dopamine D2 receptor occupancy and extrapyramidal side-effects: a systematic review and dose-response meta-analysis. *Mol. Psychiatry* **28**, 3267–3277 (2023).

239. Nordström, A.-L. et al. Central D2-dopamine receptor occupancy in relation to antipsychotic drug effects: A double-blind PET study of schizophrenic patients. *Biol. Psychiatry* **33**, 227–235 (1993).

240. Kapur, S. A new framework for investigating antipsychotic action in humans: lessons from PET imaging. *Mol. Psychiatry* **3**, 135–140 (1998).

241. Kapur, S. & Remington, G. Atypical Antipsychotics: New Directions and New Challenges in the Treatment of Schizophrenia. *Annu. Rev. Med.* **52**, 503–517 (2001).

242. Farde, L. Positron Emission Tomographic Analysis of Central D1 and D2 Dopamine Receptor Occupancy in Patients Treated With Classical Neuroleptics and Clozapine. *Arch. Gen. Psychiatry* **49**, 538-544 (1992).

243. Weston-Green, K. Antipsychotic Drug Development: From Historical Evidence to Fresh Perspectives. *Front. Psychiatry* **13**, doi:10.3389/fpsyt.2022.903156 (2022).

244. Breier, A. et al. Effects of clozapine on positive and negative symptoms in outpatients with schizophrenia. *Am. J. Psychiatry* **151**, 20–6 (1994).

245. Seeman, M. V. History of the dopamine hypothesis of antipsychotic action. *World J. Psychiatry* **11**, 355–364 (2021).

246. Nord, M. & Farde, L. Antipsychotic Occupancy of Dopamine Receptors in Schizophrenia. *CNS Neurosci. Ther.* **17**, 97–103 Preprint at https://doi.org/10.1111/j.1755-5949.2010.00222.x (2011).

247. Shapiro, D. A. et al. Aripiprazole, a novel atypical antipsychotic drug with a unique and robust pharmacology. *Neuropsychopharmacology* **28**, 1400–11 (2003).

248. Lagerholm, B. C. & Thompson, N. L. Theory for Ligand Rebinding at Cell Membrane § Surfaces. *Biophys. J.* **74**, 1215–1228 (1998).

249. Leucht, S. et al. Comparative efficacy and tolerability of 15 antipsychotic drugs in schizophrenia: a multiple-treatments meta-analysis. *Lancet* **382**, 951–962 (2013).

250. Elson, E. L. Fluorescence correlation spectroscopy: Past, present, future. *Biophys. J.* **101**, 2855–2870 Preprint at https://doi.org/10.1016/j.bpj.2011.11.012 (2011).

251. Vauquelin, G. Effects of target binding kinetics on in vivo drug efficacy: k off, k on and rebinding. *Br. J. Pharmacol.* **173**, 2319-2334 (2016).

252. Spivak, C. E., Oz, M., Beglan, C. L. & Shrager, R. I. Diffusion Delays and Unstirred Layer Effects at Monolayer Cultures of Chinese Hamster Ovary Cells: Radioligand Binding, Confocal Microscopy, and Mathematical Simulations. *Cell Biochem. Biophys.* **45**, 43–58 (2006).

253. Tzanova, M. M., Randelov, E., Stein, P. C., Hiorth, M. & di Cagno, M. P. Towards a better mechanistic comprehension of drug permeation and absorption: Introducing the diffusion-partitioning interplay. *Int. J. Pharm.* **608**, doi:10.1016/j.ijpharm.2021.121116 (2021).

254. Silhavy, T. J., Szmelcman, S., Boos, W. & Schwartz, M. On the significance of the retention of ligand by protein. *Proc. Natl. Acad. Sci.* **72**, 2120–2124 (1975).

255. Poksay, K. S. et al. Screening for Small Molecule Inhibitors of Statin-Induced APP C-terminal Toxic Fragment Production. *Front. Pharmacol.* **8**, doi:10.3389/fphar.2017.00046 (2017).

256. Yau, E., Petersson, C., Dolgos, H. & Peters, S. A. A comparative evaluation of models to predict human intestinal metabolism from nonclinical data. *Biopharm. Drug Dispos.* **38**, 163–186 (2017).

257. Seydel, J. K., Coats, E. A., Cordes, H. P. & Wiese, M. Drug Membrane Interaction and the Importance for Drug Transport, Distribution, Accumulation, Efficacy and Resistance. *Arch. Pharm.* **327**, 601–610 (1994).

258. Vauquelin, G. Cell membranes… and how long drugs may exert beneficial pharmacological activity in vivo. *Br. J. Clin. Pharmacol.* **82**, 673–682 (2016).

259. Lee, Y. & Choi, S. Q. Quantitative analysis for lipophilic drug transport through a model lipid membrane with membrane retention. *Eur. J. Pharm. Sci.* **134**, 176–184 (2019).

260. Burke, D. A., Rotstein, H. G. & Alvarez, V. A. Striatal local circuitry: a new framework for lateral inhibition. *Neuron* **96**, 267-284 (2017).

261. Coombs, D. & Goldstein, B. Effects of the geometry of the immunological synapse on the delivery of effector molecules. *Biophys. J.* **87**, 2215–2220 (2004).

262. Copeland, R. A. The drug-target residence time model: a 10-year retrospective. *Nat. Rev. Drug Discov.* **15**, 87–95 (2015).

263. Goldstein, B. et al. Competition between solution and cell surface receptors for ligand. Dissociation of hapten bound to surface antibody in the presence of solution antibody. *Biophys. J.* **56**, 955–966 (1989).

264. Berg, H. C. & Purcell, E. M. Physics of chemoreception. *Biophys. J.* **20**, 193–219 (1977).

265. Rice, M. E. & Cragg, S. J. Dopamine Spillover after Quantal Release: Rethinking Dopamine Transmission in the Nigrostriatal Pathway. *Brain Res. Rev.* **58**, 303-313 (2008).

266. Özçete, Ö. D., Banerjee, A. & Kaeser, P. S. Mechanisms of neuromodulatory volume transmission. *Mol. Psychiatry* **29**, 3680–3693 (2024).

267. Cragg, S. J. & Rice, M. E. DAncing past the DAT at a DA synapse. *Trends Neurosci.* **27**, 270–277 (2004).

268. Khan, Z. U., Mrzljak, L., Gutierrez, A., de la Calle, A. & Goldman-Rakic, P. S. Prominence of the dopamine D2 short isoform in dopaminergic pathways. *Proc. Natl. Acad. Sci.* **95**, 7731–7736 (1998).

269. Yung, K. K. L. et al. Immunocytochemical localization of D1 and D2 dopamine receptors in the basal ganglia of the rat: Light and electron microscopy. *Neuroscience* **65**, 709–730 (1995).

270. Delle Donne, K. T., Sesack, S. R. & Pickel, V. M. Ulrastructural immunocytochemical localization of the dopamine D2 receptor within GABAergic neurons of the rat striatum. *Brain Res.* **746**, 239–255 (1997).

271. Nirenberg, M., Vaughan, R., Uhl, G., Kuhar, M. & Pickel, V. The dopamine transporter is localized to dendritic and axonal plasma membranes of nigrostriatal dopaminergic neurons. *J. Neurosci.* **16**, 436–447 (1996).

272. Ciliax, B. et al. The dopamine transporter: immunochemical characterization and localization in brain. . *J. Neurosci.* **15**, 1714–1723 (1995).

273. Ford, C. P., Phillips, P. E. M. & Williams, J. T. The time course of dopamine transmission in the ventral tegmental area. *J. Neurosci.* **29**, 13344–13352 (2009).

274. Maynard, S. A., Ranft, J. & Triller, A. Quantifying postsynaptic receptor dynamics: insights into synaptic function. *Nat. Rev. Neurosci.* **24**, 4–22 (2023).

275. Ladepeche, L. et al. Single-molecule imaging of the functional crosstalk between surface NMDA and dopamine D1 receptors. *Proc. Natl. Acad. Sci. U S A* **110**, 18005–18010 (2013).

276. Triller, A., Cluzeaud, F., Pfeiffer, F., Betz, H. & Korn, H. Distribution of glycine receptors at central synapses: an immunoelectron microscopy study. *J. Cell Biol.* **101**, 683–688 (1985).

277. Nusser, Z., Hájos, N., Somogyi, P. & Mody, I. Increased number of synaptic GABAA receptors underlies potentiation at hippocampal inhibitory synapses. *Nature* **395**, 172–177 (1998).

278. Frank, E. & Fischbach, G. D. Early events in neuromuscular junction formation in vitro: induction of acetylcholine receptor clusters in the postsynaptic membrane and morphology of newly formed synapses. *J. Cell. Biol.* **83**, 143–58 (1979).

279. Andrews, S. S. Serial rebinding of ligands to clustered receptors as exemplified by bacterial chemotaxis. *Phys. Biol.* **2**, 111–122 (2005).

280. Fyfe, T. J. et al. Structure–Kinetic Profiling of Haloperidol Analogues at the Human Dopamine D 2 Receptor. *J. Med. Chem.* **62**, 9488–9520 (2019).

281. Free, R. B. et al. Identification and Characterization of ML321: A Novel and Highly Selective D 2 Dopamine Receptor Antagonist with Efficacy in Animal Models That Predict Atypical Antipsychotic Activity. *ACS Pharmacol. Transl. Sci.* **6**, 151–170 (2023).

282. Packeu, A., De Backer, J.-P., Van Liefde, I., Vanderheyden, P. M. L. & Vauquelin, G. Antagonist-radioligand binding to D2L-receptors in intact cells. *Biochem. Pharmacol.* **75**, 2192–2203 (2008).

283. Wennerberg, M., Balendran, A., Clapham, J. C. & Vauquelin, G. Unravelling the complex dissociation of [3 H]-rimonabant from plated CB 1 cannabinoid receptor-expressing cells. *Fundam. Clin. Pharmacol.* **24**, 181–187 (2010).

284. Takeuchi, H., Mori, Y. & Tsutsumi, Y. Pathophysiology, prognosis and treatment of tardive dyskinesia. *Ther. Adv. Psychopharmacol.* **12**, doi:10.1177/20451253221117313 (2022).

285. Soares-Weiser, K. & Fernandez, H. H. Tardive dyskinesia. *Semin. Neurol.* **27**, 159–169 (2007).

286. Zutshi, D., Cloud, L. J. & Factor, S. A. Tardive Syndromes are Rarely Reversible after Discontinuing Dopamine Receptor Blocking Agents: Experience from a University-based Movement Disorder Clinic. *Tremor and Other Hyperkinet. Mov.* **4**, 266 (2014).

287. Waln, O., Jankovic, J., Cambridge, H., Arnold, W. & & Wilkins, W.-B. Reviews An Update on Tardive Dyskinesia: From Phenomenology to Treatment History and Definitions. *Tremor and Other Hyperkinet. Mov.* **3**, doi:10.7916/D88P5Z71 (2013).

288. Cornett, E. M., Novitch, M., Kaye, A. D., Kata, V. & Kaye, A. M. Medication-Induced Tardive Dyskinesia: A Review and Update. *Ochsner J.* **17**, 162-174 (2017).

289. Teo, J. T., Edwards, M. J. & Bhatia, K. Tardive dyskinesia is caused by maladaptive synaptic plasticity: A hypothesis. *Mov. Disord.* **27**, 1205–1215 (2012).

290. Creese, I., Burt, D. R. & Snyder, S. H. Dopamine receptor binding enhancement accompanies lesion-induced behavioral supersensitivity. *Science* **197**, 596–598 (1977).

291. Rogue, P., Hanauer, A., Zwiller, J., Malviya, A. N. & Vincendon, G. Up-regulation of dopamine D2 receptor mRNA in rat striatum by chronic neuroleptic treatment. *Eur. J. Pharmacol.* **207**, 165–168 (1991).

292. Seeger, T. F., Thal, L. & Gardner, E. L. Behavioral and biochemical aspects of neuroleptic-induced dopaminergic supersensitivity: Studies with chronic clozapine and haloperidol. *Psychopharmacology* **76**, 182–187 (1982).

293. Turrone, P., Remington, G., Kapur, S. & Nobrega, J. N. The relationship between dopamine D2 receptor occupancy and the vacuous chewing movement syndrome in rats. *Psychopharmacology* **165**, 166–171 (2002).

294. Ellison, G. & See, R. E. Rats administered chronic neuroleptics develop oral movements which are similar in form to those in humans with tardive dyskinesia. *Psychopharmacology* **98**, 564–566 (1989).

295. Andersson, U. et al. Striatal binding of11C-NMSP studied with positron emission tomography in patients with persistent tardive dyskinesia: no evidence for altered dopamine D2 receptor binding. *J. Neural Transm.* **79**, 215–226 (1990).

296. Blin, J. et al. Striatal dopamine D2 receptors in tardive dyskinesia: PET study. *J. Neurol. Neurosurg. Psychiatry* **52**, 1248 (1989).

297. Ward, K. M. & Citrome, L. Antipsychotic-Related Movement Disorders: Drug-Induced Parkinsonism vs. Tardive Dyskinesia—Key Differences in Pathophysiology and Clinical Management. *Neurol. Ther*. **7**, 233–248 (2018).

298. Stahl, S. M. Mechanism of action of vesicular monoamine transporter 2 (VMAT2) inhibitors in tardive dyskinesia: reducing dopamine leads to less “go” and more “stop” from the motor striatum for robust therapeutic effects. *CNS Spectr.* **23**, 1–6 (2018).

299. Patel, R. S. et al. A systematic review on treatment of tardive dyskinesia with valbenazine and deutetrabenazine. *Ther. Adv. Psychopharmacol.* **9**, doi:10.1177/2045125319847882 (2019).

300. Michel, M. C. et al. Selective regulation of β1-and β2-adrenoceptors in the human heart by chronic β-adrenoceptor antagonist treatment. *Br. J. Pharmacol.* **94**, 685–692 (1988).

301. Hedberg, A., Gerber, J. G., Nies, A. S, Wolfe B. B. & Molinoff, P. B. Effects of pindolol and propranolol on beta adrenergic receptors on human lymphocytes. CiteseerA Hedberg, JG Gerber, AS Nies, BB Wolfe, PB Molinoff. *J. Pharmacol. Exp. Ther.* **239**, 117-123 (1986).

302. Van den Meiracker, A. H. et al. Hemodynamic and β-adrenergic receptor adaptations during long-term β-adrenoceptor blockade: Studies with acebutolol, atenolol, pindolol, and propranolol in hypertensive patients. *Circulation* **80**, 903–914 (1989).

303. Aarons, R. D. & Molinoff, P. B. Changes in the density of beta adrenergic receptors in rat lymphocytes, heart and lung after chronic treatment with propranolol. *J. Pharmacol. Exp. Ther.* **221**, 439-443.

304. C. Fibiger, H. & G. Lloyd, K. Neurobiological substrates of tardive dyskinesia: the GABA hypothesis. *Trends Neurosci.* **7**, 462–464 (1984).

305. Leucht, S., Wahlbeck, K., Hamann, J. & Kissling, W. New generation antipsychotics versus low-potency conventional antipsychotics: a systematic review and meta-analysis. *Lancet* **361**, 1581–1589 (2003).

306. Pardis, P., Remington, G., Panda, R., Lemez, M. & Agid, O. Clozapine and tardive dyskinesia in patients with schizophrenia: A systematic review. *J. Psychopharmacol.* **33**, 1187–1198 (2019).

307. Mentzel, T. Q. et al. Clozapine monotherapy as a treatment for antipsychotic-induced tardive dyskinesia: A meta-analysis. *J. Clin. Psychiatry* **79**, doi:10.4088/JCP.17r11852 (2018).

308. Prou, D. et al. Intracellular retention of the two isoforms of the D2 dopamine receptor promotes endoplasmic reticulum disruption. *J. Cell Sci.* **114**, 3517–3527 (2001).

309. Takeuchi, Y. & Fukunaga, K. Differential subcellular localization of two dopamine D 2 receptor isoforms in transfected NG108-15 cells. *J. Neurochem.* **85**, 1064–1074 (2003).

310. Fishburn, C. S., Elazar, Z. & Fuchs, S. Differential Glycosylation and Intracellular Trafficking for the Long and Short Isoforms of the D2 Dopamine Receptor. *J. Biol. Chem.* **270**, 29819–29824 (1995).

311. Xu, R., Hranilovic, D., Fetsko, L. A., Bucan, M. & Wang, Y. Dopamine D2S and D2L receptors may differentially contribute to the actions of antipsychotic and psychotic agents in mice. *Mol. Psychiatry* **7**, 1075–1082 (2002).

312. Van Craenenbroeck, K. et al. Folding Efficiency Is Rate-limiting in Dopamine D4 Receptor Biogenesis. *J. Biol. Chem.* **280**, 19350–19357 (2005).

313. Zhang, M. & Wu, G. Mechanisms of the anterograde trafficking of GPCRs: Regulation of AT1R transport by interacting proteins and motifs. *Traffic* **20**, 110–120 (2019).

314. Couturier, C., Deprez, B., Vrecl, M. & Davies, J. S. Setting up a bioluminescence resonance energy transfer high throughput screening assay to search for protein/protein interaction inhibitors in mammalian cells. *Front. Endocrinol.* **11**, doi:10.3389/fendo.2012.00100 (2012).

315. Herenbrink, C. K. et al. The role of kinetic context in apparent biased agonism at GPCRs. *Nat. Commun.* **7**, 1–14 (2016).

316. Shuklinova, O., Dorożyński, P., Kulinowski, P. & Polak, S. Quality Control Dissolution Data Is Biopredictive for a Modified Release Ropinirole Formulation: Virtual Experiment with the Use of Re-Developed and Verified PBPK Model. *Pharmaceutics* **14**, 1514 (2022).

317. Wang, N. N. et al. ADME Properties Evaluation in Drug Discovery: Prediction of Caco-2 Cell Permeability Using a Combination of NSGA-II and Boosting. *J. Chem. Inf. Model.* **56**, 763–773 (2016).

318. Ritchie, M., Tchistiakova, L. & Scott, N. Implications of receptor-mediated endocytosis and intracellular trafficking dynamics in the development of antibody drug conjugates. *MAbs* **5**, 13 (2013).

319. Peluso, M. J., Lewis, S. W., Barnes, T. R. E. & Jones, P. B. Extrapyramidal motor side-effects of first- and second-generation antipsychotic drugs. *Br. J. Psychiatry* **200**, 387–392 (2012).

320. Tacke, R. et al. Sila-haloperidol, a silicon analogue of the dopamine (D2) receptor antagonist haloperidol: synthesis, pharmacological properties, and metabolic fate. *ChemMedChem* **3**, 152–164 (2008).

321. Karelson, M. et al. QSAR study of pharmacological permeabilities. *General Papers ARKIVOC* **2**, 218–238 (2009).

322. Huang, S. & Wang, Y. Golgi structure formation, function, and post-translational modifications in mammalian cells. *F1000Res.* **6**, doi:10.12688/f1000research.11900.1 (2017).

323. Paul, D. et al. Cell surface protein aggregation triggers endocytosis to maintain plasma membrane proteostasis. *Nat. Commun.* **14**, doi:10.1038/s41467-023-36496-y (2023).

324. Hutagalung, A. H. & Novick, P. J. Role of Rab GTPases in Membrane Traffic and Cell Physiology. *Physiol. Rev.* **91**, 119-149 (2011).

325. Lu, S., Jang, W., Inoue, A. & Lambert, N. Constitutive G protein coupling profiles of understudied orphan GPCRs. *PLoS One* **16**, doi:10.1371/journal.pone.0247743 (2021).

326. Zhao, P. et al. Protein kinase D and Gβγ mediate sustained nociceptive signaling by biased agonists of protease-activated receptor-2. *J. Biol. Chem.* **294**, 10649–10662 (2019).

327. Latorre, R. et al. Mice expressing fluorescent PAR2 reveal that endocytosis mediates colonic inflammation and pain. *Proc. Natl. Acad. Sci.* **119**, (2022).

328. Tiulpakov, A. et al. Mutations of Vasopressin Receptor 2 Including Novel L312S Have Differential Effects on Trafficking. *Mol. Endocrinol.* **8**, 889– 904 (2016).

329. Lan, T. H., Liu, Q., Li, C., Wu, G. & Lambert, N. A. Sensitive and High Resolution Localization and Tracking of Membrane Proteins in Live Cells with BRET. *Traffic* **13**, 1450–1456 (2012).

330. Chen, Q. & Tesmer, J. J. G. G protein–coupled receptor interactions with arrestins and GPCR kinases: The unresolved issue of signal bias. *J. Biol. Chem.* **298**, doi: 10.1016/j.jbc.2022.102279 (2022).

331. Sánchez-Soto, M. et al. G Protein-Coupled Receptor Kinase 2 Selectively Enhances β-Arrestin Recruitment to the D2 Dopamine Receptor through Mechanisms That Are Independent of Receptor Phosphorylation. *Biomolecules* **13**, doi: 10.3390/biom13101552 (2023).

332. de Vries, L., Finana, F., Cathala, C., Ronsin, B. & Cussac, D. Innovative bioluminescence resonance energy transfer assay reveals differential agonist-induced D2 receptor intracellular trafficking and arrestin-3 recruitment. *Mol. Pharmacol.* **96**, 308–319 (2019).

333. Mohan, M. L., Vasudevan, N. T., Gupta, M. K., Martelli, E. E. & Prasad, S. V. N. G-Protein Coupled Receptor Resensitization – Appreciating the Balancing Act of Receptor Function. *Curr. Mol. Pharmacol.* **5**, 350–361 (2013).

334. Holtbäck, U. et al. Receptor recruitment: A mechanism for interactions between G protein-coupled receptors. *Proc. Natl. Acad. Sci. U S A* **96**, 7271-7275 (1999).

335. Cahill, C. M. et al. Prolonged Morphine Treatment Targets δ Opioid Receptors to Neuronal Plasma Membranes and Enhances δ-Mediated Antinociception. *J. Neurosci.* **21**, 7598-7607 (2001).

336. Lohmann, C., Hüwel, S. & Galla, H. J. Predicting blood-brain barrier permeability of drugs: evaluation of different in vitro assays. *J. Drug Target.* **10**, 263–276 (2002).

337. Umek, N., Geršak, B., Vintar, N., Šoštarič, M. & Mavri, J. Dopamine Autoxidation Is Controlled by Acidic pH. *Front. Mol. Neurosci*. **11**, doi:10.3389/fnmol.2018.00467 (2018).

338. The, H. P. et al. In silico prediction of caco-2 cell permeability by a classification QSAR approach. *Mol. Inform.* **30**, 376–385 (2011).

339. Wu, G. Regulation of Post-Golgi Traffic of G Protein-Coupled Receptors. *Subcell. Biochem.* **63**, 83-95 (2012).

340. Punnonen, E.-L., Ryhänen, K. & Marjomi, V. S. At reduced temperature, endocytic membrane traffic is blocked in multivesicular carrier endosomes in rat cardiac myocytes. *Eur. J. Cell Biol.* **75**, 344–352 (1998).

341. Selcuk, M. Safe and Effective Use of Low-Dose Clozapine for Tardive Dyskinesia in a Patient with Schizophrenia and Comorbid Epilepsy: A Case Report. *Psychiatry Clin. Psychopharmacol.* **33**, 143–146 (2023).

342. Strange, P. G. Mechanisms of inverse agonism at G-protein-coupled receptors. *Trends Pharmacol. Sci.* **23**, 89–95 (2002).

343. Lane, J. R. et al. Distinct inactive conformations of the dopamine D2 and D3 receptors correspond to different extents of inverse agonism. *Elife* **9**, doi:10.7554/eLife.52189. (2020).

344. Tadokoro, S. et al. Chronic Treatment With Aripiprazole Prevents Development of Dopamine Supersensitivity and Potentially Supersensitivity Psychosis. *Schizophr. Bull.* **38**, 1012–1020 (2012).

345. Charron, A., Hage, C. El, Servonnet, A. & Samaha, A.-N. 5-HT2 receptors modulate the expression of antipsychotic-induced dopamine supersensitivity. *Eur. Neuropsychopharmacol.* **25**, 2381–2393 (2015).

346. Hashimoto, T. et al. Lack of dopamine supersensitivity in rats after chronic administration of blonanserin: Comparison with haloperidol. *Eur. J. Pharmacol.* **830**, 26–32 (2018).

347. Thompson, I. A., de Vries, E. F. J. & Sommer, I. E. C. Dopamine D2 up-regulation in psychosis patients after antipsychotic drug treatment. *Curr. Opin. Psychiatry* **33**, 200–205 (2020).

348. Seeman, P. et al. Dopamine supersensitivity correlates with D2 High states, implying many paths to psychosis. *Proc. Natl. Acad. Sci. U S A* **102**, 3513–3518 (2005).

349. Gardos, G. et al. Anticholinergic challenge and neuroleptic withdrawal: changes in dyskinesia and symptom measures. *Arch. Gen. Psychiatry* **41**, 1030-1035 (1984)

350. Yagi, G., Itoh, H. Follow-up study of 11 patients with potentially reversible tardive dyskinesia. europepmc.org G Yagi, H Itoh. A*m. J. Psychiatry* **144**, 1496-1498 (1987).

351. Glazer, W. M., Morgenstern, H., Schooler, N., Berkman, C. S. & Moore, D. C. Predictors of improvement in tardive dyskinesia following discontinuation of neuroleptic medication. *Br. J. Psych.* **157**, 585-592 (1990).

352. Fernandez, H. H., Krupp, B. & Friedman, J. H. The course of tardive dyskinesia and parkinsonism in psychiatric inpatients: 14-Year follow-up. *Neurology* **56**, 805–807 (2001).

353. Li, Z.-M., Fan, Z.-L., Wang, X.-Y. & Wang, T.-Y. Factors Affecting the Expression of Recombinant Protein and Improvement Strategies in Chinese Hamster Ovary Cells. *Front. Bioeng. Biotechnol.* **10**, (2022).

354. Yong, J. et al. Mitochondria supply ATP to the ER through a mechanism antagonized by cytosolic Ca2+. *Elife* **8**, doi:10.7554/eLife.49682 (2019).

355. Alber, A. B. & Suter, D. M. Dynamics of protein synthesis and degradation through the cell cycle. *Cell Cycle* **18**, 784–794 (2019).

356. Morello, J.-P. et al. Pharmacological chaperones rescue cell-surface expression and function of misfolded V2 vasopressin receptor mutants. *J. Clin. Invest.* **105**, 887–895 (2000).

357. Bairoch, A. The Cellosaurus, a Cell-Line Knowledge Resource. *J. Biomol. Tech.* **29**, 25–38 (2018).

358. Kim, T. K. & Eberwine, J. H. Mammalian cell transfection: the present and the future. *Anal. Bioanal. Chem.* **397**, 3173–3178 (2010).

359. Kaur, G. & Dufour, J. M. Cell lines. *Spermatogenesis* **2**, 1–5 (2012).

360. Capes-Davis, A. et al. Cell Lines as Biological Models: Practical Steps for More Reliable Research. *Chem. Res. Toxicol.* **32**, 1733–1736 (2019).

361. Bigbee, J. W. Cells of the Central Nervous System: An Overview of Their Structure and Function. *Adv. Neurobiol.* **29**, 41–64 (2023).

362. Gordon, J., Amini, S. & White, M. K. General Overview of Neuronal Cell Culture. *Methods Mol. Biol.* **1078**, 1–8 (2013).

363. Harry, G. J. et al. In vitro techniques for the assessment of neurotoxicity. *Environ. Health Perspect.* **106**, 131–158 (1998).

364. Zhang, J. et al. Recent progresses in novel in vitro models of primary neurons: A biomaterial perspective. *Front. Bioeng. Biotechnol.* **10**, doi:10.3389/fbioe.2022.953031 (2022).

365. Sahu, M. P., Nikkilä, O., Lågas, S., Kolehmainen, S. & Castrén, E. Culturing primary neurons from rat hippocampus and cortex. *Neuronal Signal.* **3**, doi:10.1042/NS20180207 (2019).

366. Pfrieger, F. W. & Barres, B. A. Synaptic Efficacy Enhanced by Glial Cells in Vitro. *Science (1979)* **277**, 1684–1687 (1997).

367. Luchena, C. et al. A Neuron, Microglia, and Astrocyte Triple Co-culture Model to Study Alzheimer's Disease. *Front. Aging Neurosci.* **14**, (2022).

368. Enright, H. A. et al. Functional and transcriptional characterization of complex neuronal co-cultures. *Sci. Rep.* **10**, 11007 (2020).

369. Naia, L. & Rego, A. C. Isolation and Maintenance of Striatal Neurons. *Bio. Protoc.* **8**, doi: 10.21769/BioProtoc.2823 (2018).

370. Valian, N., Heravi, M., Ahmadiani, A. & Dargahi, L. Comparison of Rat Primary Midbrain Neurons Cultured in DMEM/F12 and Neurobasal Mediums. Basic Clin. Neurosci. **12**, 205–212 (2021).

371. Meucci, O. et al. Chemokines regulate hippocampal neuronal signaling and gp120 neurotoxicity. *Proc. Natl. Acad. Sci. U S A* **95**, 14500–14505 (1998).

372. Khan, M. Z. et al. Regulation of neuronal P53 activity by CXCR4. *Mol. Cell. Neurosci.* **30**, 58–66 (2005).

373. Shimizu, S., Abt, A. & Meucci, O. Bilaminar Co-culture of Primary Rat Cortical Neurons and Glia. *J. Vis. Exp.* **57**, doi:10.3791/3257 (2011).

374. Chen, G. & Obal, D. Detecting and measuring of GPCR signaling – comparison of human induced pluripotent stem cells and immortal cell lines. *Front. Endocrinol.* **14**, (2023).

375. Sriram, K. & Insel, P. A. G Protein-Coupled Receptors as Targets for Approved Drugs: How Many Targets and How Many Drugs? *Mol. Pharmacol.* **93**, 251–258 (2018).

376. Fish, K. N. Total Internal Reflection Fluorescence (TIRF) Microscopy. *Curr. Protoc. Cytom.* **50**, doi:10.1002/0471142956.cy1218s50 (2009).

377. Kudalkar, E. M., Davis, T. N. & Asbury, C. L. Single-Molecule Total Internal Reflection Fluorescence Microscopy. *Cold Spring Harb. Protoc.* **2016**, doi:10.1101/pdb.top077800 (2016).

378. Masri, B. et al. Antagonism of dopamine D2 receptor/β-arrestin 2 interaction is a common property of clinically effective antipsychotics. *Proc. Natl. Acad. Sci.* **105**, 13656–13661 (2008).

379. Sulzer, D., Trudeau, L.-E. & Rayport, S. *Postnatally Derived Ventral Midbrain Dopamine Neuron Cultures as a Model System for Studying Neurotoxicity and Parkinson's Disease. in Parkinson's Disease* 491–504 (Elsevier, 2008). doi:10.1016/B978-0-12-374028-1.00037-3.

380. Kaech, S. & Banker, G. Culturing hippocampal neurons. *Nat. Protoc.* **1**, 2406–2415 (2006).

381. Ludwig, P. E. & Das, J. M. *Histology, Glial Cells.* (StatPearls, FL) (2023).

382. Mao, L. & Wang, J. Q. *Primary Striatal Neuronal Culture. in Drugs of Abuse* (Humana Press, NY) doi:10.1385/1-59259-358-5:379 (2003).

383. Facci, L. & Skaper, S. D. Culture of Rodent Cortical, Hippocampal, and Striatal Neurons. *Methods Mol. Biol.* **1727**, doi:10.1007/978-1-4939-7571-6_3 (2018).

384. Malina, I., Kampars, V., Turovska, B. & Belyakov, S. Novel green-yellow-orange-red light emitting donor-π-acceptor type dyes based on 1,3-indandione and dimedone moieties. *Dyes and Pigments* **139**, 820–830 (2017).

385. Zalejski, J., Sun, J. & Sharma, A. Unravelling the Mystery inside Cells by Using Single-Molecule Fluorescence Imaging. *J. Imaging* **9**, doi:10.3390/jimaging9090192 (2023).

386. Matsuda, T. & Oinuma, I. Imaging endogenous synaptic proteins in primary neurons at single-cell resolution using CRISPR/Cas9. *Mol. Biol. Cell* **30**, 2838–2855 (2019).

387. Ioannou, M. S., Liu, Z. & Lippincott-Schwartz, J. A Neuron-Glia Co-culture System for Studying Intercellular Lipid Transport. *Curr. Protoc. Cell Biol.* **84**, doi:10.1002/cpcb.95 (2019).

388. Roqué, P. J. & Costa, L. G. Co-Culture of Neurons and Microglia. *Curr. Protoc. Toxicol.* **74**, doi:10.1002/cptx.32 (2017).

389. Penrod, R. D., Campagna, J., Panneck, T., Preese, L. & Lanier, L. M. The presence of cortical neurons in striatal-cortical co-cultures alters the effects of dopamine and BDNF on medium spiny neuron dendritic development. *Front. Cell. Neurosci.* **9**, doi:10.3389/fncel.2015.00269 (2015).

390. Banker, G. & Goslin, K. *Culturing Nerve Cells*. (The MIT Press, 1998). doi:10.7551/mitpress/4913.001.0001.

391. Penrod, R. D., Kourrich, S., Kearney, E., Thomas, M. J. & Lanier, L. M. An embryonic culture system for the investigation of striatal medium spiny neuron dendritic spine development and plasticity. *J. Neurosci. Methods* **200**, 1–13 (2011).

392. Khakh, B. S. Astrocyte–Neuron Interactions in the Striatum: Insights on Identity, Form, and Function. *Trends Neurosci.* **42**, 617–630 (2019).

393. Ventimiglia, R., Mather, P. E., Jones, B. E. & Lindsay, R. M. The NeurotroDhins BDNF, NT-3 and NT-4/5 Promote Survival and Morphological and Biochemical Differentiation of Striatal Neurons In Vitro. *Eur. J. Neurosci.* **7**, 213–222 (1995).

394. Widmer, H. R. & Hefti, F. Neurotrophin-4/5 Promotes Survival and Differentiation of Rat Striatal Neurons Developing in Culture. *Eur. J. Neurosci.* **6**, 1669–1679 (1994).

395. Mizuno, K., Carnahan, J. & Nawa, H. Brain-Derived Neurotrophic Factor Promotes Differentiation of Striatal GABAergic Neurons. *Dev. Biol.* **165**, 243–256 (1994).

396. Shi, M. et al. Glia co-culture with neurons in microfluidic platforms promotes the formation and stabilization of synaptic contacts. *Lab Chip* **13**, 3008 (2013).

397. Majumdar, D., Gao, Y., Li, D. & Webb, D. J. Co-culture of neurons and glia in a novel microfluidic platform. *J. Neurosci. Methods* **196**, 38–44 (2011).

398. Sharma, S. Das et al. Astrocytes mediate cell non-autonomous correction of aberrant firing in human FXS neurons. *Cell Rep.* **42**, doi:10.1016/j.celrep.2023.112344 (2023).

399. Huck, J. H. et al. De Novo Expression of Dopamine D2 Receptors on Microglia after Stroke. *J. Cereb. Blood Flow Metab.* **35**, 1804–1811 (2015).

400. Fischel's, S. V. & Medzihradsky, F. Assessment of membrane permeability in primary cultures of neurons and glia in response to osmotic perturbation. *J. Neurosci. Res.* **13**, 369–380 (1985).

401. van Niekerk, E. A. et al. Methods for culturing adult CNS neurons reveal a CNS conditioning effect. *Cell Rep. Methods* **2**, doi:10.1016/j.crmeth.2022.100255 (2022).

402. Eide, L. & McMurray, C. T. Culture of Adult Mouse Neurons. *Biotechniques* **38**, 99–104 (2005).

403. Varrone, A., Bundgaard, C. & Bang-Andersen, B. PET as a Translational Tool in Drug Development for Neuroscience Compounds. *Clin. Pharmacol. Ther.* **111**, 774–785 (2022).

404. Stone, J. M., Davis, J. M., Leucht, S. & Pilowsky, L. S. Cortical Dopamine D2/D3 Receptors Are a Common Site of Action for Antipsychotic Drugs--An Original Patient Data Meta-analysis of the SPECT and PET In Vivo Receptor Imaging Literature. *Schizophr. Bull*. **35**, 789–797 (2009).

405. Ejdrup, A. L. et al. A density-based enrichment measure for assessing colocalization in single-molecule localization microscopy data. *Nat Commun*. **13**, doi:10.1038/s41467-022-32064-y (2022).

406. Zych, S. M. & Ford, C. P. Divergent properties and independent regulation of striatal dopamine and GABA co-transmission. *Cell Rep*. **39**, doi:10.1016/j.celrep.2022.110823 (2022).

APPENDIX: PIPS REFLECTIVE STATEMENT

Note to examiners:

This statement is included as an appendix to the thesis in order that the thesis accurately captures the PhD training experienced by the candidate as a BBSRC Doctoral Training Partnership student.

The Professional Internship for PhD Students is a compulsory 3-month placement which must be undertaken by DTP students. It is usually centred on a specific project and must not be related to the PhD project. This reflective statement is designed to capture the skills development which has taken place during the student's placement and the impact on their career plans it has had.

PIPS Reflective Statement

My three-month placement was at Sygnature Discovery in the Bioscience department. I worked on a neuroscience project investigating brain biomarkers in mice (control and transgenic disease model). The aim of the project was to develop and optimise an assay to determine whether specific brain biomarkers were elevated in transgenic animals compared to control animals. This would expand the set of neuroscience assays that Sygnature Discovery could offer to clients.

At the start of my placement, I had several days of training before starting in the lab including learning how to use the electronic lab notebook system that all Sygnature Scientists use to keep a detailed log of every experiment performed. Although this was a big change to how I usually keep records of completed experiments, I found it an efficient system that meant clear protocols were created which enabled others who may later join a project to easily understand past experiments and protocols. This concept has influenced the way I keep record of experiments and protocols during my PhD as I found keeping a thorough electronic record in addition to physical lab books a much more effective way of organising my project. In addition, before starting my project my

supervisor at Sygnature Discovery, Tatianna Rosenstock, trained me in cell viability assays. This was a great experience as I was able to learn how to run a new assay as well as how to culture the neuronal cell line, SH-SY5Y.

Over the three months, I set up an automated immunoassay, that allowed for the detection of brain biomarkers in three different areas of mice brain in control and transgenic mice. For the initial optimisation of this assay, on-site control animals were used. The brain tissue was homogenised in two different buffers and samples were loaded at three different concentrations using two primary antibody dilutions to establish the optimal set up where the maximum signal was produced. This initial assay was also performed in a multiplex format where different primary antibodies against different brain biomarkers were used to probe the same sample, allowing the collection of more data per sample. These primary antibodies were associated with different secondary antibodies that were detectable in different channels. Unfortunately, we saw that there was poor linearity across the sample titrations. To troubleshoot this, we tried performing the assay in a non-multiplexed format to eliminate any potential secondary antibody cross-linking leading to poor linearity. This did not improve the linearity so we then hypothesised that the sample may have been inadequately homogenised. To address this, I re-homogenised the samples using a needle and then repeated the assay. This further homogenisation step improved the linearity across sample titrations.

We then moved on to performing these immunoassays in the transgenic mice and their associated controls. Here, we used a single concentration of sample lysate, buffer and antibody according to the previous optimisation experiments. There were significantly higher levels of biomarkers in transgenic mice over the controls which validated this assay for detecting an upregulation of protein between groups. However, there was variation in the biomarker signals between animals. To ensure the variation seen between animals was not due to different lysate concentrations (despite the same homogenisation process), I thought it would be helpful to perform a RePlex assay. Here, antibodies are first stripped from the capillaries following the completion of an

immunoassay, before the RePlex total protein assay is carried out using the same samples. The biomarker signal can then be normalised to the exact concentration of protein lysate loaded. The RePlex kit was unfortunately due to arrive following the end of my placement, so this idea was taken forward by other scientists at Sygnature Discovery.

During my placement, I successfully established an immunoassay to detect brain biomarkers in transgenic mice versus their associated controls. Having never performed an immunoassay before, I learned about the concept of using primary and secondary antibodies for protein detection. I was specifically trained in two new assays (Western Blot and an automated immunoassay) which further developed my laboratory skills. I also developed my problem-solving skills through the process of optimising the automated immunoassay which required broader thinking to solves issues with sample linearity. In addition, I attended a biostats training course during my placement which gave a helpful overview of the specific statistical tests to use when analysing different data sets. This was not only useful during my placement but allowed me to think further about the statistical tests that would be best suited to the data I collected during my PhD.

My placement at Sygnature Discovery gave me the opportunity to see how a contract research organisation operates. I was also able to talk to scientists there about the different types of client projects that they are involved in which gave me an understanding of the current areas of interest in industry.